THE STRUCTURE – PERMEABILITY RELATION OF TEXTILE REINFORCEMENTS

Richard Loendersloot

Luctor et emergo

De promotiecommissie is als volgt samengesteld:

Voorzitter en secretaris:
Prof.dr.ir. H. Tijdeman — Universiteit Twente

Promotor:
Prof.dr.ir. R. Akkerman — Universiteit Twente

Leden (in alfabetische volgorde):
Prof.dr.ir. R. Benedictus — Technische Universiteit Delft
Prof.dr.ir. H.W.M. Hoeijmakers — Universiteit Twente
Prof. S.V. Lomov — Katholieke Universiteit Leuven
Prof.dr.ir. M.M.C.G. Warmoeskerken — Universiteit Twente

Deskundige:
Ir. H.G.S.J. Thuis — Nationaal Lucht– en Ruimtevaart laboratorium

This research project is performed in the framework of the UT–NLR project 'RTM', is supported by the EU project FALCOM and is partly performed in the framework of a EU funded Marie Curie Fellowship project at the KU Leuven.

The Structure–Permeability Relation of Textile Reinforcements
Loendersloot, Richard
PhD–Thesis, University of Twente, Enschede, The Netherlands
April 2006

ISBN 90–365–2337–0

Printed by PrintPartners Ipskamp B.V, Enschede, The Netherlands

THE STRUCTURE – PERMEABILITY RELATION OF TEXTILE REINFORCEMENTS

PROEFSCHRIFT

ter verkrijging van
de graad van doctor aan de Universiteit Twente,
op gezag van de rector magnificus,
prof.dr. W.H.M. Zijm,
volgens besluit van het College van Promoties
in het openbaar te verdedigen
op donderdag 13 april 2006 om 15.00 uur

Richard Loendersloot

geboren 11 maart 1977

te Wierden

Dit proefschrift is goedgekeurd door de promotor

Prof.dr.ir. R. Akkerman

Summary

The limits of production processes of composites are explored increasingly. A higher performance and a higher quality are demanded at lower cost prices. Inevitably, a thorough understanding of the processes occurring during the production is essential to meet the imposed demands. The research presented here aims to increase the fundamental knowledge on a crucial part of the Resin Transfer Moulding (RTM) production technology: the impregnation behaviour of textile reinforcements. In RTM, a near–net–shaped, dry, textile preform is manufactured and placed in a closely fitting mould. Resin is subsequently injected, typically at a pressure varying between 2 and 10 bars relative to the atmospheric pressure. The textile reinforcement is made of a fibre bundle structure, which can either be a preform made of (a stack of) woven fabrics or Non–Crimp Fabrics (NCF), or be a preform manufactured employing automated preforming technologies such as braiding and fibre placement technologies.
The work is performed in the first place as part of a joint research effort between the National Aerospace Laboratories (NLR) and the University of Twente (UT). Secondly, the research project was supported by the European project FALCOM. Finally, the work was partly done in a Marie Curie Fellowship project at the KU Leuven. It was recognised that a more fundamental level of knowledge was required to solve production process related problems. The problems encountered comprised several issues, including the textile preform manufacturing and the subsequent impregnation behaviour using Resin Transfer Moulding technology (RTM).
The main problem in the application of the RTM process for structural and/or complex shaped products – as is the aim of the NLR – is a proper prediction of the permeability of the textile reinforcement. The attempts to define basic models with which the permeability can be predicted have stranded so far. The significant amount of variation in the measured permeability of comparable fabrics under comparable circumstances hampers the further development of predictive models.
Here, a methodology is described to predict not just the averaged permeability value, but also the possible variation due to variations in the internal geometry of the preform. It is believed that the variations in the measured permeability are not solely caused by experimental scatter, but are also caused by variations in the internal structure of the material at a relatively small length scale ($\approx$ 0.1mm).
The domain of this work is consequently linked to geometrical modelling and flow modelling. The interaction between both is crucial. Moreover, there is also a twofold pointing link with the field of textile forming: the effect of shear deformation – the

main deformation mode – on the geometry and on the variations in the geometrical structure, is also accounted for. It was recognised in earlier projects that the material properties and deformation properties are interrelated. Consequently, the link between the main deformation mode of textile preforms and the geometrical model is considered to be relevant.
The preform material is limited to the class of Non–Crimp Fabrics (NCF). A layer of this type of reinforcement consists of a number of plies of uni–directionally, but mutually differently oriented fibre bundles, stitched together by a warp knitting process. The stitch thread is small compared to the fabric and does not contribute to the mechanical properties other than that it increases the shape integrity of the material.
The geometrical model comprises of a description of the internal geometry of Non–Crimp Fabrics, based on the distortion induced by the stitch threads penetrating the fabric. The distortions are referred to as Stitch Yarn induced fibre Distortions (SYD). The fibre paths are locally distorted, resulting in a wedge shaped opening in the fabric. The dimensions of the SYDs were measured on different fabrics in undeformed and deformed state. A semi–empirical relation is established to relate the dimensionless width and length of the distortions to both the fabric properties and the amount of shear deformation.
The dimensions of the SYDs are not constant over the fabric, but exhibit a certain variation. It was found that a lognormal distribution of the widths and lengths applies better than a normal distribution. The lognormal distribution is understood from the physical limit on the width of the SYDs, set by the number and diameter of the stitch threads.
The dimensions of SYDs are in the order of millimetres and hence an order of magnitude larger than the space between the fibre filaments. As a result, the flow behaviour of resin through the fabric is dominated by these distortions. The flow model describes the methodology to transform the SYDs into flow channels, with interaction points through which the fluid can enter or leave the channel.
However, it is not sufficient to analyse a single SYD, vary its dimensions and use the averaged permeability as an estimated value of the permeability. It is shown that a network of flow channels is more appropriate to estimate the permeability and its variation. A network of flow channels, based on the measured dimensions of the SYDs is analysed.
The permeability is shown to be affected not only by the variation in the SYDs dimensions but also by the type of distribution. Clustering of large channels causes fast flow paths and hence a higher averaged permeability. The degree of order in the distribution of the widths consequently plays an important role in the value of the permeability. As a result, experimentally determined permeabilities of a single type of reinforcement, measured under equal conditions can differ by a factor of 2.5.
Permeability measurements are performed employing different test rigs. A relatively low amount of variation was found in results of the separate devices. The variation is within the limits set by the model for most cases. A mutual comparison of the result obtained with different test rigs reveals a large amount of variation. This is mainly attributed to the lack of a standardised measuring method for the permeability.

Samenvatting

De grenzen van de productie processen voor composiet materialen worden steeds verder verkend. Betere prestaties en een hogere kwaliteit worden geeist tegen een lagere kostprijs. Een diepgaande kennis van de processen die plaatsvinden tijdens de productie is essentieel om aan deze eisen te kunnen voldoen. Het onderzoek waarover dit proefschrift handelt, heeft tot doel de fundamentele kennis over een van de cruciale onderdelen van het Resin Transfer Moulding (RTM) productie proces uit te breiden: het impregnatie gedrag van de textiel versterkingsstructuur. De productvorm wordt gemaakt van droog vezelmateriaal. Dit voorgevormde vezelpakket wordt geplaatst in een nauw sluitende matrijs holte. Vervolgens wordt de hars geïnjecteerd in de gesloten matrijs holte met een druk van 2 tot 10 bar. De vezelversterking bestaat uit een vezelbundel structuur, hetzij opgebouwd uit afzonderelijke lagen weefsel of legsel (Non–Crimp Fabric, NCF), hetzij gemaakt met een behulp van geautomatiseerde technologieën zoals vlechten en "fibre placement".
Het werk is in de eerste plaats uitgevoerd als onderdeel van de samenwerkingsverband tussen het Nederlands Lucht– en Ruimtevaartlaboratorium (NLR) en de Universiteit Twente (UT). In de tweede plaats is het onderzoek deel van het Europese project FALCOM. Als laatste is een deel van het werk uitgevoerd op de KU Leuven in het kader van een Marie Curie Fellowship project.
Het was duidelijk dat een fundamenteler kennisniveau nodig was om problemen rond het productie proces op te lossen. De problemen hebben zowel betrekking op het fabriceren van de vezelversterking als op het impregnatie gedrag in het geval Resin Transfer Moulding (RTM) wordt toegepast.
Het grootste probleem bij het toepassen van het RTM proces voor structurele en/of complex gevormde producten – wat het doel is van het NLR – is een gedegen voorspelling van de permeabiliteit van de vezelversterking. De pogingen om basis modellen te definiëren waarmee de permeabiliteit kan worden voorspeld, zijn tot op heden gestrand. Een aanzienlijke hoeveelheid variatie in de permeabiliteit van vergelijkbare versterkingsmaterialen, gemeten onder vergelijkbare omstandigheden vormt een groot obstakel in de voortuitgang van de voorspellende modellen.
Een methodologie om niet slechts een gemiddelde permeabiliteits waarde te voorspellen, maar ook een indicatie van de variatie als gevolg van variaties in de interne geometrie van de vezelversterking wordt hier beschreven. Het grond idee is dat de variaties in de permeabiliteit niet enkel door experiment gerelateerde spreiding veroorzaakt worden, maar ook door variaties in de interne structuur van het materiaal op een relatief kleine

lengteschaal (≈ 0.1mm).
Dit werk is daarom gerelateerd aan zowel geometrie modellering als stromings modellering. De interactie tussen beide is cruciaal. Er is bovendien nog een link naar het onderzoeksgebeid van het textiel vervormingsgedrag: het effect van afschuifvervorming – het meest belangrijke vervormingstype – op de geometrie en op de variaties in de structuur van de geometrie is ook geanalyseerd. De resultaten van eerdere projecten hebben aangegeven dat materiaal eigenschappen en vervormings eigenschappen elkaar wederzijds beinvloeden. Bijgevolg wordt de link tussen het belangrijkste type vervorming van vezelversterkingen en het geometrisch model als relevant beschouwd.
Enkel materialen uit de klasse van de Non–Crimp Fabrics (NCF) zijn hier gebruikt. Een laag van dit versterkingsmateriaal bestaat uit een aantal uni–directionele lagen vezelmateriaal, die met een onderling verschillende orientatie zijn gestapeld en vervolgens aan elkaar gestikt zijn. De stikdraad is klein ten opzichte van de vezelbundels en heeft nagenoeg geen effect op de mechanische eigenschappen, anders dan dat het de vorm integriteit van het materiaal bevordert.
Het geometrische model bestaat uit een beschrijving van de interne geometry van Non–Crimp Fabrics, gebaseerd op de verstoring die de stikdraad veroorzaakt wanneer het door de vezellagen steekt. De verstoring worden “Stitch Yarn induced fibre Distortions” (SYD) genoemd. Het pad van de vezels wordt lokaal verstoord, wat resulteert in een wigvormige opening. De afmetingen van deze SYDs zijn voor verschillende types NCF gemeten in onvervormde en vervormde staat. Een semi–empirische relatie is afgeleid om de dimensieloze breedte en lengte van de verstoring aan zowel de materiaal eigenschappen en de hoeveelheid afschuiving te relateren.
De afmetingen van de SYDs zijn niet overal in het materiaal constant, maar vertonen een zekere variatie. Een lognormale verdeling van de breedtes en lengtes voldoet beter dan een normale verdeling. Dit wordt veroorzaakt door de minimale breedte van de SYDs, die bepaald wordt door het aantal en de diameter van de stikdraden in de SYD.
De afmetingen van de SYD zijn in de orde van millimeters, wat een orde van grootte groter is dan de ruimte tussen de vezelfilamenten waaruit een vezelbundel is opgebouwd. Het stromingsgedrag van de hars door het versterkingsmateriaal wordt derhalve bepaald door deze verstoringen. Het stromingsmodel beschrijft een methodologie om de SYDs te transformeren tot stroomkanaaltjes, die onderling verbonden zijn, zodat de vloeistof in en uit het kanaaltje kan stromen.
Het is echter niet voldoende om een enkele SYD te analyseren, haar afmetingen te varieren en de gemiddelde permeabiliteit als een geschatte waarde te gebruiken voor de permeabiliteit van de gehele NCF. Een netwerk van stroomkanaaltjes is beter geschikt om de permeabiliteit af te schatten. Een dergelijk netwerk is geconstrueerd op basis van de gemeten SYD afmetingen en vervolgens geanalyseerd.
Het is aangetoond dat de permeabiliteit niet alleen door de variatie in de afmetingen van de SYDs beïnvloed wordt, maar ook door de ruimtelijke verdeling van de dimensies. Paden met verhoogde vloeistof stroom ontstaan wanneer grotere SYD bij elkaar in de buurt liggen, met als gevolg een hogere gemiddelde permeabiliteit. De hoeveelheid orde in de verdeling van de afmetingen speelt daarom een belangrijke rol

in de waarde van de permeabiliteit. Experimenteel bepaalde permeabiliteits waarden van een enkel type vezelversterking kunnen daarom een factor 2.5 verschillen.
Permeabiliteits metingen zijn verricht met behulp van verschillende opstellingen. Een relatief kleine hoeveelheid variatie tussen de resultaten is gevonden voor elke opstelling afzonderlijk. De variatie valt meestal binnen de voorspellingen van het netwerk model. Een onderlinge vergelijking tussen de resultaten van de verschillende opstellingen toont echter een grote hoeveel variatie aan. Dit is voornamelijk toegeschreven aan het ontbreken van een gestandaardiseerde meetmethode voor de permeabiliteit.

Nomenclature

Roman

a_k	coefficient ($k \in \mathbb{N}$)	[-]
a_s	proportionality factor between saturated volumetric flow and inverse square root of time	[$m^3 \cdot s^{\frac{1}{2}}$]
a_u	proportionality factor between unsaturated volumetric flow and inverse square root of time	[$m^3 \cdot s$]
A	needle spacing	[m]
b	width of an SYD	[m]
b_k	coefficient ($k \in \mathbb{N}$)	[-]
B	stitch distance in machine direction	[m]
d_0	compacted stitch yarn diameter	[m]
d_p^A	projected distance of needle spacing	[m]
d_p^B	projected distance of stitch distance in machine direction	[m]
f	frequency of occurrence	[%]
F	function	
F_{theo}	theoretical function	
F_c	critical value in statistic test	
F_s	statistical value	
h	height	[m]
h_c	cavity height	[m]
H_0	null hypothesis	
i	index	[-]
I	current	[A]
j	index	[-]
k	index	[-]
K	permeability	[m^4]
K_0	Kozeny constant	[-]
K_1	first principal permeability	[m^4]
K_2	second principal permeability	[m^4]
K^0	permeability in machine direction	[m^4]
K^{45}	permeability in 45° direction	[m^4]
K^{90}	permeability in transverse direction	[m^4]

K_0^0	nominal permeability in machine direction	[m^4]
K_0^{90}	nominal permeability in transverse direction	[m^4]
$K_{E_T}^0$	effective permeability in machine direction	[m^4]
$K_{E_T}^{90}$	effective permeability in transverse direction	[m^4]
$K_{E_T}^{nom}$	nominal effective permeability	[m^4]
K_E	effective permeability	[m^4]
$K_{E_T}^{LB}$	lower bound effective permeability	[m^4]
$K_{E_T}^{N}$	normalised effective permeability	[m^4]
$K_{E_T}^{UB}$	upper bound effective permeability	[m^4]
K_N	normalised permeability	[m^4]
K_s	saturated permeability	[m^4]
K_x	permeability in x–direction	[m^4]
K_y	permeability in y–direction	[m^4]
$K_u^{(1)}$	unsaturated permeability (flow front based calculation)	[m^4]
$K^{(2)}$	(un)saturated permeability (flow rate based calculation)	[m^4]
K^{ch}	channel permeability width averaged radius	[m^4]
K^{sy}	centre element permeability including stitch yarn	[m^4]
l	length of an SYD	[m]
l_c	length of a cylinder element	[m]
L	length	[m]
L_f	focal length of ellipse	[m]
L_T	total flow length	[m]
m_i	i^{th} central moment of a data set	
M	mass	[kg]
n	index	[-]
n_{inlet}	number of inlet nodes	[-]
n_{outlet}	number of outlet nodes	[-]
n_{set}	number of sets of SYD widths	[-]
n_{permu}	number of permutations in a set of SYD widths	[-]
N	number of elements in a set	[-]
N_1^0	number of elements of the base configuration in machine direction	[-]
N_2^0	number of elements of the base configuration in transverse direction	[-]
N_x^{ch}	number of channels in the x–direction	[-]
N_y^{ch}	number of channels in the y–direction	[-]
p	pressure	[Pa]
p_h	hydrostatic pressure	[Pa]
P	pressure in mould cavity	[Pa]
P_i	pressure of i^{th} transducer	[Pa]
P_{inj}	injection pressure	[Pa]
P_s	significance level	[-]
P_{sat}	pressure during saturated flow	[Pa]
P_{unsat}	pressure during unsaturated flow	[Pa]

r	radial coordinate	[m]
r_0	radius of inlet	[m]
r_1	major radius of ellipse	[m]
r_2	minor radius of ellipse	[m]
r_c	cylinder element radius	[m]
r_E	equivalent radius	[m]
r_f	fibre radius	[m]
r_h	hydraulic radius	[m]
r_{out}	outer radius	[m]
R_e	electrical resistance	[Ohm]
R_E	equivalent resistance	[m^{-4}]
R_{fluid}	electrical resistance of the fluid	[Ohm]
R_{ref}	electrical reference resistance	[Ohm]
s	best estimator of standard deviation	
s^+	upper limit of scatter/variation	
s^-	lower limit of scatter/variation	
S	size of the network	
t	time	[s]
t_f	time at which the flow front position is evaluated	[s]
t_i	time at instant i	[s]
t_{sat}	start time of saturated flow	[s]
t_{unsat}	arrival time of flow front at sensor	[s]
$t_{0.95}$	student–t distribution	
t^*	time fit parameter	[s]
u	fluid velocity	[$m \cdot s^{-1}$]
U	specific internal energy	[$J \cdot kg^{-1}$]
V	volume	[m^3]
V_f	fibre content	[-]
w	weighting function	
W	weight of preform	[kg]
x	cartesian coordinate	[m]
x_f	flow front position	[m]
x_i	i^{th} data value	
y	cartesian coordinate	[m]
z	cartesian coordinate	[m]

Greek

α	anisotropy	[-]
α_0	anisotropy of equivalent permeabilities	[-]
α_N	anisotropy of normalised permeabilities	[-]
α_r	anisotropy of channel radii	[-]
α_s	significance level	[-]
β	reorientation angle	[rad]

γ	shear angle	[°]
γ_{trans}	transition shear angle	[°]
δ	(infinitesimally) small part	
δ_φ	small variation in elevation angle	[rad]
Δ	difference	
ε	error	
ε_R	relative error	[-]
η	second elliptical coordinate	[-]
θ	rotation/angular coordinate	[rad]
θ_{sph}	azimuth angle	[rad]
κ	SYD dimensionless width	[-]
λ	SYD dimensionless length	[-]
μ	dynamic viscosity	[Pa·s]
$\mu_{\ln}$	mean of the logarithmic values	
ξ	first elliptical coordinate	[-]
ξ_f	position of flow front (first elliptical coordinate)	[-]
ρ_L	linear density	[kg·m^{-1}]
ρ_A	areal density	[kg·m^{-2}]
ρ	volumetric density	[kg·m^{-3}]
σ	standard deviation	
τ	shear stress	[Pa]
ϕ	porosity	[-]
φ	element flow	[m^3·s^{-1}]
φ_{sph}	elevation angle	[rad]
Φ	volumetric flow rate	[m^3·s^{-1}]
Φ_M	mass flow rate	[kg·s^{-1}]
Φ_s	volumetric flow rate for saturated flow	[m^3·s^{-1}]
Φ_u	volumetric flow rate for unsaturated flow	[m^3·s^{-1}]
χ^2	chi–squared distribution	
ψ	arbitrary function	

Special Characters

$\mathcal{A}$	cross–sectional area	[m^2]
$\mathcal{A}_E$	area of ellipse	[m^2]
$\mathcal{K}$	packing coefficient	[-]
$\mathcal{L}$	velocity gradient operator	
$\mathcal{P}$	perimeter	[m]
$\mathcal{V}$	electrical voltage	[V]
$\mathcal{V}_R$	relative voltage	[-]

Subscripts

0	initial condition or position
1	first direction/vector component
2	second direction/vector component
b	bottom face
ln	logarithmic variant of parameter
min	minimum parameter value
max	maximum parameter value
p	parallel
s	serial
t	top face
$[\cdot]$	element index number
$[\cdot,\cdot]$	two–dimensional element index number

Vectors

$\boldsymbol{F}$	body forces	$[\mathrm{m{\cdot}s^{-2}}]$
$\boldsymbol{N}$	element interpolation functions	[-]
$\boldsymbol{p}$	nodal pressures	[Pa]
$\boldsymbol{q}$	heat flow	$[\mathrm{J{\cdot}s^{-1}}]$
$\boldsymbol{r}$	ellipse radii	[m]
$\boldsymbol{x}^0$	translation	[m]
$\boldsymbol{x}^G$	global Cartesian coordinates	[m]
$\boldsymbol{x}^P$	principal Cartesian coordinates	[m]
$\boldsymbol{\varphi}$	nodal flux	$[\mathrm{m{\cdot}s^{-1}}]$
$\boldsymbol{\xi}$	elliptical coordinates	[-]

Tensors & Matrices

$\underline{\boldsymbol{D}}$	deviatoric deformation rate	$[\mathrm{s^{-1}}]$
$\underline{\boldsymbol{I}}$	unit tensor	[-]
$\underline{\boldsymbol{K}}$	permeability	$[\mathrm{m^4}]$
$\boldsymbol{M}$	element matrix	
$\underline{\boldsymbol{W}}$	vorticity	$[\mathrm{s^{-1}}]$
$\underline{\boldsymbol{\sigma}}$	stress	[Pa]
$\underline{\boldsymbol{\sigma}}_d$	deviatoric stress	[Pa]

Mathematical

∇	gradient operator
∇^2	Laplace operator
d	derivative operator
D	material derivative operator
∂	partial derivative operator
e	exponential
ln	natural logarithm
$.^T$	transpose
$.^{-1}$	inverse
$\bar{.}$	mean value
$\sum$	summation
$\mathcal{O}()$	order of magnitude
$\|\|$	parallel or longitudinal
$\perp$	perpendicular or transverse
$\cdot$	contraction
:	double contraction
$\bar{.}$	mean value
$\tilde{.}$	approximate value

Abbreviations

DOF	Degree Of Freedom
DV	Digital Video (camera)
KES–F	Kawabata Evaluation System – Fabrics
KU Leuven	Katholieke Universiteit Leuven
LCM	Liquid Composite Moulding
NLR	National Aerospace Laboratory
NCF	Non–Crimp Fabric
RTM	Resin Transfer Moulding
SYD	Stitch Yarn induced fibre Distortion
UT	University of Twente

Contents

Chapter 1

Introduction

The production technologies of fibre reinforced composite materials have received a substantial amount of attention in the past decades. The increasing application of composites for complex shaped products and structural components, accompanied by increasing demands on cost efficiency and/or product quality is the main driving force behind the investments in the improvement of the composite production technologies. The major aircraft builders have stimulated and keep stimulating the development of composite components, by aiming for large percentages of composite materials in their aircrafts [1].

Evidently, a high product quality is demanded, not only concerning the dimensional accuracy of the product. The homogeneity of the product and its resulting mechanical properties are as relevant. Moreover, this high quality should be achieved in a cost effective manner. Hence, fundamental knowledge on the production process plays a crucial role. Fundamental knowledge allows control of the process better and subsequently a guarantee of not only a higher, but also a more reproducible product quality. The industries consequently invest in increasing the knowledge level on the production technologies.

It should be noted that the entire production process is optimised, rather than only the product (or product design) itself. Optimisations on the level of the individual steps in the production process only partly cover the optimisation of the complete process. The process has to be considered as an integral process, with strong correlations between the various steps. The design engineer should be aware of these correlations. Evidently, fully integrated process simulation software is a welcome tool for the designer, to enable him to perform his task.

The complete composite production cycle is depicted in the flow diagram figure 1.1. An integrated design tool covers all the stages of the process. Different types of models are distinguished:

1. models predicting the process properties, such as deformation and impregnation

[1] The Airbus A380 contains roughly 40% composite material, a volume to be increased for the successor of the A340. Boeing aims with their new Dreamliner, which is currently being developed, at 55-70% composite material.

behaviour;

2. models predicting the material behaviour;
3. models predicting the mechanical properties.

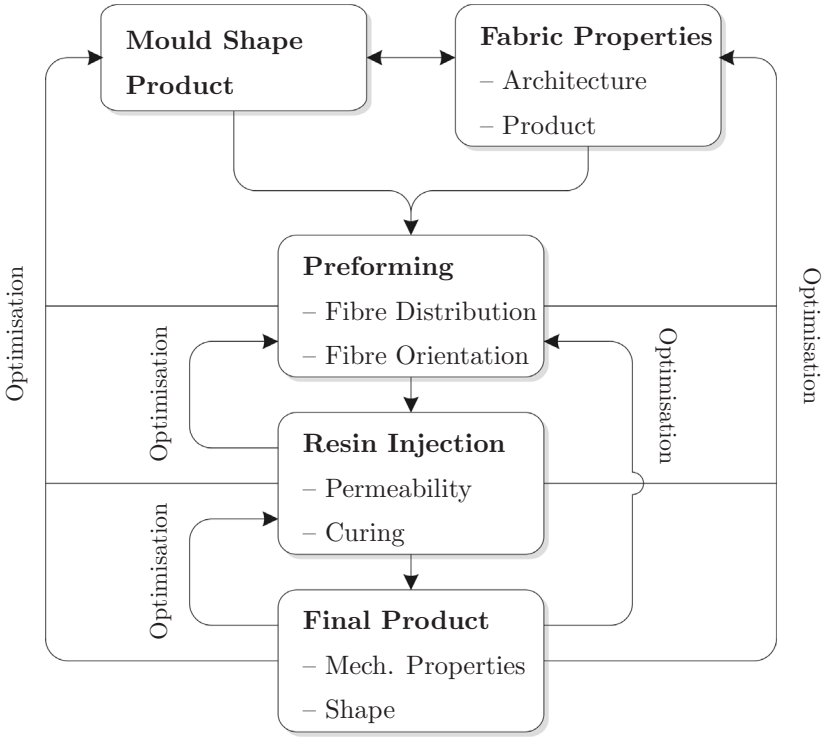

Figure 1.1: *Flow diagram of the design process of a composite product.*

The models are often developed separately. However, the parameters of the different models are generally interrelated. For example, deformation (process property models) depends on the fabric structure, but also on the fibre properties (material property models). Inversely, the fibre properties can depend on the deformation of the fabric. Similarly, impregnation properties (process property models) depend on the deformation of the fabric (process property models), but also on the material properties (material property models) and inversely.

Hence, it is essential to develop the various models in conjunction with each other. An example of a project in which this was attempted is the European funded project FALCOM (Failure, Performance and Processing Prediction for Enhanced Design with Non–Crimp–Fabric Composites, G4RD–CT–00694, [1]). Part of the work presented here, is performed in the framework of this project.

1.1 The Project's Prelude

The input for the process simulation tools comprises a cocktail of process dependent and material dependent parameters. Process and material characterisation are both the subject of several research projects. A research project in which this was illustrated, is the development of the composite landing gear for the NH90 helicopter [2]. The trailing arm of the helicopter, normally made from high strength steel, was replaced by a braided carbon fibre epoxy composite, depicted in figure 1.2.

Figure 1.2: *Composite trailing arm of the NH90 helicopter. (Braided at Eurocarbon, RTM–injection done at NLR).*

The project covered all aspects starting from the manufacturing of the braid, the design of the mould, the resin injection (Resin Transfer Moulding was used, a technology that will be introduced shortly), simulation of the injection and several tests concerning the quality and mechanical properties of the final product.
It was revealed during the project that the knowledge level on the manufacturing of the preform and the subsequent impregnation behaviour fell short of the desirable level. The process settings for the braiding machine were difficult to predict. Numerous tests had to be carried out, before the preform could be braided successfully. The experience of braiding companies is also that the experimentally obtained process settings for a certain product cannot be generalised to be used for other products.
The subsequent impregnation of the resin suffered from similar problems. Experience had shown how to obtain a well filled product (*id est* no dry spots and a void content lower than 2%). However, the process settings, such as injection strategy, but also the locations of the injection gate and vents, could not be predicted properly by a model, let alone be optimised. The bottleneck in the prediction of the impregnation behaviour is the permeability of the preform. The local permeability depends on the local internal structure. A permeability model that predicts the local permeability sufficiently well, while accounting for the preform deformation at a local level was not available. This is partly due to the complexities in the internal structure and the strong relations between the material behaviour and the deformation behaviour of the textile reinforcement.
The second part, even more important than the first, is the large amount of scatter on the measured permeability data. Variations up to of a magnitude of a decade

are found in the measured permeabilities. Evidently, adding more complexity to the predictive models, only makes sense if the models are also able to identify the sources of the variation in the permeability.

Clearly, a more fundamental level of knowledge on both the preforming stage and the processes determining the permeability of a reinforcement was desirable. Hence, a collaborative research project between the National Aerospace Laboratories (NLR) and the University of Twente (UT) was started [3]. The project aims to develop simulation tools to:

1. Predict the process settings for an over–braiding machine, given an arbitrary mandrel shape and given specified fibre orientations or specified mechanical properties;
2. Predict the local permeability and its variation of a textile reinforcement, based on its internal structure, as a function of the deformation of the reinforcement.

The project was set up in close conjunction with industrial partners who can benefit from the results obtained in the project. Constant feedback between the developments in the project and the needs of the industry has been strived for during the currently still ongoing project.
The work presented in this thesis concerns the prediction of the permeability. More precisely, it presents an analysis of the relation between the internal structure and the permeability of the class of Non–Crimp Fabrics, while bearing in mind that the prediction of the variability is as relevant as the prediction of the averaged value of the permeability. A large part of the geometrical model, describing the internal structure of the reinforcement, was done in the framework of a Marie Curie Fellowship project (HPMT-CT-2000-0030 [4]) at the Katholieke Universiteit Leuven (KU Leuven). The Marie Curie Fellowship project covered also permeability experiments on the analysed fabrics in both relaxed and sheared configurations. The outline of the thesis is presented after a brief introduction into the relevant items in the field of composites and their manufacturing technologies.

1.2 Composite materials

An extensive range of composite materials and production technologies is available. At this point, it suffices to note that only continuous fibre reinforced composites, made by a “Liquid Composite Moulding” (LCM) process are of interest here. LCM processes [5] are near–net–shape production processes in which resin is injected in a preform manufactured from dry textile material.

1.2.1 Textile Reinforcements

The reinforcement is made from textile material. Various types of textiles are distinguished, from which woven textiles are the most common. Weaves have a rich history, starting long before the emergence of fibre reinforced plastics, based

on glass, carbon and aramid fibre bundles [6]. Modern manufacturing technologies, applied to process these materials, inherited the production methods developed over the ages to process wool, cotton, flax and other natural materials. The introduction of automation enabled significantly higher production rates.
Weaves exhibit an excellent integrity of the textile. However, the deformability is limited due to the commingled configuration of the bundles. Moreover, the properties of the fibres are not used to their full extent, due to the undulation of the yarns.
Undulation is hardly present in uni–directional materials. The price of the enhanced mechanical properties in the plane of the fabric is a restricted stability of the material in dry form, compared to woven fabrics. Moreover, the resistance to delamination of a uni–directional based composite is also lower than that of woven fabric based composites, due to the absence of commingled bundles. The term uni–directional is not as strictly defined as it appears: fabrics with 80% or more of their fibres in one direction are generally considered to be part of the family of uni–directional fabrics. Uni–directional materials are mainly available as pre–preg material. The materials are either used as sheet material or as tape in tape layer machines or as impregnated bundles in filament winding [7, 8]. The application in LCM production technologies is limited, compared to woven fabric, due to the lower shape integrity.
This led to the development of the class of "Non–Crimp Fabrics" (NCF)[2], consisting of uni–directional plies of fibres, stitched together to maintain integrity of the structure. The low amount of undulation guarantees an optimal use of the mechanical properties of the fibres in the plane of the fabric. The stitches prevent a significant drop in the out–of–plane properties of the fabric, as occurs in uni–directional based composites. The deformability of dry NCFs is better than that of woven fabrics. Large deformations can be obtained with a low amount of force applied [9, 10].

1.2.2 Preform Manufacturing

A preform from dry textile material is made if a Liquid Composite Moulding process – to which this introduction is limited – is applied to manufacture the composite product. The preform has roughly the shape of the final product. Several technologies are available to build a preform. Stitching technologies and binder powder methods are the most commonly applied techniques if woven fabrics or NCFs are employed. The stitch technologies are similar to the production process of NCFs, but applied locally, at strategic points to fix the position of different layers of material with respect to each other. A small thread – compared to the fibre bundles – is used. A needle penetrates the fabric, either completely, or only partly (so–called 'tufting'). A loop of the stitch thread is left behind at the bottom side of the fabric in case of a full penetration. Possibly, the loops are mutually connected[3], for a higher stability of the preform.
Binder powder technologies can be used as an alternative to stitching. A thermoset powder is applied to the fabric. The powder becomes viscous if the temperature is

[2]The material is also referred to as "Non–Crimp stitched (bonded) Fabrics" or as Multiaxial Multiply stitched Fabrics (MMF).
[3]This process is explained in more detail in chapter 2

elevated. The powder particles migrate partly in the fibre bundles. Moreover, the elevated temperature causes some cross–linking of the binding powder and hence a bond is formed between the different layers of fabric. The stiffness of the preform is increased, since the powder is applied homogeneously onto the fabric, effectively limiting the moveability of the fibre bundles. Hence, the shape of the preform is maintained better. The binder powder does not, or hardly, affect the impregnation behaviour. The advantage of the use of binder powder compared with stitching is that stitching distorts the fabric. The disadvantages are the longer preparation time and the required heating cycle.
Alternatives to manufacture the preform are braiding [11, 12] or fibre placement technologies [13, 14]. The advantages of these technologies relative to the stitching and binder powder technologies are the larger possible complexity in preform shape, the possibility to automate the preform manufacturing process and the enhanced control over the fibre directions.
Combinations of technologies are also applied, for example, using woven fabrics or NCF in combination with braids, or improving the properties of a braid in thickness direction by applying additional stitching.

1.2.3 Liquid Composite Moulding

The family of "Liquid Composite Moulding" (LCM) production technologies is widely applied for the production of composites. Numerous variants were developed in the past decades. These variants are used on either side of the market of composites: LCM is applied for both high and low performance composites. The basic idea is that a dry, near–net–shaped, textile preform is placed in a closed cavity. Fluid resin is subsequently injected, followed by a curing stage, as depicted in figure 1.3. The final product needs hardly any post processing steps (therefore the term 'near–net–shaped' is used)
The resin can be injected under pressure ranging from just above atmospheric pressure up to 10 bars for large components with high fibre contents. Alternatively, the resin can be sucked through the preform by applying a vacuum. A combination of pressure and vacuum is also applied, in particular to control the void content in the final product.
The cavity can be formed by rigid moulds or by a rigid lower mould and a flexible upper mould, for example a foil or a plastic with a low stiffness. Rigid moulds sides result in a smooth surface and a high quality surface finish. The use of two rigid tools is limited to the range of smaller products (roughly order of 1 metre maximum). Larger structures, such as ship hulls or windmill blades use single side tooling with a flexible top mould. The injection pressure is either low or no injection pressure is applied, in case a flexible tooling is used. Moreover, vacuum must be applied to control the product shape and fibre content.
An overview of the most important variations of the family of LCM technologies is presented in table 1.1. The actual number of variants is much larger, especially since processes are being combined to profit from the benefits of the combined techniques. The number of abbreviations for the different processes is as confusing as it is large.

Table 1.1: *Various manufacturing processes of the Liquid Composite Moulding family and their basic characteristics.*

Process	Abbreviation	Description
Injection/Compression		– Matched rigid tooling. – The mould is closed hydraulically, forcing the resin to impregnate the fabric. – Short cycle times, resin solidified upon closure.
Resin Transfer Moulding	RTM	– Matched rigid tooling. – Pressure driven resin injection (typically 2–10 bars). – High product accuracy and surface finish. – Small to medium sized products.
Resin Transfer Moulding–light	RTM–light	– Single side tooling. – Low pressure driven resin injection (typically ≈0.2 bars), assisted by vacuum. – Relatively low tooling costs. – Small to medium sized products.
Resin Infusion under Flexible Tooling	RIFT	– Single side tooling. – Vacuum driven impregnation of the preform. – Relatively low tooling costs. – Limited control on local thickness and fibre content. – Limited to relatively thin walled structures. – Small to large sized products (up to 50 metres for windmill blades).
Resin Film Infusion	RFI	– Single side tooling. – Vacuum driven impregnation in thickness direction of the preform. – Relatively low tooling costs. – Small to medium sized products.

There is no standard for the names of the processes, resulting in double names: names that are used for more than one process and vice versa. The terms used in table 1.1 are found to be the most natural by the author, but this will certainly be rejected by others.

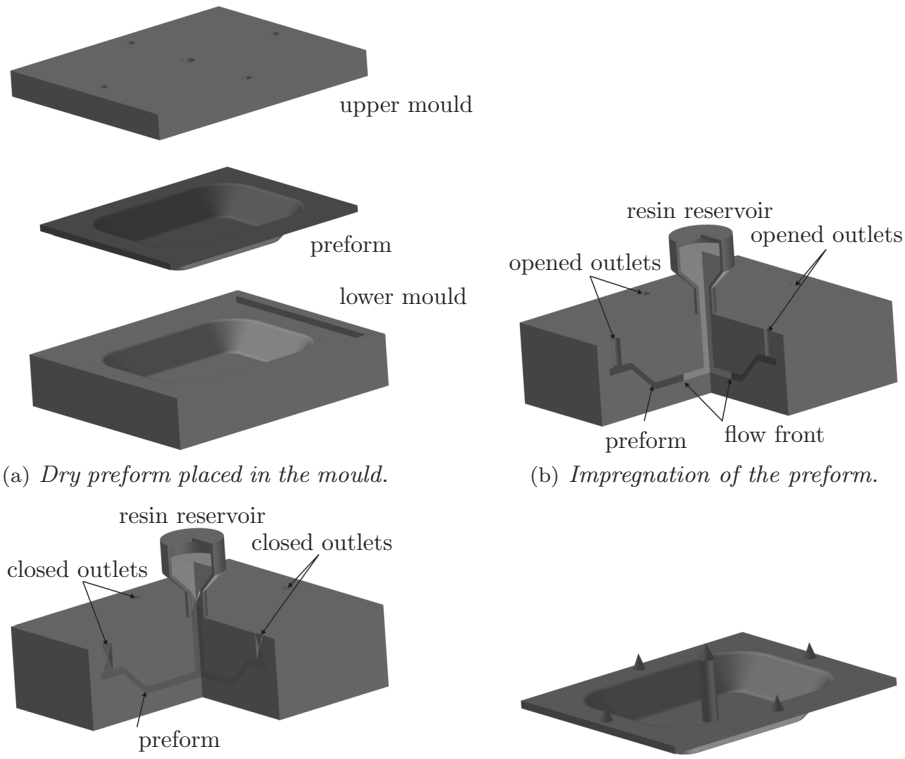

(a) *Dry preform placed in the mould.*

(b) *Impregnation of the preform.*

(c) *Curing of the resin.*

(d) *Near–net–shaped product.*

Figure 1.3: *The four basic steps in the Liquid Composite Moulding process.*

1.2.4 The Permeability of a Textile Reinforcement

A measure for the resistances that a fluid or gas experiences when flowing through a porous medium is the permeability of the medium. Darcy [15] was the first to derive a relation between the pressure drop over the medium – in his case sand – and the flow rate – the water of the fountains of Dijon. Darcy's law reads:

$$\Phi = \frac{K}{\mu} \cdot \frac{\mathrm{d}p}{\mathrm{d}x}, \tag{1.1}$$

with Φ the volumetric flow rate, K the permeability, μ the dynamic viscosity of the fluid[4] and $\frac{\mathrm{d}p}{\mathrm{d}x}$ the pressure gradient in the flow direction. Darcy derived his law by experimental observation, but in a later stage it was shown that it can be derived from the Stokes flow equation:

$$\boldsymbol{\nabla} p - \mu \nabla^2 \boldsymbol{u} = \mathbf{0}, \tag{1.2}$$

by applying a volume averaging procedure [5] ($\boldsymbol{\nabla} p$ is the pressure gradient in vector notation, ∇^2 represents the Laplace differential operator, $\boldsymbol{u}$ is the velocity vector). Darcy's law is applied in a number of fields, from which the oil industry is one of the most important[5]. The introduction of LCM processes for fibre reinforced plastics started the search for a suitable mathematical description of the flow through a textile reinforcement. Darcy's law proved to be a convenient way to relate the pressure drop over the preform (or: 'porous medium') and the volumetric flow rate of the resin to each other.

The next step was to formulate a relation between the fibre content of the reinforcement and the permeability, which was first done by Kozeny and Carman [16–18]:

$$K = \frac{r_f^2}{8K_0} \frac{(1 - V_f)^3}{V_f^2}, \tag{1.3}$$

with K_0 an empirical constant and r_f the radius of a fibre filament (not to be mistaken by the bundle radius) and V_f the fibre content. Initially (1.3) was derived for homogeneous isotropic porous media (hence the permeability is a scalar). Several researchers [17–22] have proposed adaptations for the Kozeny–Carman relation, since a textile reinforcement is not homogeneous and often also not isotropic. They made a distinction between K_0 for axial and for transverse flow. The Kozeny–Carman relation is applied frequently, despite the significant discrepancies in the values reported in the literature. A brief overview of the values suggested in the literature for the Kozeny constant is presented in table 1.2.

Table 1.2: *Values of the Kozeny constant as found in the literature for axial and transverse flow.*

Ref.		$K_{\|\|,0}$	$K_{\perp,0}$	V_f
Williams *et al.*	[17]	0.1 - 0.8	0.8 - 6	0.2 - 0.65
Gebart	[18]	1.66 - 1.78	8	
Lam and Kardos	[19]	0.35 - 0.68	11	0.57 - 0.75
Batch *et al.*	[20]	1.06	8	
Muzzy *et al.*	[21]	3 - 7	7.6	< 0.8
Gutowski *et al.*	[22]	0.7	17.9	0.4 - 0.8

[4] Originally, the viscosity was not included in Darcy's law.

[5] Darcy's law comes into play if the flow of oil through the porous rocks in the earth is analysed.

The large variations in the suggested values for the Kozeny constants are a reflection of the large amount of variation in the experimental results. Measured permeability values can hardly be reproduced and are reported to vary up to one decade [5, 23–31]. The origin of this variability is unknown, although it is generally recognised that the variations partly depend on the reproducibility of the measurement if different testing equipment is employed [32] and partly on variations in the structure of the reinforcement [28, 33].

Meanwhile, the development of predictive models for the permeability of a fibrous reinforcement continued. The number of approaches is nearly as large as the number of researchers, but in general two different approaches can be recognised: (1) the attempts to predict the permeability in a more empirical way, based on the conviction that the inherent material variations do not justify a detailed geometrical model, and (2) the attempts to find a suitable mathematical representation of the fabric reinforcement. The main drawback of the empirical methods is the lack of permeability predictions for new materials, or new configurations. An extensive set of measurements is required if a new type of reinforcement is used or developed.

This work has more affinity with the second approach, employing or searching for a mathematical approach to describe the internal geometry of a preform and subsequently feed this into a permeability prediction model. Modelling strategies are being developed that describe the internal structure and the fibre bundle paths explicitly [34–39]. Mathematical formulae, based on energy methods and geometric functions, form the base of the prediction of the fibre bundle trajectories and cross–sections in various types of textile architectures. The free space between the bundles directly follows from the geometrical model and is fed into flow modelling software [24, 40–42]. All models are based on a certain level of idealisation of the geometry of the internal structure – inherent to their mathematical character. Hence, it is certainly true that the variability observed in the experiments and consequently the variability and unpredictability of the LCM processes experienced at workshop level, will never be completely covered by a mathematical model. Even if experimental scatter is ruled out completely. As a result, identification of the variabilities in the internal structure of a reinforcement and a translation into a geometrical model and subsequently into a flow model is seen as a critical issue in the development of permeability prediction models.

The link between the internal structure of a textile reinforcement and the permeability provides an opportunity to relate the deformation behaviour to the permeability as well. The material model, deformation model and impregnation model are interrelated as was indicated earlier on (see also figure 1.1). The importance of these interrelations for process simulation of the more complex shaped and more critical components, was recognised in several projects (FALCOM [2], TECABS [43]).

A logical route to link the deformation behaviour and impregnation behaviour of a fabric is believed to be found in the incorporation of deformation mechanisms in the geometry model, which is the shared core of the three models. Drape is addressed by several authors [9, 44–46] recognising shear as the main deformation mode. Therefore, the explicit incorporation of shear in the geometrical model, is considered as the first, and possibly sufficient, step towards integration between deformation models

and impregnation models. Hence the variation in the internal geometry of both undeformed and sheared materials is investigated here.

1.3 Objective

The objective of this thesis is to develop a permeability model that is based on the internal geometry of a Non–Crimp Fabric (NCF), in which the variation in the internal structure is explicitly incorporated. The output of the model should hence be a permeability plus an indication of the expected variation on it. Moreover, the effect of shear deformation on the internal structure is an aim to be included in the model. A comparison between experimental results and the proposed model is an additional objective.

1.4 Outline

The core of the thesis is formed by three chapters. Firstly, a comprehensive description of the class of Non–Crimp Fabrics is presented in chapter 2. The exploration of the structure of the fabric, results in a geometrical description, based on the distortions in the plane of the fabric, formed by the stitch threads penetrating the fabric. The distortions are referred to as Stitch Yarn induced fibre Distortions (SYD). An experimental investigation of the dimensions of these SYDs of three different fabrics in relaxed and sheared state leads to generalised rules for both the SYD dimensions, including the variation of the dimension, and the relation between the dimensions and the fabric deformation. The generalised rules are semi–empirical and depend mainly on the macroscopic properties of the fabric, such as the number of individual plies and their orientation and the stitch pattern and stitch thread that were used.
The second task is to formulate a method to transform the geometrical parameters to a flow model, such that the averaged and – in particular – the variability of the permeability can be determined. The main assumption of the flow model, presented in chapter 3, is that the flow in the SYDs, defined in the geometrical model, dominates the overall flow. The dimensions of the SYDs are an order of magnitude larger than the space between the filaments inside the fibre bundle. It is shown that the fluid is able to flow from one SYD of one ply into an SYD of another ply at different locations of the SYD. The locations where the SYDs interact, are determined by the stitch distances A and B, the fibre orientation in the bundle and the length of the SYD.
The second assumption is that it is not sufficient to analyse the effect of variable SYD dimensions on the permeability, on a single SYD. A network of SYDs is used to analyse the flow of the fluid through the reinforcement. Therefore, each section of the SYD between two interaction points is treated as a channel. A network is then formed, describing the flow resistances from interaction point to interaction point. The resistance of the channel is based on the dimensions and shape of the section of the SYD and on a Poiseuille flow. An analogy with an electrical system of resistances is found appropriate and a finite element formulation is implemented to solve the system

of flow equations. The variability of the dimensions of the SYDs is implemented by assigning dimensions to the SYDs in accordance with the measured averaged value and standard deviation. The resulting variable flow resistance of the channels in the network is translated to an overall permeability, including an estimate for the amount of variation that can be expected.
A comparison between experimental data and the numerical models is the subject of chapter 4. The experiments that were performed aim to achieve more than a verification of the model presented in chapter 3. A mutual comparison between different measuring techniques is presented in addition. Measurements were performed at three different institutes, with partly different and partly equal fabrics.
Moreover, the permeability of sheared fabrics is measured. The experimental data is compared to the observed changes on the internal geometry of the fabric under shear, as presented in chapter 2.
Finally, the conclusions and recommendations for further research are summarised in chapter 5.

Chapter 2

Geometrical Model

The prediction of the permeability of a fibrous reinforcement depends on a large number of parameters. A crucial part of the permeability prediction is reserved for the representation of the internal geometry of the reinforcement [47, 48], especially for reinforcements with a high fibre content. It is recognised that the number of parameters in the geometry model that affect the permeability, combined with the possible variations in and interrelation between these parameters, confronts the researchers with difficult questions. A distinction between different length scales can be made to describe each of the parameters on its most suitable length scale. Generally three length scales are recognised [49–51], as depicted in figure 2.1: the macro scale (preform/fabric scale), the meso scale (fibre bundle scale) and the micro scale (fibre filament size). Properties calculated at smaller length scales are incorporated in the larger length scales in a homogenised form.

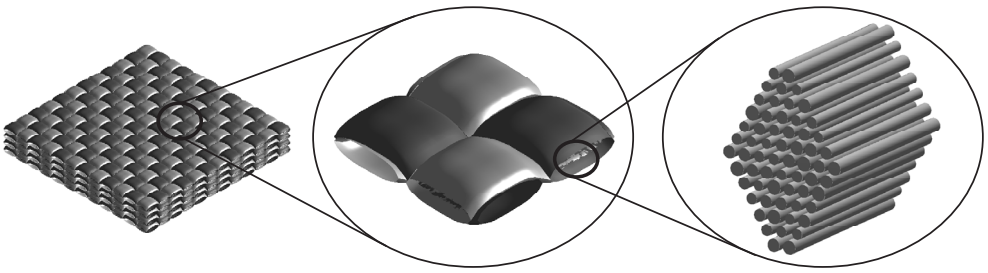

Figure 2.1: *The three length scales as generally used in composite modelling.*

The global flow characteristics are found on the macro scale (10^{-1}–10^{0} m, [34]); resin flow simulations generally show only macro (preform) scale flow progression. Fabric characteristics such as weave type, bundle size (the number of filaments in a

bundle) and orientation are defined at this scale. Diallo *et al.* [52] listed a number of parameters: type of fluid, cavity pressure, fabric structure and orientation and resin saturation. The influence of these parameters on the permeability was investigated by experiments. This approach is typical for the macro scale permeability predictions. The main conclusion of their work is that there are large differences in the permeability for different fabrics, even if they have the same fibre content. No explanation of these differences is presented by them. The applicability of the empirical approach is limited to low fibre content products, in which the macroscopic characteristics of the reinforcement dominate.

The resolution of the macro scale is not sufficient to distinguish typical meso level geometrical characteristics like bundle shape, size and interaction, which have to be taken into account for more accurate permeability predictions. The meso length scale describes the textile reinforcement locally at the order of the tow sizes (in the range of 10^{-2}–10^{-3} m, [34]). The textile reinforcement is subdivided into repetitive sections, in which all the typical features of a fabric are defined. The free space between bundles ('inter bundle' space) is defined by describing the bundle path and shape. This allows a significantly more detailed analysis of the flow through a reinforcement compared to the macro level based flow simulation [47]. The effect of local fabric deformation or of the bundle size can be modelled. Moreover, multilayer effects, such as nesting, can be accounted for [47, 53].

The impregnation of the bundles themselves becomes more critical in products with higher fibre contents. The dimensions of inter bundle channels approach the dimensions of the intra bundle channels – the channels between the filaments inside a fibre bundle. To this end, the micro level (10^{-5} m, [34]) is introduced, describing the fibre bundle as a set of fibre filaments rather than a homogeneous continuum (either permeable, or impermeable).

Flow along and perpendicular to the fibre bundles and the influence of capillary flow is typically investigated at this level. Lundström and Gebart [54], Loendersloot and Akkerman [55], Huber and Maier [56] and Bechtold and Ye [57] investigated the effect of the packing of a fibre bundle (see figure 2.2) and observed a significant influence for both transverse and longitudinal flow. An increase in the longitudinal permeability is found for non–ideally packed fibres [54, 55], whereas a decrease is found for the transverse permeability for an increasing disorder in the packing [54, 56, 57].

The distinction of the different levels shows that flow channels exist at two levels: between and inside the bundles (meso and micro level respectively). The term 'single porosity' refers to the negligence of the micro level flow. 'Double porosity' applies to the models in which the flows at meso level as well as at micro level are accounted for.

The main question remains to what level the mathematical model should be elaborated. In general it is recognised that the micro level porosity has to be accounted for in addition to the meso level porosity at higher fibre contents [48, 58]. However, the incorporation of a second length scale in a prediction method strongly increases the computational requirements of such a model, resulting in an unacceptable loss of efficiency in engineering practice. Belov *et al.* [24] have stated that neglecting the double porosity is justified for a first approximation of the permeability. The single

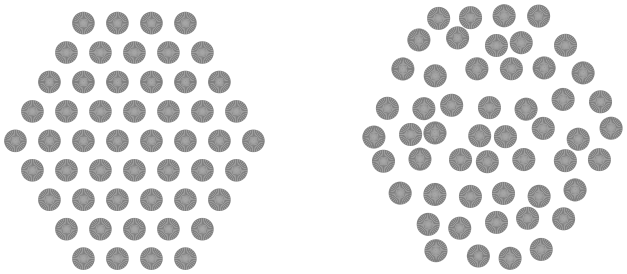

(a) *Regular array* (b) *Irregular array*

Figure 2.2: *Regular and irregular packing of fibre filaments inside a bundle.*

porosity model underestimates the permeability by 20–30%, which is acceptable, especially when the large scatter, observed in experimental results, is taken into account. Standard deviations of 30% are common, maximum values may differ by an order of magnitude from the minimum values [25, 27, 59]. Evidently, the experimental scatter and its origin are dominant factors in the prediction of the permeability. The origin of the variability of the permeability is partly found in the internal structure of the reinforcement material. Consequently, a prediction of the amount of variation on the permeability provides an important contribution to flow modelling software and process control.

An accurate permeability prediction requires a detailed description of the geometry on the one hand. On the other hand, the applicability of a model in an engineering environment is limited by its required computational effort. It is attempted to find a suitable method to satisfy both needs. Generally speaking, most available models are based on a unit cell description. A unit cell is the smallest unit that can represent the entire structure. Unit cell descriptions are widely applied to link lower level features of a material or process to a higher level. Unit cell descriptions are also adopted for the geometrical models presented here. However, a less conventional type of unit cell is defined. The unit cells are not simply a subdivision of the continuum, as is the case in conventional unit cell models [47, 51]. The geometrical model for a Non-Crimp Fabric (NCF) is based on a specific geometric characteristic of stitched fabrics: the distortions induced by the stitch thread piercing through the fabric. The model essentially describes only a part of the domain, which is recognised as the dominant flow region. This flow domain possesses a high aspect ratio: the length of the domain is much larger than the width and the height. The meso level solution of the flow domain formed by this distortion is used for a macro level (fabric/preform level) prediction of the permeability. The macro level prediction is based on a number of meso level flow domain solutions rather than on a single solution. This method allows the explicit incorporation of the variability in flow domain dimensions as observed in practice.

2.1 Structure and Manufacturing of Non-Crimp Fabrics

Non–Crimp Fabrics (NCF) consist of uni–directional plies of fibres which are stitched together by a relatively thin thread compared to the bundle size. The stitching provides the fabric with sufficient stability in dry form for preforming. NCF can therefore be used in Liquid Composite Moulding (LCM) processes, as woven fabrics. Other uni–directional reinforcements cannot be used in LCM and are generally only available as pre–preg material.
The term 'non–crimp' refers to the low amount of undulation ('crimp') of the fibre bundles (figure 2.3) compared to woven fabrics. The fabric is also referred to as 'Multiaxial Multiply stitched Fabrics' (MMF). The latter term is employed by Lomov *et al.* in a series of articles on this type of material [10, 60–63]. The term crimp refers to the reduction in effective length of the fibre bundle compared to the actual length of the centre line of the bundle, see figure 2.3. Strictly speaking, the term 'non–crimp' is not correct, since the fabric does show undulation in and out of the plane of the fabric due to the stitching [64]. The in–plane undulation causes a slight drop in mechanical properties relative to uni–directional material [62], but the in–plane mechanical properties are improved compared to woven fabrics of equal fibre content. An additional advantage of NCFs is the enhanced impregnation behaviour compared to woven fabric due to the uni–directionality of the fibrous plies. This aspect invoked a growing application of Non–Crimp Fabrics in aerospace/aircraft manufacturing and windmill industries, especially in the field of LCM production technologies.

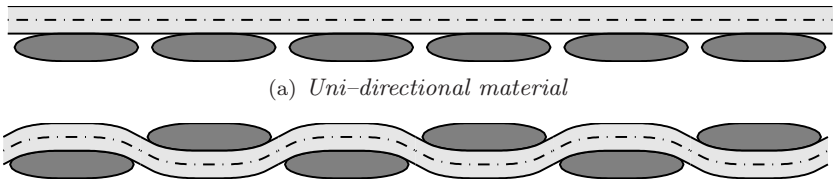

(a) *Uni–directional material*

(b) *Undulating (woven) material*

Figure 2.3: *Schematic difference between uni–directional material and undulated material (woven fabrics and braids).*

A single layer NCF is manufactured from a stack of uni–directional plies of fibres [65]. The uni–directional plies are positioned on the machine bed after which they are stitched together to obtain a single ply of NCF material [66]. An NCF production machine is shown in figure 2.4. The orientation of the fibres on the machine bed is defined as the angle between the fibres and the manufacturing direction (θ in figure 2.4(b)). In practice, the angles of the uni–directional plies are limited to 0^o, 90^o and $\pm 45^o$, combined as $0^o/90^o$ or $\pm 45^o$ fabrics (biaxial NCF), $45^o/90^o/\text{-}45^o$ fabrics (triaxial) and $45^o/0^o/\text{-}45^o/90^o$ fabrics (quadriaxial). Other configurations for triaxial and quadriaxial fabrics can be used as well. Additional chopped fibres or random mat layers may be placed under, between or on top of the fibrous plies.

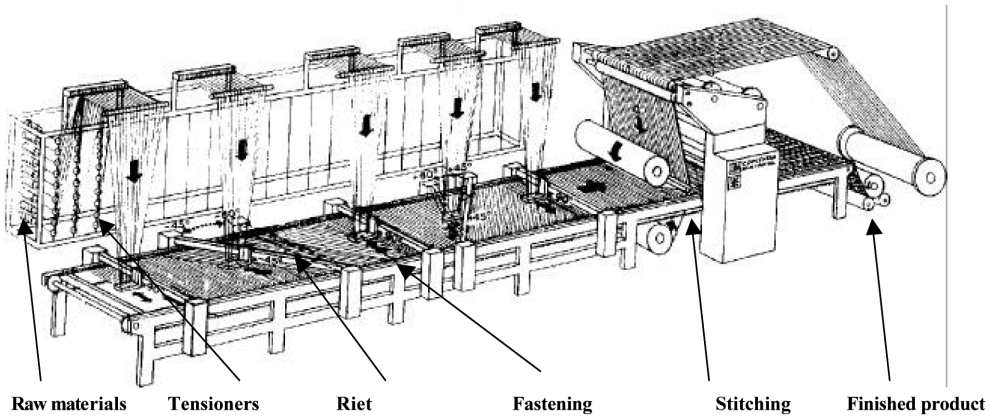

(a) *Machine layout*

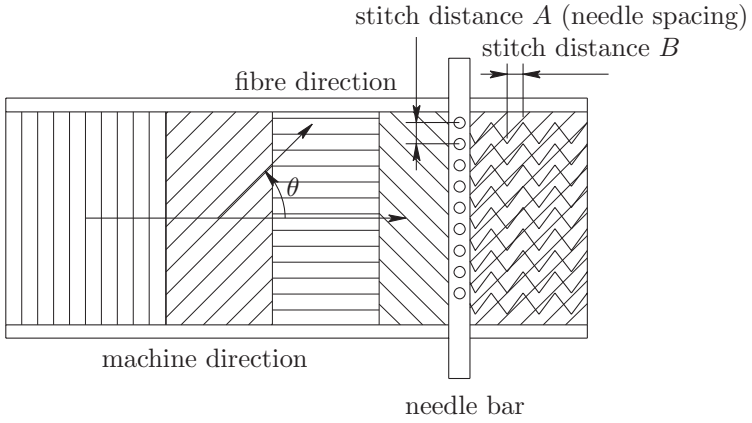

(b) *Machine parameters*

Figure 2.4: Liba *machine for the production of a Non–Crimp stitched Fabric [66].*

The basic production parameters of an NCF are depicted in figure 2.4(b): the orientation of the fibres (θ) and the stitch distances A and B. Stitch distance A depends on the needle spacing and stitch distance B, the distance between subsequent needle penetrations in machine direction, depends on the speed of the loom and the frequency of knitting actions. A rectangular grid of needle penetrations results, since the stitch distances are constant during the manufacturing process.

The stitching process is described in numerous articles, e.g. [60, 66–68]. The warp knitting process of a chain knit stitch pattern is schematically shown in figure 2.5. Other patterns are made in a similar way. The fibre bundles are spread on the machine bed during production, reducing the distinction between fibre bundles: a more or less continuous bed of fibres is formed. The stitches subsequently penetrate this fibre

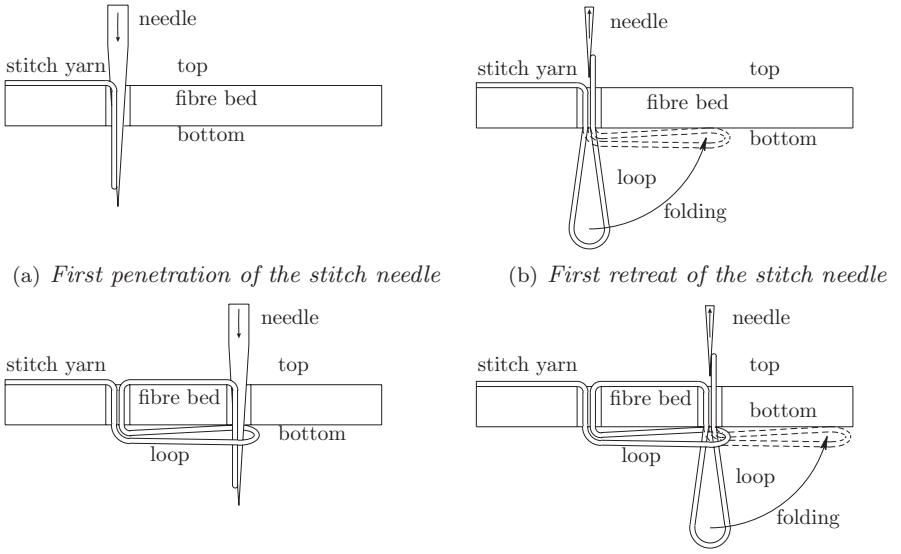

(a) *First penetration of the stitch needle* (b) *First retreat of the stitch needle*

(c) *Second penetration of the stitch needle* (d) *Second retreat of the stitch needle*

Figure 2.5: *Schematic of the warp knitting process of a chain knit pattern in four steps. The arrows in the needle indicates the direction of motion of the needle.*

bed and the fibres are forced aside by the needle and the stitch thread penetrating the individual layers, figure 2.5(a). Subsequently the needle retreats, while pulling the thread back through the fabric such that a loop of the stitch thread is left at the bottom face, figure 2.5(b). The loop is 'folded' onto the fabric surface by the machine. The stitch thread is pushed through the loop, figure 2.5(c), during the next knitting action. Again the needle is retreated, figure 2.5(d) and the new loop is folded onto the fabric surface, fixing the position of the previous loop. The loops at the bottom face can be considered as oriented in the manufacturing direction, inherent to the stitching process. A rotation from the centre line of the loop with respect to the machine direction is referred to as 'tilt' [60]. Tilt is also clearly visible in the images of the bottom faces of the fabrics shown in figure 2.7.

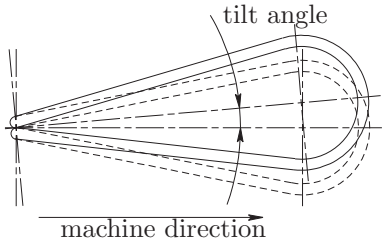

Figure 2.6: *Tilt of a loop at the bottom face of an NCF. Solid lines refer to the tilted position of the loop, the dashed lines to its original position.*

Stitch patterns are formed by moving the needles in the transverse direction, in addition to the relative movement in machine direction. Three different stitch patterns are shown in figure 2.7: a tricot, a tricot/chain and a chain warp knit. Note that the pattern at the top face differs for each fabric, but the loops at the bottom face are identical for all stitch patterns, inherent to the manufacturing process. Different types of stitch thread as well as different stitch tensions are applied. Mechanical properties [69, 70], drape properties [9, 71] and consequently impregnation properties are affected by these stitching parameters. A comprehensive study on the internal geometry and

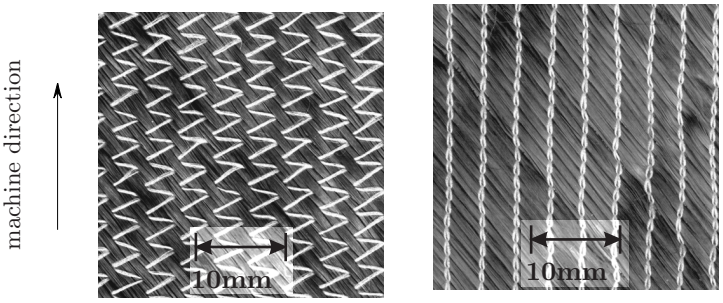

(a) *Tricot (left top, right bottom)*

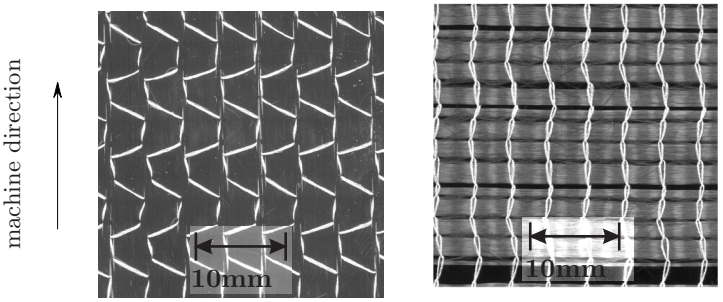

(b) *Tricot/Chain (left top, right bottom)*

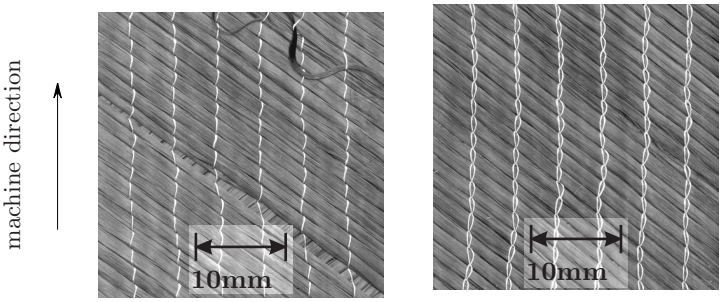

(c) *Chain (left top, right bottom)*

Figure 2.7: *Three different stitch patterns. Note: the pattern on the top face differs, whereas the loops at the bottom face are identical for all patterns.*

on the effects of the stitch thread material and stitch tension on the performance of Non–Crimp Fabrics was performed in the European project FALCOM (Failure, Performance and Processing Prediction for Enhanced Design with Non–Crimp Fabrics – G4RD–CT–00694) [1]. The research on the internal geometry and the permeability prediction of NCF described in this thesis is carried out as a part of the FALCOM project in conjunction with the Marie Curie Fellowship project (HPMT-CT-2000-0030 [4]) carried out at the Katholieke Universiteit Leuven (KU Leuven).
Mouritz *et al.* [72] stated that the needle hardly damages the fibres when penetrating the fabric: less than 0.5% of the fibres are damaged during the stitching process of dry fabric. However, the fibre filament paths are distorted due to the stitch yarn left behind by the needle. A double wedge shaped distortion in the plane of the fibres in each layer is formed [73], illustrated by figure 2.8. Moreover, the loops, which are formed on the bottom face of the fabric (see figure 2.5), are forced between the fibres of the lower layers, leading to differences between the distortions on the top face and the bottom face of the fabric.

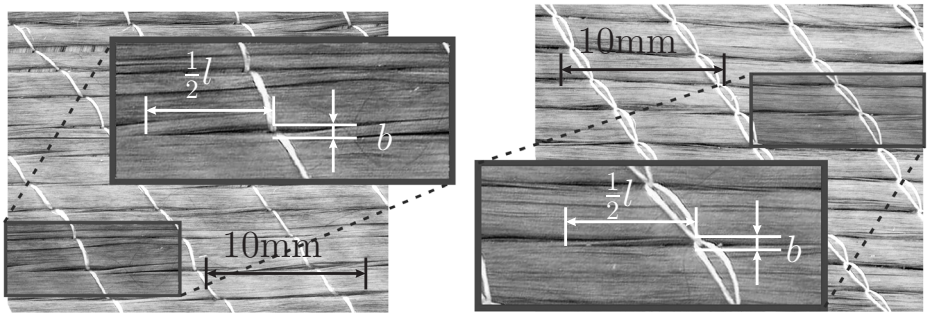

(a) *Top face* (b) *Bottom face*

Figure 2.8: *Stitch Yarn Distortions (SYD) on the top and the bottom face of a biaxial* $\pm 45^{o}$ *NCF (chain knit pattern), with* b *the width of the SYD and* l *the length.*

The distortions in the inner layers of triaxial and quadriaxial NCFs are formed in the same way as the distortions at the top and bottom faces, but they cannot be analysed by visual inspection. Lomov *et al.* [60] and Edgren and Asp [64, 74] studied the internal structure of an NCF based composite employing microscopy. The microstructure of the NCF composite is shown in figure 2.9. The composite was manufactured from 6 layers of triaxial Devold NCF. It was manufactured using the RTM process. Epoxy resin (DERAKANE 411–350 Epoxy Vinyl Ester) was used and the fibre content is 53.3% [75]. The machine direction corresponds with the horizontal of the image. The bundles in the top and bottom ply of a layer are oriented at 45° and -45°, respectively, with respect to the machine direction. The mid ply bundles are oriented in normal direction to the plane of the paper.
Firstly, it is observed that the distinction between separate bundles has virtually disappeared as a result of spreading the fibres on the machine bed (notice, for

example, the mid ply of the second layer). The separations between what appears to be separated bundles, indicate the presence of a distortion, induced by the stitch yarn. One example of traces of fibres travelling from one apparent bundle to the neighbouring one is indicated by the circle on the right hand side.

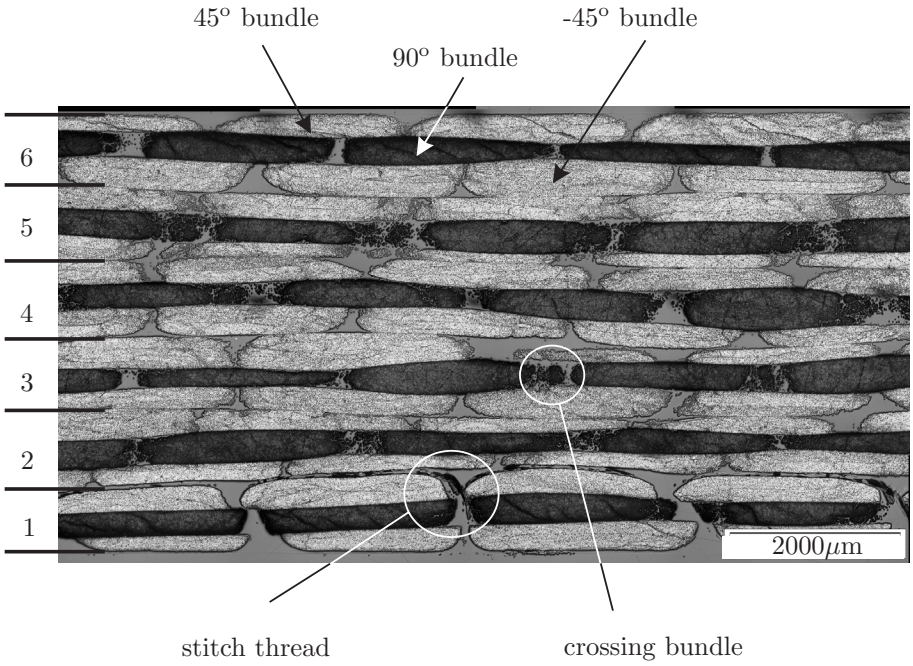

Figure 2.9: *Internal geometry of a six layer triaxial NCF composite (fibre content 53.3%) [75]. A part of a stitch thread is recognised in the left circle. The second circle shows a crossing bundle: fibres appearing to cross from one bundle to another. The numbers indicate the individual layers.*

Secondly, it is noticed that the top and bottom plies in each layer are rounded off. This rounding off is caused by the stitch yarns, which are, apart from the one indicated by the left hand side circle, not visible in this micrograph. The shape of the apparent bundles of the mid plies is more or less rectangular.
Weimer and Mitschang [73] report on the distortions resulting from the stitching process as 'stitch holes'. The stitch tension and stitch thread direction with respect to the fibre direction are held responsible for widening of the stitch holes, but no quantification of this effect is presented in their paper. The definition of the distortions for modelling purposes was first presented in Lomov *et al.* [60], who referred to them as 'cracks' and 'channels'. Here the term Stitch Yarn induced fibre Distortion (SYD) is used to comprise both these terms. Lekakou [76] and Schneider [77] also describe these distortions and refer to them as 'fisheyes'. Note that the distortions are not continuous in the direction of the fibres, as can be seen in figure 2.8. The model of Lundström

[78] assumes continuous channels formed by the stitches. Recent modifications in this model account for so–called fibre crossings [79, 80], which implies a similar limitation to the channels as implicitly accounted for in the geometrical description using the SYDs.
The geometrical description and subsequent permeability prediction model of an NCF is primarily based on the SYDs, since the dimensions of the distortion are an order of magnitude larger (meso level) than the space between the filaments inside a fibre bundle (micro level). Consequently, the overall (macro level) flow is assumed to be dominated by the meso level flow. A simple duct flow analysis illustrates the dominance of the meso flow. The space inside the fibre bundles and between the fibre bundles is approximated by a duct. Consider a laminar flow of an incompressible fluid in a duct with radius r_{out} and length L. The pressure gradient is assumed to be constant over the length of the duct ($\partial p/\partial x = \Delta P/L$, P=pressure). The fluid velocity $u(r)$ in the duct, expressed in radial coordinates and applying no–slip boundary conditions, is:

$$u(r) = \frac{r^2 - r_{out}^2}{4\mu}\frac{\Delta P}{L}, \tag{2.1}$$

with μ the viscosity of the fluid. Integration of (2.1) yields the expression for the volumetric flow Φ:

$$\Phi = \int_{\theta=0}^{2\pi}\int_{r=0}^{r_{out}} u(r)\, r\mathrm{d}\, r\mathrm{d}\,\theta = \frac{\pi}{8\mu}\frac{\Delta P}{L} r_{out}^4 \rightarrow \Phi \sim r_{out}^4. \tag{2.2}$$

The flow is proportional to the fourth power of the radius, implying a strong effect of the radius of the duct on the flow. The permeability (according to Darcy's law (1.1) proportional to the volumetric flow) inside the bundle is roughly estimated four orders of magnitude smaller than the permeability in the flow domains formed by the stitches for each order of magnitude difference in the dimensions of the inter and intra bundle channels. Consequently, the meso flow dominates the overall flow. The same conclusion was drawn by Drapier *et al.* [81]. They investigated the permeability in the direction perpendicular to the plane of the fabric. The distortions are approximated as channels through the thickness of the fabric. A higher stitching density increased the permeability according to their measurements. This confirms the hypothesis that the flow is dominated by the meso level channels.

2.2 SYD model

The definition of a Stitch Yarn induced fibre Distortion contains two assumptions:

1. The shape of the SYD is constant through the thickness of the fabric;
2. The length axis of the distortion is oriented in the fibre direction;

The first assumption implies that through–thickness–effects are not accounted for. It is assumed that the shape of the distortion does not vary over the thickness.

This assumption violates the observations on the internal geometry obtained from micrographs (see figure 2.9). The stitch thread affects the shape of the bundle in the top and bottom ply of a layer, resulting in a shape as depicted in figure 2.10(a). The cross-sectional shape of the domains in the mid plies are more or less rectangular (see figure 2.10(b)).

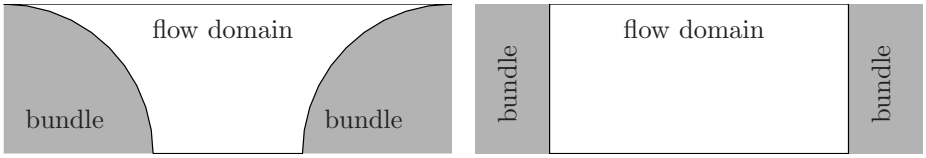

(a) *Flow domain top and bottom ply.* (b) *Flow domain mid ply.*

Figure 2.10: *The shape of the flow domain for the top and bottom plies versus the shape of the domain of the mid plies. The shapes are based on micrograph pictures of NCFs composite specimen.*

The shape of the domain can affect the flow significantly, as shown by (2.2). However, a more correct description of the domain complicates the geometrical model and the subsequent flow modelling. The variation in through–thickness direction of the flow domain is therefore disregarded.

The alignment of the length axis with the fibre direction in a ply results in a stack of differently oriented SYDs around a stitch thread penetration location. The distortions are oriented perpendicular to each other for an orthogonal biaxial NCF in undeformed state. A third and fourth orientation is added for a triaxial and quadriaxial NCF respectively. The resulting stacks of SYDs are shown in figure 2.11. The thick solid

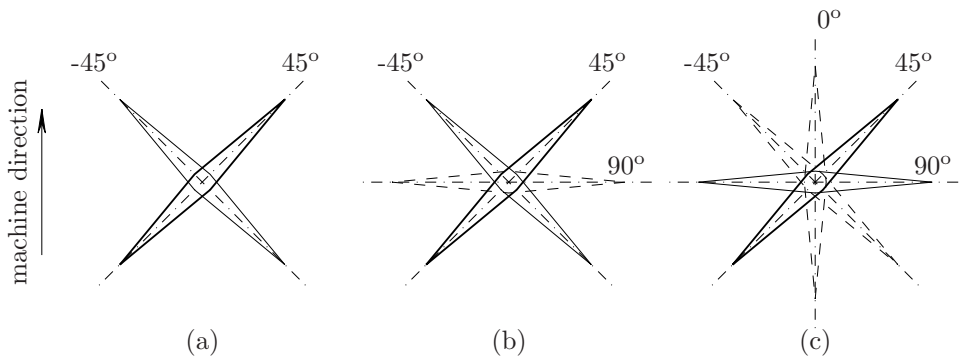

Figure 2.11: *A stack of SYDs of a ±45° biaxial (a), +45°/90°/-45° triaxial and 45°/0°/-45°/90° quadriaxial fabric. The thick solid lines refer to top face SYDs, the dotted lines to inner ply SYDs and the thin solid lines to bottom face SYDs. The machine direction (0°) is indicated by the arrow.*

lines belong to the SYD on the top face of the fabric, the dotted lines to SYDs of mid plies and the thin solid lines to the SYD at the bottom face of the fabric.

It is also evident from figure 2.11 that an anisotropic permeability is expected for the triaxial NCF, given the resin flow in the SYDs dominates the overall flow. The permeability in 90° direction (perpendicular to the machine direction) will be larger than the permeability in 0° direction (machine direction). The permeability of the biaxial and quadriaxial NCF is expected to be isotropic.

The SYDs are only found at the locations where the needles penetrate the fabric (a rectangular grid is formed as mentioned before). The resin mainly flows in overlapping locations from one SYD to another SYD, that is located in another, neighbouring ply. The centre of the SYD is the most obvious overlap region, but overlapping locations are also found at the tips of the SYDs. The number and locations depend on the length of the SYDs – which can vary as will be discussed further on – the stitch distances and the orientation θ of the SYDs with respect to the machine direction. Possible locations of the overlapping regions are limited to integer multiplications of the projected distance d_p of the stitch distances A and B on the stitch yarn distortion (see figure 2.12).

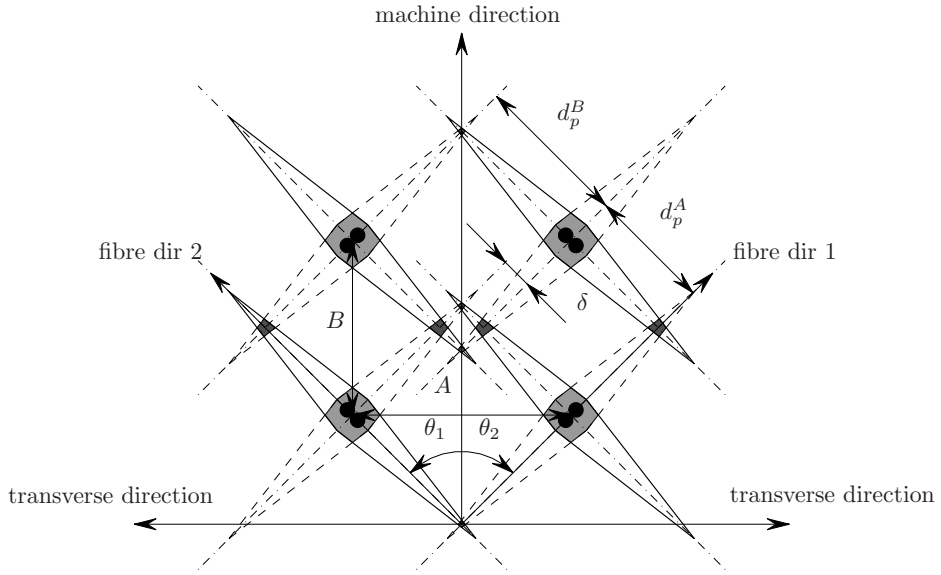

Figure 2.12: *Schematic representation of the SYD configuration of a biaxial NCF. The solid lines correspond to the top ply SYDs, the dashed lines to the bottom SYDs. The projected distances and the distance between the tips are indicated by d_p^A, d_p^B and δ respectively. The angles of the fibre direction with respect to the machine direction are θ_1 and θ_2. The light gray areas indicate the interaction regions between the SYDs of the top and bottom plies in the centre of the SYD; the dark gray areas indicate the interaction regions in the tip regions. The black circles point to the stitch threads penetrating the fabric.*

It can be derived that the relations between the projected distances d_p and stitch distances A and B are:

$$d_p^A = \frac{A}{\sin\theta_1 - \cos\theta_1 \tan\theta_2}; \tag{2.3}$$

$$d_p^B = \frac{B \tan\theta_2}{\cos\theta_1 \tan\theta_2 - \sin\theta_1}. \tag{2.4}$$

The angle between both fibre families is not necessarily equal to 90°; the angle is 45° in triaxial and quadriaxial fabrics. Note that shear deformation of the fabric does not affect the projected distances, provided a trellis frame shear is applied.
The projected distances can also be used to calculate the separation δ between neighbouring SYDs. The distance δ equals the absolute difference between d_p^A and d_p^B, as illustrated by figure 2.12:

$$\delta = \left| d_p^A - d_p^B \right|. \tag{2.5}$$

The separation δ can be small, for specific combinations of the stitching parameters and fabric properties (for example nearly equal values for A and B combined with long and wide SYDs). A small separation allows resin to flow more easily from one distortion to another than a large separation. Semi-continuous channels are formed if the separation is extremely small and is only formed by a small number of fibres crossing from one side of the SYD to the other.
The stitch thread itself is not modelled here. This simplification is based on the assumption that the permeability of the stitch thread is significantly higher than the bundle permeability, since the fibre count of the stitch thread is an order of magnitude smaller than the fibre count of the bundles. Nordlund *et al.* [79, 82] showed that taking the stitch yarn into account in the permeability prediction of the meso level flow channels does affect the permeability, but only to a limited extent. The permeability at the location of the stitch thread may decrease up to 20% depending on the width of the thread with respect to the flow channel. They concluded that the effect of the crossings of fibres from one bundle to a neighbouring one is stronger than the effect of the stitch thread.
The geometry description does not necessarily assume a single porosity. Double porosity can be implemented using appropriate boundary conditions. This will be addressed in more detail in chapter 3.

2.2.1 SYD Dimensions

The dimensions of the distortions depend on a number of parameters. The parameters are partly related to manufacturing conditions and partly to fabric and stitch yarn properties. The most relevant parameters are listed below:

- fibre yarn properties (tow-size, stiffness, compression behaviour);
- stitch yarn properties (tow-size, stiffness, compression behaviour);
- stitch pattern;

- stitch tension;
- orientation of the stitch yarn with respect to the fibres;
- fibre treatment (e.g. sizing);
- needle dimensions and type;
- stitch process;
- loom speed.

It is not clear yet, how each of these parameters affects the dimensions of the SYDs. A comprehensive description of the material, manufacturing process and treatments may reveal the relation between these parameters and the dimensions of the distortions. However, this does not appear to be a practical solution. The aim here is to relate the basic properties of the NCF (such as the number of layers, the stitch pattern and the fibre content) to the permeability of the material. The model complexity increases to an unacceptable level for use in practical situations, if all above mentioned characteristics are taken into account. Hence, a more practical approach is to attempt to find global trends for the main characteristics, such as the stitch pattern and the stitch tension, the latter defined in a qualitative sense, e.g. 'high' or 'low'. A semi–empirical relation can then be employed, requiring a minimal number of experiments for each type of fabric.
The dimensions of the SYD are assumed to be proportional to the stitching thread diameter, which is formulated in the empirical relation proposed by Lomov *et al.* [60] and revised by Loendersloot *et al.* [63, 83]. The width b (figure 2.8) of an SYD is given by:

$$\begin{array}{lll} \text{(Top face SYD)} & b = \kappa_t \times d_0 & \text{(a)}; \\ \text{(Bottom face SYD)} & b = \kappa_b \times d_0 & \text{(b)}; \\ \text{(Inner SYD)} & b = 2d_0 & \text{(c)}. \end{array} \tag{2.6}$$

Here, d_0 refers to the compacted diameter of the stitch yarn [60] and is calculated by:

$$d_0 = \sqrt{\frac{4\rho_L}{\pi\rho\mathcal{K}}}, \tag{2.7}$$

with ρ_L and ρ the linear and volumetric density of the yarn respectively and $\mathcal{K}$ the packing coefficient, which is equal to 0.907 for a perfect hexagonal packing. The empirical proportionality constant κ is defined separately for the front and the back face of the fabric (subscripts f and b respectively). The revision of the initially presented relations [60], which made no distinction between top and bottom face proportionality constants κ, is based on an analysis of different NCFs. An intolerable discrepancy was found between the values of the proportionality constant based on the dimensions of the distortions on the top face and those related to the bottom face. The suggestion of proportionality to the stitch thread diameter arises from the observation that the number of stitch threads present in the SYD is a physical lower bound of the width of the SYD.
A dimensionless length λ is defined using the stitch distances A and B. The grid lines connecting the needle penetrations in and perpendicular to the machine direction (the

dashed lines in figure 2.13) form a boundary for the length of the SYD. The fibres are forced aside by the stitch piercing the plies. As a consequence, the SYDs will close once passing one of the lines 1–2, 2–3, 3–4 or 4–1. Which line is passed, depends on the fibre direction with respect to the machine direction (θ in figure 2.13). No distinction is made between the lengths of the top or bottom face and the lengths of inner SYDs, resulting in the relation:

$$l = \begin{cases} \lambda \dfrac{B}{\cos|\theta|} & \text{for} \quad |\theta| < \arctan\frac{A}{B}; \\ \lambda \dfrac{A}{\sin|\theta|} & \text{for} \quad |\theta| \geq \arctan\frac{A}{B}. \end{cases} \tag{2.8}$$

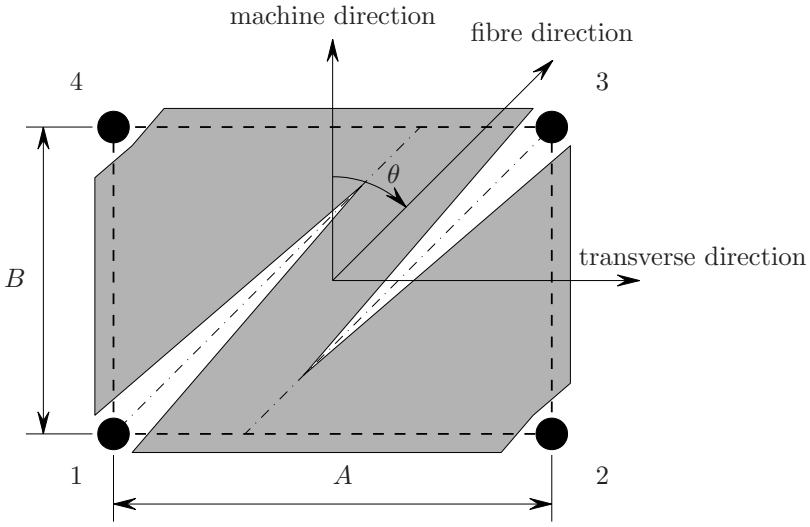

Figure 2.13: *The dimensionless length of the SYD is based on the stitch distances A and B.*

The experimental analysis of the dimensions of the inner SYDs is significantly more complex than the analysis of the outer SYD dimensions. The methodology to analyse the dimensions, as presented in the following section, is not capable of determining the inner SYD dimensions. It is based on optical inspection of the two faces of the fabric. This type of optical analysis can consist of visual inspection by the bare eye, or be digitalised for example using a camera or flat bed scanner, combined with image analysis software. However, only the outside can be captured. No information can be retrieved from the inside of the material. Alternatives are the use of microscopy or X–ray tomography [40]. Both require the preparation of composite specimens, possibly causing distortions in the internal structure compared to the dry fabric. Moreover, relatively expensive equipment is needed.
Most others reporting on stitch thread induced distortions in the fibrous plies [63, 77–79, 82–84] use an optical approach, similar to the one adopted here. Hence, they also

limited themselves to biaxial materials and did not report a method to measure inner SYDs. The width of SYDs in inner plies was measured on micrographs by Lomov *et al.* [60], which resulted in the third relation of (2.6). Edgren and Asp [64, 74] only studied the bundle shape. However, both articles confirm the idea that the dimensions of the inner SYDs are smaller than the outer SYDs. The thread position is approximately vertical in the SYD, whereas the threads bend towards a horizontal position in the outer SYDs. A schematic cross-section of a triaxial NCF around a stitch thread is depicted in figure 2.14. It shows that the stitch threads will widen the SYDs of the top and bottom plies. This widening results in the bundle shape as recognised in the micrographs (figure 2.9) made by Edgren and Asp. It is shown below (see section 2.3) that the averaged minimum value of κ of the SYDs at the outer plies approaches the value of 2. It is thus reasonable to use the relation (2.6)(c) for the inner SYDs, assuming the absence of widening effects, other than the presence of the stitch threads.

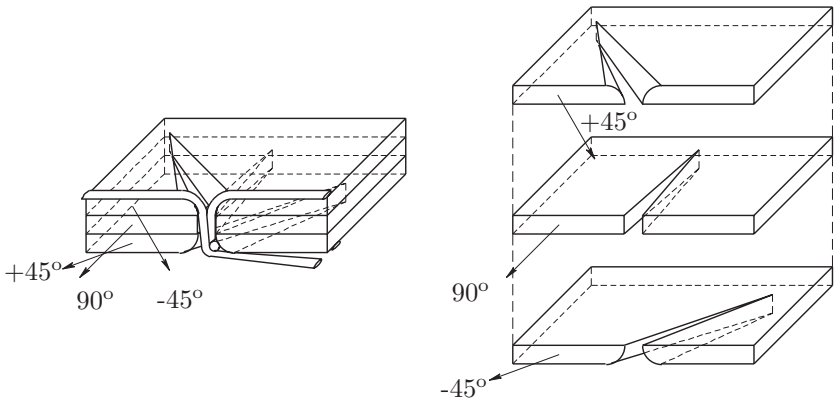

Figure 2.14: *Schematic drawing of the stitch thread in the SYD in different layers of the fabric (45°/90°/-45°, the arrows indicate the fibre direction). To the right the exploded view of the layers (stitch thread omitted for clarity of the figure).*

The proposed empirical relation lacks generality in the sense that it is only defined for the specific set of undeformed fabrics presented in [60]. As mentioned above, it will be impossible from a practical point of view to create a comprehensive model, predicting the SYD dimensions based on the manufacturing conditions and material specifications of both the fibres and the stitch thread. It lies beyond the scope of this thesis to reveal all the underlying processes. This work is restricted to the extension of the practical applicability of the proposed relations (2.6) and (2.8), mainly by observation of the influence of the stitch pattern and the stitch tension (again: only qualitatively). Additionally, the effect of shear is investigated, based on the explicit linkage of deformation and impregnation models.

2.2.2 Materials and Experiments

The proposed model is based on the analysis of three different fabrics. The three fabrics evaluated will be referred to as B1, B2 and B3 for convenience. Figure 2.7(a) – (c) shows the fabrics B1–3 respectively. Fabrics B1 and B2 were studied previously in references [10, 61, 62], fabric B in reference [60] is the same fabric as B1 here. These studies only involve unsheared configurations. Results of sheared configurations on fabrics B1 to B3 were presented in [63, 83, 85, 86]. The fabric data is presented in table 2.1. The properties of fabric B1 and B3 correspond more to each other than the properties of B2 correspond to those of B1 or B3: both B1 and B3 have 12K fibre bundles and a $\pm 45^{o}$ configuration of the bundles. However, the stitch thread of fabric B3 is slightly different from the one used in B1 and B2 and the areal density of B3 is significantly higher than the areal density of B1 and B2. Moreover, the stitch tension of fabrics B1 and B2 appears to be higher than the stitch tension of fabric B3. The stitches on the bottom face of the three fabrics are shown in figure 2.15. The magnification of the images is equal. Clearly the loops of B1 and B2 are similar, but those of B3 lie more loosely, non–straightened on the fabric, indicating a lower stitch tension.

Table 2.1: *Material data from the studied Non–Crimp Fabrics (* calculated with* (2.7)*) Note: 1 tex = 1 g·km*$^{-1}$.

		B1	B2	B3
manufacturer		Saertex	Saertex	Devold
areal density	[kg m^{-2}]	0.322	0.329	0.541
fibre		Toray	Toray	Tenax
		T700 50E	T700 50E	HTS 5631
fibre count in tow	[-]	12K	24K	12K
orientation	[^{o}]	± 45	0/90	± 45
stitch		PES	PES	PES
linear density	[tex]	7.6	7.6	5
stitch yarn diameter*	[mm]	0.088	0.088	0.071
knit pattern		tricot	tricot/chain	chain
gauge	[needles/inch]	5	5	5
stitch length	[mm]	-	-	2.5

The dimensions of the SYDs were measured by analysis of scanned images of the fabric. A standard PC–scanner (HP1200) and standard PC are used. The scanner used for the experiments has a resolution of 1200dpi. This method was also used by Schneider [77]. The resolution of modern scanners is sufficient to acquire the desired information from the images. It should be noted, though, that there is no information on the accuracy of a scanner. This may vary from type to type and brand to brand. Calibration of the scanner is recommended prior to the experiments. The maximum achievable accuracy of the experimental method depends on the resolution of the

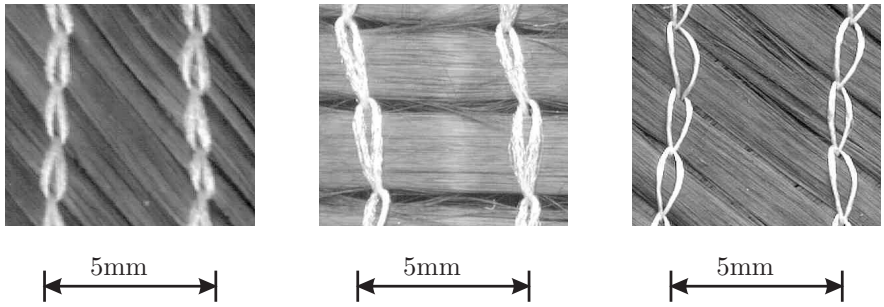

(a) *Bottom face B1.* (b) *Bottom face B2.* (c) *Bottom face B3.*

Figure 2.15: *Differences in the stitch loop shape of the three NCFs indicate different stitch tensions.*

scanner: The relative measuring accuracy per pixel ε_R equals:

$$\varepsilon_R = \frac{25.4}{1200} = 0.021 \qquad [\text{mm} \cdot \text{pixel}^{-1}]. \tag{2.9}$$

The presented results were obtained by taking the centre coordinates and edge coordinates of 100 SYDs (see figure 2.16, the centre coordinate at the crossing of lines 1–4 and 2–3 is not indicated). In practice, the points 1 and 4 in figure 2.16 and points 2 and 3 were not taken from the same SYD in most cases. It appeared to be difficult to determine the width and length of many SYDs accurately due to poor contrast between the bundle and the SYD space. Consequently, the data are weakly correlated. The number of widths and lengths taken as a pair from a single SYD is too low to draw any conclusions on the relation between the SYD dimensions. The centre coordinates are taken from a grid of 11×26 needle penetrations (A and B direction respectively).

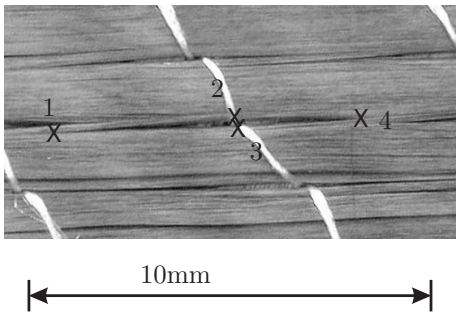

Figure 2.16: *The distance between coordinates 1 and 4 gives the length and the distance between 2 and 3 the width of the SYD.*

2.3 Results and Statistical Treatment

Experimentally acquired constants inherently possess a certain variation. However, the variation in the dimensions of the SYDs is too high to be neglected and appears to be inherent to the material rather than to the analysis method. The variation is therefore treated as an explicit feature of the geometrical model of NCFs. The incorporation of variation in the geometrical model allows an estimate of the upper and lower bounds of the predicted permeability values. This approach is fundamentally different from providing an averaged value and a possible deviation on this averaged value, based on numerical errors or limited accuracy due to assumptions or simplifications in the model. Here, it is aimed to identify the source of the variation explicitly. It is assumed here that the variations in the internal structure – *id est* at micro–level – of the material are reflected in the large amount of scatter that is observed in measured permeability values [25, 27, 59]. As a consequence, the dimensions of the SYDs are presented as averaged values with a certain distribution. The consequences and inherent complications for the flow modelling are presented in chapter 3.

2.3.1 Stitch Distance and Needle Spacing

The measured stitch distances A and B are collected in table 2.2. The manufacturer's specifications are given between brackets. Deviations ranging from 1% (fabric B2) up to 12% (fabric B3) with respect to the specifications were observed. These deviations are attributed to fabric relaxation and deformation occurring due to storage of the fabric on a roll and initial handling for preform preparation. The data exhibits a statistical variation of 0.02 up to 0.11 (B2 and B1 respectively).

Table 2.2: *Measured stitch distances A and B. The value between brackets indicates the manufacturer's specification.*

	B1		B2		B3	
A [mm]	4.94±0.11	(5.08)	5.03±0.02	(5.08)	5.71±0.04	(5.08)
B [mm]	1.71±0.08	(-)	2.64±0.05	(-)	2.20±0.02	(2.5)

2.3.2 Relaxed Configuration

Both the width b and length l of the SYD were analysed for relaxed and sheared configurations. The averaged values of b and l, including the lower and upper bounds of the scatter, are tabulated in table A.1 and table A.2. The measured values were made dimensionless according to equations (2.6) and (2.8) for further analysis. The data for the relaxed configurations is discussed first. The sheared configurations are treated in section 2.3.3.
Deviations of the fibre orientation with respect to the specified orientation in undeformed state can be as large as 8° [83, 85]. The term 'relaxed configuration' rather

than 'unsheared configuration' is found more appropriate to indicate the state of the specimen and will be used throughout the thesis. Part of the scatter in the dimensions of the SYDs of relaxed configurations originates from this fibre misalignment. A maximum error of 13% is estimated employing the model presented in section 2.3.3, that accounts for the effect of shear on the SYD dimension (assuming 8° shear and a linear decrease of the width to half of the initial width, between 0° and 30°).
The dimensions of the SYDs in relaxed state are not corrected for a possible initial misalignment. This approach corresponds to the engineering practice, since the misalignment of the fibre bundles is caused by taking the fabric off the roll and thus allowing it to relax. The excellent deformability causes the fabric to shear without any significant force applied [10, 87]. Consequently, maintaining a perfect alignment of the fibre bundles is an impossible task in practice. Note, that both impregnation and mechanical behaviour are affected by the misalignment of the fibre bundles.

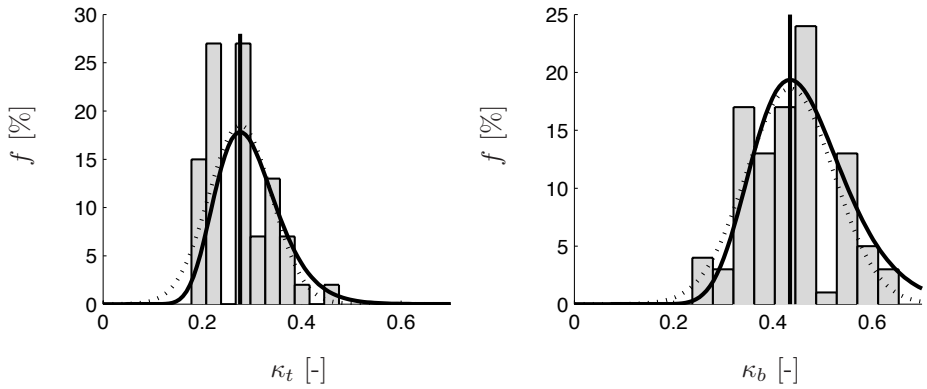

(a) *top face* (b) *bottom face*

Figure 2.17: *Histograms of the dimensionless widths κ for fabric B1. The dotted and solid lines are the normal and lognormal distribution functions based on the averaged value and estimated standard deviation of the measured data.*

Normality The histograms of the measured dimensionless widths κ are presented in figures 2.17 to 2.19. The histograms of the dimensionless lengths λ in figures 2.20 and 2.21. The frequencies of the intervals of the histograms are presented in tables A.5 to A.7. Histogram data is not available for the lengths of the SYDs of fabric B1. A normal and a lognormal distribution function is plotted on top of the histograms (dotted and solid line respectively). The distribution functions are obtained from the estimated standard deviation σ and averaged value $\bar{x}$ of the measured data.
The validity of the assumptions of the type of distribution of the data is tested by performing statistic tests [88, 89]. A 'null hypothesis' H_0 (the data is distributed according to the tested law) is postulated and subsequently tested. The outcome of the statistic test is the statistic value F_s, which is compared with the critical value F_c. The null hypothesis is rejected if $F_s > F_c$. Here a Jarque–Bera test of

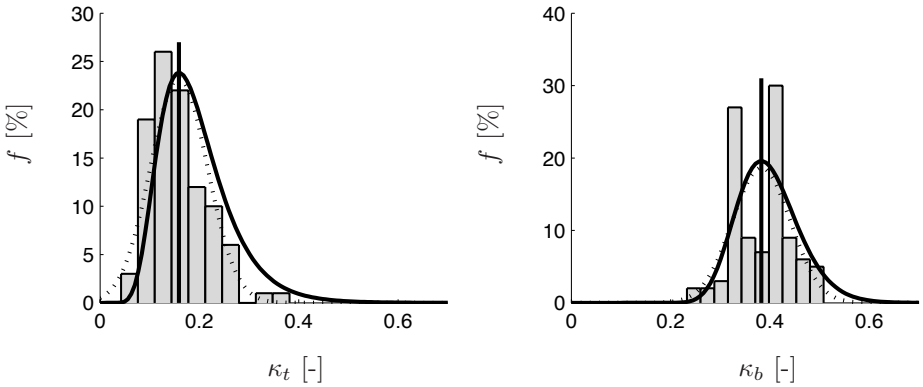

(a) *top face* (b) *bottom face*

Figure 2.18: *Histograms of the dimensionless widths κ for fabric B2. The dotted and solid lines are the normal and lognormal distribution functions based on the averaged value and estimated standard deviation of the measured data.*

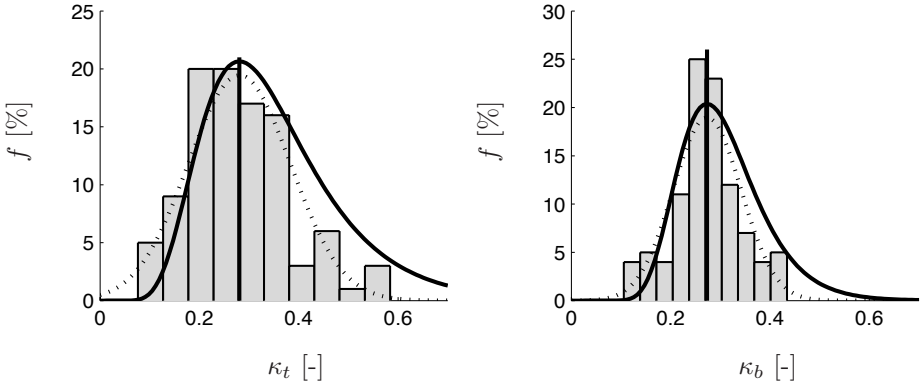

(a) *top face* (b) *bottom face*

Figure 2.19: *Histograms of the dimensionless width κ for fabric B3. The dotted and solid lines are the normal and lognormal distribution functions based on the averaged value and estimated standard deviation of the measured data.*

goodness–of–fit is employed. Other tests, such as the standard chi–squared (χ^2) test, the Kolmogorov–Smirnov, Anderson–Darling or Shapiro–Wilk test can be used as well. More information on goodness–of–fit tests is found in appendix B. The statistic value F_s in the Jarque–Bera test equals [90–92]:

$$F_s = \frac{N}{6}\left(\frac{m_3^2}{m_2^3} + \frac{1}{4}\left(\frac{m_4}{m_2^2} - 3\right)^2\right), \tag{2.10}$$

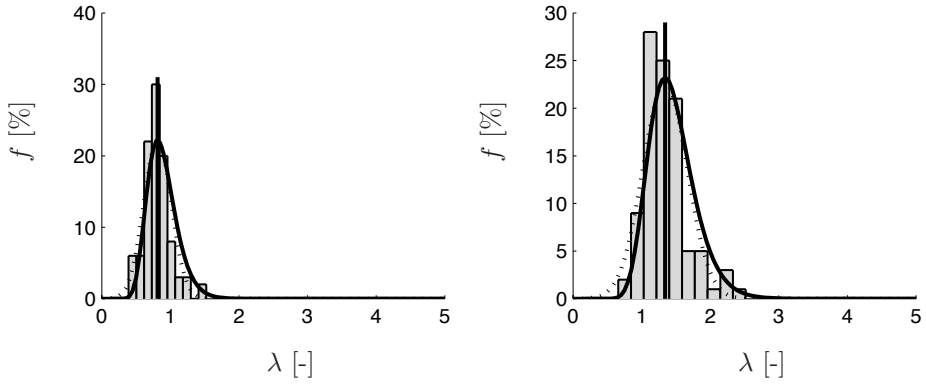

(a) *top face* (b) *bottom face*

Figure 2.20: *Histograms of the dimensionless lengths λ for fabric B2. The dotted and solid lines are the normal and lognormal distribution functions based on the averaged value and estimated standard deviation of the measured data.*

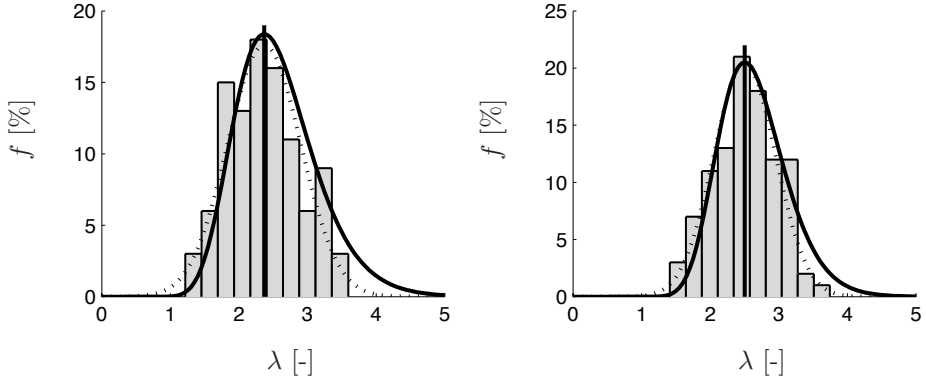

(a) *top face* (b) *bottom face*

Figure 2.21: *Histograms of the dimensionless lengths λ for fabric B3. The dotted and solid lines are the normal and lognormal distribution functions based on the averaged value and standard deviation of the measured data.*

with N the sample size and m_k the k^{th} central moment of the data:

$$m_k = \frac{1}{N-1} \sum_{i=1}^{N} (x_i - \bar{x})^k \,. \tag{2.11}$$

The first central moment equals zero by definition and the second central moment corresponds to the variance computed using the full sample size N, rather than $N-1$. The third and fourth central moment are the skewness and kurtosis of the data. The skewness is a measure for the symmetry of a distribution around the averaged value. The kurtosis is a measure for the sensitivity for deviations between the measured

values and expected values based on the assumed distribution. A normal distribution has a kurtosis equal to 3.
The critical value of the test F_c is the statistic value of a $\chi^2_{1-\alpha_s,k}$ distribution with k the number of degrees of freedom and α_s the significance level. Two degrees of freedom ($k = 2$) apply for this type of statistic tests and α_s is typically 0.05. The chi-squared statistic value $\chi^2_{1-\alpha_s,k}$ is tabulated in standard text books on statistics (e.g. [89]). The critical value F_c equals 5.991 for $k = 2$ and $\alpha_s = 0.05$. The results of the statistic test for the κ–values and λ–values are collected in table 2.3. A value of 1 for H_0 indicates that the null hypothesis is rejected, whereas a value of 0 implies that the hypothesis cannot be rejected. Two null hypotheses were tested:

1. H_0: the data is normally distributed;
2. H_0: the data is lognormally distributed.

Table 2.3: *Normality of the distributions of the dimensionless width and length of the fabrics B1, B2 and B3 in relaxed configuration according to the Jarque-Bera goodness test (critical value: $F_c = 5.991$).*

		κ				λ			
		linear		logarithmic		linear		logarithmic	
		H_0	F_s	H_0	F_s	H_0	F_s	H_0	F_s
B1	top	1	13.92	0	3.18	-	-	-	-
	bottom	0	2.02	0	0.92	-	-	-	-
B2	top	1	21.63	0	3.23	1	29.90	0	4.10
	bottom	0	2.07	0	3.50	1	36.05	0	3.38
B3	top	1	6.56	0	4.12	0	1.82	0	2.39
	bottom	0	0.10	1	17.84	0	0.41	0	4.24

The results of the statistical test show that in nearly all cases the assumption of a lognormal distribution holds. In some cases (κ_b of fabric B2, λ_t and λ_b of fabric B3) the statistical value of the normal distribution is lower, indicating it is a better assumption, although the hypothesis of a lognormal distribution is not violated. The null hypothesis of a logarithmic normal distribution is only rejected for the distribution of the widths of the SYDs on the back face of fabric B3, whereas the null hypothesis of a normal distribution is rejected in 50% of the cases. It can be stated that a lognormal distribution for both the width and the length of the SYDs is an appropriate assumption for the three fabrics discussed here. Moreover, a lognormal distribution corresponds with the physical limitations of the widths and lengths: extremely small or short SYDs are unlikely or even impossible to occur due to the presence of the stitching yarn, whereas wider or longer SYDs may be observed. See appendix B for more details on the statistical analysis of the data.

Averaged Length and Width The averaged values of the dimensionless width κ and length λ for the three different fabrics are presented in figure 2.22 and in tables

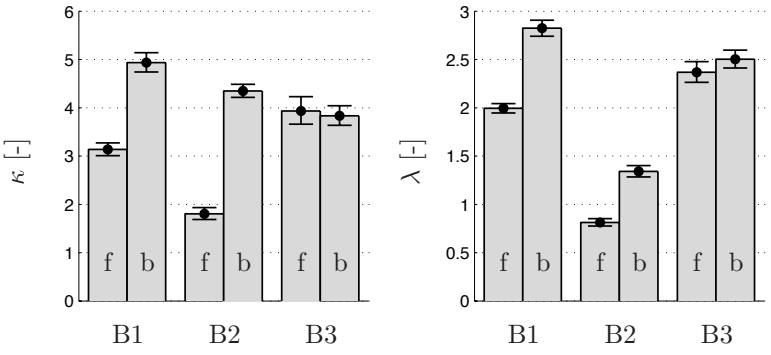

(a) *Dimensionless widths* (b) *Dimensionless lengths*

Figure 2.22: *Averaged values of the dimensionless widths κ and lengths λ of the SYDs on top (f) and bottom (b) face of the three analysed fabrics.*

A.3 and A.4. The error bars indicate the scatter s, which is based on the assumption that the data is lognormally distributed. The lower and upper bounds s^- and s^+ of the average x (where x designates κ or λ) are calculated as:

$$\begin{aligned} s^+ &= \mathrm{e}^{\mu_{\ln}} \left(\mathrm{e}^{\frac{t_{0.95}(N-1)s_{\ln}}{\sqrt{N}}} - 1 \right); \\ s^- &= \mathrm{e}^{\mu_{\ln}} \left(1 - \mathrm{e}^{\frac{-t_{0.95}(N-1)s_{\ln}}{\sqrt{N}}} \right), \end{aligned} \tag{2.12}$$

with

$$s_{\ln} = \sqrt{\frac{1}{N-1} \sum_{i=1}^{N} (\ln x_i - \bar{x}_{\ln})^2}; \tag{2.13}$$

$$\bar{x}_{\ln} = \frac{1}{N} \sum_{i=1}^{N} \ln x_i \tag{2.14}$$

and $t_{0.95}(N-1)$ the student–t–distribution with $N-1$ degrees of freedom and a 95% significance level. This definition of the scatter corresponds to the 95% confidence interval for a lognormal distribution. An exception is made for fabric B1. The logarithmic data of the lengths of the SYDs of this fabric were not available. Hence, the 95% confidence intervals are based on the normal distribution rather than on the lognormal distribution ((2.12) to (2.14)). The confidence interval is symmetric with

respect to the averaged and defined as:

$$s^+ = s^- = \frac{t_{0.95}(N-1)s}{\sqrt{N}}, \tag{2.15}$$

with s the estimated standard deviation of the data set.

Fabrics B1 and B2 show a similar and large difference between top and bottom face averaged widths (figure 2.22(a)): the top face widths are roughly a factor 1.5 to 2 smaller than the bottom face widths. The averaged dimensionless widths of both faces of fabric B3 are equal in size. Moreover, the dimensionless widths of the bottom face are roughly equal for all fabrics. Note that the pattern on the bottom face of the fabric is the same for all fabrics, inherent to the manufacturing process.

The values for the dimensionless width for the three fabrics are relatively close to each other and it is difficult to relate the values and the differences between, for example, κ_t and κ_b of fabric B1 and B2 to the material properties presented in table 2.1 or the stitch distances in table 2.2.

The lengths of the SYDs on the bottom face of B1 and B2 are consistently larger than those on the front, whereas there is no significant difference between the lengths on the bottom and top face of B3. The difference is slightly less than the differences between the widths. The presumed higher stitch tension of fabrics B1 and B2 compared to the stitch tension of fabric B3 (see section 2.2.2) is a plausible explanation of the increase of the dimensions of the SYDs. A higher stitch tension forces the loops on the bottom face into the SYD, resulting in a widening effect. The increase in length is likely to be related to the widening effect.

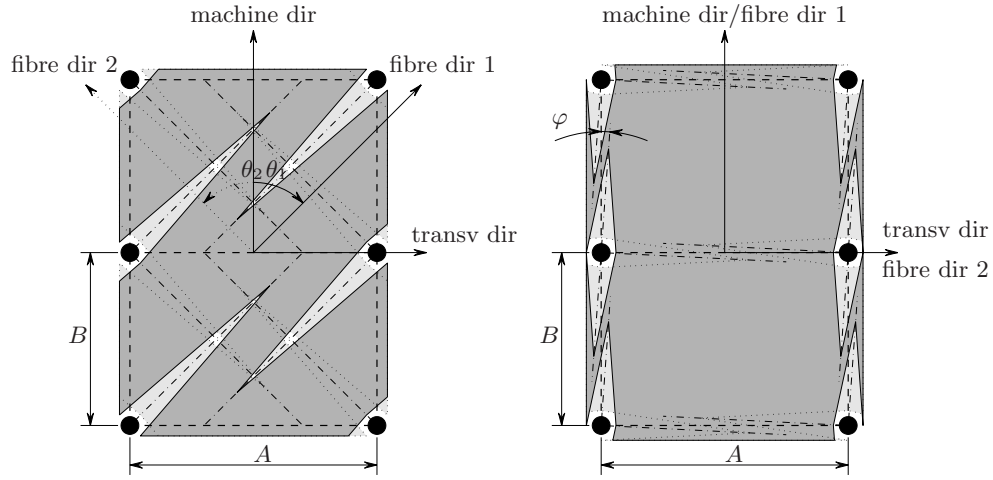

(a) $\pm 45^o$ *fabric,* $[\theta_1, \theta_2]$*=[45°,-45°]* (b) *0/90° fabric,* $[\theta_1, \theta_2]$*=[0°,90°]*

Figure 2.23: *The SYD length is more restricted for 0/90° fabrics compared to* $\pm 45^o$ *fabrics with unequal stitch distances A and B.*

The lengths of fabric B2 are smaller than the lengths of B1 and B3 (figure 2.22(b)). The fibre orientation is held responsible for the different length of fabric B2, see figure 2.23. The length of the SYDs of the 0/90° fabric is restricted more than the length of the ±45° fabrics, since the tips of the SYDs are closer to each other. A similar limitation in length will occur for a ±45° fabric with stitch distances A and B nearly equal to each other ($A \approx B$). The SYDs on the bottom face of the fabric are limited in the same way, but the distance to the neighbouring stitch penetration differs: the distance between two subsequent penetrations equals A on the top face and B on the bottom face. Consequently, the ratio of λ_t over λ_b is expected to equal the ratio of the ratio A over B, resulting in an expected bottom face dimensionless length of (see tables 2.2 and A.4 for the numbers):

$$\tilde{\lambda}_b = \frac{A}{B}\lambda_t = \frac{5.03}{2.64} \cdot 0.81 = 1.55. \tag{2.16}$$

A value of 1.34 (table A.4) is measured for λ_b, which is roughly 15% lower than the predicted value.

2.3.3 Influence of Deformation

The effect of in–plane shear deformation on the dimensions of the SYDs was analysed to enable the incorporation of fabric deformation in the geometric model of the NCFs. Shear angles of 15°, 30°, 45° and 60° were applied to specimens of the three fabrics. The results are compared to those of the relaxed configurations, discussed in the previous section. Table 2.4 lists the samples of each of the NCFs that were analysed.

Table 2.4: *Samples of each of the fabrics (* measured in [60]).*

$\gamma[^\circ]$	relaxed	15	30	45	60
B1	x*		x	x	
B2	x		x	x	
B3	x	x	x	x	x

Specimen Preparation The specimens were prepared in a small, square frame, also referred to as a trellis frame. The sides of the frame were made from 150mm×20mm strips of 3mm thick aluminium sheet material. The dimensions of the frame were 150mm×150mm. The fabric was clamped tightly on two opposite sides. The corners of the fabrics were cut away to prevent it from being stuck in the hinges of the frame. No special clamping device was used, since the specimens were small. Small strips of the same aluminium sheet material served as clamps and were fastened to the frame using M4 bolts piercing through the fabric. The applied shear frame and shear method is depicted schematically in figure 2.24.

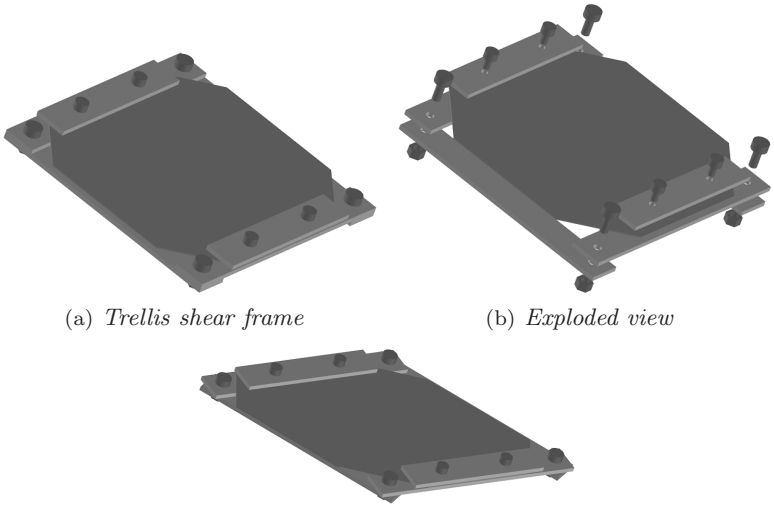

(a) *Trellis shear frame* (b) *Exploded view*

(c) *Sheared*

Figure 2.24: *Small trellis shear frame used to shear the specimens.*

The fabric was clamped in the frame such that the fibre directions of both fibre families were parallel to the sides of the frame, preventing fibre tensioning during shear. The shear was applied carefully, allowing or even actively helping the fabric to shear homogeneously and to prevent wrinkles. A glue, SICOMET© type 85, was applied near the edge of the specimens to maintain the shear angle after releasing the fabric from the frame. Warpage of the specimen is likely to occur, after it is released from the frame. The fabric is not sheared homogeneously near the edges, causing fibre tensions in the fabric. Moreover, tension is built up as a result of the in–plane compaction of the fibre bundles. The glue prevents the fabric from reducing the shear angle, resulting in warpage out of the plane of the specimen. The shear angle is maintained, though, provided a sufficient amount of glue is applied. The fabric is flattened under the PC scanner, regaining the shape it had in the frame. The specimens are scanned and analysed subsequently.

Normality Histograms of the measured κ and λ of the top face of fabric B3 are presented in figures 2.25 and 2.26. The histograms of the bottom face of B3 and top and bottom faces of B1 and B2 are found in appendix A.
The data of the sheared configurations is treated in the same way as the data of the relaxed configurations (section 2.3). The results of the Jarque–Bera goodness–of–fit test are presented in appendix B, table B.1. Again it is found that the hypothesis that the measured data is normally distributed is rejected for most of the configurations ($H_0 = 1$ in table B.1). It is assumed that all configurations are lognormally distributed for further modelling purposes.

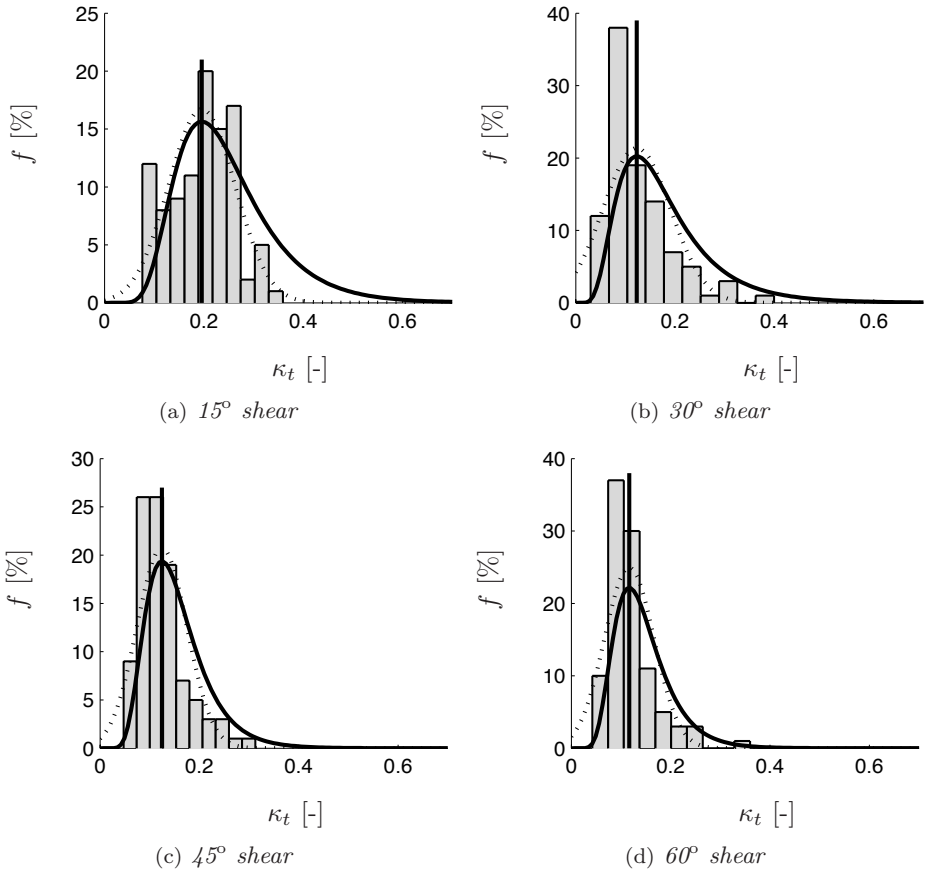

(a) *15° shear* (b) *30° shear*

(c) *45° shear* (d) *60° shear*

Figure 2.25: *Histograms of the dimensionless widths κ_t for fabric B3 in 15° to 60° sheared configurations. The dotted and solid lines are the normal and lognormal distribution functions based on the averaged value and estimated standard deviation of the measured data.*

Averaged Widths The measured κ_t and κ_b values are presented in figures 2.27 to 2.29(a & b) and in appendix A, tables A.3 and A.4. A clear indication of a decrease of κ is observed for shear angles between 0° and 30°, if the initial value of κ is higher than 2. The value of 2 can be considered as the minimum value of κ. It corresponds to the number of stitch yarns accommodated by the SYD. Hence, it is plausible to believe that in–plane compaction of the plies, occurring during shear, decreases the width of the SYDs up to a value of 2 for κ. This hypothesis is elaborated below.
The value of κ appears to be mainly influenced by:

- Stitch tension and stitch pattern.
- In–plane compaction of the fibrous plies during shear;

Two different types of stitch tension are distinguished, each of which affects the SYD dimensions in a different way: (1) tension due to the manufacturing process and (2)

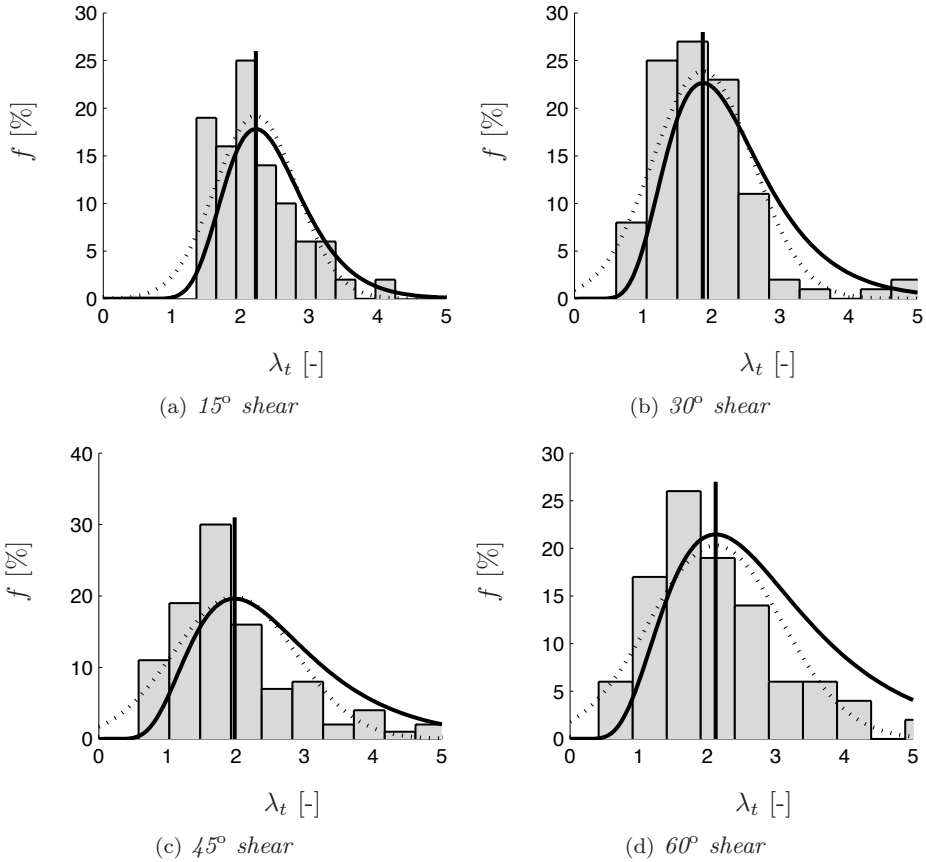

(a) *15° shear* (b) *30° shear*

(c) *45° shear* (d) *60° shear*

Figure 2.26: *Histograms of the dimensionless lengths λ_t for fabric B3 in 15° to 60° sheared configurations. The dotted and solid lines are the normal and lognormal distribution functions based on the averaged value and estimated standard deviation of the measured data.*

tension due to the deformation of the fabric. The effect of the stitch pattern and stitch tension was studied by Wiggers *et al.* [71]. An asymmetric shear behaviour of the stitches is implemented by them in a model describing the stitch tension. It is found to correspond well to the experimental results. The research performed in the framework of the FALCOM–project [9, 87] pointed out that stitch tension and pattern are interrelated to the shear behaviour and to the amount of in–plane compaction and vice versa. In–plane compaction is likely to occur during shear, based on the following consideration: a trellis type of shear results in a decrease of the initial area A_0 of the fabric in the shear frame proportional to the cosine of the shear angle γ:

$$\mathcal{A}(\gamma) = \mathcal{A}_0 \cos\gamma. \tag{2.17}$$

The decrease of the surface area is compensated by an increase of the thickness $h(\gamma)$

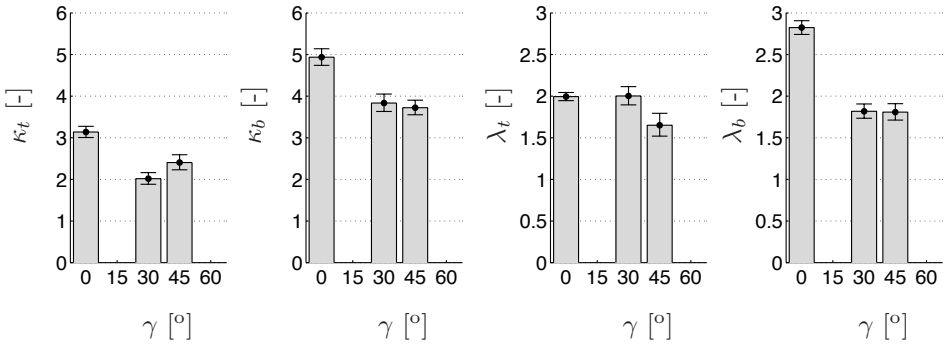

(a) *Top* (b) *Bottom* (c) *Top* (d) *Bottom*

Figure 2.27: *Measured values of top and bottom face dimensionless width κ and length λ of fabric B1 for various shear angles. The error bars indicate the scatter of the measured values.*

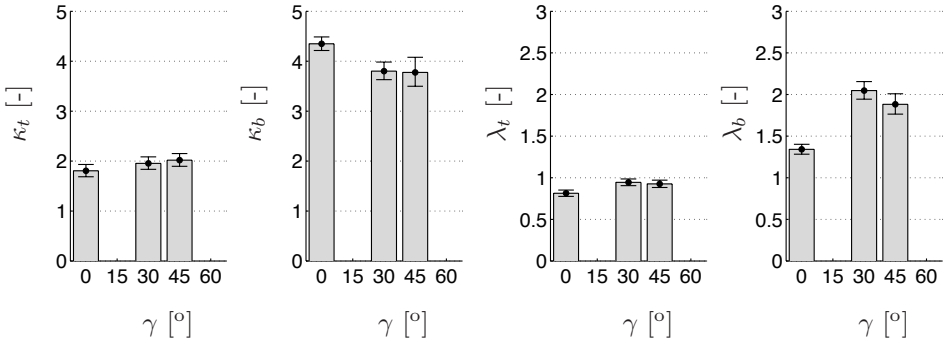

(a) *Top* (b) *Bottom* (c) *Top* (d) *Bottom*

Figure 2.28: *Measured values of top and bottom face dimensionless width κ and length λ of fabric B2 for various shear angles. The error bars indicate the scatter of the measured values.*

(h_0 the initial thickness). Assuming a constant volume V, such that:

$$h(\gamma) = \frac{h_0}{\cos\gamma}, \tag{2.18}$$

corresponds to the ideal situation, in which no in–plane compaction is observed. However, observations during trellis frame experiments [9, 87] lead to the conclusion that:

1. the fibre bundles appear to be compacted during shear;
2. the thickness increases more than inversely proportional to the cosine of the shear angle (*id est* violating (2.18)).

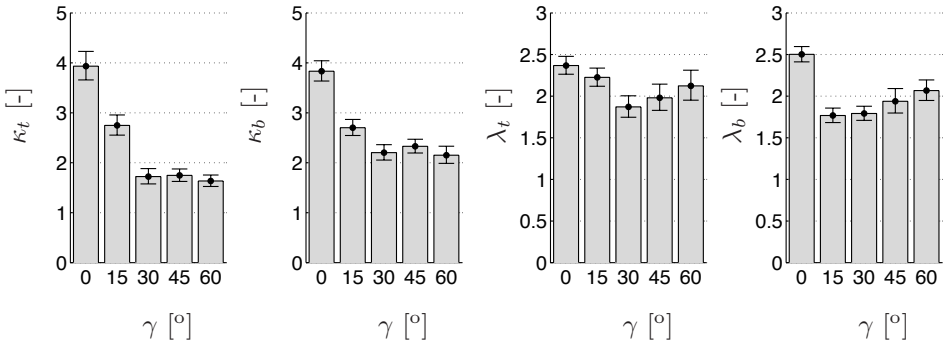

(a) *Top* (b) *Bottom* (c) *Top* (d) *Bottom*

Figure 2.29: *Measured values of top and bottom face dimensionless widths κ and length λ of fabric B3 for various shear angles. The error bars indicate the scatter of the measured values.*

These effects appear to contradict each other. The most likely explanation is dilatation, as found in the theory of soil mechanics. Dilatation means that the volume of sheared soil can increase due to a decrease of the packing [93]. Similar processes are likely to occur for fibre bundles, consisting of non–ideally packed fibres. The bundle size increases during shear, increasing the amount of in–plane compaction and as a result, the dimensions of the SYD will decrease.

The assumption of in–plane compaction corresponds well with the observed behaviour of the averaged widths of the SYDs (figures 2.27 to 2.29(a & b)). The fibres reduce the SYD width and the stitch thread is moved and compacted as a consequence. Figure 2.30 visualises this concept. The width of the SYD decreases gradually with increasing shear angle. The decrease of the width of the SYDs stops as the stitch yarn is compacted fully and the threads are rearranged such that the most compacted position is reached (situation changes from figure 2.30(a) to either figure 2.30(b) or figure 2.30(c) or an intermediate state of the latter two).

The compaction behaviour of the stitch thread is relevant in this process. Unfortunately, it is hard to obtain accurate data on the properties of the stitch yarn, since manufacturers of the thread are generally not involved in measuring these properties. Moreover, the threads are small (typical linear density of the yarn in the order of 10^1 tex[1]), making it virtually impossible to measure the compaction behaviour properly, even when using specialised textile testing equipment such as the "Kawabata Evaluation System for Fabrics" (KES–F) [94, 95].

The considerations discussed above lead to the conclusion that the value of κ is affected by two competing phenomena: (1) in–plane fabric compaction, causing a decreasing SYD width and (2) stitch yarn compaction, restricting the decrease of the SYD width. Both occur simultaneously where in–plane fabric compaction is the dominant deformation mechanism at lower shear angles while stitch yarn compaction dominates at higher shear angles.

[1] 1 tex = 1 g·km^{-1}

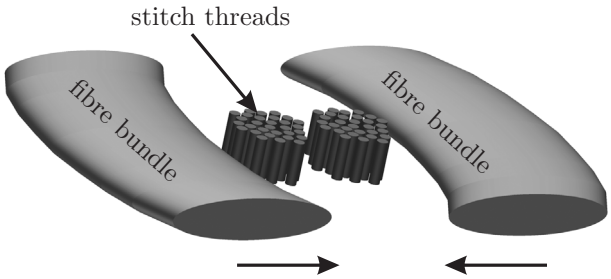

(a) *relaxed configuration*

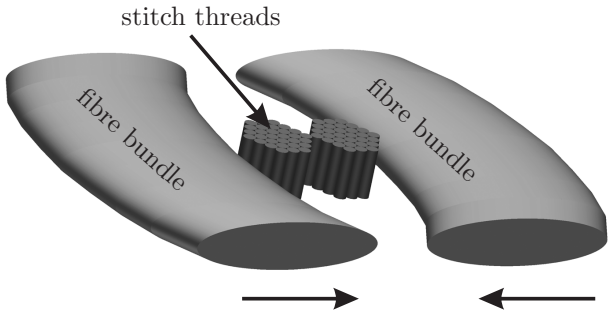

(b) *compacted, maximum space taken by stitch thread*

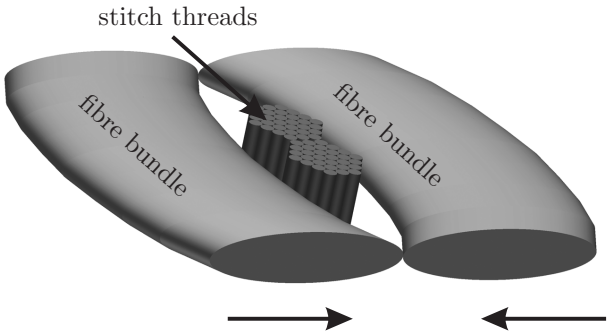

(c) *compacted, minimum space taken by stitch thread*

Figure 2.30: *Compaction of a fibre bundle and stitch thread resulting in closer packing of the stitch thread and a smaller SYD width. The minimum width depends on the position of the stitch threads (b and c).*

The data of fabric B3 (figure 2.29(a & b)) show that the minimum averaged values of κ for both faces is reached at a shear angle of roughly 30°. This suggests that the transition between the two compaction mechanisms occurs close to this shear angle. The data of fabrics B1 (figure 2.27) and B2 (figure 2.28) show a similar drop of the averaged value to a minimum value of 2, although less obvious, due to the absence of information on 15° sheared specimens. The minimum value for κ_t for all fabrics is roughly two, *id est* corresponds to twice the most compacted diameter of the stitch yarn. Fabric properties such as stitch yarn and stitch pattern appear not to affect the minimum averaged value of κ_t. The maximum dimensionless width that can be found equals 2 if it is assumed that (1) the stitch yarn has an ideal, maximum packed and circular cross–section; (2) the in–plane compaction of the fibre bundles is maximal; and (3) the stitch yarns lie next to each other in width direction of the SYD. This case is depicted in figure 2.30(b). An absolute minimum of 1 is expected under the same assumptions (figure 2.30(c)), but with the stitch yarns in longitudinal direction of the SYD. In practice, the actual packing will not be ideal, for example due to randomness and twist in the stitch thread, and the arrangement of the stitch yarns will deviate from the two extremes presented.
The value of κ_t of fabric B2 is approximately 2 for all shear angles. The different lay up (0°/90°, compared to ±45°) combined with the tricot/chain knitting pattern causes less widening of the SYDs, since part of the stitch thread runs nearly parallel to the length direction of the SYD, see figure 2.7(b).
The dimensionless width of the bottom face of fabrics B1 and B2 does not approach the value of 2, whereas κ_b of fabric B3 does. The width κ_b of B1 and B2 approaches the value of 4. A plausible cause is the presumed higher stitch tension. The assumption of the higher stitch tension is based on the relative loop sizes of the fabrics, as visualised in figure 2.15 and explained in section 2.3. The stitch loops are partly forced in the SYD, increasing its averaged width.
Finally, it should be noted that the width of the SYD cannot be determined unambiguously using the applied optical method. The bundle contour is curved, as is seen in figure 2.9 and schematically depicted by figure 2.10(a). This curved shape cannot be distinguished on the scanned images of the fabric. Hence, it is unknown whether the maximum or the minimum or an intermediate width of the SYD is measured.

Averaged Lengths The length of the SYDs appears not to be affected by shear. The locations of the stitch penetrations move along lines parallel to the sides of the frame during shear in case of a 0°/90° fabric. Consequently, the distances between the stitch penetrations, measured along the direction of the fibres, remain equal during shear.
A different situation is observed for a ±45° fabric, since the machine direction is not parallel to either of the sides of the shear frame. The rectangular $A \times B$ connecting neighbouring stitch penetration is rotated, stretched in one direction and contracted in the other direction. This effect is shown in figure 2.31. The stretching of the rectangle allows an elongation of the SYDs, whereas the contraction in the other direction results in a shortening effect: the width in the tips is reduced to zero. Both

effects appear to balance each other, apart from three exceptions that could not be explained: the higher λ's at the bottom face of fabrics B1 and B3 for the relaxed configurations (figures 2.27(d) and 2.29(d)) and the lower value of λ_b of fabric B2 (figure 2.28(d)).

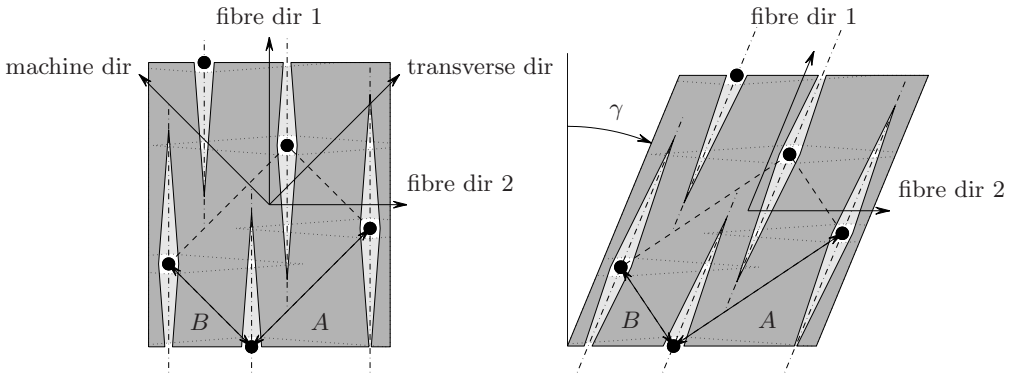

(a) *No shear.* (b) *Sheared.*

Figure 2.31: *Effect of shear on the location of the stitch penetrations (black dots) for a ±45° fabric. A and B refer to the needle spacing and stitch distance, γ is the shear angle.*

2.4 Model Formulation

The above considerations and observations lead to a formulation of the behaviour of the dimensionless width and length. A bilinear function appears to be appropriate for describing the change of width of the SYDs during fabric shear. The function $\kappa(\gamma)$ is defined as:

$$\kappa(\gamma) = \begin{cases} \kappa_{min} - (\kappa_{min} - \kappa_0)\,\dfrac{\gamma_{trans} - \gamma}{\gamma_{trans}} & \text{if} \quad \gamma \leq \gamma_{trans} \\ \kappa_{min} & \text{if} \quad \gamma > \gamma_{trans} \end{cases}, \tag{2.19}$$

with κ_0 and κ_{min} the values of κ at 0° shear (initial value) and its minimum value respectively. The transition shear angle is indicated by γ_{trans} and indicates the transition between both compaction mechanisms. The values of κ_0 and κ_{min} for the top and bottom face of the three fabrics are given in table 2.5. The bottom row of table 2.5 indicates the suggested values for a general fabric model. A distinction for fabrics with a relatively high and a relatively low stitch tension is made (B_H and B_L respectively). The effect of the variations in the averaged widths on the permeability and its variation will be discussed in section 3.3. A constant value of the length of the SYD will be assumed in the models, based on the averaged values (table 2.5). The suggested value for the lengths for a general fabric ($B_{\pm 45}$) is 2. An exception is made for 0°/90° fabrics ($B_{0/90}$), suggesting a value of 1 for the top face and A/B for the bottom face (see also figure 2.23).

Table 2.5: *The initial and minimum values for the empirically determined dimensionless width κ and length λ for top and bottom face and the transition shear angle γ_{trans}. B_{H} and B_{L} are suggested values for high and low stitch tension fabric respectively.*

	top			bottom			
	κ_0 [-]	κ_{min} [-]	λ [-]	κ_0 [-]	κ_{min} [-]	λ [-]	γ_{trans} [°]
B1	3.14	2.07	1.88	4.94	3.78	2.15	30
B2	1.93	1.93	0.89	4.35	3.79	1.76	30
B3	3.93	1.70	2.11	3.83	2.23	2.01	30
B_{H}	3.0	2.0	-	5.0	4.0	-	30
B_{L}	3.0	2.0	-	5.0	2.0	-	30
$B_{\pm 45}$	-	-	2	-	-	2	30
$B_{0/90}$	-	-	1	-	-	A/B	30

2.5 Multi Layer

So far the discussion was limited to the characterisation of single layer Non–Crimp Fabrics, whereas preforms mostly consist of a stack of layers. In practice it is observed that the measured permeability value of a single layer of fabric differs from the measured permeability value of a stack of layers. A plausible explanation of the differences in the permeability values is the nesting phenomenon [28, 53]: the thickness of a stack of fabric is smaller than the sum of the individual layer thicknesses. However, nesting is caused by bundle undulation, whereas NCF bundles hardly undulate out of the plane of the fabric. It could therefore easily be assumed that nesting does not occur.
NCFs can be considered as purely uni–directional layers of fibres, oriented in different directions. The question rises whether the permeability is affected by the stitch threads lying in the plane of the fabric on the top and bottom face of the fabric. This part of the stitch threads is pressed into the bundle, as shown in figure 2.32.

Figure 2.32: *Cross–section of the fibre bundles (light gray area) in longitudinal direction. The dark gray areas represent the cross–section in transverse direction of the stitch threads which are pressed into the fibre bundle.*

All plies of a biaxial NCF are either a top or a bottom face, but triaxial and quadriaxial NCFs also possess inner plies. The effect of stitch threads in the plane of the fibres will thus be stronger – if present – for biaxial material compared to for tri– and

quadriaxial material. On the other hand, the stitching is flattened to a maximum on the top and bottom faces of the fabric [60]. The flattened diameter of a stitch thread is small compared to the fibre bundle diameter and the effect of the threads on the permeability is expected to be small.
It is not expected that the stitch threads lying on the top and bottom face of the fabric will form a thin, but nearly continuous layer between two layers. Micrographs, such as figure 2.9, do not suggest the existence of such a layer.
It is assumed that the SYDs form a network of flow channels. The resin flows from one flow domain to another in overlap regions. The locations of the overlap regions are fairly well described within a single layer (see section 2.2, (2.3) and (2.4)). The overlap regions of the centres of the SYD exhibit a regular pattern, whereas the variation in the lengths of the SYDs results in an irregular pattern of overlap regions found near the tips of the SYDs.
However, the centres of the SYDs of different layers will not coincide for a stack of multiple NCFs. A random shift in the in–plane directions x and y (Δ_x and Δ_y) is introduced, see figure 2.33. This results in an unknown pattern of interaction regions between the SYDs of the facing plies of different fabric layers. A number of limiting cases for the shift has to be analysed, as it is impossible to calculate the effect of all possible shifts. Selecting a limited but representative set of shifts, allows to set upper and lower bounds for the effect of stacking on the permeability of the stack compared to the permeability of a single layer.

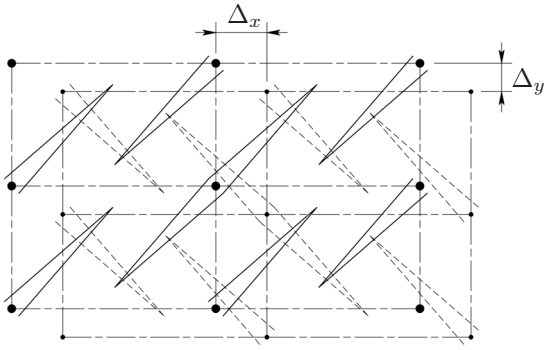

Figure 2.33: *A random shift* (Δ_x, Δ_y) *between the needle penetration locations of facing plies of stacked layers of NCFs complicate the determination of the flow channels through the NCF. The large dots are the centres of the SYD (solid lines) in one layer, the small dots the centres of the SYDs (dashed lines) in a second layer.*

The validity of the assumptions can be tested by analysing microscopic images of different types of Non–Crimp Fabric. Moreover, experiments comparing the permeability of biaxial and triaxial or quadriaxial stacks with an equal number of individual plies and overall equal orientation of the fibres can also reveal this effect. Note that the order of plies is different for a stack of bi–, tri– or quadriaxial layers, due to the stacking order within a single layer of NCF.

2.6 Conclusions on the Geometrical Model

The model of the internal geometry of an NCF, presented in this chapter, is based on the distortions formed by the stitch threads piercing through the fabric, leading to Stitch Yarn induced fibre Distortions (SYD). Three different types of biaxial Non–Crimp Fabrics were analysed in relaxed and sheared configuration. The conclusions that were drawn on the dimensions of the SYD are:

- The averaged width of the SYD mainly depends on the stitch yarn diameter. The dimensionless width κ was defined separately for either side of the fabric, in contrast with an earlier study. The structure of the stitch pattern differs on either side of the fabric: the bottom face contains loops oriented in the machine direction, the top face can have various patterns, but has no loops. This causes a difference in the dimensions of the SYDs.

- The averaged value of κ of the top faces lies between 2 and 4, depending on the stitch pattern and the orientation of the fibre families of the fabrics with respect to the machine direction. The averaged value of κ of the bottom faces is somewhat higher than the top face dimensionless width (between 3 and 5), which is attributed to the loops that are forced into the SYD. The stitch tension appears to be the determining factor in this process. However, an explicit relation between the dimensionless width on the one hand and the fabric properties and the manufacturing specifications on the other hand could not be established.

- Shear deformation of the fabric results in a decrease of the averaged width of the SYDs. The minimum value of 2 was found to be reached at a shear angle of roughly 30°. It was shown that the minimal value of the width is related to the closest packing of the stitch yarns in the SYD: a further decrease of the SYD width is obstructed by the stitch threads in the SYD. Increasing the shear angle results in an increase of the fibre bundle compaction, but not in a further decrease of the width of the SYDs.

- The averaged length of the SYD mainly depends on the stitch distances in machine and in cross direction and on the orientation of the fibre families. The dimensionless length λ of a $\pm 45°$ NCF differs from the dimensionless length of a $0°/90°$ NCF. The in–plane fabric compaction is maximum on the lines connecting the neighbouring stitch penetrations in machine and cross directions. Consequently, the half–lengths are limited to roughly the distance from the centre of the SYD along the fibres to these lines.

- The averaged length of the SYDs appears not to be affected by shear deformation. The two competing mechanisms occurring during a Trellis type of shear (elongation and compaction over the diagonals of the shear frame) are in balance, resulting in a constant length for varying shear angle.

The dimensions of SYDs exhibit a certain variability. The amount of variation was determined and the data was subjected to a goodness–of–fit test to determine the type of distribution. It was found that:

- The amount of variation on the dimensionless width was equal to roughly 5 to 10% of the averaged value. A similar amount of variation was measured on the dimensionless length. No difference was observed between the different types of fabric concerning the amount of variation.
- The measured data exhibits a lognormal distribution. The hypothesis that the data exhibits a lognormal distribution had to be rejected in only a small number of cases, whereas the hypothesis of normal distribution of the data had to be rejected for nearly half of the data sets.
- The lognormal distribution is attributed to the physical limitation on the dimensions formed by the stitch thread: the dimensions of the SYD cannot be smaller than the space required for the stitch threads inside the SYD.

Chapter 3

Network Flow Model

The permeability of a porous medium is often considered to be a purely geometrically determined property. This implies that only the internal geometry of the textile reinforcement determines the value of the permeability. The geometrical parameters discussed in the previous chapter would consequently be sufficient to predict the permeability. Properties such as the tow size, stitch pattern, stitch thread, but also fibre content and fabric deformation can be accounted for in the geometrical description.

However, there is no permeability model available yet that is able to predict the experimentally determined permeability of a fabric. The discrepancy between model and experiment must partly be attributed to the sensitivity for variations in the permeability experiments, resulting in a large amount of scatter, but it partly concerns shortcomings of the theoretical models. The currently available permeability models (described in [16, 47, 78, 96] for example) employ an idealised description of the internal geometry. It is observed that the permeability appears to depend on more than just these geometrical parameters. Flow and fluid characteristics and fluid–structure interaction also affect the resistance that the fluid experiences, apart from the obstruction formed by the geometrical structure of the flow path. The permeability appears to vary as a function of the injection pressure, viscosity, the injected fluid and its interaction with the reinforcement material, the architecture of the reinforcement and the material from which it is made (including surface treatments) and the degree of saturation of the fibre mat.

The origin of the dependency of the permeability on these parameters is found in the simultaneous occurrence of hydrostatic and capillary flow. The internal geometry of the reinforcement, the fluid characteristics and the flow characteristics all affect the balance between the hydrostatic and the capillary forces. The balance between both flow types affects the permeability to a large extent. The difference in flow types results in a difference in fluid velocity inside and around the fibre bundles. Consequently, the flow front is not straight on the meso–level and micro–level scale (see figure 2.1 for an explanation of the length scales), as schematically shown in figure 3.1. It is shown in the figure 3.1 that transverse flow from the meso–level domain (inter

bundle space) to the micro–level domain (intra bundle space) or vice versa occurs in addition to the global longitudinal flow. The direction of the transverse flows depends on whether the meso or micro flow is dominant.

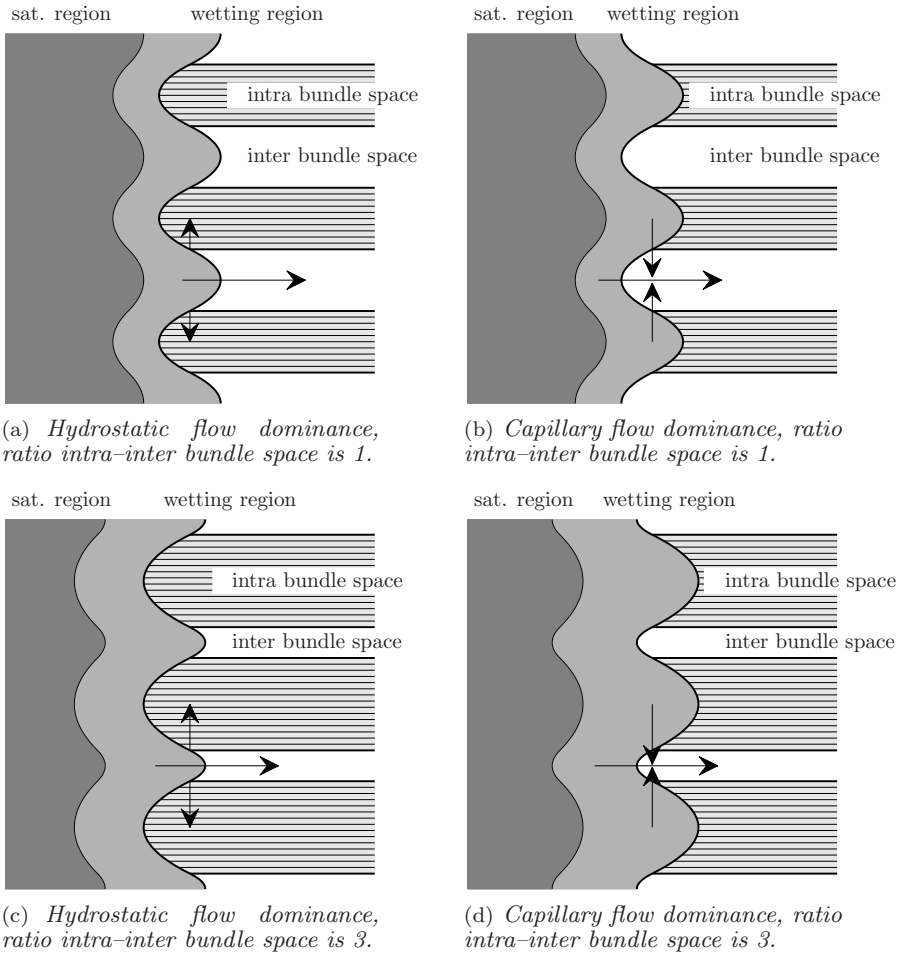

(a) *Hydrostatic flow dominance, ratio intra–inter bundle space is 1.*

(b) *Capillary flow dominance, ratio intra–inter bundle space is 1.*

(c) *Hydrostatic flow dominance, ratio intra–inter bundle space is 3.*

(d) *Capillary flow dominance, ratio intra–inter bundle space is 3.*

Figure 3.1: *Potential hydrostatic and capillary flow dominance for a relatively low and a relatively high fibre content. The horizontal arrows indicate the global flow direction, the vertical arrows indicate the direction of the transverse flow. The light gray region refers to the wetting region (partly filled with fluid), the dark gray area to the fully saturated region.*

Hence, it appears that the route to an accurate prediction of the permeability for an arbitrary textile reinforcement leads to a multi scale flow model. Generally, the incorporation micro–level and meso–level flows is done in two different ways: either using separate but complimentary models, or a fully integrated model.

The first strategy requires knowledge on the micro–level flow along and perpendicular to the fibre bundle. These types of flows were studied extensively by many authors [97–102]. The effect of the fibre arrangement inside the bundle on the flow is studied by others in addition [54–57]. The micro–level models are used as an input for the macro–level models. However, the link between the macro– and micro–level models is weak and it is difficult to account for the variations in the internal structure, such as the variations in the dimensions of the SYDs discussed in chapter 2.
The second strategy certainly performs better considering the representation of the actual internal geometry. Generally, the models implement an extended version of the Stokes equation (Brinkman's equation [103–105]). The main drawback is the extensive computational effort resulting from the large number of elements. The large number of elements is inherent to the explicit incorporation of the micro–level flow domain in the model.
Both types of flow models can be developed up to a level where they predict the permeability reasonably well. That is: the predicted value will be sufficiently close to the averaged measured permeability value (maximum deviation $\approx$50%). None of both types of models is able to indicate the possible deviation from the averaged value. As mentioned, the variation in the experimentally determined permeability values partly depends on the measurement itself, but it also depends on the internal structure of the reinforcement. A large portion of the experimental scatter observed in woven fabrics can be attributed to nesting, as shown by Hoes *et al.* [25–28]. Non–Crimp Fabrics hardly show any nesting, but the internal structure does exhibit a certain variation, as discussed in chapter 2. The effects of these variations on the permeability are yet unknown. Hence, a strategy is proposed to incorporate the effect of the variability in the internal structure of a textile reinforcement explicitly in a permeability prediction model.
The proposed permeability prediction model is based on a channel flow approach. The distortions (SYDs) discussed in chapter 2 act as meso–level flow channels. This approach differs from a unit cell approach, where the entire domain is divided in elementary units. A unit cell is the smallest unit that can represent the internal structure. Hence, it suffices to analyse a unit cell to find the properties of the entire structure[1]. The fully integrated models (for example, the model presented by Belov *et al.* [105]) generally use a unit cell approach, resulting in a continuous physical domain description, incorporating both the intra and inter bundle space. The intra bundle space is not described explicitly in the channel flow model. This does not imply that the unit cell approach *does* and the flow channel approach does *not* include the micro–level flows in the bundle. A frequently applied option to incorporate micro–level flows is the use of a 'sink'–term [106–108]: a certain amount of fluid is assumed to flow from the inter bundle space to the intra bundle space.
The aim of the channel flow model presented here is focussed on the effect of the variability of the internal structure, *id est* a more qualitative prediction of the permeability, whereas the exact value of the permeability is less important. The

[1] An example of a unit cell description of woven fabrics and how the elastic properties are derived from the unit cells can be found in Lamers [51]. The approach to find the macroscopic flow properties based on a unit cell approach is similar.

model is based on the meso–level flow only. It is assumed that the hydrostatic (meso–level) flow dominates the behaviour of the permeability for pressure driven processes, such as RTM, which are of the main interest in this work. A meso–level based flow analysis consequently suffices to determine the qualitative effect of the variability found in the internal structure. Moreover, Belov *et al.* [24] showed that a permeability prediction based on the meso–level flow predicts a 30% lower permeability compared to a prediction based on a full micro–meso–level model, but qualitatively, the predictions hardly differ. It can be concluded that a model that accurately predicts the value of the permeability requires the inclusion of micro–level flows, especially for high fibre contents, whereas the analysis of the variability in the permeability due to the variability in the internal structure is more efficient if a meso–level model is employed. Using the meso–level model presented here in conjunction with a full micro–meso–level model results in an improved prediction of the permeability.

Summarising, the presented model consists of the two parts:

1. Meso–level flow equations describing the flow in a channel;
2. A network formulation, including a solution routine to estimate the macro–level permeability and its variation, based on the meso–level channel flow equations.

These two topics are discussed in the next two sections, followed by a discussion on the results obtained with the model.

3.1 Channel Flow

The general solution of the steady state flow of an incompressible Newtonian fluid in a certain domain is based on conservation laws (mass, momentum and energy), constitutive equations and boundary conditions [109, 110]. Here, the basic fluid mechanics equations that are employed in the channel flow model are summarised.

3.1.1 General Fluid Mechanics

The conservation of mass, also known as the continuity equation, is given by:

$$\frac{\mathrm{D}\rho}{\mathrm{D}t} + \rho\left(\boldsymbol{\nabla}\cdot\boldsymbol{u}\right) = 0, \tag{3.1}$$

with ρ the density of the fluid, t the time and $\boldsymbol{u}$ the velocity of the fluid. $\mathrm{D}/\mathrm{D}t$ denotes the material derivative, which reads (operating on the density ρ):

$$\frac{\mathrm{D}\rho}{\mathrm{D}t} = \frac{\partial\rho}{\partial t} + \left(\boldsymbol{u}\cdot\boldsymbol{\nabla}\right)\rho. \tag{3.2}$$

The conservation of momentum reads:

$$\rho\frac{\mathrm{D}\boldsymbol{u}}{\mathrm{D}t} = \boldsymbol{\nabla}\cdot\underline{\boldsymbol{\sigma}} + \rho\boldsymbol{F}, \tag{3.3}$$

with $\boldsymbol{F}$ the body forces acting on the fluid and $\underline{\boldsymbol{\sigma}}$ the Cauchy stress tensor:

$$\underline{\boldsymbol{\sigma}} = -p_h \underline{\boldsymbol{I}} + \underline{\boldsymbol{\sigma}}_d, \tag{3.4}$$

with p_h the hydrostatic pressure, $\underline{\boldsymbol{I}}$ the unit tensor and $\underline{\boldsymbol{\sigma}}_d$ the deviatoric stress tensor. The change of energy within the system by the First Law of thermodynamics:

$$\rho \frac{\mathrm{D}U}{\mathrm{D}t} = -\boldsymbol{\nabla} \cdot \boldsymbol{q} + \underline{\boldsymbol{\sigma}} : \nabla \boldsymbol{u} + \rho \dot{\phi}, \tag{3.5}$$

with U the specific internal energy and $\boldsymbol{q}$ the heat flux and $\dot{\phi}$ a heat source. The last term in (3.5) represents the mechanical power. The heat flux and source equal zero, since only isothermal flow is analysed. The constitutive equation for viscous flow of an incompressible Newtonian fluid relates the rate of deformation to the stress, according to:

$$\underline{\boldsymbol{\sigma}}_d = 2\mu \underline{\boldsymbol{D}}, \tag{3.6}$$

with μ the viscosity of the fluid and $\underline{\boldsymbol{D}}$ the deviatoric rate of deformation, defined as the symmetric part of the velocity gradient $\underline{\boldsymbol{\mathcal{L}}}$ [51]:

$$\underline{\boldsymbol{\mathcal{L}}} = \boldsymbol{u}\,\boldsymbol{\nabla} = \frac{1}{2}\left(\boldsymbol{u}\,\boldsymbol{\nabla} + \boldsymbol{\nabla}\boldsymbol{u}\right) + \frac{1}{2}\left(\boldsymbol{u}\,\boldsymbol{\nabla} - \boldsymbol{\nabla}\boldsymbol{u}\right) = \underline{\boldsymbol{D}} + \underline{\boldsymbol{W}}. \tag{3.7}$$

The anti–symmetric part is defined as $\underline{\boldsymbol{W}}$, the vorticity. The expression for the rate of deformation $\underline{\boldsymbol{D}}$ is substituted in the constitutive relation (3.6). Subsequently, the definition of the stress tensor (3.4) is used to rewrite the expression for the conservation of momentum :

$$\begin{aligned} \rho \frac{\mathrm{D}\boldsymbol{u}}{\mathrm{D}t} &= \boldsymbol{\nabla} \cdot \left(-p_h \underline{\boldsymbol{I}} + 2\mu \frac{1}{2}\left((\boldsymbol{u}\,\boldsymbol{\nabla}) + (\boldsymbol{u}\,\boldsymbol{\nabla})^T \right) \right) + \rho \boldsymbol{F} \\ &= -\boldsymbol{\nabla} p_h + \mu \nabla^2 \boldsymbol{u} + \rho \boldsymbol{F} \end{aligned} \tag{3.8}$$

with ∇^2 the Laplace operator. This equation is known as the Navier–Stokes (NS) equation [110, 111]. The NS–equation – and its derivatives – is also referred to as the impulse equation of a fluid.
The flow is assumed to be stationary, since wetting is not accounted for. Consequently, the time dependent part of (3.2) – $\dfrac{\partial \boldsymbol{u}}{\partial t}$ – equals zero[2]. The second term of the material derivative – $\boldsymbol{u} \cdot \boldsymbol{\nabla}\boldsymbol{u}$ – also equals zero, since inertia effects are neglected for low Reynolds numbers. There are no body forces acting on the fluid (gravity is not accounted for; $\boldsymbol{F} = 0$). As a result, the NS–equation reduces to the Stokes equation for viscous flow:

$$\boldsymbol{\nabla} p - \mu \nabla^2 \boldsymbol{u} = \boldsymbol{0}. \tag{3.9}$$

The continuity equation (3.1) must be satisfied in addition to (3.9). The material derivative $\frac{\mathrm{D}\rho}{\mathrm{D}t}$ equals zero, since the density is constant (incompressible fluid). The continuity equation becomes:

$$\boldsymbol{\nabla} \cdot \boldsymbol{u} = 0. \tag{3.10}$$

[2]The material derivative acts on $\boldsymbol{u}$ here, rather than on ρ

The integration constants resulting from solving the differential equations (3.9) and (3.10), depend on the boundary conditions. Both Dirichlet and Neumann conditions (or a combination) can be applied. Dirichlet conditions apply, for example, if a flow along (or perpendicular to) a fibre or an impermeable bundle is analysed[3].

3.1.2 Solutions for a Channel Flow

The above derived general flow equations are applied to a channel. The aim is to find a relation between the flow and the permeability of the channel[4]. The flow is assumed to be one–dimensional. The solution of the axial fluid velocity u is found by solving the impulse equation (3.3) on an infinitesimally small part of the flow domain, as depicted in figure 3.2. The equations are derived in the cylindrical coordinates (x, r, θ) rather than in the cartesian coordinates (x, y, z).

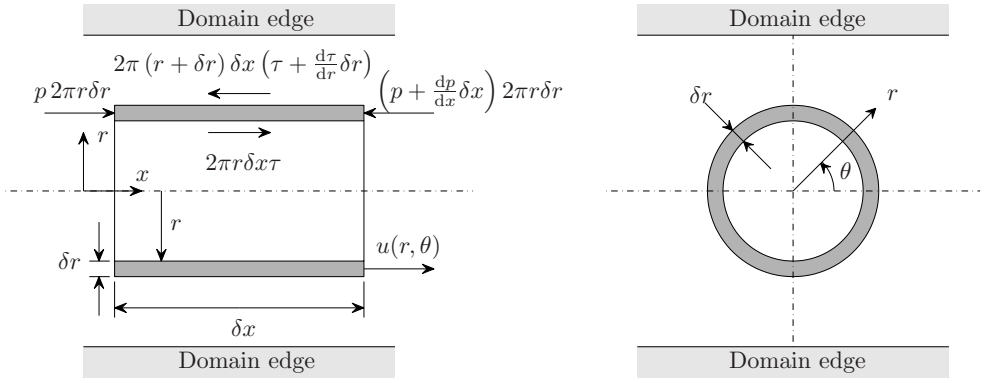

(a) (x, r)–*plane* (b) (r, θ)–*plane*

Figure 3.2: *The impulse acting on an infinitesimally small part of the flow domain. p: pressure; τ: shear stress; (x, r, θ): cylindrical coordinates; δ: infinitesimally small part.*

The total impulse on the infinitesimally small part is given by:

$$\begin{aligned} & p\,\pi r\delta r - \left(p+\frac{\mathrm{d}p}{\mathrm{d}x}\delta x\right)2\pi r\delta r + 2\pi r\delta x\tau - 2\pi\,(r+\delta r)\,\delta x\left(\tau+\frac{\mathrm{d}\tau}{\mathrm{d}r}\delta r\right) = \\ & -2\pi\delta x\delta r\,r\frac{\mathrm{d}p}{\mathrm{d}x}r - 2\pi\delta x\delta r\,r\frac{\mathrm{d}\tau}{\mathrm{d}r} - 2\pi\delta x\delta r\tau - 2\pi\delta x\delta r\frac{\mathrm{d}\tau}{\mathrm{d}r}\delta r = \\ & -2\pi\delta x\delta r\left(r\frac{\mathrm{d}p}{\mathrm{d}x}+\frac{\mathrm{d}(\tau r)}{\mathrm{d}r}\right) = 0. \end{aligned} \tag{3.11}$$

[3]Employing a sink term [106–108], see previous discussion, is not achieved by different boundary condition, but by a different definition of the continuity equation: $\boldsymbol{\nabla}\cdot\boldsymbol{u} = -S$. Only then, a net transport of fluid is possible.

[4]Permeability is generally only associated with porous media and not with the flow resistance of a channel. However, the comparison is logical here, since the porous geometry is effectively represented by a series of small channels.

The higher order term (last term on the second line of (3.11)) is neglected to obtain the final result. The constitutive equation (3.6) and the definition of the deviatoric rate of deformation (3.7)[5] for a one–dimensional situation is now substituted in the part between brackets of the last equation of (3.11):

$$\tau = -\mu \frac{\mathrm{d}u(r,\theta)}{\mathrm{d}r}. \tag{3.12}$$

$$r\frac{\mathrm{d}p}{\mathrm{d}x} - \mu \frac{\mathrm{d}}{\mathrm{d}r}\left(r\frac{\mathrm{d}u(r,\theta)}{\mathrm{d}r}\right) = 0. \tag{3.13}$$

The velocity profile $u(r,\theta)$ is solved by a double integration over r, leading to the general solution, formulated as:

$$u(r,\theta) = \frac{1}{4\mu}\frac{\mathrm{d}p}{\mathrm{d}x}r^2 + \psi, \tag{3.14}$$

$$\nabla^2\psi = 0, \tag{3.15}$$

with $u(r,\theta)$ the fluid velocity in axial direction, μ the viscosity and ψ an arbitrary function. The problem is now reduced to finding the function ψ, *id est* solving a homogeneous second order partial differential equation. The general solution for ψ is [112]:

$$\begin{aligned}\psi = a_0 + b_0 \ln r + \\ \sum_{k=1}^{\infty}\left(a_k r^k \cos k\theta + b_k r^k \sin k\theta + c_k r^{-k}\cos k\theta + d_k r^{-k}\sin k\theta\right).\end{aligned} \tag{3.16}$$

The coefficients in this general function depend on the shape of the domain and the boundary conditions. Here, only the function representing the flow in a channel with a circular cross–section is relevant. This velocity profile is represented by:

$$u(r,\theta) = \frac{r^2 - r_{out}^2}{4\mu}\frac{\mathrm{d}p}{\mathrm{d}x}, \tag{3.17}$$

with r_{out} the radius of the duct. The flow Φ through a channel is found by integrating the velocity profile over the cross–sectional area $\mathcal{A}$ of the channel:

$$\Phi = \int_{\mathcal{A}} u(r,\theta)\,\mathrm{d}\mathcal{A} = \int_{\theta=0}^{2\pi}\int_{r=0}^{r_{out}} u(r,\theta) r \mathrm{d}r\mathrm{d}\theta. \tag{3.18}$$

Substitution of (3.17) in (3.18) leads to:

$$\Phi = \frac{\pi r_{out}^4}{8\mu}\frac{\mathrm{d}p}{\mathrm{d}x}. \tag{3.19}$$

[5] the shear stress is generally referred to using the symbol τ, but sometimes also using $\sigma_{r\theta}$ (as would apply in this case). The shear stress is one of the components of the deviatoric stress tensor $\underline{\boldsymbol{\sigma}}_d$

Comparing this to the relation between the volumetric flow and the pressure drop proposed by Darcy (1.1), yields:

$$\Phi = \frac{\pi r_{out}^4}{8\mu}\frac{\mathrm{d}p}{\mathrm{d}x} = \frac{K}{\mu}\frac{\mathrm{d}p}{\mathrm{d}x} \Rightarrow K = \frac{\pi r_{out}^4}{8}, \tag{3.20}$$

with K the permeability of the channel. Equation (3.20) is generalised for channels with a non–circular cross–section by using the hydraulic radius. The hydraulic radius is defined as the radius of a channel with circular cross–section, of which the flow resistance equals the flow resistance of the channel with a non–circular cross-section [110]. The flow resistance is related to the cross–sectional area $\mathcal{A}$ and the perimeter $\mathcal{P}$ of the cross–section. The hydraulic radius is twice the ratio between both:

$$r_h = \frac{2\mathcal{A}}{\mathcal{P}}. \tag{3.21}$$

The radius of the channels (either r_{out} or r_h) is typically of the order of millimetres ($\mathcal{O}(10^{-3})$m), hence the permeability of a single channel is $\mathcal{O}(10^{-12})\mathrm{m}^4$.

A relation between the flow through a channel, the flow resistance (or meso–level permeability) and the channel dimensions is established. This relation is used to transform the measured dimensions of the SYDs, as presented in chapter 2, into the flow resistances. The next step in the process is the prediction of a macroscopic permeability, based on the mesoscopic permeabilities.
The permeability K is a scalar value, according to the definition in (3.20). However, the permeability of a fabric is a second order tensor. The complete permeability tensor $\underline{\boldsymbol{K}}$ can be derived by analysing the scalar values of the permeability for different directions of the pressure gradient (or flow). Three individual directions of the pressure gradient are required to construct the in–plane permeability tensor $\underline{\boldsymbol{K}}$: one to determine the orientation of the in–plane principal directions and two to determine the value of the principal permeabilities. A set of two analyses suffices if the principal directions are known.

3.2 Network Formulation

A single channel is considered to be insufficient to predict the permeability and its possible variability due to the variations in the internal structure of the fabric (see also [33]). The permeability of a single channel as a function of its dimensions can be determined straightforwardly, but this does not lead to an estimate of the variation of a set of connected channels with variable dimensions. The variability in the dimensions of the channels is therefore implemented in a numerical model by analysing a network of channels rather than a single channel. Effectively a piece of fabric is analysed instead of only the smallest representative element of the fabric.
The network is built using the information provided by the geometrical model. The channels are mutually connected in the interaction regions, as described in section 2.2. The fluid can flow from one SYD to another via these interaction regions. The size and

location of the interaction regions follow directly from the geometrical model, although the variability in the dimensions complicates the size of the interaction regions. The resistance observed by the fluid flowing from one interaction point to another is purely based on meso–level flow. Flow inside the bundles is not accounted for at this stage, since it is believed that the meso–level flow dominates the permeability behaviour (as previously discussed, see also [105]). Moreover, accounting for micro–level flow complicates the network model, whereas the relatively large size of the network (compared to a single NCF unit cell) requires a relatively fast solution strategy to be useful in practical applications.
Firstly, the methodology to create a network of flow channels, based on the SYDs is discussed. Secondly, the fluid velocity field solution of a network applying basic flow equations is presented.

3.2.1 From SYD to Network

The single SYDs are connected to each other, forming a network through which the fluid flows. The channels in a single ply are not connected (they run parallel to each other), but they are connected to the channels of neighbouring plies, with a different orientation of the bundles and consequently of the channels. It was explained in section 2.2 that the locations of the main interaction points between two SYD unit cells are found in the centre of the cells, where the stitch needle penetrates the fabric (see figure 3.3). The locations of the needle penetrations form a regular grid, since the speed of the loom and the needle spacing are constant during manufacturing (see also section 2.1).
Additional interaction regions are found in the tip region of the SYD channel (see figure 3.3). The location of these interaction regions can also be calculated based on the needle spacing A and stitch distance in machine direction B. The number of additional interaction regions depends on the length of the SYD, but generally a maximum of one on each tip will be found, since the dimensionless length λ approaches a value of 2 for most cases (see section 2.3 for a more elaborate discussion).
The fluid flowing through the SYD channel experiences a resistance, depending on the dimensions of the channel and the interaction with the boundaries. The interaction with the boundaries can be described in various ways. The goal here is to formulate a (network) model in which the variation of the channel dimensions is properly incorporated in the prediction of the permeability and of its variation. The resistance the fluid experiences in a single channel is therefore in the first place based on simple flow equations, as were derived in section 3.1.2 and impermeable bundles. It is shown by Ruijter [113] that it is also possible to solve the flow equations in the SYDs by applying a finite difference technique. The solution is certainly more accurate compared to the solution obtained with the channel flow equations. However, the solution routine is relatively complex – hence difficult to adapt for specific situations, such as variations in the size and location of the interaction regions – and the solution times are longer. Consequently, the simple equations are found to be more suitable to be used here.
Firstly, a network of SYDs is formed using the stitch parameters A and B. Secondly,

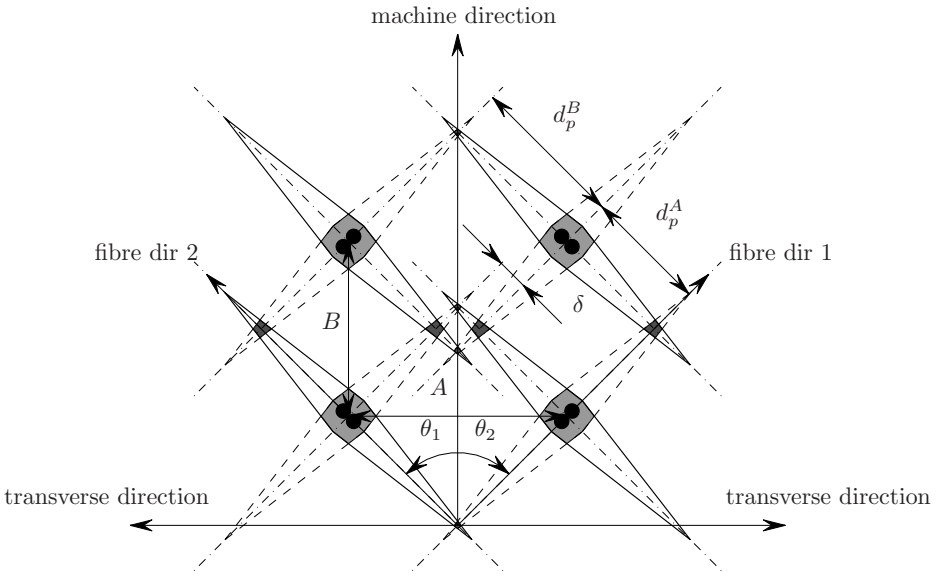

Figure 3.3: *Schematic representation of the SYD configuration of a biaxial NCF. The solid lines correspond to the top ply SYDs, the dashed lines to the bottom SYDs. The projected distances and the distance between the tips are indicated by d_p^A, d_p^B and δ respectively. The angles of the fibre direction with respect to the machine direction are θ_1 and θ_2. The light gray areas indicate the interaction regions between the SYDs of the top and bottom plies in the centre of the SYD; the dark gray areas indicate the interaction regions in the tip regions. The black circles point to the stitch threads penetrating the fabric.*

randomly generated dimensions are assigned to the SYDs, such that the averaged size and the variation in the dimensions correspond to the measured ones (see section 2.3). The variation in the dimensions can be distributed to the network in a random way, or according to a certain predefined pattern. The effect of this spatial distribution of the dimensional variations will also be presented.

The spatial distribution of channel dimensions and resulting channel resistances is a meso–level phenomenon. It sets bounds for the variation in the macro–level permeability, as used in simulation software. Consequently, the type of distribution differs from the distribution of the permeability applied in flow simulation software, see Desplentere *et al.* [114] who studied the variation on the macro–level permeability on the filling of the preform. Their approach was to assign varying permeabilities to different predefined regions of the preform. An additional constraint in their models is that the distribution of the permeability is smooth, since sharp transitions in the macro–scale permeability are not likely to occur in practice.

Large SYDs can be close to small SYDs, resulting in steep transitions of the meso–level permeability. It could even be argued that large SYDs are always surrounded by small SYDs, based on the compaction behaviour in the plane of the fabric. However,

the correlation between the dimensions of neighbouring SYDs was not analysed and is hence not available.

3.2.2 A Simple Network

Initially, the network model is kept rather basic in order to be able to identify the properties of the network model properly. The model is based primarily on the geometrical parameters of fabric B3, the $\pm 45^{o}$ biaxial fabric from Devold (see section 2.3). The network of SYD flow channels is constructed based on four assumptions:

1. Each channel is assumed to be connected to five other channels: one in the centre and two in each of the corners.
2. The distance between the centre connection and the edge connection regions of the overlapping channels is equal for all channels.
3. The shape of the SYDs is assumed to be symmetrical with respect to both in–plane axes of its local coordinate system.
4. The top face and bottom face SYD at each stitch penetration point are equal.
5. A set of channel widths is generated, such that the average and standard deviation correspond to the measured values. The widths are randomly assigned to the channels, or according to a certain predefined distribution.
6. An equivalent channel radius is defined based on the geometry of the SYDs (see figure 2.10).

Sub. 1:
The length of the channels is variable, but it is assumed that the length is in all cases large enough to connect to channels of the next row in machine direction (see figure 3.3). There is no direct connection between SYDs in the same ply, since the SYDs are oriented parallel with respect to each other. The tips are separated by the distance δ (see figure 3.3). It is likely that some fluid will flow from tip to tip if the distance δ is small compared to the bundle width, but initially this flow is neglected.
A different situations applies for a $0^{o}/90^{o}$ fabric. It was shown that the tips of the SYDs are close to each other, see figure 2.23. Channels, oriented in and perpendicular to the machine direction, are more easily formed.

Sub. 2:
The distance between the centre interaction points and the interaction points in the tip region is equal in all SYD unit cells. Possible irregularities in the pattern of needle penetrations will affect this distance between the interaction points. However, the irregularities are small (see table 2.2) and assumed to be negligible in the first stage of the network analysis.

Sub. 3:
The origin of the local coordinate system is located in the centre of the SYD. One axis is aligned in the longitudinal direction (hence runs from tip to tip), the second axis is perpendicular to the first. The shape is assumed to be symmetric with respect to these two axes.

Sub. 4:
The dimensions of a top face SYD and a bottom face SYD are assumed to be equal at each stitch penetration. A difference between the averaged size of the top and bottom face was found for the fabrics B1 and B2 (see section 2.3.2). The averaged dimensions of fabric B3 were found to be equal on either side of the fabric. The latter situation is assumed here. Additionally, the assumption is made that not only the averaged value, but also the values on either side of the fabric at a stitch penetration are equal. In fact, a strong correlation between the dimensions of top and bottom face is assumed, which is plausible, since the dimensions depend on the stitch thread.

Sub. 5:
The variability of the dimensions of the SYD channels is distributed over the entire network according to a certain pattern. Initially, a fully random distribution is used. However, the distribution can be adapted such that an enhanced flow path is formed. For example, assigning the larger widths to the SYDs around the centre line of the network, leads to a flow path around the centre line, which dominates the overall flow.

Sub. 6:
The shape of the cross–section is non–circular, as discussed in section 2.2[6]. The cross–section is replaced by a circular cross–section with a hydraulic radius r_h, such that the flow resistance is equal (section 3.1.2, equation (3.21)). Moreover, the channel is wedge shaped. The hydraulic radius depends on the longitudinal coordinate (x) in the channel ($r_h = r(x)$). It can be shown that an equivalent, constant channel radius r_E can be derived, such that the flow resistance of a channel with a varying cross–section equals the resistance of the equivalent channel. It is assumed that the hydraulic channel radius changes linearly. Concave and convex quadratic functions can also be used to describe the channel radius function, but the deviations with respect to a linear channel radius function are small due to the high length to width ratio of the channel. Therefore, only a linearly varying channel radius function is used, as depicted in figure 3.4.
The linear channel radius is defined by:

$$r(x) = \frac{r_2 - r_1}{L} x + r_1, \tag{3.22}$$

with $r_{1,2}$ the radii at the entrance and exit of the channel and L the length of the channel. The derivation of the equivalent radius of a channel with a linearly varying radius is presented in appendix C. The equivalent radius reads:

$$r_E = \left(\frac{3 r_1^3 r_2^3}{r_1^2 + r_1 r_2 + r_2^2} \right)^{\frac{1}{4}}. \tag{3.23}$$

[6]Note that the height is assumed to be constant, since the cavity height remains constant in Resin Transfer Moulding (RTM). A variable cavity height, as can occur in Resin Infusion under Flexible Tooling (RIFT), results in a variation in the layer thickness and consequently in the flow channels.

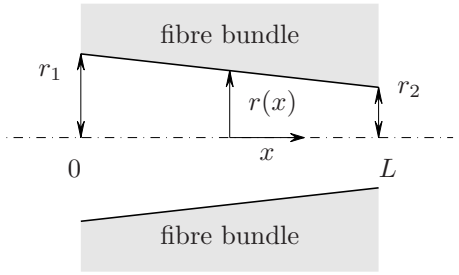

Figure 3.4: *A linearly varying channel radius is used to describe the shape of the SYD in the plane of the fabric.*

The shape of the SYDs is defined: the length L is assumed to be constant for all widths and the width (or equivalent channel radius) is derived by employing the above derived functions. As a direct result, the width in the centre of the SYD determines the local width inside the SYD (for example r_1 and r_2 in (3.23)). The width in the centre is also the measured width, that was discussed in chapter 2. Therefore, the term 'width of the SYD' will refer to the centre width only, throughout the remainder of the text.

3.2.3 Subdividing the SYD

The SYD channels are split into four parts, separated by the interaction regions. These parts are treated as separate sub channels. The dimensions of these sub channels are based on the dimensions assigned to the SYD.

The transformation from an SYD to a series of flow channels and subsequently to flow resistances is shown in figure 3.5. Three different sections are recognised: the centre sections (I), the edge sections (II) and the dead ended sections (III). The dead ended sections are assumed not to contribute to the flow. The blocks in figure 3.5(c) represent the flow resistance of the channel sections in figure 3.5(b). The white spaces between the channel sections are virtual spaces, only used to indicate the separation.

The interaction region is modelled as a point without flow resistance. The fluid can flow freely from one SYD channel into the other channel. Only the resistance between the interaction points is defined. This simplification limits the number of flow resistances in the system and consequently allows for a fast analysis of large networks. Implementation of a flow resistance in the interaction regions enables the analysis of flow in the out–of–plane direction (see section 3.4.4).

The values of the resistances are calculated using (3.23). The distance between the interaction points is determined using the equations for the projected distances δ, as discussed in section 2.2 (figure 2.12, equations (2.3) and (2.4)). The distances between

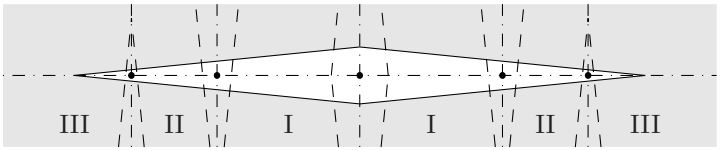

(a) *Single SYD at the top face, the dashed lines indicate bottom face SYDs connected with the top face SYD. The gray area refers to the fibre bundles. I: centre section, II: edge section, III: dead ended section.*

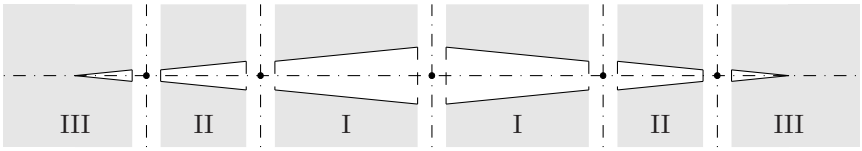

(b) *SYD divided in separate parts between the interaction points (the white space is fictitious). I: centre section, II: edge section, III: dead ended section.*

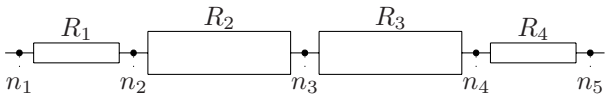

(c) *Separated parts of the SYD replaced by flow resistances R_i. The thick dots (n_j) indicate the interaction points with connected SYDs.*

Figure 3.5: *The subdivision of an SYD into a series of four flow channels and subsequent flow resistances. The centre, edge and dead ended section are indicated with Roman numerals.*

the interaction points in case of a $\pm 45^{\circ}$ biaxial NCF are:

$$d_p^A = \frac{A}{\sqrt{2}}; \tag{3.24}$$

$$d_p^B = \frac{B}{\sqrt{2}}, \tag{3.25}$$

with A and B the needle spacing and the stitch distance, respectively. This is the only configuration that was analysed. The parameters are different for other types of fabrics (see chapter 2).

3.2.4 Analogy with an Electric System

Replacing each of the SYDs in a network as depicted in figure 3.3, by a set of four resistances (see figure 3.5(c)), results in a network of flow resistances as shown in figure 3.6(a). The network shown is formed by the SYDs of a grid of 3×4 needle penetrations, in cross direction (x) and machine direction (y) respectively. The stitch penetrations are separated by the stitch distance A and B. Hence, this system represents a fabric of $2A \times 3B$, which is roughly $10 \times 6\text{mm}^2$ (table 2.1).
The light gray blocks represent the flow resistances of the centre sections of the SYD,

the darker blocks to the edge section SYDs. The dashed lines indicate the SYDs, the dots the centres of the SYD where the stitch threads penetrate the fabric.

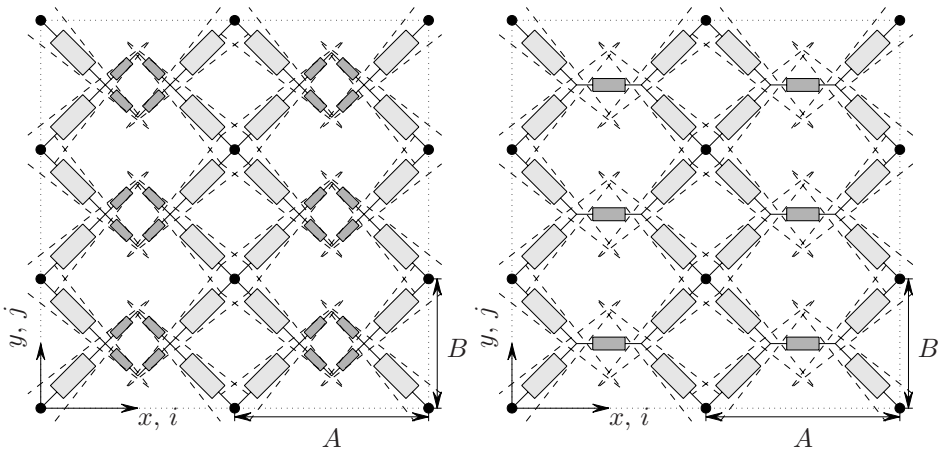

(a) *Complete network* (b) *Reduced network.*

Figure 3.6: *Complete and reduced network of 2×3 basic elements (2A×3B) of flow resistance representing a flow domain. The SYDs are indicated by the dashed lines. The centre and edge section resistances are coloured light and dark gray respectively. The dots indicate the location where the needle penetrated the fabric. The x–direction corresponds to the cross direction, y–direction to the machine direction.*

Each channel has a certain resistance, that can be calculated employing the equations presented in section 3.1 and the equations (3.21) to (3.23). The resulting system of flow equations is solved analogously to the solution of the effective resistance of an electrical circuit consisting of parallel and serial resistances. The pressure difference ΔP and voltage drop $\mathcal{V}$ are corresponding variables, as are the fluid flow φ and the current I. Consequently, the ratio $\frac{\pi r_E^4(x)}{8\mu L}$ corresponds with the inverse of the electrical resistance R_e, with r_E the effective radius of the channel, L the length of the channel and μ the dynamic viscosity:

$$\varphi = \frac{\pi r_E^4}{8\mu L}\Delta P \leftrightarrow I = \frac{1}{R_e}\mathcal{V}. \tag{3.26}$$

The reduced network, figure 3.6(b), is obtained by replacing the four small, dark gray resistances in the tip regions of the SYDs by an effective resistance R_E. The effective resistance R_E of N resistances $R_{[n]}$ connected in series (subscript s) or in parallel

(subscript p) is given by:

$$\begin{aligned} R_{E,s} &= \sum_{n=1}^{N} R_{[n]}; \\ R_{E,p} &= \left(\sum_{n=1}^{N} \frac{1}{R_{[n]}} \right)^{-1}. \end{aligned} \tag{3.27}$$

The equivalent resistances of the four resistances of the tip region is straightforwardly derived using (3.27).

$$R_E = \frac{\left(R_{[1]} + R_{[2]}\right)\left(R_{[3]} + R_{[4]}\right)}{R_{[1]} + R_{[2]} + R_{[3]} + R_{[4]}}, \tag{3.28}$$

with the resistance $R_{[1]}$ connected in series with $R_{[2]}$, $R_{[3]}$ in series with $R_{[4]}$ and the combination $R_{[1]} - R_{[2]}$ parallel to $R_{[3]} - R_{[4]}$, as indicated in figure 3.7.

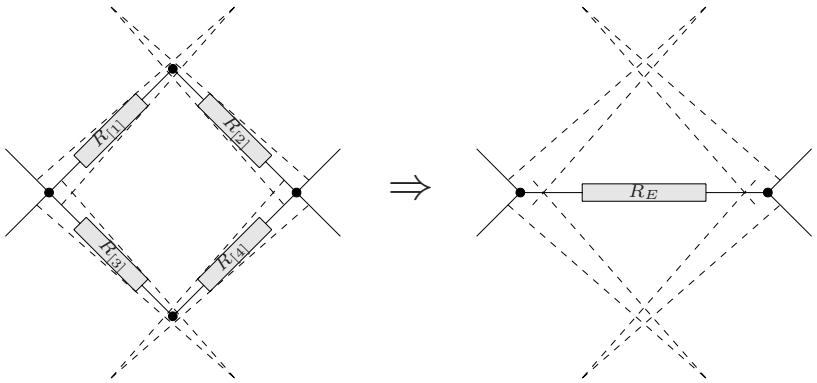

Figure 3.7: *The set of flow resistances formed near the interaction points at the edge of the SYDs can be replaced by an effective resistance.*

The relation between the permeability and the flow resistance of the network is derived based on the relations between the permeabilities and the flow resistances of the individual channels.
The flow resistances are calculated based on the dimensions of the SYD. The resistance of the n^{th} resistance in a system of N resistances is expressed in terms of the equivalent radius r_E, (3.23), and the length L of the channel. Subsequently, the relation between the channel radius and the permeability K, (3.20), is employed to obtain the relation between the resistance and the permeability:

$$R_{[n]} = \frac{8\mu L_{[n]}}{\pi \left(r_{E,[n]}\right)^4} = \frac{\mu L_{[n]}}{K_{[n]}}, \tag{3.29}$$

The flow resistance and permeability are inversely proportional to each other. Effective permeabilities for channels connected in series and in parallel can be derived,

similarly to the effective resistances defined in (3.27). Equation (3.29) is substituted in (3.27) and the equivalent resistance is substituted for the ratio of the effective permeability K_E over the total flow length L_T, resulting in the following equations:

$$\begin{aligned} K_{E,s} &= L_{T,s} \left(\sum_{n=1}^{N} \frac{L_{[n]}}{K_{[n]}} \right)^{-1}; \\ K_{E,p} &= L_{T,p} \sum_{n=1}^{N} \frac{K_{[n]}}{L_{[n]}}, \end{aligned} \tag{3.30}$$

The total flow length in the flow direction equals the sum of the channel lengths (read: the total distance that the fluid has to flow) and consequently depends on the local orientation of the channel with respect to the flow direction. Let $\theta_{[n]}$ be the angle between the n^{th} channel and the flow direction. The lengths $L_{T,s}$ and $L_{T,p}$ are then given by:

$$\begin{aligned} L_{T,s} &= \sum_{n=1}^{N} L_{[n]} \cos\theta_{[n]}; \\ L_{T,p} &= L_{[n]} \cos\theta_{[n]} \quad n \in [1..N]. \end{aligned} \tag{3.31}$$

Note that here the absolute value of the angle $\theta_{[n]}$ is equal, if all channels are connected in parallel with each other. The equations reduce, if all channels have the same length L, to:

$$\begin{aligned} L_{T,s} &= L \sum_{n=1}^{N} \cos\theta_{[n]}; \\ L_{T,p} &= L \cos\theta_{[n]} \quad n \in [1..N], \end{aligned} \tag{3.32}$$

Substituting (3.32) into (3.30) leads to:

$$\begin{aligned} K_{E,s} &= \sum_{n=1}^{N} \cos\theta_{[n]} \left(\sum_{n=1}^{N} \frac{1}{K_{[n]}} \right)^{-1}; \\ K_{E,p} &= \cos\theta_q \sum_{n=1}^{N} K_{[n]} \quad q \in [1..N]. \end{aligned} \tag{3.33}$$

These relations are used to derive the equivalent permeability of the four edge sections depicted in figure 3.7, similar to the expression for the effective resistance (3.28). The effective permeability K_E, using $|\theta_i| = \frac{\pi}{4}$ in (3.32), is found to be equal to:

$$K_E = 2\sqrt{2} \left(\frac{K_{[1]}\, K_{[2]}}{K_{[1]} + K_{[2]}} + \frac{K_{[3]}\, K_{[4]}}{K_{[3]} + K_{[4]}} \right). \tag{3.34}$$

Effect of Variability The dimensions of the SYDs – and consequently the channel radii – are not constant in the network, but exhibit a certain variation. This variation corresponds to the measured variation in the dimensions of the SYD, as was explained in section 3.2.2. The possible effect of the variation in the dimensions is analysed here. The flow resistance of the channel sections is inversely proportional to r_E^4, see (3.29). Let δr be a variation in the channel radius, with respect to the mean channel radius $\bar{r}_E$ of all channels. Hence, it is found that:

$$R_E \sim \frac{1}{(\bar{r}_E + \delta r)^4} = \frac{1}{\bar{r}_E^4 \left(1 + \frac{\delta r}{\bar{r}_E}\right)^4} = \frac{1}{\bar{r}_E^4} \frac{1}{\left(1 + \frac{\delta r}{\bar{r}_E}\right)^4}. \tag{3.35}$$

The last term of the equation is approximated by a Taylor expansion, according to:

$$\frac{1}{\left(1 + \frac{\delta r}{\bar{r}_E}\right)^4} \approx 1 - 4\left(\frac{\delta r}{\bar{r}_E}\right) + 10\left(\frac{\delta r}{\bar{r}_E}\right)^2 - 20\left(\frac{\delta r}{\bar{r}_E}\right)^3 + 35\left(\frac{\delta r}{\bar{r}_E}\right)^4 + \mathcal{O}\left(\left(\frac{\delta r}{\bar{r}_E}\right)^5\right). \tag{3.36}$$

Suppose that the system consists of N flow channels, connected in a series. The effective flow resistance is then calculated using (3.27). It is also possible to determine the mean flow resistance $\bar{R}_E$, using (3.35) and (3.36):

$$\begin{aligned} \bar{R}_E \sim & \frac{1}{\bar{r}_E^4}\left(\overline{1 - 4\left(\frac{\delta r}{\bar{r}_E}\right) + 10\left(\frac{\delta r}{\bar{r}_E}\right)^2 - 20\left(\frac{\delta r}{\bar{r}_E}\right)^3 + 35\left(\frac{\delta r}{\bar{r}_E}\right)^4}\right) = \\ & \frac{1}{\bar{r}_E^4}\left(1 - 4\left(\frac{\overline{\delta r}}{\bar{r}_E}\right) + 10\left(\frac{\overline{(\delta r)^2}}{\bar{r}_E^2}\right) - 20\left(\frac{\overline{(\delta r)^3}}{\bar{r}_E^3}\right) + 35\left(\frac{\overline{(\delta r)^4}}{\bar{r}_E^4}\right)\right). \end{aligned} \tag{3.37}$$

This equation shows how the variation in the averaged flow resistance depends on the variation in the channel radii. The averaged flow resistances cannot be based on the averaged channel radii. The variation has to be accounted for as well. The numerators in the fractions correspond to the central moments of the set of channel widths, (see appendix B, equation (B.7)), since δr is defined as the variation with respect to the mean value. The numerator of the first fraction (the first central momentum) equals zero by definition. The second numerator equals the variance of the mean channel radii. The third numerator corresponds to the skewness and equals zero for a normal distribution[7]. However, a lognormal distribution was found for the distribution of the SYD dimensions and consequently for that of the equivalent channel radii (see section 2.3). Hence, this term does not vanish. The last fraction is the kurtosis, divided by $\bar{r}_E^4$. Higher order central moments can be accounted for, but do not have a specific meaning.

Equation (3.37) applies for a serial connection of the flow resistances. A similar exercise can be done for a system in which the flow resistances are connected in parallel. However, it suffices at this point to note that the averaged flow resistance

[7] In general: all fractions with an uneven power drop in case of a distribution that is symmetrical around its mean value.

of a network is not only affected by the averaged channels dimension, but also by the (type of) distribution of the channel dimensions.

An estimate can be made of the maximum and minimum flow resistance of the network as shown in figure 3.6, based on the variation in the channel dimensions. A pressure gradient in the machine direction is applied[8].
It is assumed that the permeability is dominated by the centre sections of the SYDs, if the flow is in machine direction, the y direction in figure 3.6. The permeability of these channel sections is significantly larger (see (3.23)) than the effective permeability of the end sections of the SYD (here the effective permeability K_E, defined in (3.34)). Moreover, the pressure gradient perpendicular to the flow direction (which is parallel to the effective flow resistance) is zero or relatively small. The contribution to the overall permeability is therefore small. The neglect of the flow in the edge sections of the SYDs allows solving the effective resistance of the system directly.
The variation of the SYD widths is not randomly in this case, but it is assumed to vary between the minimum and maximum SYD width. A linear increase or decrease of the width is assumed either in machine (y) or cross (x) direction, as depicted in figure 3.8. The size of the resistance corresponds to the relative size of the SYDs.

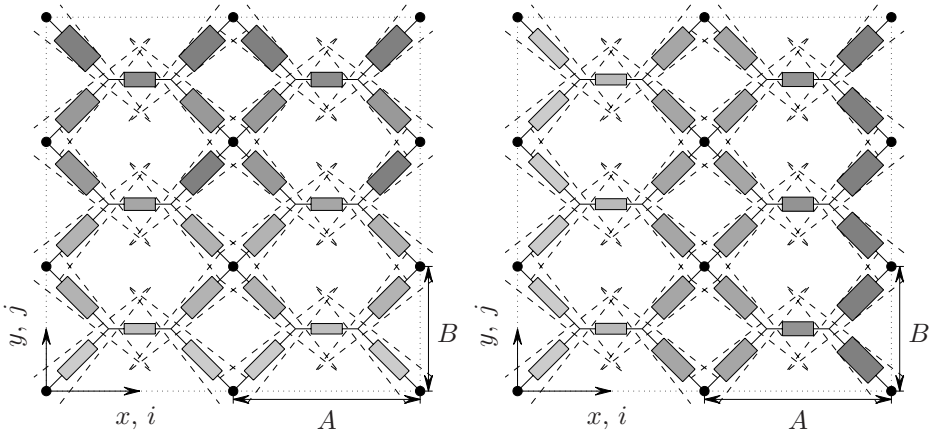

(a) *Parallel to flow direction.* (b) *Perpendicular to flow direction.*

Figure 3.8: *Schematic representation of the two limiting cases. The size and colour of the resistances correspond to the magnitude of the width of the SYD. The dots indicate the location where the needle penetrated the fabric. x: cross direction, y: machine direction. The pressure gradient is applied in the machine direction.*

The width is assumed to remain constant in the other direction than the direction in which the linear variation is applied. The maximum flow resistance is found if the

[8]see also the remark at the end of section 3.1.2; the machine direction and cross direction are assumed to correspond with the principal directions. The derivation presented below is similar if a pressure gradient in cross direction is applied

variation of the widths is parallel to the flow direction. The small channels become the bottleneck. The minimum flow resistances is found if the widths are constant in the flow direction. The efficiency of the channels is maximal in that case, since there are no bottlenecks obstructing the maximal flow.
The lower and upper bound permeabilities are compared to the permeability of a network that has constant channel radii. The permeability of a network with a constant SYD width is referred to as the nominal permeability.

Nominal Permeability The nominal equivalent permeability $K_{E_T}^{nom}$ for a network with $N_x^{ch} \times N_y^{ch}$ equally sized channels is derived using the effective resistance K_E, defined in (3.34). The channel permeabilities $K_{[i]}$ equal K^{ch}, the permeability of a channel with averaged radius $\bar{r}_E$:

$$K_{E_T}^{nom} = \sum_{i=1}^{N_x^{ch}/2} \left(N_y^{ch} \left(\sum_{j=1}^{N_y^{ch}/2} \frac{1}{2\sqrt{2}K^{ch}} \right)^{-1} \right) = \frac{N_x^{ch}}{\sqrt{2}} K^{ch}. \tag{3.38}$$

Lower Bound The next step is to define individual channel permeabilities, based on the dimensions of the SYD. The equivalent radius $r_{[i,j]}$ of the SYD at location $[i,j]$ in the network (the dots in figure 3.8), is defined relative in size to the mean equivalent radius $\bar{r}_E$:

$$r_{[i,j]} = a_{[i,j]} \bar{r}_E. \tag{3.39}$$

Subsequently, the individual channel permeabilities $K_{[i,j]}$, defined by (3.20) can be derived as:

$$K_{[i,j]} = \frac{\pi r_{[i,j]}^4}{8} = \frac{\pi a_{[i,j]}^4 \bar{r}^4}{8} = a_{[i,j]}^4 K^{ch} \tag{3.40}$$

Substitution of (3.40) in (3.34) leads to an expression for the equivalent permeability of a set of four SYD channels $K_{E,[i,j]}$ connected as depicted in figure 3.7:

$$K_{E,[i,j]} = 2\sqrt{2} \left(\frac{a_{[i,j]}^4 a_{[i,j+1]}^4}{a_{[i,j]}^4 + a_{[i,j+1]}^4} + \frac{a_{[i+1,j]}^4 a_{[i+1,j+1]}^4}{a_{[i+1,j]}^4 + a_{[i+1,j+1]}^4} \right) K^{ch}. \tag{3.41}$$

The coefficients $a_{[i,j]}$ are related to the width of the SYDs and only depend on the coordinate in flow direction (here the machine direction, see figure 3.8). The width of the domains is determined in the centres of the SYDs and the SYDs are assumed to be symmetric and equal at top and bottom face (see section 3.2.2). Consequently, the four flow resistances connected to the SYD centre are equal, leading to two conventions:

$$\begin{array}{lll} a_{[i,j]} = a_{[i+1,j]} & i \in [1..N_x^{ch}] & j \in [1..N_y^{ch}]; \\ a_{[i,2j]} = a_{[i,2j+1]} & i \in [1..N_x^{ch}] & j \in [1..N_y^{ch}/2 - 1]. \end{array} \tag{3.42}$$

The value of the coefficients ($a_{[i,j]}$) is based on a linear decrease (or increase) of the width of the channels ($b_{[i,j]}$) in flow direction. The maximum and minimum widths of the channels are equal to the averaged value plus respectively minus twice the

standard deviation, based on a lognormal distribution of the SYD dimensions ($\sigma_{\ln}$, see section 2.3):

$$\begin{aligned} b_{max} &= \bar{b} \cdot \mathrm{e}^{+2\sigma_{\ln}} \\ b_{min} &= \bar{b} \cdot \mathrm{e}^{-2\sigma_{\ln}} \end{aligned} \tag{3.43}$$

The factor 2 roughly equals the statistical value of a student–t distribution with a 95% significance level and 25 or more degrees of freedom (number of SYD widths here) [89], *id est*:

$$b_{min} \leq b \leq b_{max} \tag{3.44}$$

applies for 95% of the channel widths b, for a randomly generated set with averaged value $\bar{b}$ and standard deviation $\sigma_{\ln}$. The function describing a linear decrease of the channel widths, over the domain and in the machine direction, is given by:

$$b_{[i,2j-1]} = \mathrm{e}^{\left(\frac{-8\sigma_{\ln}}{N_y^{ch}}(j-1)+\left(\ln \bar{b}+2\sigma_{\ln}\right)\right)} \quad j \in [1..N_y^{ch}/2+1]. \tag{3.45}$$

The equations (3.21), (3.22) and (3.23) are used to transform each width to an equivalent channel radius $r_{[i,j]}$, from which $a_{[i,j]}$ follows via the definition in (3.40) and (3.42).
The effective lower bound (LB) permeability $K_{E_T}^{LB}$ can then be written as:

$$K_{E_T}^{LB} = \frac{N_x^{ch} N_y^{ch}}{\sqrt{2}} \left(\sum_{j=1}^{N_y^{ch}/2} \frac{a_{[2i,2j-1]}^4 + a_{[2i,2j]}^4}{a_{[2i,2j-1]}^4 a_{[2i,2j]}^4} \right)^{-1}. \tag{3.46}$$

The ratio between the effective permeabilities in (3.38) and (3.46) provides an indication for the lower bound of the permeability. The lower bound for the permeability is depicted in figure 3.9 as a function of the relative size of the network. A base configuration of size $2A \times 3B$ is used ($\approx 10 \times 6\mathrm{mm}^2$). The lower bound of the permeability converges to roughly 40–45% of the nominal permeability, equation (3.38), for the measured averaged value and standard deviation of fabric B3 (see section 2.4).

Upper Bound The upper bound is found by following the same procedure but applying a different definition for the coefficients $a_{[i,j]}$, based on a linear decrease of the channel widths in the direction perpendicular to the flow direction (*id est* in x direction, figure 3.8). The conventions for $a_{[i,j]}$ read in this case:

$$\begin{aligned} a_{[i,j]} &= a_{[i,j+1]} \quad i \in [1..N_x^{ch}] \quad j \in [1..N_y^{ch}]; \\ a_{[2i,j]} &= a_{[2i+1,j]} \quad i \in [1..N_x^{ch}/2-1] \quad j \in [1..N_y^{ch}]. \end{aligned} \tag{3.47}$$

The effective upper bound permeability $K_{E_T}^{UB}$ of the network is then found to be equal to:

$$K_{E_T}^{UB} = \sqrt{2} K^{ch} \left(\frac{a_{[1,j]}^4}{2} + \sum_{i=1}^{N_x^{ch}/2} a_{[2i,j]}^4 + \frac{a_{[N_x^{ch},j]}^4}{2} \right) \quad j \in [1..N_y^{ch}]. \tag{3.48}$$

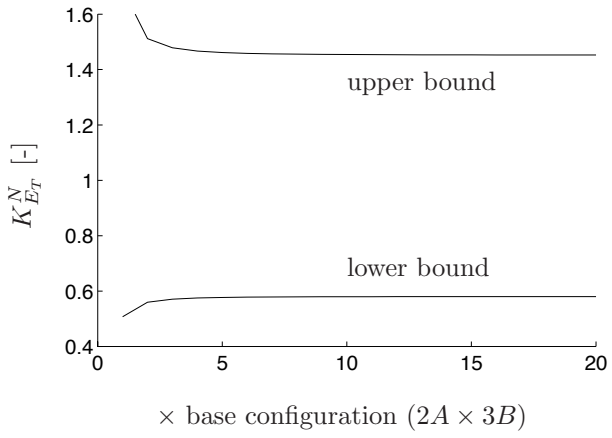

Figure 3.9: *The upper and lower bound for the normalised permeability in machine direction of a network with a linearly decreasing width of the SYDs (perpendicular and parallel to the flow direction, respectively) versus the relative size of the network (base size $2A \times 3B$). The permeability is normalised on the permeability of a network with equally sized SYDs.*

Note the different treatment of the coefficients $a[1, j]$ and $a_{[N_x^{ch}, j]}$: the flow is smaller here due to the presence of the domain boundary. Only two channels are connected to each SYD centre, instead of four as in the other SYD centres (see figure 3.6).
The relative upper bound of the flow resistance ((3.48) divided by (3.38)) is plotted in figure 3.9. The upper and lower bound deviate by a roughly equal relative amount from the nominal permeability (3.38): the upper bound is approximately 45–50% higher, whereas the lower bound is approximately 40–45% lower. Note that the permeabilities can vary by a factor three due to the variations in the SYD widths. The effect of the variation can hence be considered as significant.

Anisotropy The network exhibits an anisotropy by definition: the fluid can flow relatively easily through the large channels connected to each other in the centres of the SYDs (light gray resistances in figure 3.6). The edge channel sections, connecting the edges of neighbouring SYDs (dark gray resistances in figure 3.6, see also section 3.2.3), are much smaller and consequently their permeability is much lower (see (3.20): $K \sim r^4$). However, the fluid must use these channels if the flow direction is altered from machine direction to the cross direction (from y to x in figure 3.6). The anisotropy is estimated by considering a small network of $N_x^{ch} \times 1$ elements and a flow in the cross direction (figure 3.10(a)). This results in an estimate of the equivalent permeability in the cross direction ($K^{90}_{E_T}$). Subsequently it is compared to a network of $1 \times N_y^{ch}$ elements and a flow in the machine direction (figure 3.10(b)), resulting in an estimate for the permeability in the machine direction ($K^0_{E_T}$). The anisotropy is defined as the ratio $K^{90}_{E_T}$ over $K^0_{E_T}$. Note that this is only valid if K^0 and K^{90} are oriented in the principal directions which is assumed to be the case here. This assumption is based on the (symmetrical) structure of the network.

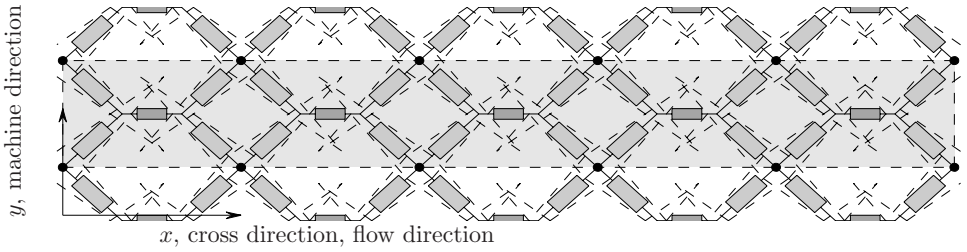

(a) $N_x^{ch} \times 1 = 5 \times 1$, *flow in cross direction.*

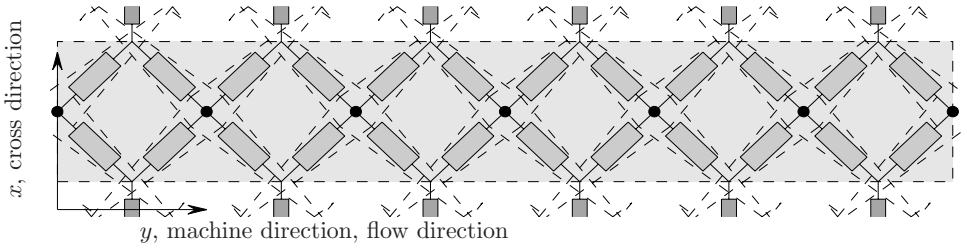

(b) $1 \times N_x^{ch} = 1 \times 6$, *flow in machine direction.*

Figure 3.10: *The two different flow situations: flow in cross direction and flow in the machine direction of the fabrics. The gray area is the flow area used to determine the equivalent permeabilities. Note that the machine and cross direction in both figures are rotated 90° with respect to each other.*

The first network consists of a series of alternating sets of four channels: a set of large channels (light dark colour) is followed by a set of small channels (dark gray colour), again followed by a set of large channels. The equivalent resistance of a set of four channels is given by (3.41). The channel radii are based on a constant width for all SYDs. Let $r_E^{(1)}$ be the equivalent radius of the large channels, calculated using (3.23), and $r_E^{(2)}$ the equivalent radius of the small channels, calculated in the same way. The ratio of both radii is defined as:

$$\alpha_r = \frac{r_E^{(2)}}{r_E^{(1)}}. \tag{3.49}$$

The permeabilities are then related to each other as:

$$K^{ch,2} = \alpha_r^4 K^{ch,1}. \tag{3.50}$$

The equivalent permeabilities are calculated using (3.41) and via the equations for the equivalent permeability of a series of flow resistances, (3.30)–(3.33), it can be derived that:

$$K_{E_T}^{90} = \frac{N_x^{ch}}{2}\left(\sum_{i=1}^{N_x^{ch}}\left(\frac{1}{2\sqrt{2}K^{ch,1}} + \frac{1}{2\sqrt{2}K^{ch,2}}\right)\right)^{-1} = \frac{2\sqrt{2}\alpha_r^4}{1+\alpha_r^4}K^{ch,1}. \tag{3.51}$$

The anisotropy α_0 is defined as the ratio of the permeability in transverse direction (3.51) over the permeability in longitudinal direction (3.38) (with $N_x^{ch} = 2$):

$$\alpha_0 = \frac{K_{E_T}^{90}}{K_{E_T}^{0}} = \frac{2\alpha_r^4}{1+\alpha_r^4}. \tag{3.52}$$

A strong anisotropy is found, as shown in figure 3.11, where the anisotropy α_0 is plotted versus the ratio $r_E^{(2)}/r_E^{(1)}$. It is not expected that the anisotropy is indeed as strong as the graph indicates. The permeability in the edge sections of the SYD is probably higher than the value based on the local dimensions of the SYD suggests, since the separation between the bundles of neighbouring SYDs is small. This was discussed previously in section 2.2. The separation between two SYDs in their tip region is formed by a relatively low number of filaments compared to the total number of filaments in a bundle. The permeability across the bundle is consequently significantly higher than the bundle permeability, which is neglected here. The higher permeability of the crossing filaments in the tip region enhances the flow between neighbouring SYDs and reduces the anisotropy. The anisotropy of the network is compared with experimental data in chapter 4.

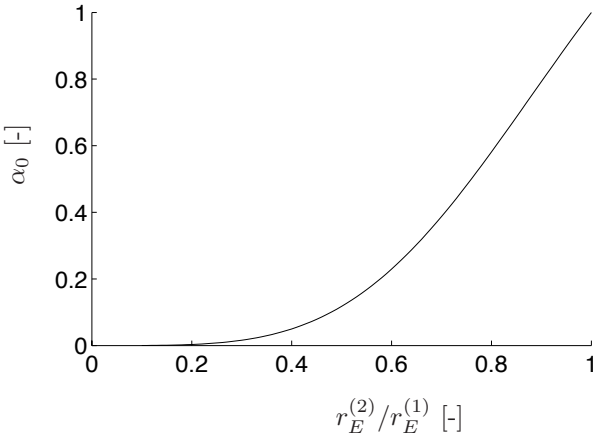

Figure 3.11: *Anisotropy of the network model versus the ratio of the equivalent radii of the centre and edge sections of the SYD for a network with equally sized SYDs for the entire domain.*

3.2.5 Finite Element Formulation

A finite element discretisation [115, 116] was implemented to solve the permeability of the network. Each of the resistances of the network is treated as a two node line element. One–dimensional elements are used, since the flow in the elements is one–dimensional, as was shown in section 3.1.2. Each node has one degree of freedom: the pressure p.

The nodal network representation of the flow domain is shown in figure 3.12. A pattern of five elements is recognised, referred to as a repetitive block. The figure shows a set of six repetitive blocks, indicated by the dashed lines. The dimensions of a repetitive block are $A \times B$, *id est* for the studied fabrics roughly 5×2mm.

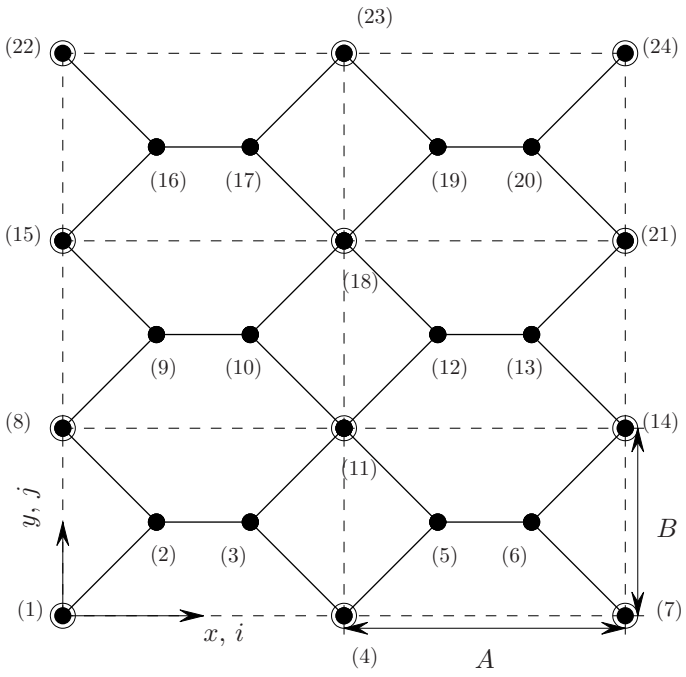

Figure 3.12: *Elements (lines) and nodes (dots with corresponding numbers) representing the network of flow channels. The dashed lines indicate the repetitive blocks of the system. The encircled nodes correspond to the centres of the SYDs.*

The fluid flow Φ in the elements of the network is given by the integral of the fluid velocity profile u over the cross–sectional area $\mathcal{A}$, as was shown in section 3.1.2:

$$\Phi = \int_{\mathcal{A}} u \, \mathrm{d}\mathcal{A}. \tag{3.53}$$

It was shown that the continuity equation for this type of flow, states that the gradient of velocity field equals zero (3.10). Consequently, the gradient of the flow also equals zero:

$$\frac{\mathrm{d}\Phi}{\mathrm{d}x} = 0. \tag{3.54}$$

The condition (3.54) can be multiplied with an arbitrary weighting function w and

be integrated without losing its generality:

$$\int w \frac{\mathrm{d}\Phi}{\mathrm{d}x}\,\mathrm{d}x = 0, \tag{3.55}$$

The integral form is subsequently rewritten using the chain rule of differentiation, resulting in:

$$[w\Phi] - \int \frac{\partial w}{\partial x}\Phi\,\mathrm{d}x = 0. \tag{3.56}$$

The constitutive equation, relating the pressure gradient to the flow, is given here by Darcy's law (1.1). Substitution of the constitutive equation in the integral (3.56) yields:

$$\int \frac{\partial w}{\partial x}\frac{K}{\mu}\frac{\partial p}{\partial x}\,\mathrm{d}x = [w\Phi]. \tag{3.57}$$

Equation (3.57) still holds for the entire continuum in which it is defined. The weak formulation is introduced as a first approximation to solve the integral equation. The validity of (3.57) is restricted to a set of discrete points – the nodes shown in figure 3.12. An interpolation of the pressure is employed between the nodes (hence, (3.57) may not be satisfied exactly at all arbitrary points in the domain). Here, a linear interpolation is employed, implying the assumption of a linear pressure drop (read: constant pressure gradient) over the elements. Strictly taken, this applies only for channels with a constant radius. However, a constant, equivalent radius r_E was derived in section 3.2.2. This justifies the use of linear interpolation functions here. Higher order interpolation functions can be implemented straightforwardly in the system, if desired. The linear element interpolation function $\boldsymbol{N}(x)$ reads:

$$\boldsymbol{N}(x) = \{1 - x, x\}^T, \tag{3.58}$$

with x the normalised coordinate between two adjacent nodes. The weighting functions w are arbitrary and therefore the shape functions (3.58) can be chosen as well, which is known as the method of Galerkin [115, 116]. Substitution of the shape functions in (3.57) leads to:

$$\int \frac{\partial \boldsymbol{N}}{\partial x}\frac{K}{\mu L}\frac{\partial \boldsymbol{N}}{\partial x}\mathrm{d}x \cdot \boldsymbol{p} = \boldsymbol{M} \cdot \boldsymbol{p} = \boldsymbol{\varphi}, \tag{3.59}$$

with $\boldsymbol{p}$ the vector containing the nodal pressures, $\boldsymbol{\varphi}$ the vector containing the nodal fluxes and $\boldsymbol{M}$ the system matrix.
The finite element discretisation is implemented in MATLAB©. A direct solving routine is employed, combined with a Jacobi–preconditioner [117] to control the condition of the system matrix $\boldsymbol{M}$. Details on this procedure can be found in appendix D.
Pressure boundary conditions are applied to the network to solve the flow. A pressure of 1 is applied at one side of the domain and a pressure of 0 is applied at the opposite side. This results in a pressure gradient inversely proportional to the length of the network in flow direction. The sides of the network on which the pressure conditions

are set, depend on whether a flow in the machine direction or perpendicular to the machine direction is chosen.
It is also possible to apply boundary conditions on the flow or to use a combination of pressure and flow boundary conditions. The results do not depend on the type of boundary conditions. Pressure boundary conditions are applied, since they result in a rather smooth pressure gradient over the domain.
Period boundary conditions are applied on the edges perpendicular to those on which the pressure boundary conditions are set. The nodal flows at the nodes at the opposite side of the domain are merged. Hence, the effect of the boundary vanishes.
The overall permeability of the network is determined by applying Darcy's law (1.1). The total flow in the system and the calculated pressure drop equal:

$$\begin{aligned} \Phi &= \frac{KA}{\mu}\frac{\mathrm{d}p}{\mathrm{d}x} \Rightarrow K = \frac{\mu\Phi}{A}\frac{L}{\Delta p} \\ \Phi &= \sum_{i=1}^{n_{inlet}} \varphi^{(i)} \\ \Delta p &= \frac{1}{n_{inlet}} \sum_{i=1}^{n_{inlet}} p^{(i)} - \frac{1}{n_{outlet}} \sum_{i=1}^{n_{outlet}} p^{(i)} \end{aligned} \tag{3.60}$$

The number of nodes at which inlet and outlet boundary conditions are applied are n_{inlet} and n_{outlet} respectively.
The permeability of the entire network, based on a set of SYDs with variable widths (*id est* varying element permeabilities), is normalised on the permeability of the network based on equally sized SYDs. The latter is referred as the *nominal permeability*.

3.3 Results of Simple Network

A network formulation was presented in the previous section. Some of the basic features of such a network were discussed and the method to solve the system of flow equations was explained. Here, a number of different networks is analysed. Several aspects of the model are analysed, using the parameters provided by the geometrical model presented in chapter 2. The aim is to derive appropriate parameters for the flow model, such that the network model can represent a piece of NCF and can provide an estimate of the averaged permeability value and the expected variability. The latter is considered to be the most relevant, as was discussed in the introduction of this chapter. The analyses of the flow networks addressed the following aspects:

1. The effect of the size of the SYDs.
2. The effect of the amount of variation in the SYD widths.
3. The effect of permutations of the SYD widths and newly generated sets of dimensions.
4. The size of the network.
5. The direction of the flow.
6. The spatial distribution of the randomly generated SYD unit cell dimensions.

7. The pressure and flow fields.
8. The statistic properties of the network permeability.

The model parameters of the network are presented in table 3.1. The parameters are based on the geometrical parameters (either measured or specified by the manufacturer) of the fabrics B1, B2 and B3 presented in section 2.2.2.
A program was implemented in MATLAB© to calculate the effect of the size of the network and the number of sets of SYD widths and subsequent permutations within each of these set (n_{set} and n_{permu} respectively). The steps of the program are:

1. Generate a random set of channel widths b, based on the averaged width $\bar{b}$ and the (logarithmic) standard deviation ($\sigma_{\ln}$).
2. Assign the channel widths according to a certain distribution to the set of channels.
3. Generate a random permutation of the widths generated at step 1 and re–assign the widths to the channels according to this permutation. Repeat this step n_{permu} times.
4. Calculate the channel permeabilities using the channel dimensions b and h (resulting in the element permeabilities, use (3.21), (3.22)–(3.29)), see also sections 3.2.2 and 3.2.3).
5. Generate a random permutation of the permeabilities calculated in the previous step and re–assign the permeabilities to the channels according to this permutation. Repeat this step n_{permu} times.
6. Construct and solve $\boldsymbol{M} \cdot \boldsymbol{p} = \boldsymbol{\varphi}$ (3.59) for the initial set and its permutations.
7. Repeat steps 1 to 5 n_{set} times.
8. Post process the results.

Table 3.1: *Model parameters used in the network of flow resistances.*

Parameter			value
viscosity	μ	[Pa·s]	$30{\cdot}10^{-3}$
SYD width	b	[m]	$0.28{\cdot}10^{-3}$
SYD logarithmic width	$b_{\ln}$	[m]	$0.26{\cdot}10^{-3}$
SYD height	h	[m]	$0.5{\cdot}10^{-3}$
Logarithmic standard deviation	$\sigma_{\ln}$	[-]	$0.33{\cdot}10^{-3}$
Needle spacing	A	[m]	$5{\cdot}10^{-3}$
Stitch distance	B	[m]	$2{\cdot}10^{-3}$

3.3.1 Width of the SYDs

A relatively small network of $10A \times 15B$ ($\approx 50 \times 30\text{mm}^2$) was used to analyse the effect of the width on the permeability of the network. The width was varied between 50% and 150% of the measured averaged SYD width, based on a lognormal distribution

of the data ($b_{\ln} = 0.26$mm, see table 3.1). The permeability is normalised in the permeability of the network with the averaged measured width. The normalised permeability increases strongly with increasing width, as shown in figure 3.13(a). The permeability is proportional to r_E^4, according to (3.20) and (3.23). A linear relation is found if the fourth square root of the permeability is plotted versus the variation in width, depicted in figure 3.13(b).

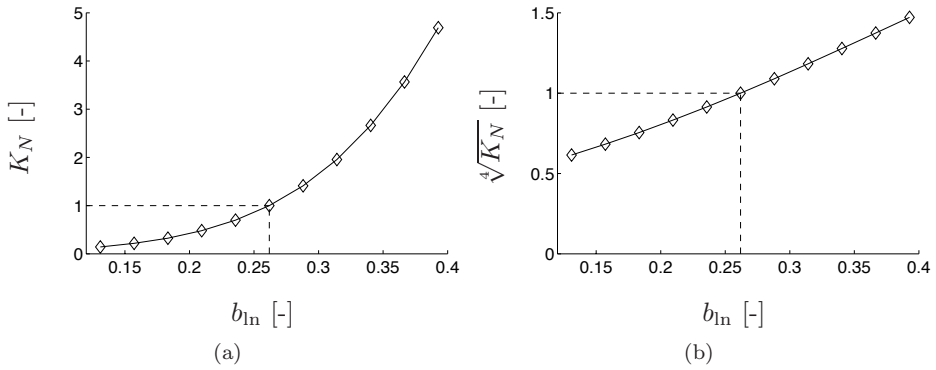

Figure 3.13: *The normalised permeability for a network with constant SYD dimensions varying from 50% and 150% of the measured averaged SYD width. A lognormal distribution of the data is used ($b_{\ln} = 0.26mm$). The permeability is normalised on the permeability of the network with the mean width.*

3.3.2 Amount of Variation on the SYD Widths

The effect of the amount of variation on the SYD widths is analysed by increasing the standard deviation on the dimensions of the channels stepwise between 0 and 150% of the maximum measured standard deviation ($\sigma_{\ln} = 0.331$, see table 3.1). The standard deviation of the other fabrics (B1 and B2) is similar to the values of fabric B3 that were used (see appendix A for the exact numbers). The data is normalised on the network with constant channel dimensions. The normalised permeability is calculated for various networks. The graphs in figure 3.14 show the results of a variable amount of variation on two networks. A relatively small one, of size $10A \times 15B$ ($\approx 50 \times 30$mm^2) and a relatively large one, $40A \times 60B$ ($\approx 200 \times 120$mm^2). The larger network is in both directions four times as large as the smaller network.

The amount of variation has a significant effect on the permeability. The total variation due to permutations of the widths within each set (5) and newly generated sets (5) is indicated in the figure by the error bars and found to be small compared to the effect of the amount of variation. The effect of the amount of variation on the permeability is also independent of the size of the network: the averaged value decreased for both networks to roughly 70% of the nominal permeability.

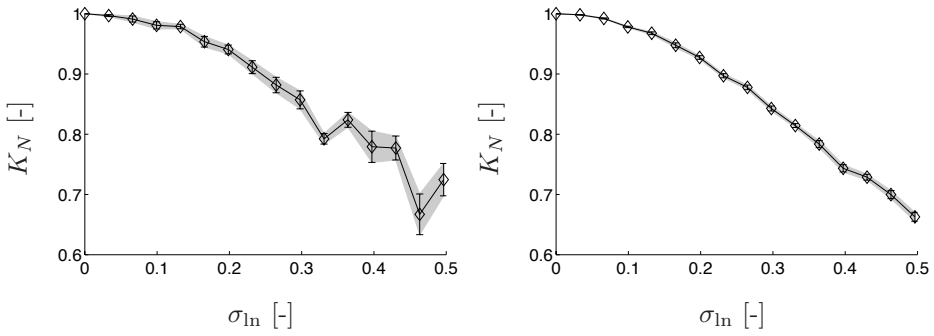

(a) $N_x \times N_y = 10 \times 15$ (b) $N_x \times N_y = 40 \times 60$

Figure 3.14: *The normalised permeability as a function of the amount of variation based on the logarithmic standard deviation (measured standard deviation: $\sigma_{\ln} = 0.331$). The error bars indicate the total variation for 5 different sets of widths, permutated 5 times.*

3.3.3 Different Sets of SYD Widths and Permutations

The effect of the varying element permeabilities is analysed for a constant size of the network (again: $10A \times 15B$, $\approx 50 \times 30\text{mm}^2$). Ten different sets ($n_{set} = 10$) were generated randomly, all based on the measured averaged SYD width and standard deviation. The number of permutations n_{permu} within each set is varied between 5 and 50.

The calculated variation in the permeability is depicted in figure 3.15. The normalised permeability (solid diamond) and the variation (the error bars, $s = \frac{2\sigma}{\sqrt{N}}$, for set size N and standard deviation σ, see appendix B) due to the permutation of the SYD widths is plotted for all 10 sets. The averaged permeability of all sets and all permutations is represented by the solid line.

The variation within a set does not depend on the number of permutations within each set according to the graphs. The variation is roughly 10% of the nominal permeability. The averaged permeability of all sets hardly depends on the number of permutations. The permeability is affected greater by generating a new set than by applying a permutation within an existing set, as indicated by figure 3.16. The graphs show the variation of the i^{th} permutation for all sets. Each data set, from which the averaged value plus the variation is shown, contains one normalised permeability of all different sets. The averaged value, the diamonds, are nearly constants for all data sets. The variation, entirely caused by differences between newly generated sets, is also nearly equal for all data sets. Consequently, it can be concluded that the variation in the normalised permeability is mainly caused by differences between sets of SYD widths and is hardly affected by differences (permutations of the channels) within each set. The variation in the permeability is twice as large as the variation within a single set (figure 3.15), *id est.* roughly 15% of the nominal permeability. The variation decreases with the increasing number of sets, as expected: the variation on a set depends on the number of elements in the set (see also appendix B).

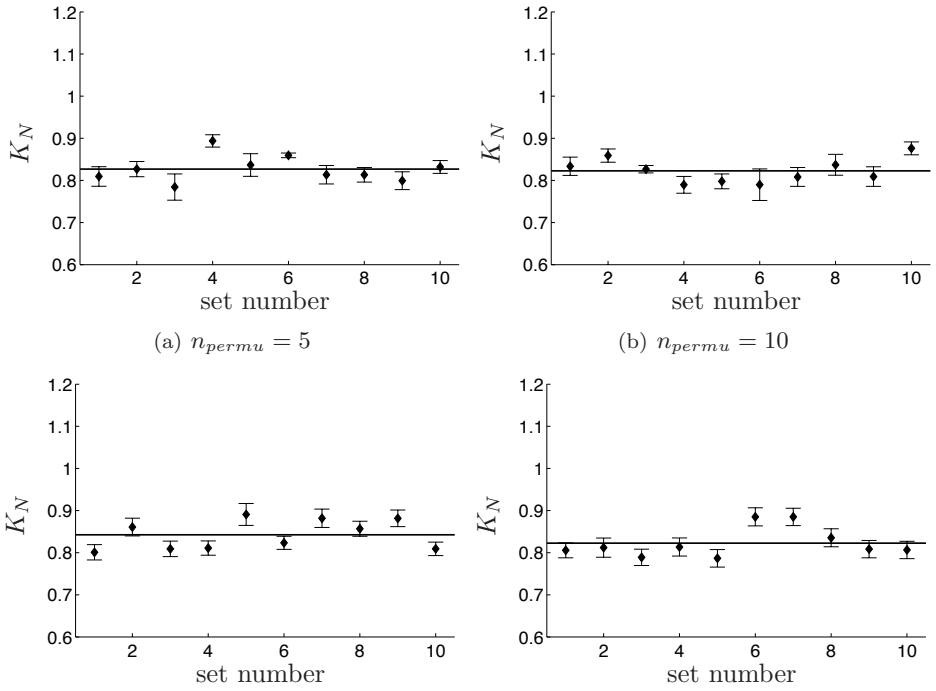

(a) $n_{permu} = 5$ (b) $n_{permu} = 10$

(c) $n_{permu} = 25$ (d) $n_{permu} = 50$

Figure 3.15: *Variation of the normalised permeability of a network (size* $10A \times 15B$*) for a series of 10 different sets of randomly generated SYD widths. The number of permutations is varied between 5 and 50. The solid line represents the averaged normalised permeability.*

The analysis shows that the effect of a variation on the local permeability of a network depends largely on the specific set of widths. The (random) spatial distribution of the randomly generated SYD widths is only responsible for a small amount of variation in the permeability. However, the difference between two sets of randomly generated SYD width, both with the same averaged value and standard deviation, can be as large as 15% of the nominal permeability. The variation reduces if the number of sets is increased, which is generally valid for randomly generated data. In practice, the number of permeability measurements on a certain fabric are generally low, hence possibly resulting in relatively large variation.

3.3.4 Size Dependency

The size of the network is varied to study the size dependency and to obtain a minimum size at which the solution can be considered as size independent and a maximum size at which the permeability can be determined with sufficient numerical accuracy. A limited number of sets and permutations is used to avoid excessive

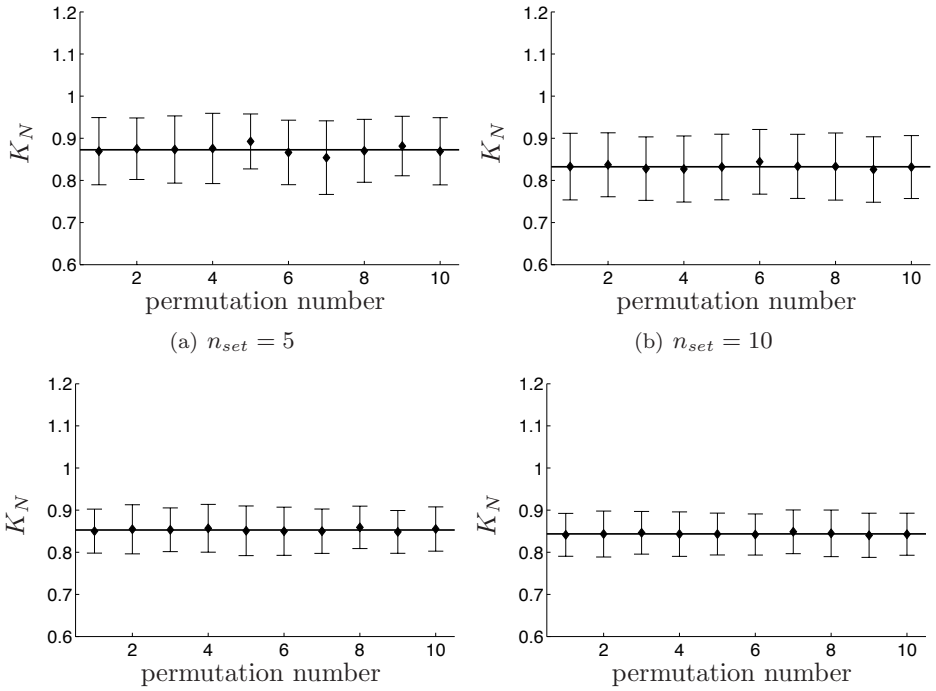

(a) $n_{set} = 5$ (b) $n_{set} = 10$

(c) $n_{set} = 25$ (d) $n_{set} = 50$

Figure 3.16: *Variation of the normalised permeability of a network (size* $10A \times 15B$*) for each permutation. The number of sets is increased from 5 to 50. The solid line represents the averaged normalised permeability.*

computation times. Increasing the size of the network is expected to result in less variation in the permeability of the entire network. A random distribution of the channels is used here. The size of the network is varied from 4×6 to 80×120 repetitive blocks (each of size $A \times B$) of flow channels. This corresponds to a piece of fabric of $20 \times 12\text{mm}^2$ for the small network, to $400 \times 240\text{mm}^2$ for the large network. The length–width ratio of the fabric remains constant for all analysed networks, hence their size is expressed relative to the base configuration of 4×6 repetitive blocks.
Note that the number of degrees of freedom in the system increases proportional to the square of the relative size. Let N_i^0 be the size of the base configuration and S the relative size of the network. The total number of degrees of freedom N_{tot} is related to the relative size of the network according to the quadratic equation:

$$N_{tot} = 3N_1^0 N_2^0 S^2 + \left(N_1^0 + N_2^0\right) S + 1. \tag{3.61}$$

The condition number (see also appendix D) and required solution time depend on the number of degrees of freedom (*id est* the size of the system that is being solved). Five new sets were generated for each network size ($n_{set} = 5$) and five permutations were performed on each of the sets ($n_{permu} = 5$). The normalised permeability in the

machine direction (K_N^0), as a function of the relative size of the network, is depicted in figure 3.17. A rapid convergence to roughly 82% of the nominal permeability is observed. The variation in the permeability is large for relatively small systems. The permeability and the variation on it become stable if the relative size is roughly equal to 10 in this example. This corresponds to a system of 40×60 repetitive blocks, a piece of fabric of roughly 200×120 mm^2. Generally, specimens for permeability measurements are larger than these dimensions. This implies that a relatively stable value of the permeability should be measured in ideal circumstances, provided that the assumption of a random distribution of the SYDs widths is valid.

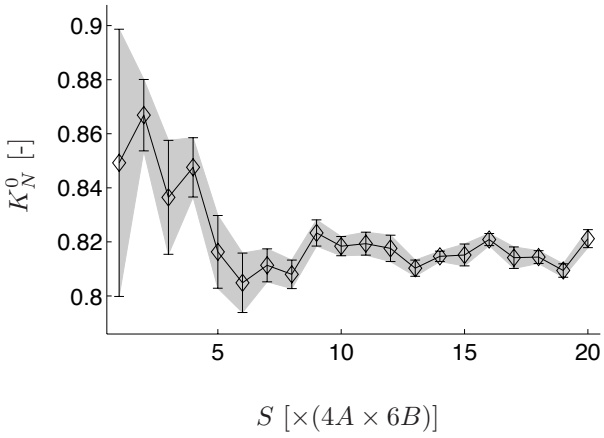

Figure 3.17: *The normalised permeability in the machine direction as a function of the relative size of the network (× base configuration of $4A \times 6B$) for a pressure gradient perpendicular to the machine direction. Five different sets of dimensions and five permutations per set are calculated for each set. The error bars indicate the variation on the total of 25 calculations per data point.*

3.3.5 Influence of the Flow Direction

The network has a strong anisotropy, as was discussed previously in section 3.2.4. It was concluded that the permeability strongly depends on the flow direction. Here, it is analysed whether the *variation* on the permeability is also affected by the direction of the flow. The pressure gradient is applied perpendicular to the machine direction in this case, rather than in the machine direction (the permeability based on flow in the machine direction is shown in figure 3.17).

The normalised permeability in the cross direction of the network (K_N^{90}) is plotted versus the relative size of the network in figure 3.18 (normalisation on the nominal permeability for a flow in the direction). The size of the network is increased up to 20 times the base configuration of 4×6 repetitive blocks. The normalised permeability is hardly affected by the variation on the width of the SYDs. Only relatively small

networks exhibit a variation of maximal 10% of the nominal permeability. A stable solution, only a few percent below the nominal permeability, is obtained for networks whose size is at least roughly 5 times the size of the base configuration. The explanation is found in the constant height of the channels (read: constant thickness of the plies). The variation is only applied on the width of the SYD, as was discussed in section 3.2.2. The width in the edge sections is relatively small compared to the width in the centre sections (see section 3.2.3). The equations (3.21) and (3.23) are employed to determine the equivalent channel radius, which is subsequently used to determine the permeability of that channel (equation (3.20)). The variation on the hydraulic diameter is relatively small if the width is relatively small compared to the height. The amount of variation was analysed in section 3.3.2. According to expectations, a smaller deviation from the nominal permeability is found if the variation in the channel permeability decreases.

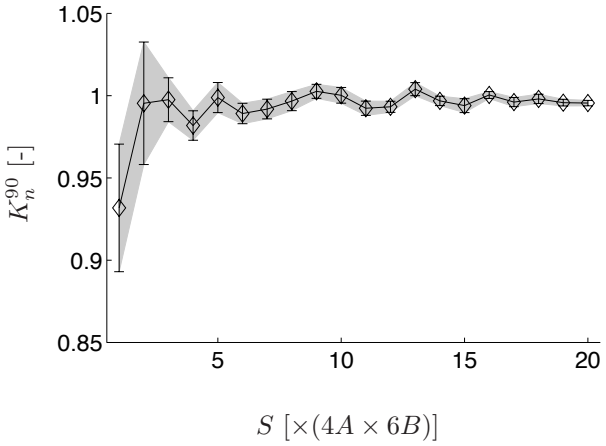

Figure 3.18: *The normalised permeability in cross direction as a function of the relative size of the network ($\times$ base configuration of $4A \times 6B$) for a pressure gradient perpendicular to the machine direction. Five different sets of dimensions and five permutations per set are calculated for each set. The error bars indicate the variation on the total of 25 calculations per data point.*

Note that this implies that the anisotropy weakens for a system with a random distribution of SYD widths, compared to the anisotropy based on the nominal permeabilities. The anisotropy value is roughly 20% higher than the nominal anisotropy, if a random distribution of the SYD widths is assumed. The anisotropy will be discussed in more detail in section 3.3.7.

3.3.6 Upper and Lower Bounds for the Permeability

Two limiting cases were defined in section 3.2.4 to estimate the lower and upper bounds of the normalised permeability. Here, the same cases are applied on the entire

network, *id est* the flow in the edge sections of the SYDs is not neglected. The widths of the channels in the two limiting cases are based on the averaged width and the standard deviation as measured. The two limiting cases that were defined, are:

1. a constant gradient from the minimum to the maximum width of the SYDs in the flow direction, see figure 3.8(a);
2. a constant gradient from the minimum to the maximum width of the SYDs perpendicular to the flow direction, see figure 3.8(b).

Note that the standard deviation of these sets does not equal the specified standard deviation, since the widths are not generated randomly.
The maximum and minimum widths of the channels are determined using the equations (3.43)–(3.45). The flow experiences the maximum resistance if the widths are varied in the direction parallel to the flow and the minimum resistance if the widths are varied in the direction perpendicular to the flow. Chains of large channels are formed in the latter case, as can be seen in figure 3.8(b). The effect is similar to race–tracking, but it occurs on a smaller length scale.
The normalised permeabilities in the machine direction (K_N^0) as a function of the relative size of the network are depicted in figure 3.19. The size of the network is varied from $4A \times 6B$ to $40A \times 60B$ ($20 \times 12\text{mm}^2$–$200 \times 120\text{mm}^2$).

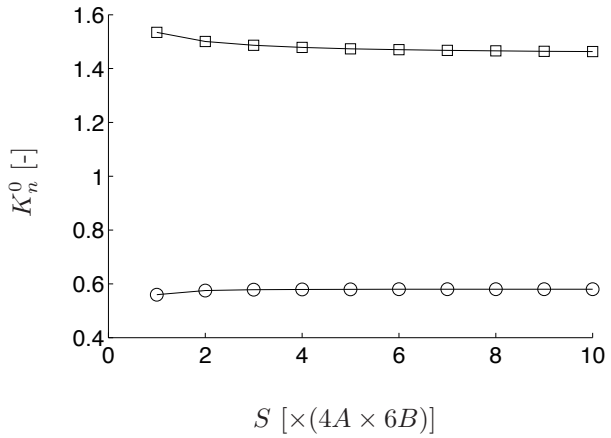

Figure 3.19: *Upper and lower bounds of the normalised permeability versus the relative size of the network (base configuration: $4A \times 6B$), based on a linearly varying SYD width either in the flow direction (○) or perpendicular to the flow direction (□).*

The results are equal to the results obtained in section 3.2.4 (figure 3.9), where the upper and lower limits were estimated neglecting the flow in the edge sections of the SYD. It is expected that the permeability of a network with an arbitrary type of spatial distribution is bounded by the permeability of a network with a spatial distribution in which the SYD in– or decreases linearly in one dimension.
The space between the limits is slightly larger for smaller networks. This is caused by the larger gradient in the small networks. However, the difference is relatively

small and the upper and lower bounds reach a constant value for a relative size of the network of 3. This corresponds to a network of $12A \times 18B$ ($\approx 60 \times 36\text{mm}^2$).

3.3.7 Various Spatial Distributions of SYD Widths

The effect of the type of spatial distributions is investigated by defining a number of spatial distributions (between brackets: the name used to refer to the distribution):

1. fully random distribution of the SYD widths ('random');
2. decrease of the widths in the machine (y) direction ('horizontal');
3. decrease of the widths in the cross (x) direction ('vertical');
4. decrease of the widths over the diagonal of the domain ('diagonal');
5. decrease of the widths from the centre towards the edges ('central outward');
6. increase of the widths from the centre towards the edges ('central inward');
7. small–large–small variation of the widths in the machine (y) direction ('central band');
8. large–small–large variation of the widths in the machine (y) direction ('edge band').

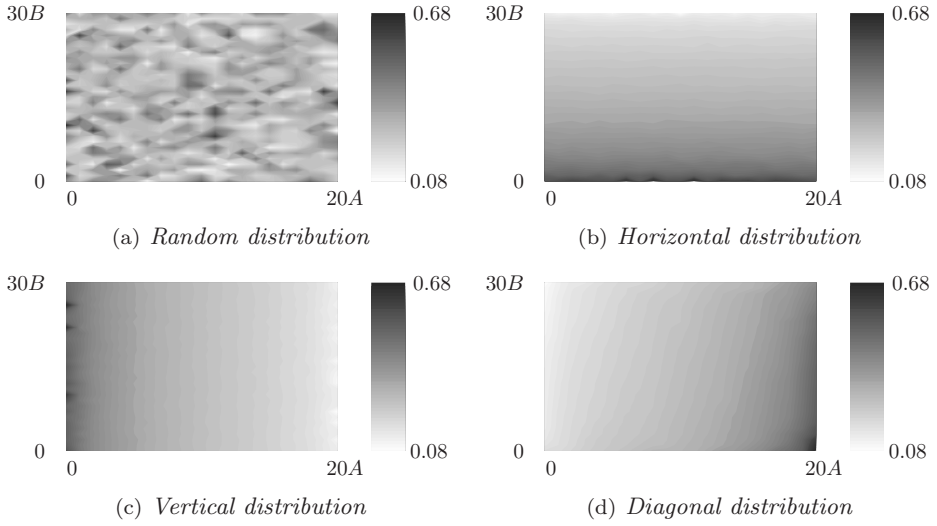

(a) *Random distribution* (b) *Horizontal distribution*

(c) *Vertical distribution* (d) *Diagonal distribution*

Figure 3.20: *First four types of spatial distributions of the widths in the network.*

Representative plots of the different cases are shown in figures 3.20 and 3.21. The plots are generated using a grid of 20×30 repetitive blocks (see figure 3.12), which corresponds to a piece of fabric of roughly $100\times60\text{mm}^2$. The flow direction corresponds with the vertical direction, as indicated by the arrow. The darker the colour, the larger the channel dimension. All sets are based on the same randomly

generated set of widths. The distributions are formed by sorting of the set of widths. If possible, a randomisation of a subsection is applied. Consider, for example, the horizontal distribution, depicted in figure 3.20(b): all widths of the bottom row of SYDs are smaller than those of the row of SYDs directly above the bottom row. The sizes are also sorted within each row, by nature of the sorting procedure in MATLAB©. A random permutation is applied to the SYD in each row, such that there is no undesired ordering in vertical direction. Similar randomisation procedures were performed in other cases.

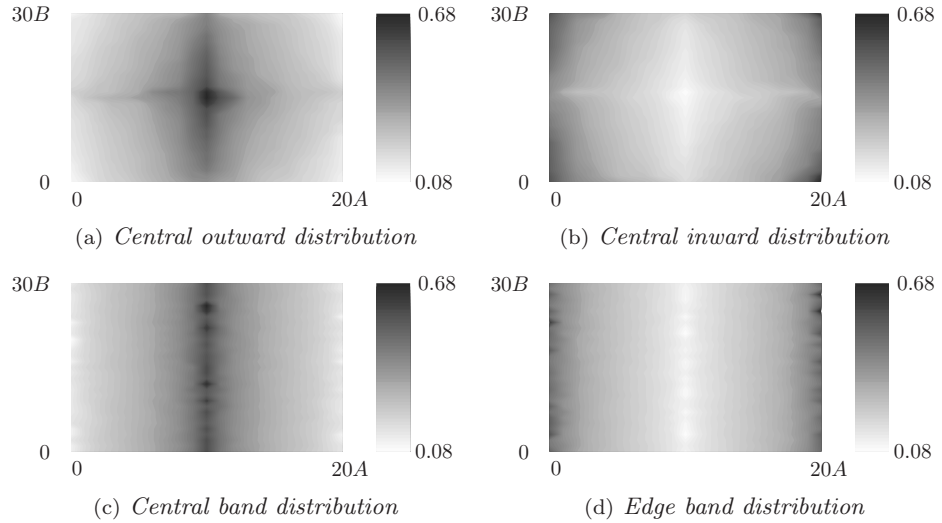

(a) *Central outward distribution* (b) *Central inward distribution*

(c) *Central band distribution* (d) *Edge band distribution*

Figure 3.21: *Second four types of spatial distributions of the widths in the network.*

The normalised permeability in machine direction (K_N^0) for the eight different distributions are calculated for various network sizes, ranging from 4×6 repetitive blocks (base configuration $\approx 20 \times 12\text{mm}^2$) to 40×60 repetitive blocks ($\approx 200 \times 120\text{mm}^2$). The number of sets, equal for all distributions, and number of permutations within each set are both set to 5. The results are presented in figure 3.22.

The first observation is that the variation in the permeability due to a different spatial distribution is much larger than the variation due to different sets of widths for a certain distribution. Evidently, the spatial distribution is an important parameter for the prediction of the variation in the permeability.

The random distribution (○) and the horizontal distribution (□) are close to the lower boundary (■, see also figure 3.19), whereas the other distributions are closer to the upper boundary (⧫, see also figure 3.19). The higher level of ordering in the non–random spatial distribution causes the tendency towards the limits. Chains of larger channels are formed in these distributions, resulting in micro–level race–tracking. Consequently, the overall flow is enhanced when the chains of larger channels are mainly (or partly) oriented in the flow direction (vertical, diagonal, central and band

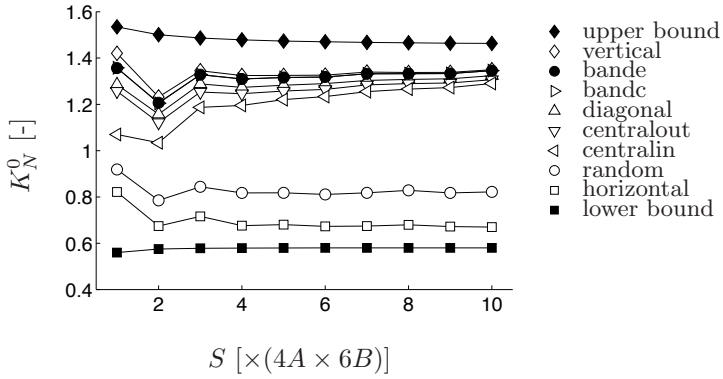

Figure 3.22: *The normalised permeabilities in machine direction of the eight spatial distributions of the SYD widths as a function of the relative size of the network. The pressure gradient is applied in the machine direction. The order of the legend corresponds with the order of the lines. (base configuration: $4A \times 6B$, $n_{set} = 5$, $n_{permu} = 5$).*

distributions), whereas the flow is slowed down when the chains are mainly oriented perpendicular to the flow direction (horizontal distribution). This is confirmed by changing the direction of the pressure gradient from the machine direction to the cross direction: the normalised permeability in cross direction (K_N^{90}) tends towards the lower boundary, since the chains of large channels are mainly formed in the direction perpendicular to the flow, see figure 3.23.
The differences between the normalised permeabilities of the vertical, central and band distributions are not significant. A variation of roughly 10% is observed. Clearly, the amount of ordering has a strong effect on the permeability of the network.
A lower normalised permeability is expected for the central distributions, if a squarer grid is used. Here, a rectangular grid was used. The central distribution consequently resembles a band distribution more than desirable.
The anisotropy of the network is also affected by the variation in the network permeability. Previously, the anisotropy α_0 was defined as the ratio of the permeability in cross direction K_0^{90} over the permeability in machine direction K_0^0 for a network with equally sized channels (subscript '0'), see equation (3.52). Let α_N be the anisotropy of a network with an arbitrary spatial distribution, using the normalised permeabilities (K_N^0 and K_N^{90}) as depicted in the figures 3.22 and 3.23, and α the anisotropy based on the absolute permeabilities (K^0 and K^{90}):

$$\begin{aligned} \alpha_N &= \frac{K_N^{90}}{K_N^0}; \\ \alpha_0 &= \frac{K_0^{90}}{K_0^0}; \\ \alpha &= \frac{K^{90}}{K^0}. \end{aligned} \tag{3.62}$$

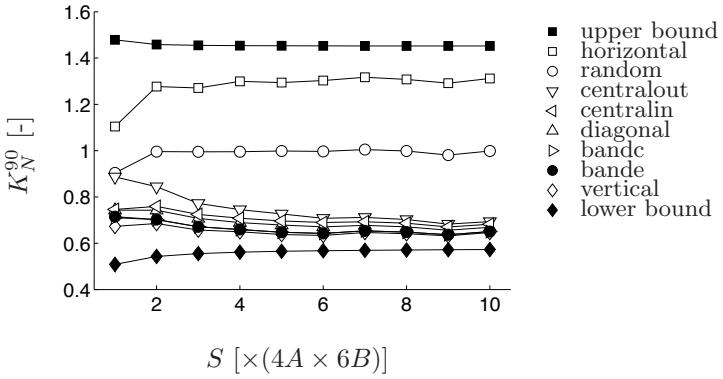

Figure 3.23: *The normalised permeabilities in cross direction of the eight spatial distributions of the SYD widths as a function of the relative size of the network. The pressure gradient is applied in the cross direction. The order of the legend corresponds with the order of the lines. (base configuration:* $4A \times 6B$, $n_{set} = 5$, $n_{permu} = 5$*).*

$$\alpha_N = \frac{K_N^{90}}{K_N^0} = \frac{K^{90}/K_0^{90}}{K^0/K_0^0} = \frac{\alpha}{\alpha_0}. \tag{3.63}$$

The value of α_n indicates whether the anisotropy is weakened ($\alpha_N > 1$) or strengthened ($\alpha_N < 1$). The anisotropy α_N equals 1 if the change of the normalised permeability in both directions is equal. The anisotropy α_N is plotted as a function of the size of the network in figure 3.24.

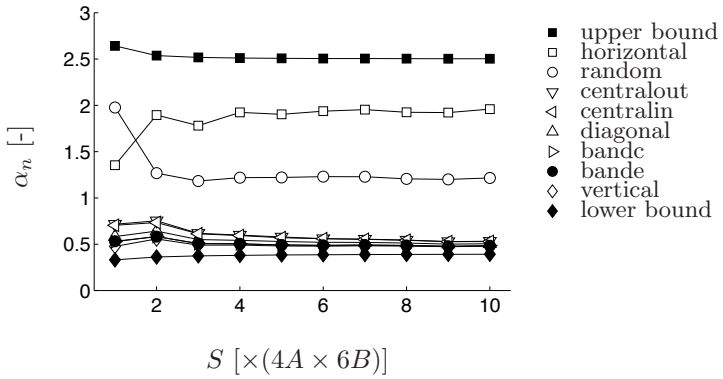

Figure 3.24: *The anisotropy based on the normalised permeabilities of the eight spatial distributions of the SYD widths as a function of the relative size of the network. The order of the legend corresponds with the order of the lines. (base configuration:* $4A \times 6B$, $n_{set} = 5$, $n_{permu} = 5$*).*

The anisotropy α_N is larger than one for the random and horizontal spatial distributions, resulting in an increase of the value of α, *id est* a weakening of the anisotropy (isotropic permeability: $\alpha = 1$). The anisotropy is stronger for the other spatial distributions, for which α_N is smaller than 1. This also indicates that a clustering of larger channels occurs in the non–random spatial distributions. The flow in the direction in which the majority of the chains of large channels are oriented (here the machine direction), increases more than the flow in the other direction. A higher degree of anisotropy results (or a lower in case of a horizontal distribution since then the majority of the chains is oriented in the cross direction).
The anisotropy changes least for the random distribution. A weakening of the anisotropy of roughly 25% is observed, where a variation of 100% or more applies for the other distributions. There is no clustering, which explains the weak effect. However, the permeability in the cross direction is less affected by the variations in the SYD widths, resulting in some weakening of the anisotropy.

3.3.8 Pressure Field and Flow Field

The pressures in the nodes and the flow through the elements in the network depend on the local permeability and observation of the pressure field and flow field helps to understand the effect of the variability in the SYD widths.
Contour plots of the distribution of the SYD widths and the nodal pressures are presented in figure 3.25. The level of grayness indicates the relative magnitude of the SYD width (a) and nodal pressure (b), respectively. A dark tint corresponds with a high value, a light tint to a low value. A random spatial distribution of the SYD widths is applied. The results are obtained with a network of 40×60 repetitive blocks. The pressure is set to 1 at one boundary and to 0 at the opposite boundary (bottom and top boundary in figure 3.25(a) and left hand side and right hand side boundary in figure 3.25(b) respectively).
The maximum and minimum width of the SYDs, indicated on the colour bar, are slightly different for both sets. A different base set of widths was used for the analysis of both flow directions. However, both sets of widths are based on the same averaged width and standard deviation as specified in table 3.1.
The pressure gradient differs locally, depending on the channel permeability, and consequently on the distribution of the SYD widths. The pressure gradient applied in the cross direction is generally smoother than the pressure gradient in the machine direction applied on the same network. The pressure in case of a pressure gradient in machine direction is not smooth, which is explained by the low permeability of the edge sections of the SYDs and the consequent channelling of the flow. This is more clearly visualised in the figures 3.26 and 3.27, which depict the flow through the network.
The flow for a pressure gradient in the machine direction is shown in figure 3.26, the flow for a pressure gradient in the cross direction is shown in figure 3.27. The elements are represented by rectangular blocks. The colour of each block is proportional to the relative magnitude of the flow in the element. The flows in a relatively large system of $40A \times 60B$ ($200 \times 120\text{mm}^2$) are shown.

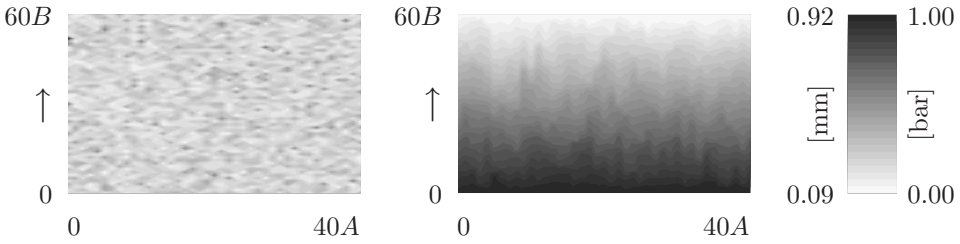

(a) *Width distribution and nodal pressures for a pressure gradient in the machine direction (the arrow indicates the main flow direction)*

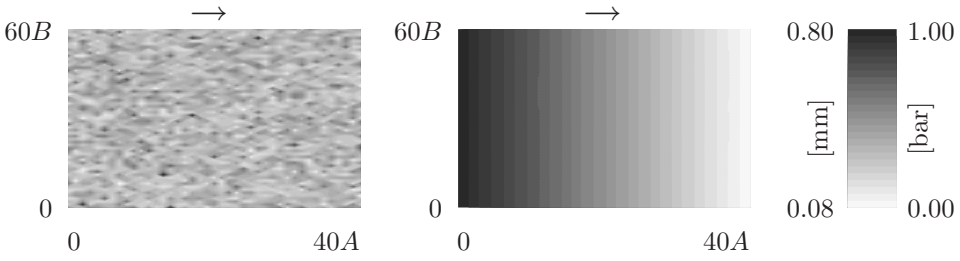

(b) *Width distribution and nodal pressures for a pressure gradient in the cross direction (the arrow indicates the main flow direction)*

Figure 3.25: *Distribution of SYD widths and the nodal pressures for a random spatial distribution of the channel widths (network size:* $40A \times 60B$ $200 \times 120mm^2$*).*

The network model predicts a significant channelling effect of the flow if the pressure gradient is applied in the machine direction. The centre sections of the SYDs are used efficiently, but the local pressure gradient in the cross direction is low and the permeability of the edge sections is low. Hence, the flow is nearly zero in the edge sections and hardly any fluid is flowing from one 'column' of centre SYD sections to a neighbouring one. The local pressure in the columns of centre SYD sections does not decrease linearly over the column and differs from column to column, due to difference in the local permeability. Consequently, the pressure gradient is not smooth.

The channelling effect is observed in all distributions for a pressure gradient in the machine direction. The smallest channel permeability is dominating the total flow in the chain of channels. Consequently, the flow field of the central distributions (see figures 3.21(a) and 3.21(b)) resemble the flow field of the horizontal distribution (figure 3.20(b)) and the band distributions (figures 3.21(c) and 3.21(d)). The normalised permeabilities of the central distributions are lower than those of the horizontal and band distributions. Part of the relatively wider channels loose their efficiency, due to the presence of smaller channels further in the chain.

The fluid has to pass the small edge sections if the pressure gradient is applied in the cross direction figure 3.27. The flow is more evenly distributed. Flow paths, or meso–

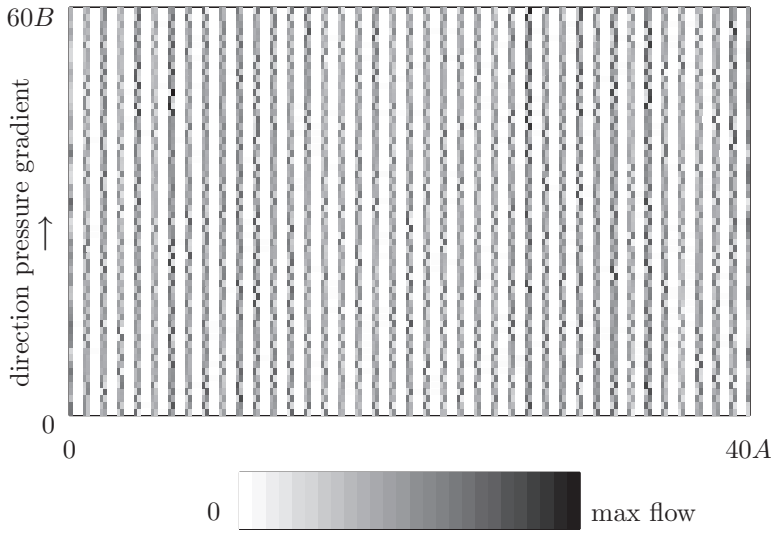

Figure 3.26: *Element flows in a network of* $40A \times 60B$ *(*$200 \times 120mm^2$*). A pressure gradient, indicated by the arrow, is applied in the machine direction.*

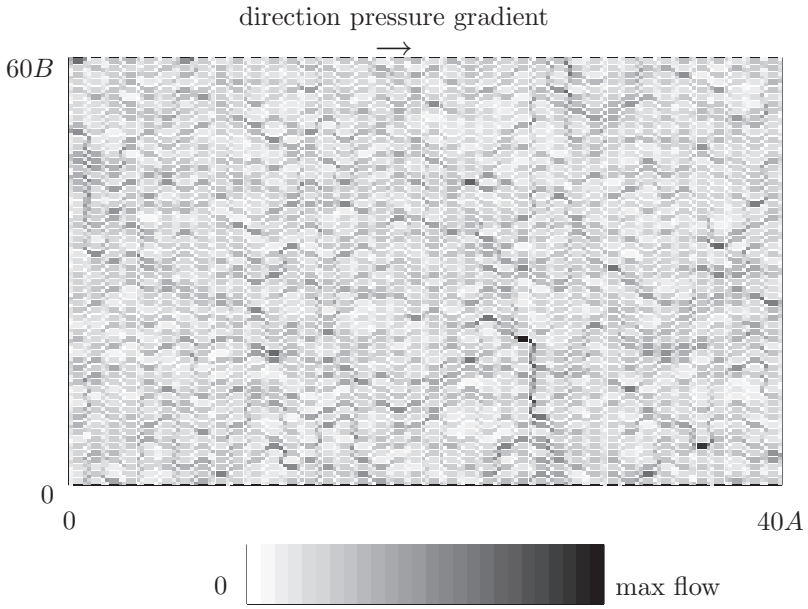

Figure 3.27: *Element flows in a network of* $40A \times 60B$ *(*$200 \times 120mm^2$*). A pressure gradient, indicated by the arrow, is applied in the cross direction.*

scale race–tracking, are recognisable by the chains of darker rectangles. The fluid has more route options available to flow through the fabric. It is less confined compared to the situation of a pressure gradient in the machine direction. The flow paths, consisting of the centre sections of the SYDs, are surrounded by low permeability barriers, formed by the edge sections of the SYDs. The flow paths that are formed for a pressure gradient in the cross direction are a mixture of centre sections and edge sections. Hence the flow is able to move more freely through the fabric, resulting in a smoother pressure gradient.
The degree of order in the other spatial distributions is higher than the degree of order in the random spatial distribution (in fact: no order at all). This results in a more structured flow distribution. The local variations are smaller, since the local permeabilities vary less.

3.3.9 Statistics on the Results

The overall permeability of the network is calculated for a number of sets and a number of permutations within each set. An averaged permeability including an estimation of the variation results. The averaged permeability was shown to vary between roughly 50% and 150% of the nominal permeability, depending on the spatial distribution of the dimensions of the SYDs. Variations of roughly 15% on the normalised permeability were found for a random distribution. Hoes *et al.* [25–27] performed a large number of measurements on glass woven fabrics and concluded that variations between 20–30% can be expected. The variation predicted by the network model can be considered as reasonable, compared to the experimental results of Hoes *et al.*, although their measurements concern a different type of reinforcement (woven fabric versus NCF).
A second conclusion of Hoes *et al.* was that the measured permeability data exhibits a normal distribution. It was shown in chapter 2 that the widths and lengths of the SYDs exhibit a lognormal distribution. Hence, a normality test is performed on the permeabilities predicted by the network model, to determine whether the distribution of the data is normal or logarithmic. The number of data values equals the number of sets multiplied by the number of permutations and is relatively limited (25 permeabilities versus 100 SYD widths).
A Jarque–Bera goodness–of–fit test is performed on the data (see appendix B). The skewness and kurtosis of the data is analysed and compared to the expected values based on a chi–squared distribution. The statistical value F_s should be lower than the critical value, otherwise the hypothesis that the data exhibits a normal distribution has to be rejected. The value P_s indicates the significance level. A significant difference with a normal distribution is present if P_s is lower than the significance level (generally 5%). The outcome of the normality test for a network with a size from $4A \times 6B$ to $40A \times 60B$ is presented in table 3.2. A random distribution of the channel dimensions was applied.
The results show that the hypothesis that the linear distribution of the permeability is normal holds for all networks ($H_0 = 0$), despite the lognormal distribution of the channel dimensions (compare the data in table 2.3: the hypothesis of a linear normal

Table 3.2: *The normality of the network permeabilities for various sizes of the network and a random distribution of the channel dimensions. A Jarque–Bera normality test is used (critical value $F_c = 5.991$)*

	normal distr.			lognormal distr.		
size $A \times B$	H_0	P_s	F_s	H_0	P_s	F_s
4×6	0	0.33	2.20	0	0.44	1.64
8×12	0	0.66	0.83	0	0.68	0.76
12×18	0	0.62	0.96	0	0.59	1.07
16×24	0	0.44	1.64	0	0.45	1.62
20×30	0	0.57	1.12	0	0.58	1.09
24×36	0	0.58	1.09	0	0.57	1.12
28×42	0	0.73	0.62	0	0.71	0.67
32×48	0	0.63	0.91	0	0.63	0.94
36×54	0	0.67	0.80	0	0.70	0.72
40×60	0	0.47	1.51	0	0.47	1.53

distribution is rejected frequently there, $H_0 = 1$). It is also tested whether the data is lognormally distributed. It cannot be concluded from the data that the hypothesis of a lognormal distribution of the permeability values is significantly better.

3.3.10 Conclusions on the Analysis of a Simple Network

The amount of variation on the permeability of the network does not depend on the type of distribution. A similar variation around the mean permeability of each type of distribution is found for all spatial distributions. It can therefore be concluded that the variation on the permeability only depends on the variation on the dimensions of the channels and on the size of the network.

The amount of variation on the permeability, using a certain spatial distribution, is relatively small compared to the effect of the type of distribution. Consequently, it appears to be useful to investigate a way to express the degree of order of the SYD dimensions, in particular if the effect of fabric deformation is also accounted for (for example implementation of the effect of shear on the order of the SYD widths).

The normalised permeability of a network tends towards the bounds, set by an idealised linear variation of the channel widths over the domain. The more ordered the distribution is, the more it approaches the boundary. The ordering allows the formation of clustering of large channels. The main orientation of these clusters determines whether the solution tends towards the upper or the lower boundary, roughly 50% above and 40% below the nominal permeability, respectively. A random set of widths results in a permeability of roughly 85% of the nominal permeability for a pressure gradient in the machine direction. The permeability is hardly affected if the pressure gradient is applied on the cross direction. This is caused by the dominance of the edge sections in the permeability in the cross direction. This effect is not observed for other spatial distributions.

The analysis of the various cases showed that the network model predicts that the permeability of a fabric can vary between 0.6 and 1.5 times the nominal permeability. In practice this implies that permeability values can vary by a factor of 2.5. This amount of variation is not uncommon, as will be discussed in chapter 4, where the experimental results are presented.

3.4 Recommendations for Extended Networks

The previously presented model employed basic assumptions and basic functions to construct a network of flow channels, see section 3.2.2. The applicability of the model is limited to an analysis of the effects of a variation in the widths of the SYDs on the permeability in the plane of the fabric. The model does not include:

1. more than 2 plies;
2. the stitch threads;
3. the effect of multiple layers stacked on top of each other;
4. the permeability in the out–of–plane direction of the fabric.

These topics are briefly discussed in this section.

3.4.1 Multiple Plies

The model that was presented in section 3.2.2 applies for biaxial fabrics. However, the class of Non–Crimp Fabrics accommodates also fabrics with more than two plies stitched together, each with their own orientation of the fibres with respect to the machine direction[9]. An extension of the model to triaxial and quadriaxial fabrics requires a renewed analysis of the location of the interaction regions. The stacking sequences of triaxial and quadriaxial NCFs are respectively equal to [+45°/90°/-45°] and [+45°/0°/-45°/90°], see figure 3.28.
The interaction regions in the centre of the SYDs remain. However, the interaction regions in the edge do not exist anymore: the SYDs of the +45° ply and the -45° ply still overlap, but are separated by either a 0° or a 90° ply. However, the edges of the SYDs in the 0° and/or 90° plies are most likely separated by a relatively low number of fibre filaments. This is comparable to the situation of 0°/90° biaxial fabrics (see figure 2.23). Consequently, the flow resistance from one stitch penetration to the neighbouring stitch penetration point in the direction along the fibre is relatively low. The thickness of a single layer of NCF equals the sum of the ply thicknesses. The triaxial and quadriaxial fabric are respectively 1.5 and 2 times thicker than the biaxial fabric, given all plies consist of the same fibres. As a result, it may be necessary to account for some flow resistance in thickness direction. This is discussed in the following section.

[9] This structure is explicitly named in the term adopted by Lomov *et al.* [10, 60–63] who refer to this class of fabrics as: "Multiaxial Multiply Stitched Fabrics"

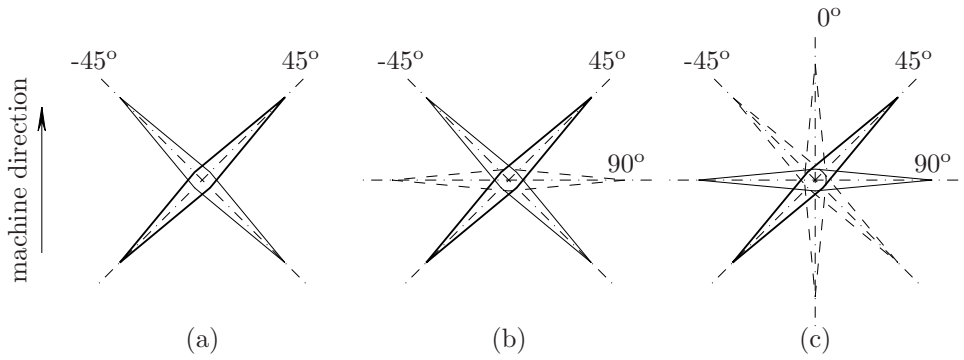

Figure 3.28: *A stack of SYDs of a ±45° biaxial (a), +45°/90°/-45° triaxial and 45°/0°/ -45°/90° quadriaxial fabric. The thick solid lines refer to top face SYDs, the dotted lines to inner ply SYDs and the thin solid lines to bottom face SYDs. The machine direction (0°) is indicated by the arrow.*

3.4.2 Stitch Thread

The SYDs are formed by the stitch threads piercing through the fabric, as explained in chapter 2. So far, the stitch thread was not taken into account. However, the stitch thread does affect the flow. Firstly, since it partly blocks the centre of the SYD and secondly, since the part of the stitch thread that lies on top of the fabric forms additional channels.

Stitch Thread in SYD The presence of the stitch yarn in the centre of the SYD results in a locally lower permeability. Nordlund *et al.* [79, 80, 82] studied the effect of the stitch thread on the permeability and concluded that the local permeability can decrease up to 20%. The central node in the SYDs is replaced by an element, which number of nodes corresponds to the number of elements originally connected to the central node: a four node element replaces the centre node of the SYD in a biaxial fabric (see figure 3.29), a six node element replaces the centre node in a triaxial fabric and an eight node element in a quadriaxial fabric. The methodology to implement the stitch thread element is briefly explained for a biaxial fabric, the derivation for the other configurations is similar.
The permeability (both longitudinal and transverse) of the stitch thread is unknown and it is hard to measure, since size of the thread is small. Moreover, the permeability of the centre of the SYD does not equal the stitch thread permeability exactly, since the threads (two in total, see section 2.1) do not fill the entire space. The flow resistance is therefore estimated using the results of Nordlund *et al.* [79, 80, 82]. A decrease of 20% of the permeability in the section containing a stitch thread compared to the sections that do not contain a stitch thread, according to Nordlund *et al.*.
The flow path through the thickness, formed by the stitch yarns, is modelled as a cylinder with a radius $r_c = 2d_0$ (the dimensionless width of an SYD is roughly 4, see

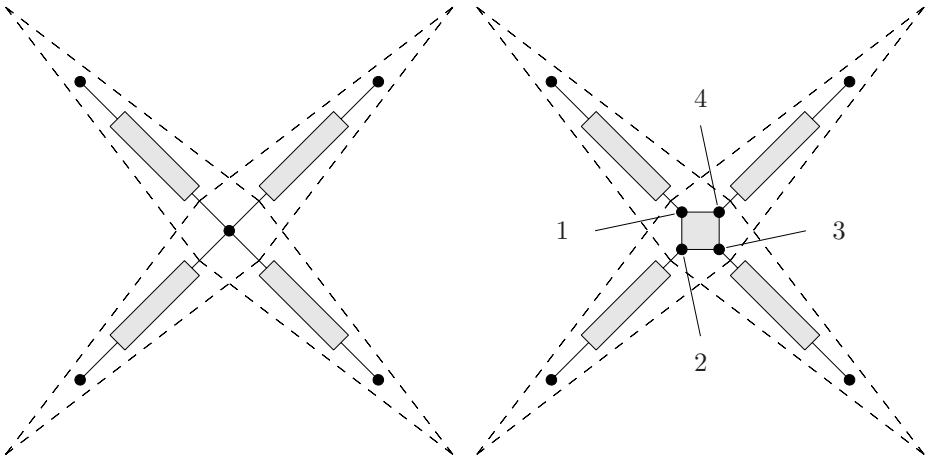

(a) *Single centre node.* (b) *Four node element in centre.*

Figure 3.29: *A four node element replacing the centre node of an SYD. The resistance of the element corresponds to the flow resistance of the stitch thread.*

table 2.5) and with a length l_c equal to the thickness of a single layer (≈ 0.5 mm). The element matrix of this four node element is constructed using the theory presented in section 3.2.5. The system matrix of the element in the centre of the SYD $\boldsymbol{M}$ reads:

$$\boldsymbol{M} = \frac{K^{sy}}{\mu} \begin{bmatrix} \sum_{j=2}^{4} \frac{1}{L_{[1,j]}} & \frac{1}{L_{[1,2]}} & \frac{1}{L_{[1,3]}} & \frac{1}{L_{[1,4]}} \\ \frac{1}{L_{[1,2]}} & \sum_{j=1,j\neq 2}^{4} \frac{1}{L_{[2,j]}} & \frac{1}{L_{[2,3]}} & \frac{1}{L_{[2,4]}} \\ \frac{1}{L_{[1,3]}} & \frac{1}{L_{[2,3]}} & \sum_{j=1,j\neq 3}^{4} \frac{1}{L_{[3,j]}} & \frac{1}{L_{[3,4]}} \\ \frac{1}{L_{[1,4]}} & \frac{1}{L_{[2,4]}} & \frac{1}{L_{[3,4]}} & \sum_{j=1}^{3} \frac{1}{L_{[4,j]}} \end{bmatrix}, \tag{3.64}$$

with K^{sy} the permeability of the centre of the SYD including the stitch yarn, $L_{[i,j]}$ the distance between nodes i and j, or the distance between the channel sections connected to the node. Consequently, the distance between two resistances of the same SYD equals twice the stitch thread radius r_c, whereas the distance between the two resistances of different SYDs also depends on the distance in thickness direction l_c between the centres of the two plies. Note that symmetry is used: $L_{[i,j]} = L_{[j,i]}$

and the lengths L are given by:

$$\begin{aligned} L_{[1,2]} &= \sqrt{r_c^2 + l_c^2} \\ L_{[1,3]} &= 2r_c \\ L_{[1,4]} &= \sqrt{r_c^2 + l_c^2} \\ L_{[2,3]} &= \sqrt{r_c^2 + l_c^2} \\ L_{[2,4]} &= 2r_c \\ L_{[3,4]} &= \sqrt{r_c^2 + l_c^2} \end{aligned} \tag{3.65}$$

The number of degrees of freedom increases to:

$$N_{tot} = 6N_1 \times N_2, \tag{3.66}$$

which is roughly twice the number of degrees of freedom in the simple network representing a biaxial fabric (equation (3.61)).

Stitch Thread between SYDs The stitch pattern determines the path of the stitch yarn from one stitch penetration to another. Lomov *et al.* [60] presented a coding to describe the stitch pattern by means of the steps in machine and cross direction that are made by the stitching needles. Moreover, they describe the shape of the stitch thread and conclude that the thread is flattened maximally for this type of stitch thread, since the threads are small compared to the fibre bundles. The maximum flattening can be measured in a compression test, although it should be noted that it is not possible to perform such a compression test on a standard static tester. Special equipment, such as the Kawabata Evaluation System for Fabric (KES-F) equipment should be used [94]. The stitch thread is pressed into the surface of the fabric when placed in the mould (figure 3.30, see also section 2.5).

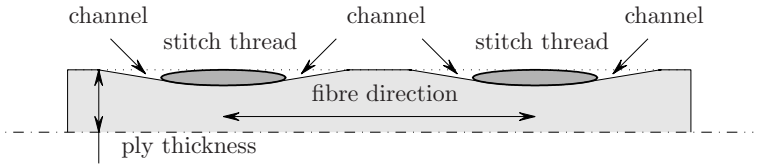

Figure 3.30: *Cross–section of the fibre bundles (light gray area) in longitudinal direction. The dark gray areas represent the cross–section in transverse direction of the stitch threads which are pressed into the fibre bundle.*

Two small channels are formed on either side of the stitch thread, as indicated by the single head arrows. Moreover, the permeability of the stitch yarn is generally significantly higher than the permeability of the fibre bundle. Therefore, it is recommended to combine the channels and the stitch yarn, representing the combination by a single flow resistance in the network system. This approach reduces

the number of additional elements in the system. No additional nodes are required to incorporate the flow resistances in the network, in contrast to the incorporation of the stitch thread inside the SYD. The stitch pattern is simply projected on the network. An example of the projection of a chain knit pattern and a tricot knit pattern on a network is presented in figure 3.31 (compare figure 3.12, which shows the elements and nodes only). The solid lines correspond to the newly introduced elements representing the channels formed by the stitch thread. The elements representing the SYD channels are dashed. The dots refer to the nodes.

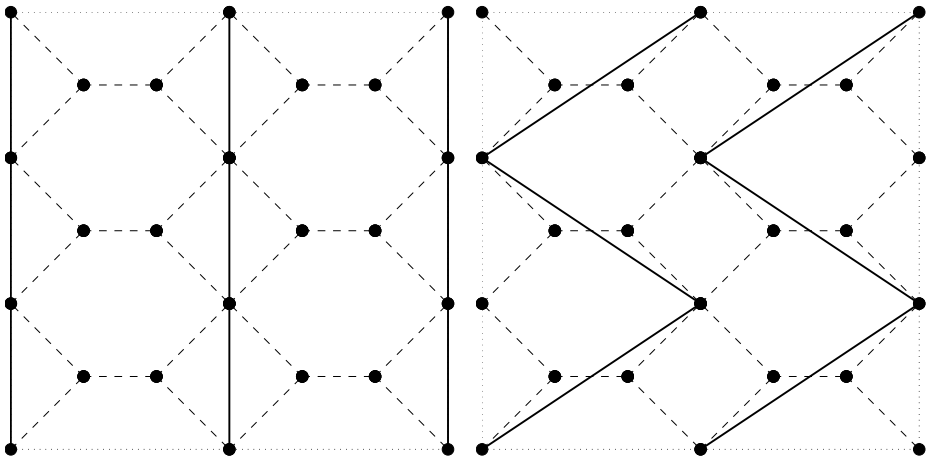

(a) *Chain knit pattern (also pattern of bottom face for all knit patterns)*

(b) *Tricot knit pattern*

Figure 3.31: *Projection of a stitch pattern (solid lines) on a network of flow channels (dashed lines).*

Note that there are no nodes added to the system: the new elements are connected to already defined nodes. A number of terms is added to the system matrix $\boldsymbol{M}$ for the additional elements. Hence, the system itself does not become larger, but the bandwidth and consequently the required solving time increases.
The flow resistance is assumed to be equal to the flow resistance of the stitch yarn in the centre of the SYD. The length of the channel formed by the stitch thread depends on the pattern and the stitch distances A and B.

3.4.3 Multilayer Network

A stack of NCFs is represented by a stack of networks. The main problem is to connect the different networks, since the stitch penetration locations of the different networks generally do not coincide (see also section 2.5). Moreover, the orientation of the networks can be rotated with respect to each other. This implies that the channel sections of an SYD (see section 3.2.3) are split into two parts at those locations where

a channel of a second layer crosses the channel section. A new node is created if necessary. This is not always the case, as can be seen in figure 3.32. The figure shows two examples of overlapping channels of different layers. No additional node has to be created in the case shown in figure 3.32(a), whereas an extra node is needed if the situation in figure 3.32(b) occurs.

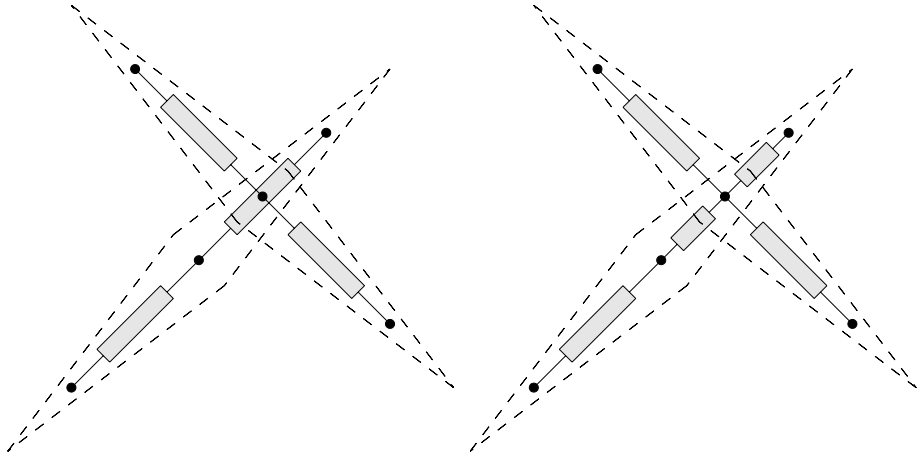

(a) *No new node*

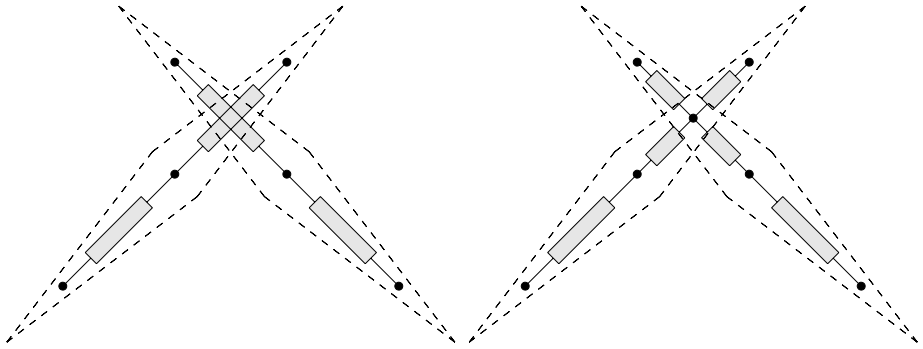

(b) *New node*

Figure 3.32: *Two networks stacked on top of each other with a relative shift results in the splitting of channel sections, either without (a) or with (b) the creation of a new node.*

The shift of the stacked networks is arbitrary. Consequently, the number of possible multilayer networks is infinite. It is sufficient for practical use to analyse a number of cases. For example, a completely coinciding network, *id est* the stitch penetrations of the different layers correspond with each other, or a network shifted exactly $\frac{1}{2}A$ and/or $\frac{1}{2}B$ with respect to each other. However, it is also recommended to analyse a network with a randomly generated shift of the different layers. The effect of randomness can

differ from predefined configurations, which exhibit a higher degree of order, as shown in section 3.3.

3.4.4 Extension to a 3D-model

The simple model is not able to predict flow in the direction perpendicular to the plane of the fabric. Two ingredients have to be added: an expansion of the network of a single layer to the third dimension and a connection between different layers. The first can be achieved by implementing an additional flow resistance in the centre of the SYD, as described in section 3.4.2. The nodes 1 and 3 in figure 3.29 lie in a different plane compared to nodes 2 and 4. The second ingredient is covered by the implementation of the multiple layers as discussed in section 3.4.3, but now an additional node has to be created at the location where the channel sections are split. Consequently, this new node lies in a different plane than the node causing the split (see figure 3.32). It is clear that the number of stitch penetrations affects the permeability in transverse direction, as measured by Drapier *et al.* [81]: the more stitch penetrations, the more channels in out–of–plane direction.
The number of degrees of freedom will increase strongly for a network model built to analyse the flow in out–of–plane direction. It is therefore recommended to use a network with a relatively limited number of repetitive blocks (see section 3.2.5, figure 3.12) in a single plane. It is more important to use sufficient layers in order to construct sufficiently long flow paths in thickness direction, in order to predict the permeability accurately (see the discussion on the size of the network in section 3.3.4)

3.5 Conclusions on the Flow Model

The flow model that was proposed in this chapter is based on the geometrical model, presented in chapter 2, combined with basic fluid dynamics. The flow model is based on the geometry of a biaxial $\pm 45^{o}$ fabric. It was revealed that:

- A single SYD can be transformed to a series of four channels, with a certain flow resistance, based on the dimensions of the flow channel.
- A network of flow resistances can be constructed, representing a collection of SYD flow channels and hence a piece of Non–Crimp Fabric.
- The variability of the dimensions can be implemented in the model explicitly, as the number of channels in the network is large enough to represent a certain variability.

A qualitative analysis of the effect of the variation in the SYD dimensions on the permeability of the entire network was performed. A quantitative analysis was not yet performed at this stage. The permeabilities were compared to the nominal permeability. The nominal permeability is defined as the permeability of a network without variation of the SYD dimensions. Variation of different parameters in the model led to the conclusions that:

- The averaged macroscopic permeability of a network of channels does not only depend on the averaged width of the channels and the variation on the width, but also on the central moments (the variance, skewness and kurtosis) of the set of SYD widths. Consequently, the analysis of a network rather than of a single SYD is required to estimate the average permeability, as well as the variation on it.
- The upper and lower bounds of the permeability can be estimated by ignoring the flow in the edge sections of the SYDs if the pressure gradient is applied in the machine direction. The fluid mainly flows through the centre sections of the SYD, with a significantly higher permeability ($K \sim r^4$).
- The upper and lower bounds for a flow in the cross direction can be estimated by ignoring the interaction between centre sections of the SYD of neighbouring stitch penetrations in machine direction. The edge sections form the bottleneck for the flow.
- The lower and upper bounds are found if a linear decrease (or increase) of the widths of the SYDs is assumed respectively perpendicular and parallel to the direction of the applied pressure gradient. The variation in the SYD widths is according to the measured dimensions equal to 5–10% of the averaged width. The lower bound lies roughly 40–45% below the nominal permeability, the upper bound roughly 45–50% above the nominal permeability, both irrespective whether the pressure gradient is in the machine or in the cross direction.
- The network exhibits a strong anisotropy. The anisotropy is stronger than the measurements or results in the literature indicate. The low permeability in the edge sections of the SYD is responsible for the high degree of anisotropy. The number of fibre filaments separating neighbouring SYDs in these regions is relatively low. It is therefore concluded that the permeability is underestimated in the edge section of the SYDs.
- The results indicate that the amount of variation has a significant effect on the permeability. The normalised permeability of a network with randomly distributed SYD widths is roughly 85% for the measured standard deviation and as low as 70% if the amount of variation is increased to 150% of the measured variation.
- The variation of the macroscopic permeability of a network due to a random permutation of the SYD widths is shown to be small (±5%) compared to the variation of the macroscopic permeability introduced by a newly generated set of SYD widths, which has the same averaged value and standard deviation (±10% variation).
- The minimum relative size of the network to obtain a mesh independent result is relatively low. A network of 40×80 repetitive blocks (≈200×160mm^2 for the fabric analysed here) is sufficient. Generally, the specimens for permeability measurements are larger.

– It is shown that the normalised permeability of a network with randomly distributed SYD widths roughly equals 85% of the nominal permeability if the pressure gradient is applied in the machine direction. The normalised permeability remains nearly equal to the nominal permeability if the pressure gradient is applied in the cross direction. The variation on the SYD dimensions has a smaller effect on the edge sections where the width is relatively small compared to the thickness of the ply.

– Analyses of various kinds of non–random spatial distributions of the SYD widths revealed that the level of order, causing clustering of larger channels, pushes the normalised permeability to either the upper or the lower bounds. The permeability approaches the upper limit if the majority of the chains of channels is oriented in the direction of the pressure gradient. The permeability approaches the lower limit otherwise.

– The variation in the permeability of different distribution may result in a factor of 2.5 between the lowest and highest permeability.

– A higher degree of anisotropy was found for all spatial distributions, except the horizontal and random distributions for which a lower degree of anisotropy was found. The change of the anisotropy is a direct consequence of the above–mentioned clustering of channels, which, depending on the direction of the pressure gradient with respect to the orientation of the chains of channels, results in an increase or a decrease of the anisotropy respectively. The anisotropy for the random distribution is least affected, due to the limited possibility for the formation of chains of channels.

– It was found that the permeability of a network is normally distributed, even though a lognormal distribution was found – and used – for the widths of the SYDs.

Chapter 4

Permeability Measurements

Experiments were performed in conjunction with the theoretical work. Firstly, to compare the measuring techniques that were available and to identify the bottlenecks of a permeability measurement. Secondly, to verify the results of the model and finally to identify the key features that have to be implemented in the model.
A brief review on measuring the permeability is presented in section 4.1. Three different permeability measuring tools were available to obtain permeability values of different reinforcements. A line injection tool was present at the National Aerospace Laboratories (NLR), a central injection tool at the Katholieke Universiteit Leuven (KU Leuven) and a line injection tool was developed at the University of Twente (UT). The apparatuses are presented in section 4.2. The calculation methods required to convert the experimental data to a permeability value are discussed in section 4.3. The three tools were used for various permeability experiments. The results are presented in section 4.4.

4.1 Review on Permeability Experiments

Permeability measurements are known for their poor reproducibility and poor repeatability. A large amount of scatter is reported by several authors [5, 23–31]. Moreover, large differences are observed in permeabilities of the same fabric, measured by different institutes [32, 118]. The verdict on the repeatability and reproducibility[1] of Lundström *et al.* [119] is more positive: they state that similar permeabilities can be measured by different institutes. However, the same equipment was used for all experiments and the measuring procedure was thoroughly explained to the operators of the partners reproducing the measurements.
An important source of the scatter in permeability is the wide variation of measuring techniques. The permeability of a reinforcement can be measured in an in–plane

[1] The repeatability is an indication for the amount of variation between subsequent measurement with the same apparatus, the reproducibility is an indication of the amount of variation between measurements performed at different locations.

system, or in an out–of–plane device or in a system that measures the in–plane and out–of–plane permeability simultaneously. Moreover, either the saturated or unsaturated permeability can be measured, the range of injection pressures can be varied and the injected fluid can be varied [120, 121]. Finally, a constant flow rate or a constant injection pressure can be used to control the process. An overview of which experiment is performed by whom was presented in [122].
The type of experiment and the process settings cause significant variations in the measured permeabilities. This observation contradicts the theoretical definition of the permeability as a purely geometric quantity. The reasons why the permeability appears not to be a purely geometric quantity were discussed in chapter 3. Here, it is important to recognise the influence of the type of measurement and process parameters: results from permeability measurements without information on the process conditions are of little significance. On the other hand, results of measurements on the same type of fabric, but on a different machine are certainly useful for a better understanding of the process condition dependency.
The permeability measurement itself is rather sensitive for small variations. This also results in a large amount of scatter on the measured permeability values, as reported in the literature (amongst others shown by Parnas [5]). The measuring techniques are constantly developing, in particular concerning the data acquisition. The developments in the area of process optimisation and control stimulate the research on the automated data acquisition systems [25, 27, 123, 124]. The advantage of automated data acquisition is not only the increased accuracy (generally a relatively large amount of data can be evaluated), but also the strongly decreased data analysis time. It even enables analysis of data real–time and subsequently of control actions to be taken.
The current status of the permeability experiments is that standard permeability measuring tools are developed with integrated data acquisition systems [124–126]. Moreover, an international benchmark project is starting up. The outcome of the benchmark is – ideally seen – a standardised permeability measurement protocol. The permeability measuring tool developed at the University of Twente during this research is aimed at being used in the benchmark project.

4.1.1 Permeability Measuring Equipment

In–plane permeability measurements are more common than out–of–plane measurements. The flow in thickness direction of the preform is often regarded as negligible. This simplification can be justified for products with a small thickness compared to the in–plane dimensions. The flow in the mould will be approximately a two–dimensional flow. However, the increasing application of RTM for structural parts has led to thicker components, in which the through thickness flow cannot be neglected [2]. Consequently, knowledge of the through–thickness permeability of fabrics is receiving an increasing amount of attention.
Another field in which knowledge on the through–thickness permeability is needed is the field of the infusion technologies [127–132]. The resin is generally injected through a transport medium on top of the preform, after which the resin impregnates

the preform through the thickness. The injection time is reduced significantly, since the effective injection length is short compared to the in–plane dimensions of the product.
Few fully three–dimensional permeability measurements are reported in the literature. The only applicable injection strategy is the radial injection strategy. The main problem is the visualisation of the flow front, which cannot be done by direct visual observation. Ahn *et al.* [133] and Nedanov *et al.* [134] use the patented SMART weave sensor system [135, 136]. Saouab *et al.* [137] use X–ray spectography to obtain information on the position of the fluid inside the mould. These techniques either are limited to be applied for non–conductive materials, or require relatively expensive equipment. It was therefore decided to measure the in–plane permeability and the out–of–plane permeability in separate measurements in the current research project. An out–of–plane permeability measuring device was not available at the start of the project and was developed and tested at the University of Twente during the project [138–141]. Only woven fabrics have been measured until now. Measurements on Non-Crimp Fabrics have not yet been performed. However, the out–of–plane permeability measurements carried out by Drapier *et al.* [81] on stitched fabrics illustrate that the permeability in transverse direction depends on the number of stitches. This confirms the dominant role of the channels formed by the stitch penetrations, on which the permeability prediction model presented in the previous chapter is based.
The in–plane measurements performed in this project are, as mentioned, employing three different test rigs at three different locations. Different measuring techniques are applied, but it is attempted to use comparable process settings and measuring conditions, for example by using the same test fluid (Polyol, see section H.1) and injection pressures in the same range.

4.1.2 Comparison of In–plane Measuring Techniques

Many institutes have performed in–plane permeability experiments and have published on it [23, 25–27, 29–31, 119, 120, 134, 142–155]. The large number of experiments and consequently wide variety of test equipment can be reduced to two variants of in–plane measurements:

1. Line injection
2. Radial injection

The first can be used for either wetting or saturated flow, the latter only for wetting flow. The fluid can either be injected with a constant pressure or with a constant flow rate. Evidently, both the flow rate and injection pressure are constant in case of a saturated permeability measurement (a stationary situation is obtained). The typical advantages and disadvantages of both types are presented in table 4.1.
The mathematics required to calculate the permeability from an experiment using a linear injection strategy are fairly simple compared to those required in case of a radial injection. There is a strong argument for the preference of a linear injection strategy. The more complicated the mathematical procedure, the more inaccuracies are likely to affect the results.

Table 4.1: *Typical advantages and disadvantages of the linear injection and radial injection technique.*

	linear injection	radial injection
+	simple mathematics simple handling saturated and unsaturated permeability stable process	full 2D permeability in single measurement less prone to race tracking
–	single direction permeability prone to race tracking	complicated mathematics more extensive data acquisition sensitive to preform inaccuracies in the centre only wetting permeability larger mould deflections

The line injection measurement is generally easier to conduct. The system requirements are lower. Firstly, less data acquisition suffices to determine the flow front position properly. Secondly, a more stable flow is obtained, since the pressure gradient is constant between the flow front and the injection point, whereas a steep and varying gradient in the pressure drop occurs in case of radial injection. This can be seen by elaborating the fluid mechanics, see appendix E. However, the reaction forces on the mould are higher, for equally sized cavities.

The central injection method is not only sensitive to small variation near the injection point, but also on the actual size of the injection port. A relatively large radius r_0 of the injection port is better than a relatively small radius, since the fraction $\ln \frac{r_0}{r_f}$ is smaller for larger values of r_0, resulting in a lower pressure gradient. This causes practical problems, related to the size of the rig and the circular cut that has to be made in the fabric right above the injection port.

The reaction forces on the mould are higher in the case of linear injection. The reaction forces are obtained by integration of the pressure field over the wetted area. However, the mould deflection may be larger for a central injection system, since the maximum pressure is found at the injection point, *id est* at a larger distance from the locations where the closing force is applied, resulting in a higher bending moment.

The main drawback of the linear injection technique is that it provides information on the permeability in a single direction only. This direction does not necessarily coincide with the principal direction of the material, either because the principal direction is unknown (for example for deformed fabrics), or due to a misalignment of the fabric in the mould. At least three separate experiments are required to obtain the full permeability tensor. The correlation between the three individual measurements is sensitive to small differences in the internal geometry of the three specimens and to inaccuracies occurring during placement of the preform in the mould. Moreover, the direction of the pressure gradient in the mould is not necessarily parallel to the

longitudinal direction of the mould. As a result a two–dimensional flow occurs: flow in longitudinal direction *and* flow in transverse direction of the mould. This effect is shown by Loendersloot and Akkerman [118], where the line injection measurements with the apparatus of the NLR were compared to the measurements of the multi cavity apparatus of SiComp [30].
Another disadvantage of the linear injection technique is that race–tracking is likely to occur. The fluid flows along the cavity edges during the entire experiment, whereas the fluid arrives at a cavity edge only at the end of the experiment in case of a radial injection. It is virtually impossible to cut and place the fabric such that channels between the edges of the rectangular cavity and the fabric are not formed.
An alternative method to overcome the problems encountered when carrying out a permeability measurement, is the use of a ring injection. This is the opposite of a central injection: the fluid flows from the – circular – edge towards the centrally located vent, rather than from the centre to the edge. This requires a circular mould, with all its practical inconveniences, such as preparation of the specimen. However, the advantages are:

- the converging flow front guarantees a low sensitivity to local variations in the preform;
- race–tracking is no issue at all;
- low mould deflections are expected, since the maximum pressures are near the locations where the clamping force is applied;
- the pressure gradient is rather constant for the main part of the measurement. A rapidly changing pressure gradient is only found near the centrally located vent, reached in the final stage of the measurement.

The last point is possibly the most important to obtain a stable and repeatable measurement. It implies that disturbances occurring in the outer edge and mid section of the preform have a minor effect on the overall flow. The converging flow front results in damping of the effect of disturbances. Disturbances in the central part, where a steep pressure gradient can cause instabilities in the flow, cannot affect the flow in other parts of the preform anymore, whereas disturbances near the centre affect the entire measurement in the case of central injection. The mathematics to transform the progression of the flow front to a permeability tensor are similar to those required for a central injection strategy.

4.2 Three Permeability Measuring Devices

A tool for in–plane permeability measurements was available at the National Aerospace Laboratories (NLR) at the start of the project. The NLR apparatus consists of a mould cavity of $480\times200\times4\text{mm}^3$, see table 4.2. The test fluid is injected by an RTM machine at one end of the apparatus as a point injection into a gutter which spans the entire width of the cavity. A line injection is created in this way. The fluid is injected with a constant flow rate, which is controlled by adjusting the injection pressure. The injection pressure is consequently low at the beginning of the

injection and increases gradually during the measurement until a stationary flow is obtained.

Two pressure transducers are placed inside the mould cavity to measure the pressure drop during injection. The distance between both transducers is 330mm. The top part of the mould is made of polycarbonate in order to see the progression of the flow front. The three polycarbonate plates, stacked on top of each other, are not stiff enough to withstand the internal pressure without exceeding the maximum allowable deflection[2]. A metal frame is placed on top of the transparent plates to reduce the deflection.

In–plane permeability measurements were also performed at the Katholieke Universiteit Leuven (KU Leuven) during a European funded research exchange project (Marie Curie Fellowship project HPMT–CT–2000–0030 [4]). The test rig of the KU Leuven (second row in table 4.2) can be used to perform permeability measurements as well as to produce composite plates. It is equipped with a pressure controlled injection unit, a heating device and two pressure transducers inside the mould cavity. The RTM rig consists of a rectangular mould (cavity $500\times300\text{mm}^2$) with central injection port and a vent on one of the short sides of the mould, see table 4.2. The top mould consists of three acrylic plates, stacked on top of each other, to allow visual observation of the flow front. Again, a metal frame is used to obtain the required stiffness. Different spacers can be used, allowing cavity thicknesses of 2mm up to 6mm. The pressure is measured near the inlet point and the mass flow is measured by weighing the resin container. A digital video camera is mounted above the centre of the tool to capture the flow front position during the injection.

An additional device was developed at the University of Twente (last row in table 4.2). A new methodology was developed to reduce the time required to perform a single measurement – consequently, a larger number of specimens can be measured – and increase the accuracy by automated mould closing and automated data acquisition. The rig consists of a rectangular cavity of $500\times200\text{mm}^2$. A line injection strategy is applied, similar to the apparatus of the NLR. The tool is equipped with six pressure transducers, positioned parallel to the flow direction and along the centre line of the cavity. Two flow front sensors are placed on either side of each of the pressure transducers.

The upper mould half is mounted onto the moving part of a universal testing machine. A thick rubber seal is used to make the mould liquid–closed. The cavity height can be varied continuously rather than stepwise. The rubber seal can be compressed over a certain range while still maintaining a fluid tight cavity. A minimum compression is required to withstand a fluid pressure of roughly 2 bars. The rubber seal is used as a fine adjustment. Various spacer frames can be used to enforce large steps in the cavity height. A detailed description of the design is found in the bachelor thesis of Haanappel and Van der Sligte [156].

[2]The allowable deflection is low ($\approx$1% of the cavity height), due to high sensitivity of the permeability for a variation in the fibre content.

Table 4.2: *Schematic view of the three tools, including their main process and data acquisition characteristics.*

NLR	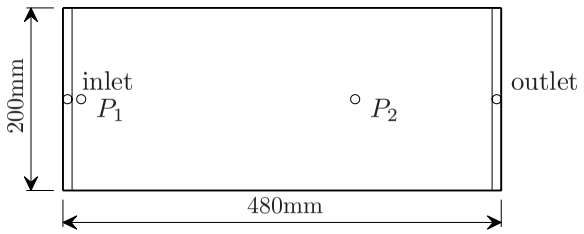	Set–up characteristics: – line injection – constant flow – transparent top mould – test fluids only	Data acquisition: – 2 pressure transducers – 1 direct flow meter
KUL	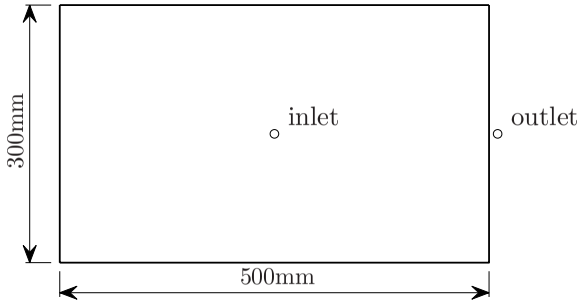	Set–up characteristics: – radial injection – constant pressure – transparent top mould – test fluids + curing fluids	Data acquisition: – 1 pressure transducer – 1 indirect flow meter
UT	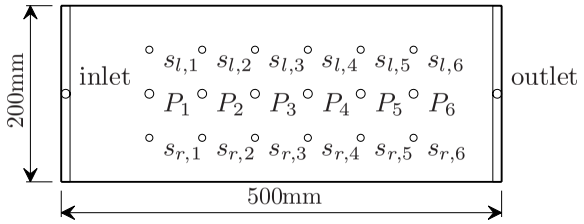	Set–up characteristics: – line injection – constant pressure – aluminium top mould – test fluids + curing fluids	Data acquisition: – 6 pressure transducers – 12 flow front sensors – 1 indirect flow meter

4.3 Calculation Methods

The data obtained during the measurements have to be transformed to a permeability value of the reinforcement. The calculations depend on the type of injection (line or radial) and the type of measurement (saturated or unsaturated).
Two variants of the permeability calculation are distinguished:

1. Flow front progression based calculation;
2. Flow rate based calculation.

The first can – in principle – only be applied to determine the unsaturated permeability, whereas the second can be applied to determine the saturated as well as the unsaturated flow. The first method is applied for the analysis of a one–dimensional flow and of a two–dimensional flow. The second is only applied in the case of a one–dimensional flow. The type of injection and the type of measurement applicable to the three different rigs are listed in table 4.3. The abbreviation refers to the institute that owns the test rig.

Table 4.3: *Overview of the calculation methods and the flow type for the three different test rigs. The abbreviation refers to the institutes owning the test rig.*

	1D, linear	2D, radial
method 1: unsaturated	UT, NLR	KU Leuven
method 2: saturated	NLR, UT	-

The saturated permeability can only be calculated using the permeability measuring rigs of the NLR and the UT. The KU Leuven rig, the only one with a central injection, is not capable of measuring the saturated permeability. The next two sections present the methods to derive the unsaturated and saturated permeability for a one–dimensional flow and the method to derive the unsaturated permeability for a two–dimensional flow from the experimental data.

4.3.1 One–Dimensional Flow

The data measured in the in–plane line injection measurements are:

- The injection pressure P_{inj};
- The pressure in the cavity P;
- The mass M of the fluid either measured at the supply point or at the outlet (UT test rig);
- The volumetric flow rate Φ (NLR test rig);
- The flow front arrival time t_i at predefined positions x_i, or vice versa the position of the flow front x_i at a predefined instant t_i.

The flow length L and the cross–sectional flow area $\mathcal{A}$ are known from the dimensions of the tool and/or the preform dimensions. The viscosity μ of the fluid is measured in a separate experiment.
Darcy's law (1.1) proposes a linear relationship between the superficial fluid velocity u (the ratio of volumetric flow Φ and cross-sectional area $\mathcal{A}$ in flow direction) and the pressure drop ΔP over the flow length L:

$$u = \frac{\Phi}{\mathcal{A}} = \frac{K}{\mu}\frac{\Delta P}{L}, \tag{4.1}$$

with K the permeability and μ the dynamic viscosity of the fluid. The flow rate is not directly measured by the devices of the KU Leuven and the UT. The difference between both calculation methods, mentioned previously, is found in the way the flow rate is derived from the measured data.

Flow Front Progression Based Calculation The first method uses the signals of the flow front sensors and can only be used for unsaturated permeability measurements. The Darcian relation between the flow and the pressure drop (4.1) is written in a general form:

$$u = \frac{\mathrm{d}x_f}{\mathrm{d}t} = \frac{K}{\mu}\frac{\Delta P}{x_f}, \tag{4.2}$$

with x_f the instantaneous flow front position, as defined in section 4.1.2.

$$x_f \mathrm{d}x_f = \frac{K\Delta P}{\mu}\mathrm{d}t. \tag{4.3}$$

Rearrangement of the variables and integration lead to a linear relation between the injection time and the square of the injection length:

$$\frac{1}{2}(x_f^2 - x_0^2) = \frac{K\Delta P}{\mu}(t_f - t_0), \tag{4.4}$$

with t_f the arrival time of the fluid at position x_f. Let Δt be the time the fluid needs to impregnate the fabric between two flow sensors, separated by the distance ΔL. The permeability $K_u^{(1)}$ is then found to be equal to:

$$K_u^{(1)} = \frac{\mu\Delta L^2}{2\Delta P\Delta t}. \tag{4.5}$$

The superscript refers to the method and the subscript refers to the type of flow (u: unsaturated, s: saturated, as will be used throughout the remainder of the text).

Flow Rate Based Calculation The second method can be used for unsaturated as well as for saturated flow. The mass M flowing out of the resin container or flowing through the outlet, is measured during the experiment and used to determine the mass

flow rate Φ_M. The mass flow rate results, after dividing it by the fluid density ρ, in the volumetric flow rate:

$$\Phi_M = \frac{\mathrm{d}M(t)}{\mathrm{d}t}; \tag{4.6}$$

$$\Phi = \frac{\Phi_M}{\rho}. \tag{4.7}$$

The flow rate is not constant during impregnation of the preform if a constant pressure injection strategy is used. This is the case for the equipment of the KU Leuven and of the UT. The NLR equipment uses a constant flow rate, resulting in a variable pressure during the wetting stage. The derivation below applies to the case of a constant injection pressure. The pressure gradient for a constant pressure injection strategy is approximated by:

$$\frac{\partial p}{\partial x} \approx \frac{\Delta P}{\Delta x} = \frac{P_{inj}}{x_f}, \tag{4.8}$$

with P_{inj} relative to the ambient pressure and the injection point located in $x = 0$. The flow front position advances in time, resulting in a decrease of the pressure gradient and consequently a decreasing flow rate. The flow rate as a function of time during the wetting stage is derived using (4.4). Rearrangement of (4.4) leads to an expression for the unsaturated flow rate Φ_u as a function of the injection time:

$$\Phi_u^2 = \frac{\mathcal{A}^2 x^2}{(\Delta t)^2} = \frac{2\mathcal{A}^2 K \Delta P}{\mu \Delta t}; \tag{4.9}$$

$$\Phi_u = \sqrt{\frac{2\mathcal{A}^2 K \Delta P}{\mu \Delta t}}. \tag{4.10}$$

This relation shows that the volumetric flow rate Φ_u is proportional to the inverse of the square root of the time t during wetting of the preform:

$$\Phi_u(t) \sim \frac{1}{\sqrt{t}}. \tag{4.11}$$

Substituting this result in the relation of the injected mass (M) and the mass flow rate Φ_M results in a relation for the mass as a function of the impregnation time (bearing in mind that $\Phi_M = \rho\Phi$):

$$M(t) \sim \sqrt{t} \rightarrow M(t) = a_u\sqrt{t} \rightarrow \Phi_u(t) = \frac{a_u}{2\sqrt{t}} \tag{4.12}$$

A fitting procedure is employed to determine the constant a_u. The flow rate at a certain arbitrary moment of the impregnation can be calculated once the function $\Phi_u(t)$ is derived.
The flow rate becomes constant after the fluid completely wetted the preform. Consequently, the injected mass $M(t)$ is proportional to the time:

$$M(t) \sim t \rightarrow M(t) = a_s t \rightarrow \Phi_s(t) = a_s. \tag{4.13}$$

Note that the mass of the fluid flowing through the outlet can also be measured in this case. Consequently, it may be necessary to introduce an offset mass M_0 to compensate for the mass of the fluid that has already passed the outlet before the time t_{sat}. Again, the proportionality constant a_s is fitted on the measured data and the function $M(t)$ employing a fitting procedure.
The functions $M(t)$ and $\Phi(t)$ are stepwise, but continuous functions:

$$M(t) = \begin{cases} a_u\sqrt{t} & \text{for} \quad t \leq t_{sat} \\ \\ a_s t & \text{for} \quad t > t_{sat} \end{cases} \tag{4.14}$$

$$\Phi(t) = \begin{cases} \dfrac{\rho a_u}{2\sqrt{t}} & \text{for} \quad t \leq t_{sat} \\ \\ \rho a_s & \text{for} \quad t > t_{sat} \end{cases} \tag{4.15}$$

Note that theoretically the flow rate during the wetting stage should converge to the flow rate in the saturated stage as $t \to t_{sat}$. This constraint can be used in the fitting procedure or in the determination of the start point of the saturated stage t_{sat}.
Substitution of (4.14) in (4.1) leads to a second, in this case stepwise expression for the 1D permeability $K^{(2)}$:

$$K^{(2)} = \begin{cases} \dfrac{\mu \Delta L}{A \Delta P} \dfrac{\rho a_u}{2\sqrt{t}} & \text{for} \quad t \leq t_{sat} \\ \\ \dfrac{\mu \Delta L}{A \Delta P} \rho a_s & \text{for} \quad t > t_{sat} \end{cases} \tag{4.16}$$

The two equations (4.5) and (4.16), which are derived for the calculation of the permeability, are used simultaneously if possible. The calculated permeabilities should be equal from a theoretical point of view, but often deviations are found. The deviations originate firstly from measuring inaccuracies. A second source of deviations is the validity of Darcy's law. Darcy's law does not account for capillary flows, for example. Finally, the measurements will differ if the flow front is not perpendicular to the longitudinal direction of the mould. This results in a two–dimensional flow – as was discussed previously in section 4.1.2 – whereas the equations are derived based on a one–dimensional flow.

Principal Permeabilities A single line injection measurement only provides information on the permeability in the flow direction. At least three measurements are required to obtain the principle in–plane permeabilities. The orientation of the machine direction of the fabric with respect to the flow direction is different in each measurement. Generally, the orientations 0°, 45° and 90° are used[3]. The derivation is presented in appendix F.

[3] A similar approach is used to determine the local strains. Three strain gauges are used to characterise the complete strain situation. See for example [157]

4.3.2 Two–Dimensional Flow

The applied method to calculate the permeability in the case of a two–dimensional flow is based on the assumption that the flow front is elliptical. The position of the flow front is analysed at a number of time steps and elliptical coordinates are employed to determine the permeability. The theory can be found in [122, 158–161]. An elliptical flow front is depicted in figure 4.1. It shows all the relevant parameters:

- The global coordinate system $\boldsymbol{x}^G$, generally aligned with the rig, but strictly taken arbitrarily defined;
- The principal coordinate system $\boldsymbol{x}^P$ of the ellipse, also referred to as the local coordinate system;
- The major and minor radii $\boldsymbol{r}$ of the ellipse;
- The angle θ between the two coordinate systems;
- The translation $\boldsymbol{x}^0$ between the two coordinate systems;
- The radius r_0 of the inlet;
- The position of the flow front $\boldsymbol{x}_f$.

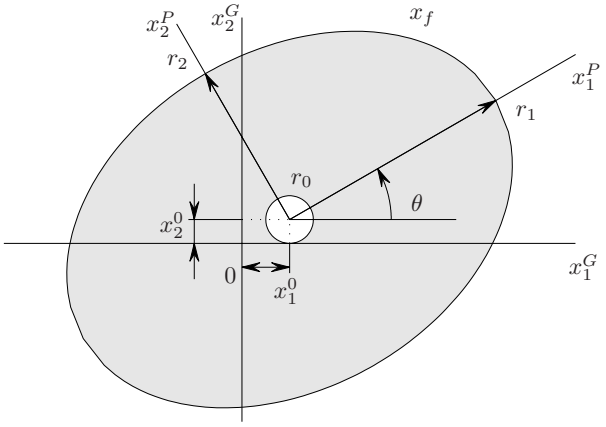

Figure 4.1: *Elliptical flow front, with major and minor radii* (r_1, r_2) *in an arbitrarily defined global coordinate system* (x_1^G, x_2^G)*. The principal directions of the ellipse correspond to the local coordinate system* (x_1^P, x_2^P)*, rotated over an angle* θ *with respect to the global coordinate system and translated over* (x_1^0, x_2^0)*. The radius of the injection point is* r_0 *and* $\boldsymbol{x}_f$ *is the position of the flow front.*

The mathematics can be found in appendix G. The procedure to convert the position of the flow front in time to a permeability value is briefly discussed below:

Radii and Orientation The major and minor radii (r_1, r_2) of the ellipse, its orientation θ with respect to the global coordinate system and the translation (x_1^0, x_2^0) are determined employing a least squares fit procedure. The flow front

positions obtained from the images taken during the measurements are used for the fit procedure. The calculated orientation of the ellipses can show changes during the progress of the experiment, as can the translation. This can either be due to imperfections in the preform, or be due to inaccuracies in the image processing used to extract a set of flow front positions from the images.
Theoretically, the orientation of the ellipse is undefined for unsheared orthogonal material (*id est* $K_1 = K_2$, a circular flow front) and the centre coincides exactly with the centre of the inlet. The orientation of a sheared fabric corresponds to the bisectrix of the smallest angle between the two fibre directions for balanced fabric (see Lai and Young [151]). The deviation between the expected circle or ellipse and the fitted ellipse gives an indication of the quality of the fit or indicates differences in the local permeability of the preform.
The theory presented in chapter 3 predicts an anisotropy for unsheared fabrics. This results in an elliptical flow front. It can also result in a rotation of the principal axes of the permeability with respect to the machine direction of the fabric, if the stitch pattern is not symmetric (see section 3.4.2). It is not unlikely that the anisotropy and orientation change during shear, since the effect of the stitch pattern on the anisotropy and the orientation can depend on the shear deformation of the fabric. This implies that the total anisotropy does not equal a superposition of the initial anisotropy and the shear induced anisotropy predicted by Lai and Young [151]. The same applies for the orientation: the total orientation is the sum of the reorientation predicted by Lai and Young [151] plus the orientation induced by the stitch pattern, which can vary as a function of the shear angle rather than being constant. Moreover, it should be remembered that the variability in the permeability is reflected in a variability in the anisotropy as well.

Elliptical Coordinates A transition to elliptical coordinates is the most natural way to solve the permeability from the flow front position (or ellipses) in time. The continuity equation and Darcy's law, normally written in Cartesian coordinates $\boldsymbol{x}^P$ are transformed to elliptical coordinates $\boldsymbol{\xi}$, a procedure that is described in appendix G. The coordinate transformation to elliptical coordinates $\boldsymbol{\xi} = (\xi, \eta)$ is:

$$\begin{aligned} x_1^P &= L_f \cosh\xi \cos\eta; \\ x_2^P &= L_f \sinh\xi \sin\eta, \end{aligned} \tag{4.17}$$

with L_f half of the focal length[4] of the (confocal) ellipse:

$$L_f = r_0 \left(\alpha^{-\frac{1}{2}} - \alpha^{\frac{1}{2}} \right)^{\frac{1}{2}}, \tag{4.18}$$

with r_0 the radius of the inlet and α the anisotropy of the principal permeabilities K_1 and K_2 and the squared major and minor radii, r_1 and r_2 respectively:

$$\alpha = \frac{K_2}{K_1} = \frac{r_2^2}{r_1^2}. \tag{4.19}$$

[4]The focal length is the distance between the two foci of an ellipse, see appendix G.

Applying the coordinate transformation and ignoring the contribution of the η-coordinate, leads to a first order differential function, see appendix G. A solution of this differential equation is:

$$F(\xi_f,\eta) = (\xi_f - \xi_0)\left(\frac{\sin 2\xi_f}{4} + \frac{\xi_f}{2}\right) - \frac{\cos^2\eta\,(\xi_f-\xi_0)^2}{2} + \frac{\cosh 2\xi_0 - \cosh 2\xi_f}{8} + \frac{\xi_0^2 - \xi_f^2}{4} = \frac{\alpha}{1-\alpha}\,\frac{K_1\Delta P}{\phi\mu r_0^2}\,t. \quad (4.20)$$

with ξ_f the flow front position (compare x_f, the Cartesian variant), ξ_0 the elliptical approximation of the radius of the inlet (r_0) and ϕ the porosity.
The function $F(\xi_f,\eta)$ can be evaluated in a number of specific points, namely at the locations $\boldsymbol{x}^P = \{r_1, 0\}$ and $\boldsymbol{x}^P = \{0, r_2\}$. The elliptical coordinates $\boldsymbol{\xi}$ can be derived explicitly for these (Cartesian) coordinates:

$$\begin{aligned} \boldsymbol{x}^P = \{r_1,0\} &\rightarrow \boldsymbol{\xi} = \left\{\operatorname{arccosh}\frac{\alpha^{\frac{1}{4}} r_1}{L_f}, 0\right\} \\ \boldsymbol{x}^P = \{0,r_2\} &\rightarrow \boldsymbol{\xi} = \left\{\operatorname{arcsinh}\frac{\alpha^{-\frac{1}{4}} r_2}{L_f}, \frac{\pi}{2}\right\}, \end{aligned} \quad (4.21)$$

The elliptical coordinates of the flow front ellipses at all available points in time are evaluated employing (4.21). The function values of $F(\xi_f,\eta)$ are proportional to the time according to (4.20). The function values of $F(\xi_f,\eta)$ based on the experimental data do not necessarily lie on a straight line, as is shown in figure 4.2. The deviation arises from the varying anisotropy and orientation of the ellipses, which were mentioned earlier. Moreover, the flow is unstable in the beginning of the measurement, resulting in a non–linear behaviour of $F(\xi_f,\eta)$ during the first seconds of the measurement. Generally, a stable situation is obtained after 5–10 seconds.
The anisotropy α in the last function of (4.20) applies to all flow front ellipses, which not necessarily corresponds to the value of the anisotropy calculated by the fitting procedure. An optimisation procedure is employed to find an overall anisotropy that fits best with the ellipse anisotropies. The anisotropy as defined in (4.19) is therefore relaxed: α in (4.18) is substituted by an iterated anisotropy $\tilde{\alpha}$ for all ellipses. The aim of the optimisation procedure is to find an anisotropy $\tilde{\alpha}$ for which the deviation between the function values of $F(\xi_f,\eta)$ and the straight line $F_{theo}(t) = a_1 \cdot t + a_2$ (the straight line in figure 4.2) is minimal, with a_1 the slope of the line and a_2 a constant. A least squares approximation is employed for this purpose.

Major and Minor Permeabilities The major and minor permeabilities of the fabric are subsequently determined from the slope a_1 of the fitted line:

$$a_1 = \frac{K_1\Delta P}{\phi\mu r_0^2}\,\frac{\alpha}{1-\alpha} \rightarrow K_1 = \frac{a_1\phi\mu r_0^2}{\Delta P}\,\frac{1-\alpha}{\alpha}. \quad (4.22)$$

The minor permeability K_2 is found by multiplying the major permeability with the anisotropy, according to (4.19).

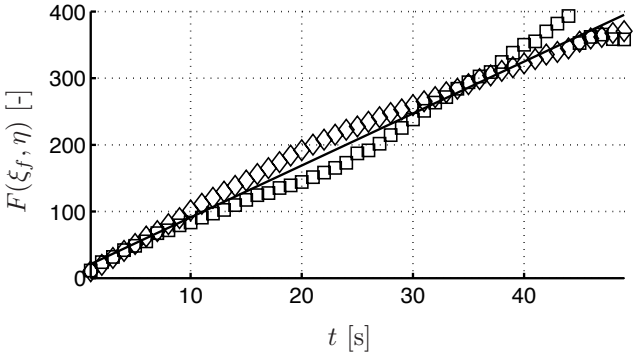

Figure 4.2: *The function values $F(\xi_f, \eta)$ versus the time (□: $F(\xi_f, \eta)$ for $\boldsymbol{x}^P = \{r_1, 0\}$, ◇: $F(\xi_f, \eta)$ for $\boldsymbol{x}^P = \{0, r_2\}$). The solid line indicates the fitted, straight line, that follows from the theory. (Data from fabric B1 – Saertex $\pm 45^o$)*

4.4 Results

The results of the permeability experiments are presented in this section. The results for each of the three apparatuses are discussed separately. However, it is attempted to allow as much mutual comparison as possible, by using either the same materials or similar process conditions.

4.4.1 Materials and Configurations

Five different fabrics were tested in total: three biaxial, a triaxial and a quadriaxial NCF. The three biaxial fabrics (B1, B2, B3) are the same as the fabrics discussed in chapter 2. The triaxial (T) and quadriaxial (Q) fabrics are from the same manufacturer as fabric B3: the only difference is the number of plies and their relative orientation. The properties of the fabrics are presented in table 4.4.

Table 4.4: *Properties of the five fabrics used for the measurements (B: biaxial, T: triaxial, Q: Quadriaxial).*

	B1	B2	B3	T	Q
manufacturer	Saertex	Saertex	Devold	Devold	Devold
areal density [kg m^{-2}]	0.322	0.329	0.534	0.801	1.068
fibre	Toray T700 50E	Toray T700 50E	Tenax HTS 5631	Tenax HTS 5631	Tenax HTS 5631
fibre count [-]	12K	24K	12K	12K	12K
orientation [^{o}]	± 45	0/90	± 45	45/90/-45	45/0/-45/90
stitch	PES	PES	PES	PES	PES
linear density[tex]	7.6	7.6	5	5	5
knit pattern	tricot	tricot/chain	chain	chain	chain
gauge [inch^{-1}]	5	5	5	5	5
stitch length [mm]	-	-	2.5	2.5	2.5

Different configurations of the materials were measured. The number of layers was varied for fabric B3 and the shear angle was varied for fabrics B1 and B2. An overview of which measurement was performed where is presented in table 4.5. The fabrics B3 and T were measured at different institutes allowing a direct comparison between the data.

Table 4.5: *Overview of the measurements that were carried out on the different fabrics at the different institutes. The first number indicates the number of layers, the second – between brackets – the number of repeated measurements. (γ: shear angle).*

	B1			B2			B3			T	Q
γ [°]	0	30	45	0	30	45	0	30	45	0	0
NLR							7(3)			5(3)	3(3)
KUL	1(4)	1(3)	1(3)	1(4)	1(3)	1(3)				5(3)	
UT							1(5)				
							2(3)				
							4(5)				

Polyol was used as a test fluid in all measurements. Polyol is the non–curing part of a polyurethane fast cast resin and is supplied by Axson (see appendix H.1 for the data sheet). Polyol is supplied with an additive to avoid moisture absorption by the Polyol. However, this additive consists of particles and disturbs the flow and consequently the permeability measurement. The additive has a higher density and sinks to the bottom of the storage container. Only pure Polyol was used in the measurements, either by using only the fluid in the upper part of the storage container, or by filtering the fluid.

Polyol itself is transparent and is invisible if injected in a carbon fibre preform. Therefore, a fluorescent (Ardrox BioPen p6f5, appendix H.2) was added to the Polyol for the measurements with the test rig of the KU Leuven. UV–lights were used as a light source and a box was placed on top of the mould to protect the environment of the set–up from the UV–radiation and to eliminate disturbances of the ambient light.

The viscosity of Polyol is temperature dependent. The viscosity was measured at the NLR with a plate–plate rheometer, using the oscillating mode (1.59 Hz) and a target strain of 0.375. Data on the viscosity measurements of Polyol is collected in appendix I. The viscosity of the Polyol–BioPen mixture was measured in addition and found to be rather insensitive for the mixing ratio. The viscosity was measured using a capillary viscometer (Schott Geräte, ref. no. 053 92, see appendix I). The time of usage of the mixture appeared to have a stronger effect than the mixing ratio. The increased viscosity may either be caused by water absorption by the Polyol, or by small particles (carbon 'dust') in the mixture from the experiments (the fluid was not filtered after being used). The mixture used in the experiments was: 1148.9 grams Polyol and 51.8 grams Ardrox BioPen, which is roughly 25:1 by volume.

4.4.2 In–Plane Measurements NLR

The NLR apparatus was introduced in section 4.1.1, table 4.2. The results acquired with this rig are presented here.
Race–tracking between the edge of the cavity and the preform inevitably occurs in a line injection set–up, since the edges of the fabric will show some damage such as raffling due to the cutting and handling. Race–tracking would not be as serious a problem if it did not result in a certain amount of 2D flow: The fluid starts impregnating the fabric from the side. Silicon straps are applied in the edge along the length of the cavity to avoid the race–tracking.
The RTM machine controls the fluid flow. Normally, a flow rate of approximately 15 $g{\cdot}min^{-1}$ is used for permeability measurements. This corresponds to a volumetric flow of approximately $0.27{\cdot}10^{-6}$ m^3 s^{-1}. The advantage of a constant flow rate is that the pressure at the beginning of the experiment is low, resulting in a relatively stable flow and little chance of fibre wash (fibres being pushed out of their position by the fluid pressure). The flow rate is measured by a flow meter. The disadvantage is a more complex control[5]. Consequently, the flow rate is not constant at the very beginning of the experiment. However, experiments show that the flow becomes stable within a short time (seconds) and can be fairly well controlled during the saturated flow.
The injection pressure increases gradually as the preform is wetted. The pressure reaches a constant value once the entire preform is wetted. A saturated flow regime is reached. The fluid is pumped through the preform for a certain time. The flow rate and pressure drop are derived from the measured data, partly using a visual interpretation of the data (to determine the moment in time at which the unsaturated permeability is calculated).
A typical graphical overview of the measurement is shown in figure 4.3. The injection pressure (P_{inj}, solid line), the pressures measured by the transducers (P_1, dashed line and P_2, dash dotted line) and the flow rate (dotted line) are plotted against the time. The results of the other measurements are presented in tabulated form in section J.1.

The point in time at which the unsaturated permeability is determined is the time at which the fluid arrives at the second pressure sensor (t_{unsat}). The signal of the sensor starts to rise at that point. A stationary flow is established once the pressures measured by both transducers reached their maximum value and remain constant. The start time of the stationary flow t_{sat} is indicated. The saturated permeability can be determined by taking the pressure drop ΔP_{sat} at any point in time between t_{sat} and the end of the measurement. Here the flow rate Φ and pressures drop ΔP_{sat} are averaged over the time span between t_{sat} and the end of the measurement.
Three configurations of NCFs of the same manufacturer (Devold) were measured: a biaxial, triaxial and quadriaxial fabric. The fibres and stitching (type and pattern) are equal for the three variants, the only difference is the number of plies and their

[5] In fact, the pressure is controlled based on the measured flow rate, such that the flow rate remains constant during the entire measurement. This can result in steep gradients in the applied pressure, especially in the first seconds of the measurement. Steep gradients complicate the control, since the pressure cannot be changed instantaneously, as is theoretically desired.

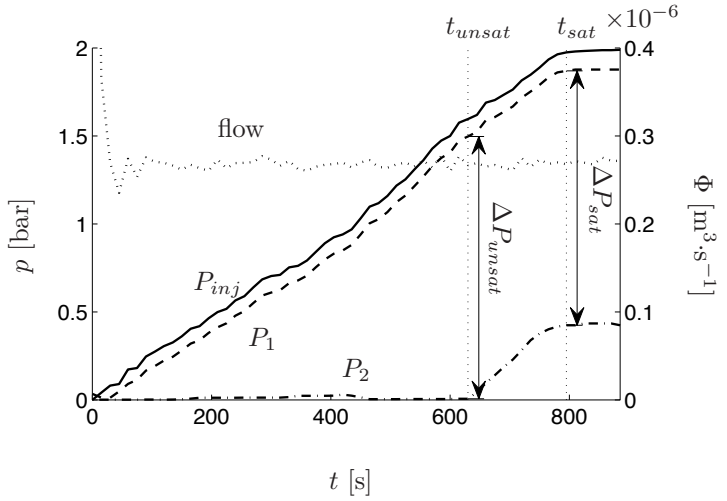

Figure 4.3: *Pressure and flow rate during the first measurement of the biaxial NCF (B3). The time step at which the unsaturated and saturated permeability are calculated are indicated by t_{unsat} and t_{sat} respectively.*

relative orientation. The biaxial NCF corresponds to the fabric B3 discussed in section 2.1. The material properties of the NCFs are listed in table 4.4. The areal density of an individual ply of the fabric equals 0.267 kg m^{-2}, resulting in the specified areal densities. The measurements were performed in the framework of the FALCOM project (G4RD–CT–00694). The data is presented in the technical project reports [32, 118].

The machine direction of the fabrics was rotated 0°, 45° and 90° with respect to the flow direction in the test rig. This results in the permeabilities K^0, K^{45} and K^{90} from which the complete permeability tensor can be constructed, if – and only if – the pressure gradient depends on the longitudinal coordinate of the mould and hence no flow in transverse direction occurs (see also the discussion on this in section 4.1.2).

Three measurements were performed on each configuration. It is preferable to perform a larger number of experiments, but the available budget and amount of material were limited in this case. The preform and fluid properties of each of the experiments are listed in table 4.6.

It was attempted to use an equal fibre content for all three fabrics (biaxial, triaxial and quadriaxial). This implies that the total number of plies should be equal, which is – given the layer thickness and the height of the cavity – impossible. Spacers were used to this end. The cavity height varies for the three types of NCF, but the fibre contents are nearly equal.

The results of the measurements are shown in figure 4.4. The averaged measured permeability (bars) and the maximum and minimum permeability (error bars) are depicted. Both the unsaturated and the saturated permeability are shown (light and dark gray fill respectively).

Table 4.6: *Preform and fluid properties for the measurements carried out at the NLR (θ: orientation of the preform; μ: viscosity; W: preform weight; V_f: fibre content; $\mathcal{A}$: cross–sectional area).*

NCF	θ [°]	μ [mPa·s]	layers		W [g]		V_f [%]	$\mathcal{A}$ [mm^2]
Biaxial	0	32.7	7	344.9	344.3	344.0	56.69	660
	45	31.5		344.1	344.1	341.9		
	90	32.7		344.9	344.3	344.0		
Triaxial	0	31.5	5	370.3	370.4	369.9	56.57	680
	45	31.5		369.8	370.9	370.3		
	90	31.5		370.0	371.1	371.6		
Quadriaxial	0	32.7	3	293.0	299.7	295.5	56.57	580
	45	31.5		298.1	298.1	298.1		
	90	32.7		297.6	297.8	297.4		

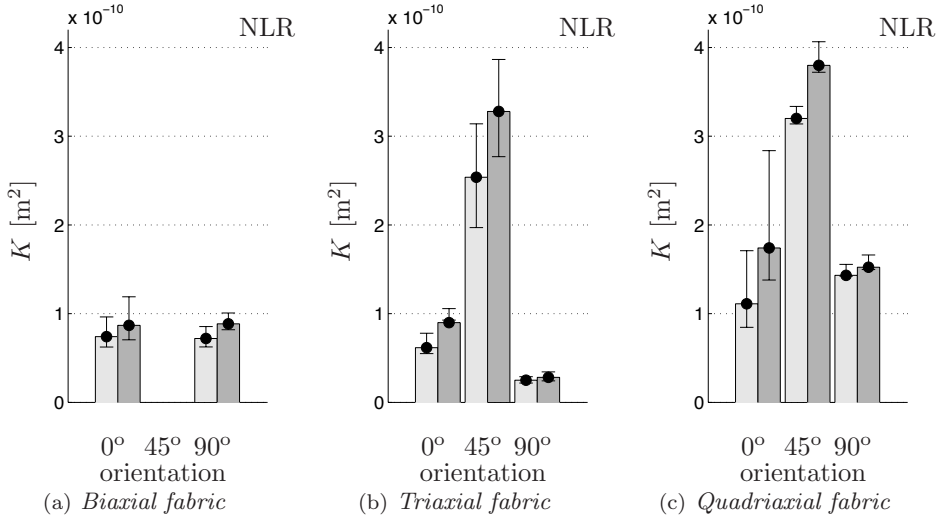

(a) *Biaxial fabric* (b) *Triaxial fabric* (c) *Quadriaxial fabric*

Figure 4.4: *Averaged measured permeability of the biaxial (B3), triaxial (T) and quadriaxial (Q) NCFs. The light gray bar refers to the unsaturated permeability, the dark gray to the saturated permeability. The error bars indicate the maximum and minimum permeability of the three measurements.*

The results of the measurement of K^{45} are omitted for the biaxial NCFs. The measured permeabilities are not accurate due to extremely low injection pressures for the given constant flow of 15 g·min^{-1}. The tabulated results (appendix J) do contain the measured values. The measured values for K^{45} of the triaxial and quadriaxial fabrics are also significantly higher than the measured K^0 and K^{90} permeabilities.

However, it was expected that the principal directions of the permeability tensor are oriented parallel (K_1) and perpendicular (K_2) to the cross direction of the material for the triaxial material (corresponding to the 90° layer), whereas the quadriaxial material was expected to be isotropic. The measured values contradict the expectations significantly. The principal directions are rotated roughly 25–40° with respect to the direction of K^0.

The permeability K^{45} can be estimated by assuming that the principal directions correspond with the directions of K^0 and K^{90} (see appendix F for a derivation):

$$K^{45} = \frac{\sqrt{2}K^0K^{90}}{\sqrt{(K^0)^2 + (K^{90})^2}}. \tag{4.23}$$

Let $K^0 = K_1$ and $K^{90} = K_2$. The expression (4.23) can be rewritten:

$$K^{45} = \frac{\alpha\sqrt{2}}{\sqrt{1+\alpha^2}}K^0. \tag{4.24}$$

with the anisotropy α as defined in (4.19). The permeability K^{45} equals K^0 if α equals 1, which is expected for isotropic material. Similarly, it shows that a high value of K^{45} (read: higher than K^0 or K^{90}) can only be found if the principal directions are rotated with respect to the directions of K^0 or K^{90}, since the fraction in (4.24) cannot exceed a value of one. Moreover, it is not always possible to fit an ellipse through the three measured permeabilities if K^{45} is large compared to K^0 and K^{90}. See appendix F for more details on this.

The model presented in chapter 3 does predict a strong anisotropy for the biaxial material. However, care should be taken, prior to drawing the conclusion that these measurements confirm the predicted strong anisotropy.

Firstly, the conclusion is too premature, since the network model does not predict a rotation of the principal axes. It predicts that the principal axes are aligned with the machine and cross direction. A rotation can only occur if the channels formed by the stitch thread on top and bottom of the fabric are taken into account *and* if the stitch pattern is not symmetric with respect to the machine direction (see section 3.4.2). The chain knit pattern is symmetric with respect to the machine direction and hence only affects the anisotropy and not the orientation of the principal directions.

Similarly, a rotation of the principal axes is not expected for a triaxial fabric with a chain knit pattern: the direction of K_1 corresponds to the direction of the fibres in the mid ply whereas the channels formed by the stitch threads are aligned in the machine direction. Flow enhancement in the machine direction due to the stitch threads therefore results in a weaker anisotropy, but not in a rotation of the principal directions. The principal directions are – and remain – oriented along and perpendicular to the machine direction.

A second reason to doubt the conclusion that the predicted anisotropy is confirmed by the measurements is that this amount of anisotropy is not reported by others, who measured the permeability of similar fabrics (for example [76, 162]. Even the results of the measurements performed by SiComp, carried out in the framework of the

FALCOM project on exactly the same material, do not indicate a strong anisotropy [32].
Finally, it must again be emphasised that the permeability tensor can only be derived from the measured data if the condition of a one–dimensional flow is satisfied (see section 4.1.2). It is strongly doubted that the pressure gradient is oriented in the longitudinal direction of the mould (the direction in which the fluid is assumed to flow), if an anisotropic material is placed in the mould such that neither of its principal directions is oriented along the longitudinal direction of the mould. This was clearly shown in a comparison between the permeability measurements of the NLR and those of SiComp [118]. However, it cannot entirely explain the extreme deviation in the results of the measurements of the NLR on the biaxial material. Firstly, since the SiComp test rig also employs a line injection strategy [30], but – as mentioned – does not confirm the extreme values. Moreover, the permeability of the 45° orientated preform deviates more for the biaxial preform than for the triaxial preform. The latter has a stronger anisotropy and hence a larger deviation of K^{45} is expected, but this was not measured.
It is concluded that the permeabilities of the preforms oriented in the 45° direction cannot be considered as accurate. A complete explanation for the deviations cannot be given, but (1) there is no confirmation of others who report similar large values for K^{45}, (2) the network model does not predict the orientation of the principal direction that accompanies the strong anisotropy, whereas (3) there are strong indications that a measurement of K^{45} does not provide a correct value of the permeability, since the pressure gradient is not parallel to the longitudinal direction of the mould. Additional measurements were performed on the triaxial fabric (T) using the test rig of the KU Leuven, which is based on a central injection strategy. The results of the comparison between the measurements are presented in section 4.4.3.

The anisotropy of the three fabrics B3, T and Q is depicted in figure 4.5. The anisotropy is based on the assumption that the principal directions correspond with the directions of K^0 and K^{90}, although the results of the experiment suggest that this is not the case. The anisotropy increases compared to the anisotropy calculated here, if the permeability K^{45} is higher than the permeabilities K^0 and K^{90}. The averaged, minimum and maximum anisotropies are found according to:

$$\begin{aligned} \bar{\alpha} &= \frac{\bar{K}^{90}}{\bar{K}^{0}}; \\ \alpha_{min} &= \frac{\min(K^{90})}{\max(K^{0})}; \\ \alpha_{max} &= \frac{\max(K^{90})}{\min(K^{0})}. \end{aligned} \tag{4.25}$$

Note that K^{θ} is an array with the permeability values of the three individual measurements of that configuration.
The averaged anisotropy is nearly equal to one for the biaxial fabric and relatively close to one for the quadriaxial fabric, but the variations are large (roughly 30–40%

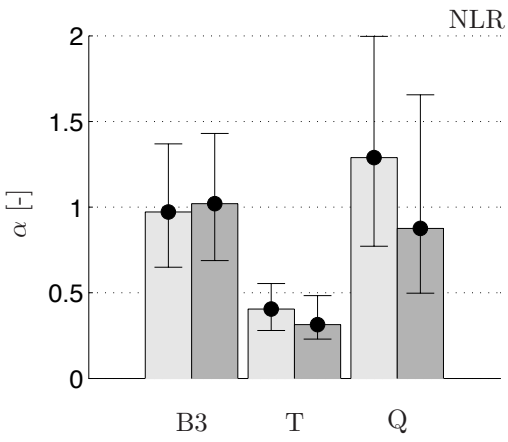

Figure 4.5: *The averaged anisotropy of the three fabrics based on the assumption that the principal directions correspond to the fabric directions K^0 and K^{90}. The light gray bar refers to the anisotropy of the unsaturated permeability, the dark gray to the anisotropy of the saturated permeability. The error bars indicate the maximum and minimum anisotropy.*

for the biaxial, 25–55% for the triaxial and 40–90% for the quadriaxial). The large amount of the scatter is a result of the absence of a correlation between the different measurements.

4.4.3 In–Plane Experiments KU Leuven

Two biaxial fabrics and one triaxial fabric were used for the measurements at the KU Leuven (see table 4.2 for a description of the test rig). Both biaxial fabrics are Saertex biaxial Non–Crimp Fabrics (B1 and B2), the triaxial fabric (T) is the Devold NCF that was also measured with the NLR test equipment. The specifications of the materials are presented in table 4.4. The measurements on fabric B1 and B2 were all performed in a single series of experiments, using the same batch of Polyol–Biopen mixture (see appendix H and appendix I for the data sheets and viscosity data respectively).

Preform Preparation for the Sheared Specimen The measurements on B1 and B2 were performed on single layer preforms in unsheared and 30° and 45° sheared configuration. All measurements were repeated three times, apart from the unsheared configurations that were repeated four times (see also table 4.5). The desired cavity could not be obtained with the available spacers. An aluminium sheet of 2mm thickness was placed at the bottom of the cavity. The plate had a hole in the centre, exactly above the injection point and was fixed with silicone gel to the lower mould.

The silicone was applied just around the injection point, preventing the fluid from flowing underneath the aluminium plate. An effective cavity thickness of 0.5mm was obtained for a 2.5mm spacer. The resulting fibre contents V_f, relative to the shear angle γ, are calculated using:

$$V_f = \frac{\rho_A}{h_c \rho \cos\gamma} \times 100\%, \tag{4.26}$$

with ρ and ρ_A the volumetric and areal densities (see table 4.4), respectively, and h_c the height of the cavity. The fibre contents are tabulated in table 4.7.

Table 4.7: *Preform and fluid properties for the measurements carried out at the KU Leuven (γ: shear angle; μ: viscosity; V_f: fibre content; h_c: cavity height).*

NCF	γ [°]	μ [mPa·s]	layers	V_f [%]	h_c [mm]
B1	0	34.5	1	36.18	0.5
	30			41.78	
	45			51.17	
B2	0	34.5	1	36.97	0.5
	30			42.68	
	45			52.28	
T	0	34.5	5	56.25	4

The fibre contents of the unsheared biaxial preforms were relatively low. A higher and equal fibre content for all preforms was preferred, but this was not possible with the available set of spacers. Therefore, it was opted to perform all measurements using the same spacers, *id est* no changes to the test rig were made between the different measurements. Hence, the measuring conditions were as constant as possible.
The shear was applied using a trellis frame. The shear method is similar to the method described in section 2.3.3. The size of the trellis frame was large enough to make a rectangular preform of 500×300mm^2 (size of the cavity). SICOMET© type 85 glue was applied near the edge of the specimen to maintain the shear angle after releasing the fabric from the trellis frame. The specimen was then cut at the final size through the glued layer. Cutting with a knife through the fibres that are impregnated by the glue rather than through the dry fibres causes less damage to the specimen, since the freedom to slide under the knife is reduced. The specimen preparation is shown schematically in figure 4.6.
A hole of 10mm diameter was punched in the centre of the preforms, right above the injection point. The fluid wets the fabric purely in the in–plane direction in this way. However, small deviations in the initial preform internal geometry, or in the positioning of the hole with respect to the injection point can cause relatively large errors.

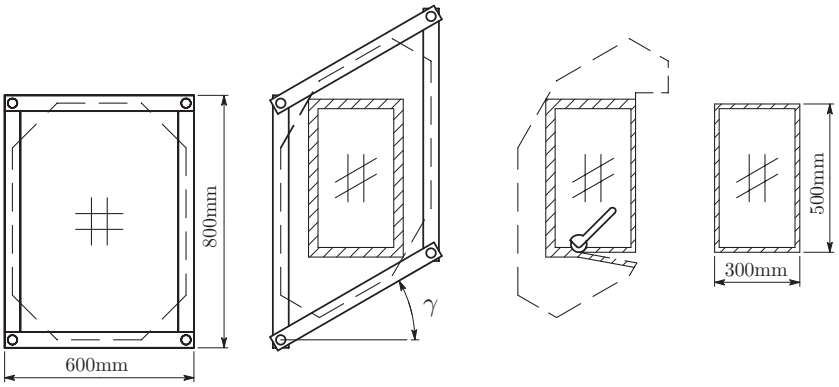

Figure 4.6: *Specimen preparation for the sheared configurations using the trellis frame and* SICOMET© *glue (dashed area).*

Process Conditions and Data Acquisition The RTM machine of the KU Leuven is pressure controlled and is also used to invert the injection process. A vacuum is created in the resin reservoir and the (majority of the) Polyol is sucked back into it for re–use.

An injection pressure of roughly 1 bar was initially used for the biaxial fabrics, but appeared to be relatively high. A lower injection pressure of 0.5 bar was used to slow down the injection process. The measured injection pressures are presented in table J.2.

The pressure near the inlet was measured by a Jumo type 4 pressure transducer. The output of the transducer is a 0 to 10 volts signal, which corresponds to -1 to 9 bars

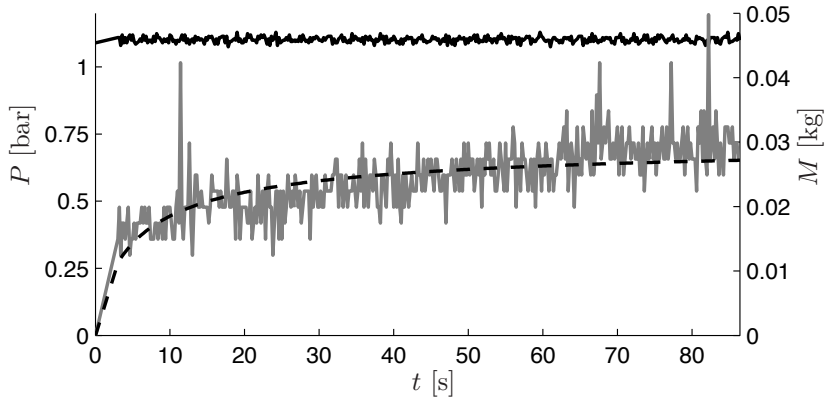

Figure 4.7: *Pressure (solid black line) and mass of the fluid reservoir (gray line) versus time during the injection of the first measurement on B1 (relaxed configuration). The dashed line indicates the fitted mass function.*

pressure, relative to the ambient pressure. The mass flow was measured by weighing the resin reservoir. The weight was monitored using a load cell. The signal of the load cell (1kN) was amplified such that 10V corresponded to 50N. A digital video camera was mounted above the centre of the tool to capture the flow front position during the injection.
The measured injection pressure and weight reduction of the fluid reservoir of the first measurement on B1 in relaxed configuration is shown in figure 4.7. The results of the other measurements were similar.
The mass reduction in time was converted to a volumetric flow rate employing a power law function. The power law function has no direct physical meaning, but the change of mass cannot be explicitly converted to a flow rate as it can be in the scase of a line injection (see section 4.3.1). The applied formulae read:

$$\begin{aligned} \frac{M(t) - M_0}{M_{max} - M(t)} &= \left(\frac{t}{t^*}\right)^a; \\ M(t) &= \frac{M_0 + M_{max}\left(\frac{t}{t^*}\right)^a}{1 + \left(\frac{t}{t^*}\right)^a}; \\ \frac{\mathrm{d}M(t)}{\mathrm{d}t} &= \frac{(M_{max} - M_0)\left(\frac{t}{t^*}\right)^a a}{t\left(1 + \left(\frac{t}{t^*}\right)^a\right)^2} = \Phi_M = \rho\Phi. \end{aligned} \tag{4.27}$$

The parameter M_0 was set to 0, since the injected mass at $t = 0$ equals 0 kg. The parameters t^* and a were free and solved iteratively employing the minimisation algorithm. The parameter M_{max} was set to the averaged value of the last ten data points. No consistent trend in the fitted parameters was found. The values of the fit parameters for all measurements are collected in table J.2.
The relatively large amount of scatter on the measurement is caused by the low ratio of the mass flow rate over the total weight of the resin reservoir. Better results are expected if the weight of the resin reservoir is not completely carried by the load cell. A smaller load cell can then be used, which is more suitable for the low mass flow rates here.

Flow Front Position The flow front positions were determined by analysing the images of the digital video camera (DV) recording the measurements. The amount of data is large (25 frames per second are made, a single measurement lasts roughly 30 to 200 seconds), limiting a manual analysis of the images. An algorithm was implemented in MATLAB© to analyse the flow front position and convert it into a permeability. The algorithm allows a significant increase in number of points per image and number of images that can be evaluated compared to a (time–consuming) manual analysis of the images.

Firstly, the images captured by the DV were converted to a series of uncompressed `TIFF` images. Only the first frame of each second was converted, to reduce the amount of data. The images were subsequently processed in PHOTOSHOP©. The contrast between the fluid and the fabric was increased. Moreover, the images were converted to an 8–bits gray scale `TIFF` format. The images were then analysed by the MATLAB© algorithm, which determined the location of the flow front.
The four images in figure 4.8 show how the image of the DV camera is converted via the image processing steps in PHOTOSHOP© and MATLAB©:

(a) Original image (in gray scale, in fact the DV image is in colour);
(b) 8–bits gray scale image after contrast was increased PHOTOSHOP©. This is the input for the algorithm implemented in MATLAB©.
(c) Image after the final filter step.
(d) Series of flow front position (circles) and fitted ellipse (solid line), based on the image presented in (c).

A number of additional corrections and conversions were applied to the obtained flow front coordinates from figure 4.8(d):

1. Correction for the camera position;
2. Correction for the pixel aspect ratio of the DV camera;
3. Conversion from pixels to millimetres.

Sub. 1:
The position of the camera is (generally) rotated with respect to the mould. The position (in Cartesian coordinates $\boldsymbol{x}$) of the camera can be expressed in spherical coordinates as:

$$\begin{aligned} x_1 &= r\cos\varphi_{sph}\cos\theta_{sph};\\ x_2 &= r\cos\varphi_{sph}\sin\theta_{sph};\\ x_3 &= r\sin\varphi_{sph}, \end{aligned} \tag{4.28}$$

where r is the distance between the mould and the camera, θ_{sph} the azimuth angle and φ_{sph} the elevation angle. $\theta_{sph} = 0$ and $\varphi_{sph} = \frac{\pi}{2}$ if the position of the camera is exactly aligned. However, this is generally not the case. The bars of the frame (see the black areas in figure 4.8(a)) were used to obtain the camera azimuth orientation with respect to the mould. The elevation angle cannot be obtained from this image but was assumed to be small. Hence, the error is small, since:

$$\sin\left(\tfrac{\pi}{2} + \delta_\varphi\right) \approx 1 - \frac{\delta_\varphi^2}{2}, \tag{4.29}$$

with δ_φ a small variation in the elevation angle.
Sub. 2:
The pixels of a DV video camera are rectangular. A width of 720 pixels on a DV camera correspond with 768 pixels on a normal computer screen.

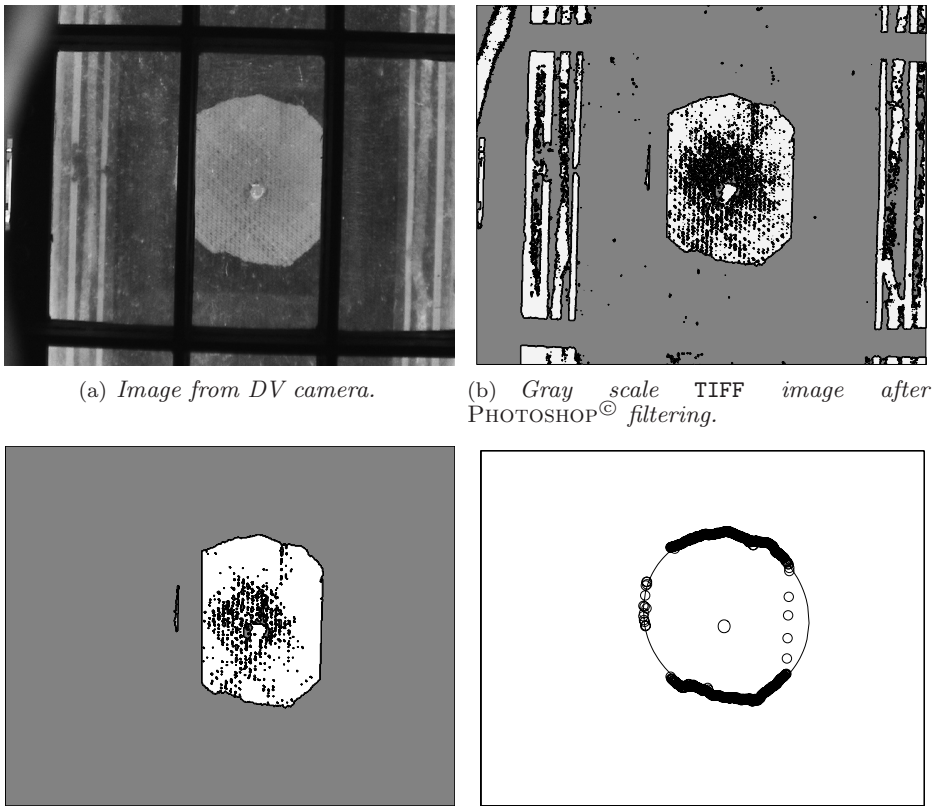

(a) *Image from DV camera.*

(b) *Gray scale* `TIFF` *image after* PHOTOSHOP© *filtering.*

(c) *Black and white image after* MATLAB© *filtering.*

(d) *Flow front positions and fitted ellipse.*

Figure 4.8: *Filter steps to convert the flow front at* $t = 10s$ *of original image (a) to a black and white image (b and c), used to determine the flow front position (d). The solid line in (d) is the ellipse fitted through the flow front positions.*

Sub. 3:
The width of the cavity on the image and the actual width of the cavity are used to convert the pixels to millimetres.

Image distortion was not accounted for. Distortion of the image can be caused by a misalignment of the camera, as discussed, but also by the shape of the lens. This distortion is equal for all images and can be quantified by shooting an image of a well-defined grid and comparing the image and the real grid coordinates. However, the distortion was assumed to be small here, since the deviation is generally related to the distance from the centre of the image. The majority of the measured points were lying relatively close to the centre of the image.

The measured flow front positions were used to fit ellipses through the data points

and calculate the permeability, employing the theory described in section 4.3.2. An example of the ellipses that were fitted through the data points is depicted in figure 4.9. The measured flow front positions of every fourth second of the measurement of fabric B1 in relaxed configuration are shown. The solid lines are the ellipses fit through the data points. The radii of the ellipses increase with increasing time, but the flow rate slows down (*id est* the area of the ellipses does not increase linearly). The injection pressure was constant, resulting in a decreasing pressure gradient. Consequently, the volumetric flow decreases and the flow front progression slows down.

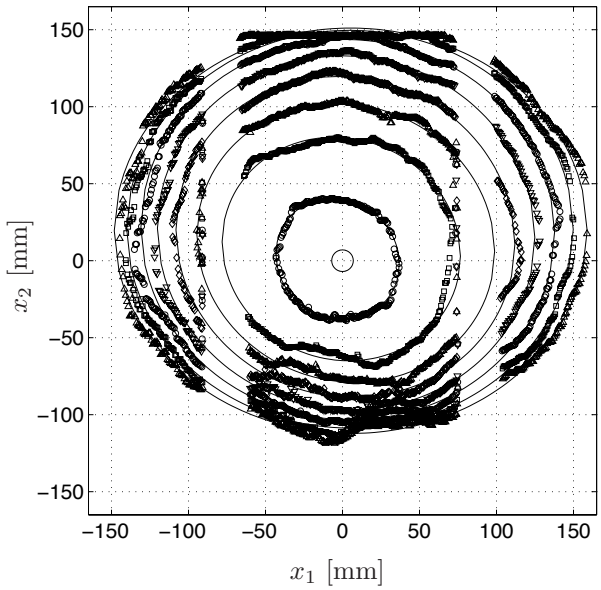

Figure 4.9: *The flow front positions at every fourth second of the measurement. An alternating series of five markers ('○', '□','△', '◇', ▽') is used for the different ellipses from the centre to the outer sides of the mould. Note the sections on which no data points are found, corresponding to the locations of the metal frame on top of the mould. (Fabric B1, relaxed configuration.)*

The number of flow front positions depends – evidently – on the size of the flow front: the larger the size, the larger the number of data points. However, there are sections without any data points. This is caused by the metal frame on top of the upper mould, which is clearly visible in figure 4.8(a). The flattening of the data points of the outer flow fronts on the top of figure 4.9 are also caused by sections of the metal frame. This is a known problem of visual tracking of the flow front, since transparent moulds generally do not possess sufficient stiffness. Metal frames are placed on top of the transparent mould to acquire sufficient stiffness, hence partly obstructing the visual determination of the flow front position. However, the algorithm to convert the image of the DV camera to flow front positions determines the flow front position

at a large number of points (the ellipse in figure 4.8(d) is based on roughly 200 flow front positions). Consequently, missing flow front positions, or even erroneous flow front positions, have a minor effect on the dimensions of the ellipse that is fitted on the data.
It was attempted to relate the increasing size of the ellipses to the flow rate derived via the measured mass flow rate. The area $\mathcal{A}_E$ of an ellipse equals:

$$\mathcal{A}_E = \pi r_1 r_2, \tag{4.30}$$

with r_1 and r_2 the major and minor radii of the ellipse. Multiplying the area with the height of the cavity and the fibre content, results in the amount of fluid present in the fabric. The flow rate was estimated by analysing the increase of amount of fluid estimated by the flow front ellipses at different points in time. The obtained flow rate was compared to the flow rate estimated using (4.27). However, it appeared to be impossible to obtain a descend fit between both estimations, mainly due to the large amount of scatter on the measurement of the mass, but also due to the absence of a proper synchronisation between the mass measurement and the DV images. It is expected and confirmed by the measurements with the UT test rig (section 4.4.4), that a smaller load cell provides a more accurate measurement of the mass flow rate.

Permeability Values of Biaxial, Sheared NCF The function $F(\xi, \eta)$, equation (4.20), versus time is depicted in figure 4.10. The function values of $F(\xi, \eta)$ in both elliptical coordinates defined in (4.21) (□ and ◊ respectively) are calculated, again for fabric B1 in relaxed configuration.

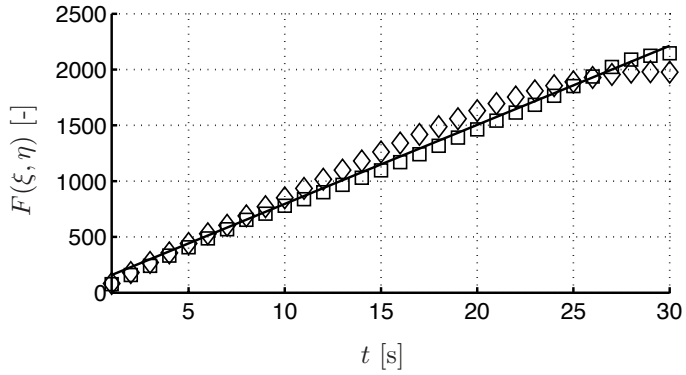

Figure 4.10: *The function $F(\xi, \eta)$ versus the time. □; first elliptical coordinate, ◊: second elliptical coordinate. (Fabric B1, relaxed configuration).*

The value of the elliptical extents should lie on a straight line according to the theory. The solid line is a fitted line through the data points. The fitted line does not cross the origin of the coordinate system. This indicates an unstable flow in the first seconds of the measurement (the data points near $t = 0$ are closer to zero than the fitted

line), possibly combined with a synchronisation error: $t = 0$ can deviate slightly from the actual start of the impregnation (1/25 second, due to the frame rate of the DV camera, $t = 0$ is the time of the first image at which the flow front was visible). The permeability is proportional to the slope of the line (see section 4.3.2, equation (4.22)).
The results of the measurements on the fabric B1 and B2 for relaxed configurations and 30° and 45° sheared configurations are presented in the figures 4.11 and 4.12.

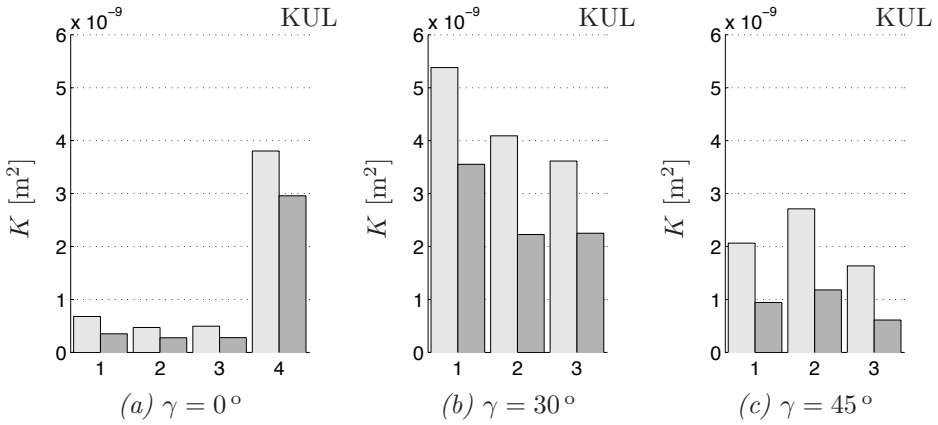

Figure 4.11: *Measured permeabilities of fabric B1 in relaxed and 30° and 45° sheared configuration. The light gray bar refers to the principal permeability K_1, the dark gray to the principal permeability K_2.*

The first three measurements of the permeability of both fabrics in relaxed configuration (figure 4.11(a) and figure 4.12(a)) show a significant lower permeability. Moreover, a large difference between major and minor principal permeabilities (light gray and dark gray bar respectively) is observed for fabric B2. An additional measurement on the relaxed configurations was performed at the end of the series of measurements for each of the fabrics. The results of the fourth measurement do not show a strong anisotropy and the permeability is roughly 3 times as high as the major principal permeability of the first three experiments.
The origin of the deviations between the measurements is unknown. However, the mould was slightly changed between the experiments: the 2mm spacer combined with a 1.5mm plate inside the cavity were used for the first three measurements, whereas a 2.5mm spacer and a 2mm plate were used for all other experiments. A cavity of 0.5mm should result in both cases, but it is not unlikely that a small difference has occurred. An estimate of the effect of a deviation in the cavity height is made using the Kozeny–Carman relation [16–18] between the permeability and the fibre content:

$$K = \frac{r_f^2}{8K_0} \frac{(1 - V_f)^3}{V_f^2}, \tag{4.31}$$

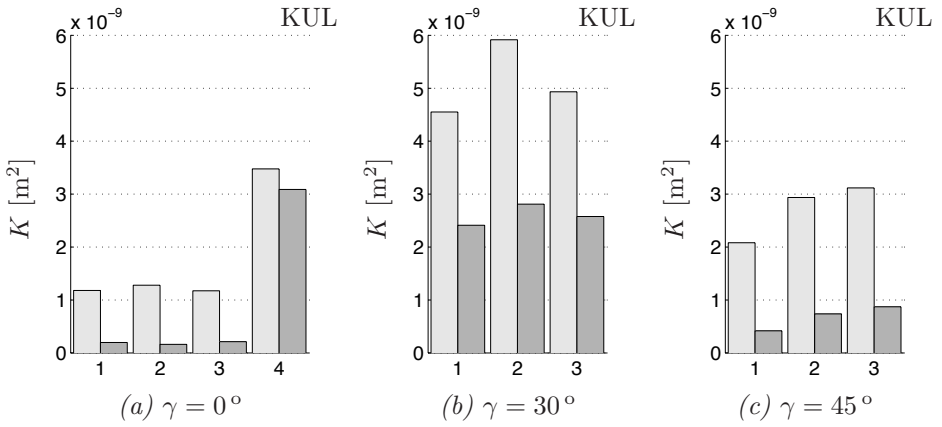

Figure 4.12: *Measured permeabilities of fabric B2 in relaxed and 30° and 45° sheared configuration. The light gray bar refers to the principal permeability K_1, the dark gray to the principal permeability K_2.*

with K_0 as empirical constants and r_f the radius of a filament. The fibre content $V_{f,2}$ for a permeability $K^{(2)}$ that is 3 times lower than the permeability $K^{(1)}$ at $V_{f,1} = 0.36$ is found by solving:

$$K^{(1)} \frac{V_{f,1}^2}{(1 - V_{f,1})^3} = K^{(2)} \frac{V_{f,2}^2}{(1 - V_{f,2})^3}. \tag{4.32}$$

A fibre content of roughly 47% is estimated. The cavity height to obtain this fibre content is slightly less than 0.4mm, a deviation of more than 20% of the intended cavity height. However, the strong anisotropy is not explained. Hence, the difference cannot be explained by a deviation in the actual cavity height only. An explanation for the anisotropy could not be found. Again, the conclusion could be drawn that the measured anisotropy confirms the predictions of the network (see section 4.4.2). However, the results of the sheared configurations do not confirm this anisotropy.
The results of the first three measurements are considered to be erroneous, although a good explanation of the deviations cannot be found. The fourth measurements were done using exactly the same spacer and spacer plate as used for the measurements on the sheared configurations. The permeabilities of the fourth measurements are more consistent with the permeabilities of the sheared configurations (figure 4.11(b)&(c) and figure 4.12(b)&(c)), which confirms the assumption that the first three measurements should be discarded.

The permeabilities of the sheared configurations were compared to the results presented by Endruweit and Ermanni [146] and those presented by Smith *et al.* [163]. The experimental results and predicted permeabilities initially show an increase of the permeability in the first principal direction, followed by a decrease of the permeability for larger shear angles (according to the theory presented by Advani [16]). The

location of the maximum value of the permeability in the first principal direction (see figure 4.13 for the definition of the directions) depends on the geometry parameters used by the authors: Endruweit and Ermanni use the ratio of the fibre radius and the dimensions of the unit cell that they use, whereas Smith *et al.* use a parameter based on the Kozeny–Carman equation.

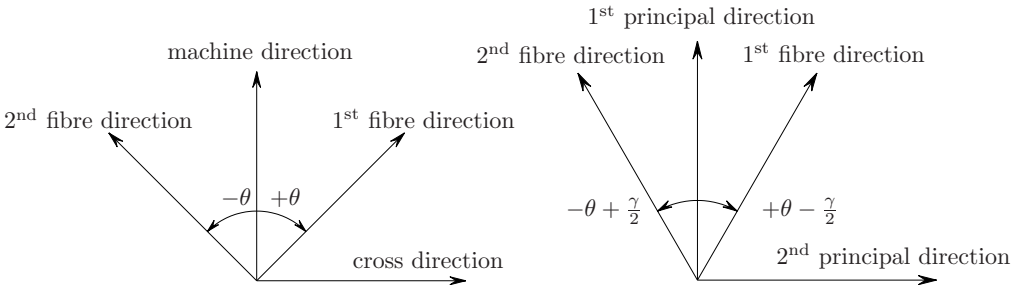

(a) *Relaxed configuration.* (b) *Sheared configuration.*

Figure 4.13: *Relaxed and sheared configuration of a ±θ fabric. The applied shear angle is γ. The principal directions are theoretically undetermined for an isotropic material, but assumed to correspond to the machine directions.*

The increase of the first principal permeability is explained by the reorientation of the fibres towards the first principal direction. This effect is counteracted by the increasing fibre content (inversely proportional to the cosine of the shear angle, see equation (4.26)). The relative effect of both effects is equal at a certain shear angle. The shear angle at which the first principal permeability is equal to the principal permeability of the unsheared configuration is different for each fabric.

The result of the measurements on fabrics B1 and B2 confirm the expected behaviour. The permeability in the first principal direction of the 30° sheared preforms is higher than the other two first principal permeabilities (light gray bars in the figures 4.11 and 4.12). The permeabilities in the second principal direction decrease (dark gray bars in the figures 4.11 and 4.12). The maximum permeability is reached at a higher shear angle than results in [146] and [163] indicate, although it should be noted that their measurements concerned different fabrics and consequently other geometry parameters are more appropriate here.

It was shown in chapter 2 that the width of the SYDs decreases from their initial width in relaxed configuration to a minimum width if shear is applied (see section 2.3.3). A decrease of the permeability in addition to the decrease due to the increasing fibre content is hence expected for shear angles up to the threshold shear angle (see equation (2.19)). This effect vanishes as the shear threshold angle is reached, since the width of the SYDs remains constant from this point. It was also indicated that two in–plane compression mechanisms were observed: closing of the SYDs (meso–level in–plane compression) and compaction of the fibre bundles (micro–level compression). It is not possible to quantify the contribution of these simultaneously occurring phenomena

based on the available experimental data. However, the results shown by Endruweit and Ermanni [146] indicate a difference in the quality of the fit between the measured data and their model for relatively low and relatively high shear angles. A further investigation on this topic is recommended, using the network model and an extended set of experimental data.

Anisotropy and Reorientation of Biaxial, Sheared NCF The anisotropy of the permeabilities for the different shear angles is depicted in figure 4.14. The bars indicate the averaged anisotropy of the flow front ellipses at all time–steps for each of the measurements. The error bars indicate the variation s, defined as (see also appendix B):

$$s = \frac{t_{0.95}(N-1)\sigma}{\sqrt{N}}, \tag{4.33}$$

with $t_{0.95}$ the student–t distribution with $N-1$ degrees of freedom and a 95% confidence interval, σ the estimated standard deviation and N the number of elements (here number of flow fronts) in the set. Note that the anisotropy is defined as the ratio of the minor permeability over the major permeability and is equal or lower than 1 as a result.

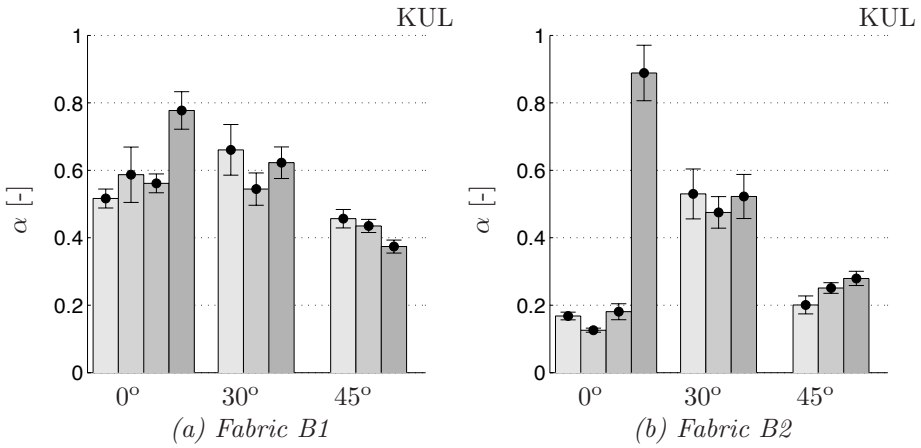

Figure 4.14: *The anisotropy α for the fabrics B1 and B2 for different shear angles. The error bars indicate the variation.*

The anisotropy of the first three measurements on both fabric B1 and B2 in relaxed configuration was considered to be erroneous, as discussed previously. The fourth measurement shows an averaged anisotropy of 0.8–0.9. Ideally seen, the anisotropy should be one, since the fabric is balanced. However, a small amount of anisotropy is likely to be observed in practice due to variations in the microstructure and an initial amount of misalignment of the fibres with respect to the original orientation ($\pm 45^{\circ}$

or $0^o/90^o$). The initial shear angle can to be up to 7-8^o for these types of fabrics [31, 83, 85]. However, the pattern of the stitch threads can also cause anisotropy of the permeability (see the discussion in section 3.4.2).
The anisotropy is weaker than expected based on the theory presented by Advani [16]. The theory assumes that the permeability of a number of stacked plies can be calculated by a superposition of the individual ply permeability tensors. It can be derived that the principal permeabilities for a biaxial fabric equal:

$$\begin{aligned} K_1 &= K_x \left(\cos^2\left(\theta+\tfrac{\gamma}{2}\right)+\sin^2\left(\theta-\tfrac{\gamma}{2}\right)\right)+K_y\left(\sin^2\left(\theta+\tfrac{\gamma}{2}\right)+\cos^2\left(\theta-\tfrac{\gamma}{2}\right)\right); \\ K_2 &= K_x \left(\sin^2\left(\theta+\tfrac{\gamma}{2}\right)+\cos^2\left(\theta-\tfrac{\gamma}{2}\right)\right)+K_y\left(\cos^2\left(\theta+\tfrac{\gamma}{2}\right)+\sin^2\left(\theta-\tfrac{\gamma}{2}\right)\right), \end{aligned} \tag{4.34}$$

with K_x and K_y the longitudinal and transverse permeability of the bundles in a single ply, θ the fibre orientation and γ the shear angle (see figure 4.13). The transverse bundle permeability is generally small compared to the longitudinal bundle permeability [148, 163]: $K_y \ll K_x$. The anisotropy can then be approximated by discarding the contribution of K_y:

$$\alpha = \frac{\sin^2\left(\theta+\frac{\gamma}{2}\right)+\cos^2\left(\theta-\frac{\gamma}{2}\right)}{\cos^2\left(\theta+\frac{\gamma}{2}\right)+\sin^2\left(\theta-\frac{\gamma}{2}\right)} \tag{4.35}$$

The expected anisotropies for 30^o and 45^o shear of the fabric equal 0.33 and 0.17 respectively. These values are substantially lower than the measured anisotropies. This is partly due to the neglect of K_y: the anisotropy increases to 0.42 and 0.27, respectively, for $K_y = 0.1K_x$. It is partly caused by the stitches. The shear is applied such that the stitch threads are not (or least) loaded in tension, see figure 4.15. As a result, the enclosed angle between the fibre families becomes larger in machine direction and smaller in cross direction. The first principle direction corresponds to the direction in which the enclosed angle is the smallest.
The anisotropy of fabric B1 is slightly weaker than that of fabric B2 for the sheared configurations, although the anisotropy in relaxed configuration is stronger. A possible explanation is found in the stitch patterns of the fabrics combined with the fibre orientations. Fabric B1 has a tricot warp knit stitch pattern and a $\pm 45^o$ orientation of the fibres. The stitch threads on the bottom are oriented in the machine direction. The stitch pattern on top shows a pattern as shown in figure 4.15(a). The main direction of the pattern is also oriented in the machine direction. Hence, the first principal direction is expected to be aligned with the machine direction. However, the first principal direction switches to the cross direction if the fabric is sheared. As a consequence, a weaker anisotropy is found (compared to the predictions according to Advani [16]), since the stitches still enhance the flow in the second principle direction. The anisotropy is expected to be stronger for fabric B2 than for fabric B1, since the flow in the direction of the stitches contributes to both principal directions, rather than only the cross direction (see figure 4.15(b)).

The orientation angle β of the flow front ellipses with respect to the machine direction is shown in figure 4.16. The principle axes are expected to be oriented in the

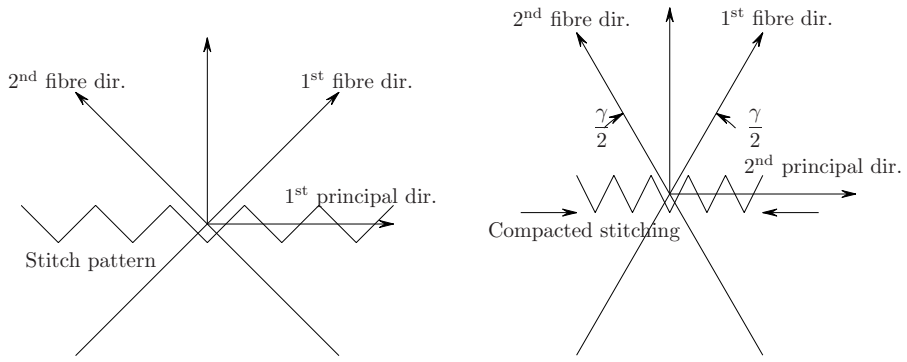

(a) *Tricot stitch in unsheared and sheared state*

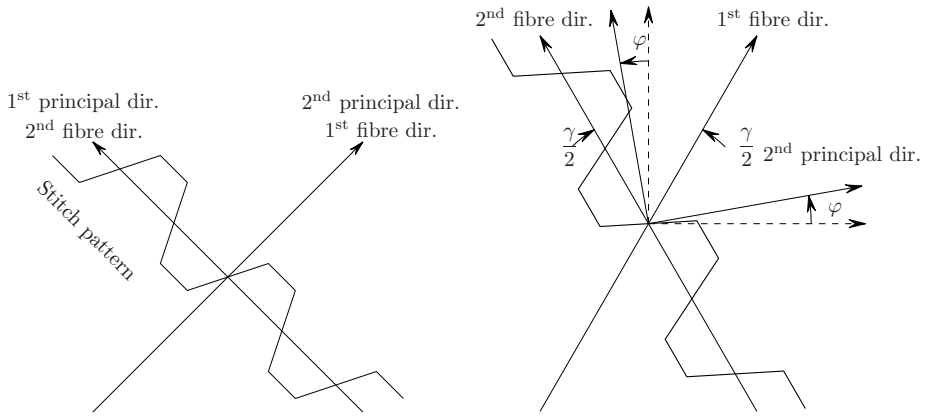

(b) *Tricot chain stitch in unsheared and sheared state*

Figure 4.15: *The effect of a tricot and tricot chain stitch pattern on the orientation of the principal directions, with shear angle γ and rotation of the principal directions φ.*

bisectrices of the directions of the two fibre families for balanced fabrics (see Lai and Young [151]). Consequently, the angle between the bisectrix and the machine direction equals half the shear angle. The stitches cause a slight unbalance in fabric B2, since the main direction of the stitch threads does not correspond with either of both principal directions. The angle φ in figure 4.15(b) indicates the rotation of the principal direction relative to the bisectrices. It was therefore expected that the angle β is larger than half the shear angle. However, this is not evidently confirmed by the measured orientation of the ellipses.

Measurements on Triaxial NCF The permeability of the triaxial fabric was measured on a five–layer preform in unsheared configuration using a 4mm cavity,

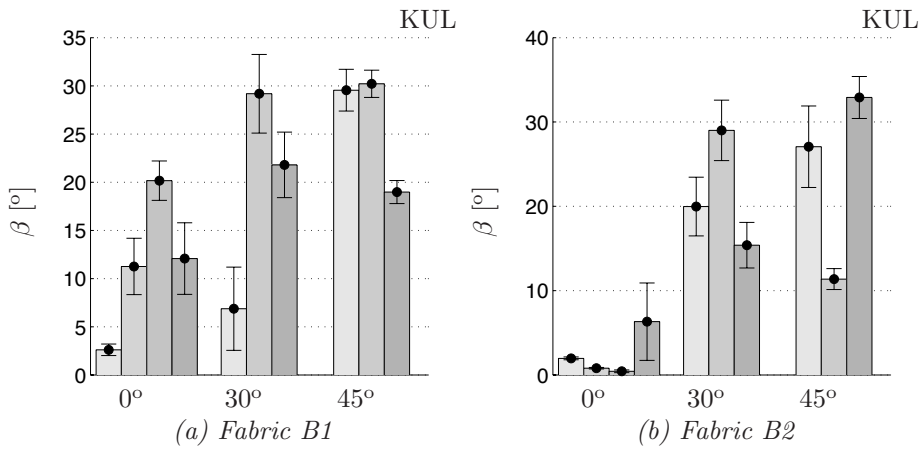

Figure 4.16: *The orientation angle β for the fabrics B1 and B2 for different shear angles. The error bars indicate the variation.*

resulting in a fibre content of 56.25%[6]. No additional spacers inside the mould cavity are used. The number of layers in the preform and the cavity height are equal to the number of layers and the cavity height specified in the measurement of the triaxial fabric, as discussed in section 4.4.2. A constant injection pressure of 1.5–2 bars was used for the measurements on the triaxial fabric (see table J.2 for a complete overview of the process settings).

The main difference between the test rigs of the NLR and the KU Leuven is the injection strategy: a central injection versus a line injection. The advantage of the central injection is that the complete in–plane permeability tensor is obtained in one single measurement. Another difference is that the KU Leuven rig employs a pressure controlled injection, whereas the NLR employs a flow rate controlled injection. This should not affect the measured permeability. The measurements carried out with the set-up of the KU Leuven are mainly used to verify the results of the K^{45} measurements, that raised some questions.

Three measurements were done. The measured data is treated in the same way as the data of the measurement on the triaxial fabrics. The permeabilities K, anisotropies α and ellipse orientations β that were obtained are depicted in figure 4.17. The light gray bars refer to the first principal permeability, the dark gray to the second principal permeability. The anisotropies and ellipse orientations are the averaged values of all ellipses in a single measurement.

The value of the permeability corresponds reasonably well with the values measured by the NLR. The first principal permeability is somewhat lower compared to the results of the NLR ($\approx 2.5 - 3.1 \times 10^{-11}\mathrm{m}^2$ versus $\approx 5.2 - 7.8 \times 10^{-11}\mathrm{m}^2$), whereas the

[6]The specifications of the manufacturer were used, instead of weighing the preform, as was done for the measurements at the NLR. This results in a small difference in the fibre contents: 56.25% versus 56.57%

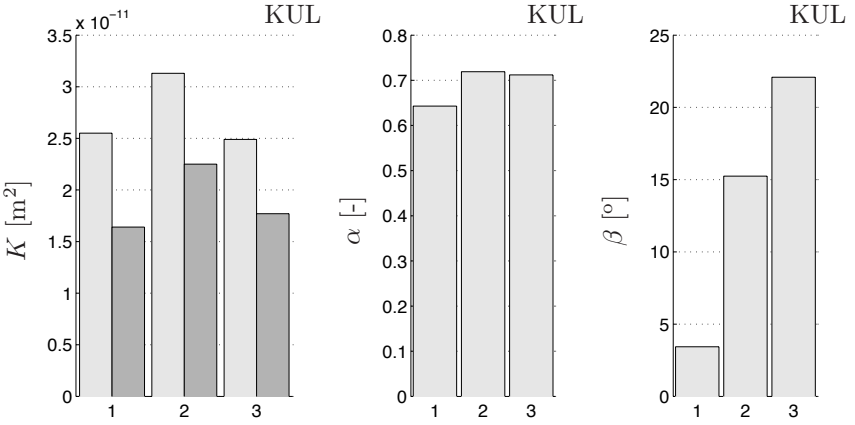

(a) *Principal permeabilities* (b) *Anisotropy* (c) *Ellipse orientation*

Figure 4.17: *The results of the measurements on the triaxial Non-Crimp Fabric. The light gray bars indicate the first principal permeability, the dark gray the second principal permeability.*

second principal permeabilities are closer to each other ($\approx 1.6 - 2.2 \times 10^{-11}\text{m}^2$ versus $\approx 2.1 - 2.9 \times 10^{-11}\text{m}^2$). Consequently, the anisotropy is weaker than predicted by the NLR (≈ 0.7 versus ≈ 0.5). More important to note is that there is no indication of a large value for $K^{(45)}$. The values measured by the NLR are most likely erroneous. The measurements of the biaxial and quadriaxial material also resulted in large values for K^{45}, for which no explanation or confirmation from other experiments were found.

4.4.4 In-Plane Experiments UT

The test rig developed at the University of Twente (see table 4.2) was used for a series of experiments on fabric B3. Measurements were performed on single and multi layer preforms (2 and 4 layers), as indicated in table 4.5. Only the permeability in machine direction (K^0) was measured. The aim is to verify if repeatable results can be obtained with the test rig and if the results obtained with the rig of the NLR can be reproduced.

Six pressure transducers are placed along the centre line of the lower part of the mould. The transducers are Kobold type 3251.075.192 sensor (closed membrane, hence also suitable for curing resin systems) and can measure pressure from 0 up to 10 bars relative to the atmospheric pressure. The output is a 0..10V signal.

The progress of the flow front is measured by the pressure transducers and by twelve flow front sensors, located on either side of each of the pressure transducers. The flow front sensors are based on the difference between the electrical resistance of air and the injected fluid. The fluid shortcuts an electrical circuit, resulting in a signal of the volt meter, as indicated in figure 4.18.

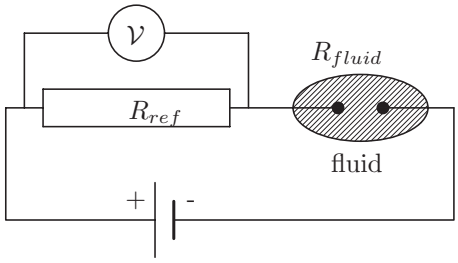

Figure 4.18: *Schematic drawing of a flow sensor circuit. The electrical circuit is shortcut by the fluid, resulting in a change in the voltage drop $\mathcal{V}$ measured over the reference resistance R_{ref}.*

The reference resistance has to be of the same order of magnitude as the resistance of the injected fluid. A wheatstone bridge is used, since it is an effective amplifier to measure small variations over high resistances, such as the resistance of the test fluid Polyol. The contact points of the sensor are embedded in polyamide. A similar system of fluid detection is used by Hoes *et al.* [25, 27]. Their equipment is only capable of measuring glass fibre preforms. Carbon fibres shortcut the circuit since they are conductive. The small change in resistance if the test fluid arrives at the sensor is consequently not detected by the sensors. Contact with the preform should therefore be avoided. A conical hole is drilled in the top of the sensor applied here. The sensor wires are placed slightly below the surface of the mould. A similar approach is adopted by Liu and Parnas [123]. The fluid can enter the small hole, but the fibres cannot. The conical shape of the hole also allows the plate to be released easily if a curing epoxy is used.

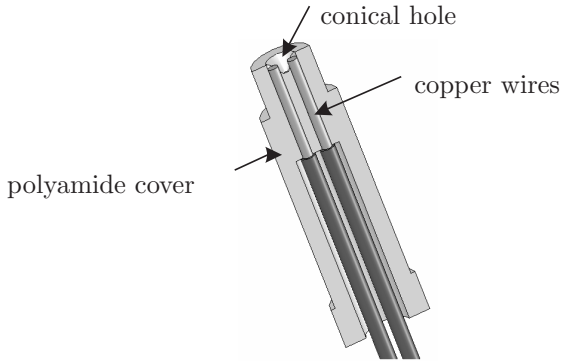

Figure 4.19: *Cross–sectional view of a flow sensor.*

The number of required channels of the data acquisition shuttle is reduced by connecting the flow front sensors in each row in parallel. A jump in the voltage occurs each time the fluid reaches the next sensor. Only two channels are required in this way.
The flow rate was measured by weighing the pressure vessel, similar to the method employed at the test rig of the KU Leuven (section 4.4.3). The pressure vessel was placed on a large cantilever construction. The weight of the vessel is compensated by a balance weight. A 100N load cell was used to measure the change of mass during the injection.
The resulting output is depicted in figure 4.20. The reduction of the mass of the pressure vessel is shown in the top graph. The pressures measured by the six transducers are plotted in the graph in the middle. The signal of the flow front sensors is shown in the lower graph. The data from the second measurement on a single layer NCF is used to generate the plot. The other measurements showed similar results.
The decrease of the weight of the pressure vessel corresponds to the weight of the fluid that is injected. Hence, a measure for the flow rate is obtained. Theoretically, the mass of the injected fluid as a function of the time is proportional to the square root of the time during the wetting stage. The flow rate is consequently proportional to the inverse of the square root of the time (see equations (4.14) and (4.15)). The flow rate becomes constant once a stationary flow is established in the preform (fully saturated preform). It was therefore expected that the increase of mass starts with a parabolic function, followed by a straight part. This can unfortunately not be confirmed by the measured mass as depicted in figure 4.20. A large amount of noise is observed at the beginning of the measurement. The noise is most likely caused by the relatively high flow rate in the first part of the injection. This cannot be avoided in a measurement using a constant injection pressure. All other results show a similar amount of noise at the start of the measurement. A rather constant mass flow rate was observed in the remainder of the measurement. This indicates a stationary flow in the saturated part of the preform. Consequently, the second part of the curve can be used to determine the saturated permeability.
The pressures measured by the six pressure transducers were used to measure the pressure drop over the preform, but they were also used to detect the arrival time of the fluid (see also section 4.4.2, where the same method is used, with only two transducers). The arrival of the flow front was also detected by the flow front sensors. The activation of a sensor results in a jump of the output signal, see figure 4.20. The fluid was expected to arrive at the same moment at the pressure transducers as the moment at which it arrives at the flow front sensors on either side of the pressure transducers, since a line injection is applied. Small deviations in the arrival time can occur due to local differences in the permeability. The actual flow front is never a perfectly straight line. However, large deviations in the arrival times indicate race–tracking or a pressure gradient that is not parallel to the longitudinal direction of the mould. This was elaborately discussed in section 4.1.2 and section 4.4.2.
The jumps in the two output signals of the flow front sensors were small (the order of tenths of volts on a 0–5V scale, with maximum amplification of the wheatstone

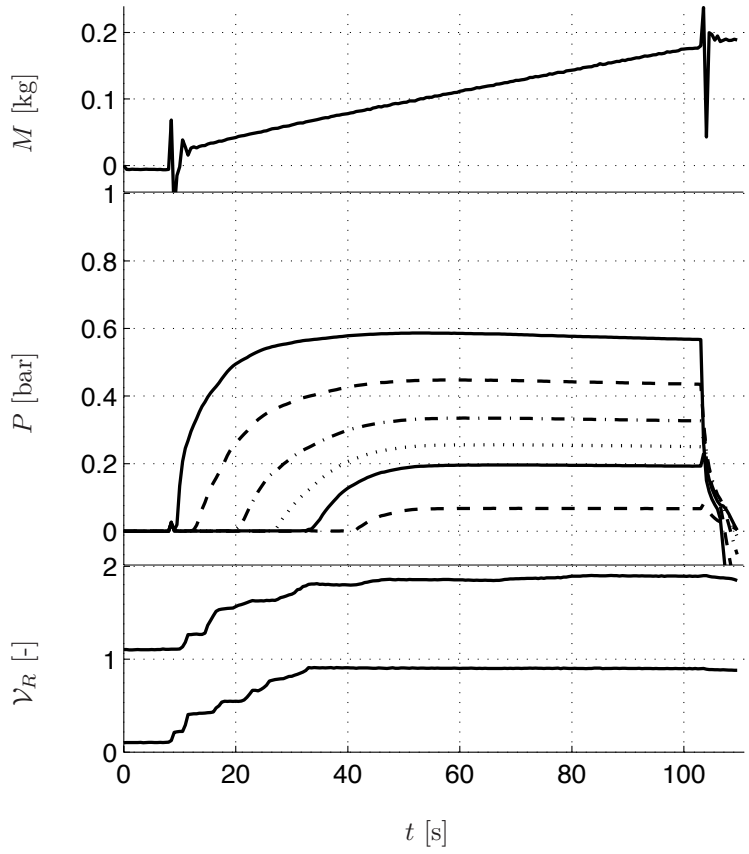

Figure 4.20: *Typical raw output data from a permeability measurement with the UT test rig. On top: the mass reduction of the pressure vessel; in the middle: pressures of the six pressure transducers; at the bottom: signal of the flow sensors. (Results from single layer NCF).*

bridge). The signals were scaled between 0 and 1 and 1 and 2 respectively[7], which facilitates mutual comparison of the data. Moreover, unintended and occasional shortcutting of the sensors by the carbon fibres was filtered out of the signal. A reasonable agreement was found for the signals shown in figure 4.20 and the fluid arrival times as measured by the pressure transducers. Unfortunately, the sensor signal was not always as undisturbed as in this case. Frequent shortcutting of the fibres occurred, resulting in an unusable output signal. Therefore, the signal of the flow sensors was not used to calculate the permeability. Instead, the signal of the pressure transducers was used to determine the flow front arrival times and subsequently the permeability of the preform.

[7]The actual size of the step is not relevant: it is only important to know when the sensor is activated.

A linear pressure drop was expected and hence the pressures measured by the transducers numbers 2 to 5 should lie on the line connecting the pressures measured by the first and last transducer, as depicted in figure 4.21(a). The graphs are based on the results of a measurement of a single layer fabric, but are representative for the other results.

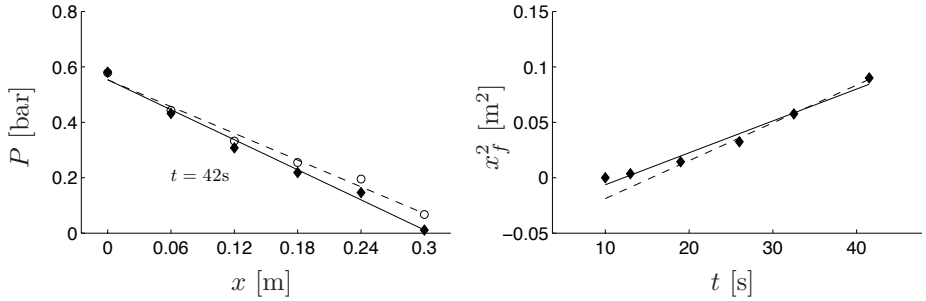

(a) *Pressure versus longitudinal coordinate.* (b) *Squared flow front position versus impregnation time.*

Figure 4.21: *(a): The pressure drop over the preform during unsaturated (⧫) and saturated (○) flow. The solid and dashed lines are fits through the data points of the unsaturated and saturated flow respectively. (b): The square of the flow front position in time. The solid line is a fit through all data points, the dashed line only takes the last four data points into account.*

The pressure drop was analysed at two instants: firstly, the moment at which the fluid reached the sixth and last pressure transducer (this time is indicated in the graph). A solid line is fit through the measured pressures, indicated by the black diamonds. Secondly, the pressure drop half way through the saturated stage was determined. The pressures reach a constant value if the preform is entirely saturated (stationary flow, horizontal lines in figure 4.20). The saturated stage is reached for most of the measurements. The open circles correspond to the measured pressures in the saturated stage, the dashed line is a fit through these data points.
The measured values are close to the fitted lines. Small deviations are explained by local inhomogeneities in the structure of the NCF, such as the variation in the internal structure as discussed in chapter 2. The deviations are consistent for the unsaturated and the saturated flow: a measured value is either lower than expected for both fits, or higher. Hence, the origin of the deviation is most likely found in variations in the preform material rather than in the apparatus.
The pressure drop for the saturated flow is lower than for the wetting flow. This implies that the saturated permeability is higher than the unsaturated permeability. This was also found in the experiments performed with the test rig of the NLR.

The squared flow front positions were expected to be linearly related to the impregnation time according to equation (4.5). A good agreement was found, as shown by the solid line in figure 4.21(b). The graph is representative for the other

results. A consistent deviation is observed in the first part. The deviation is expected to be due to instabilities in the flow in the first part of the impregnation. The pressure drop was high in the beginning, possibly causing some fibre wash or other unexpected phenomena. The dashed line was fitted on the last four flow front positions only. A better correlation between the data points and the fitted line was found when only the last four data points were taken into account. The permeabilities that were calculated from both fits, differ 10–20% from each other.

The saturated permeability was also measured. The measurement of the weight of the fluid container was much more accurate than for the measurements using the rig of the KU Leuven (apart from the instabilities measured in the first seconds). The smaller load cell (100N versus 1kN for the KU Leuven set–up) evidently provides better results. The volumetric flow rate was determined by fitting a straight line through the data points in the saturated region. The point in time at which the last pressure reached 80% of its maximum pressure was used as a starting point of the saturated region. The volumetric flow rate equals the slope of the line divided by the density of the fluid (see equations (4.13)–(4.15)).

The measured permeabilities are shown in figure 4.22. The permeability values are corrected for a fibre content of 56.69% using Kozeny–Carman's equation (4.31), since the fibre content was not constant for the different configurations. The fibre content equals the target fibre content in the measurements performed with the NLR test rig, thus allowing a mutual comparison between the measured permeabilities.

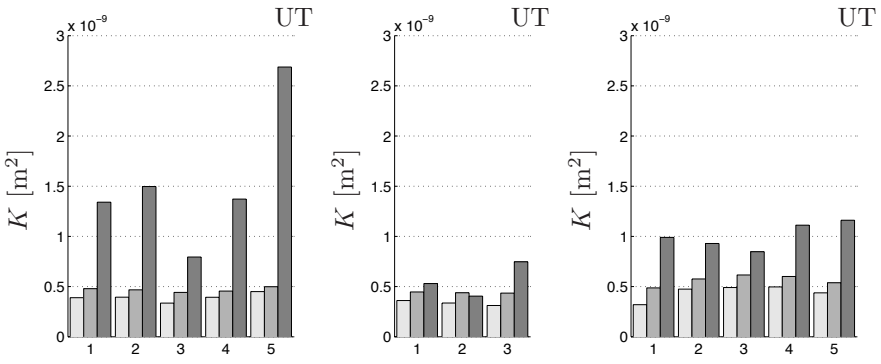

(a) *1 layer* (b) *2 layers* (c) *4 layers*

Figure 4.22: *Measured, normalised (un)saturated permeability values for the single, double and four layer preforms. The unsaturated permeability is based on all flow front positions (light gray bars) or on only the last four flow front positions (semi dark gray bars). The darkest bars indicate the saturated permeability.*

The repeatability of the results for the unsaturated permeability for each set was fairly good. The variation was small and well within the bounds of variation predicted by the network model presented in chapter 3. The differences between the permeability

of the single and multiple layer preforms are small and are not significant.
The saturated permeabilities show larger deviations than the unsaturated permeabilities. The saturated permeability of a single layer preform was significantly higher than the unsaturated permeability of a single layer preform. The variation was also larger. It is likely that edge effects have caused this larger deviations. The saturated permeability of the double layer preform was roughly the same as the saturated permeability. The differences are not significant. The results obtained with the test rig of the NLR also indicate a slightly, but not significantly, higher saturated permeability.
The saturated permeability of the four layer preforms was roughly 1.5–2 times the unsaturated permeability, significantly higher than the unsaturated permeability. Nesting is a possible cause, but generally nesting does not play a significant role for NCFs (see also section 2.5. The variation in the saturated permeability is not consistent with the variation in the unsaturated permeability: a higher unsaturated permeability was not leading to a higher saturated permeability. The origin of the deviations could not be identified.
The measured permeabilities were roughly 5 times as high as the permeability measured by the NLR, see figure 4.4. There is no explanation found for this deviation. The result obtained by SiComp [32] on the same fabrics indicate a lower permeability than measured by the NLR. It is stated in the report [32] that: "a comparison between the experiments [...] showed that it is almost impossible to compare the results due to the different test techniques that were used. Therefore, [...] it is very important to develop a standardised method and protocol for determining the permeability of a fibre reinforcement [...]". This conclusion is strongly confirmed by the measurements presented here, despite the good repeatability and the consistency of the measured data for multiple layer preforms.

4.5 Conclusions on the Permeability Measurements

A number of measurements was performed on different fabrics and at different institutes, using different test rigs. It was not only aimed to compare the experimental results with the models, but also to perform a mutual comparison between the experimental methods. Once again it should be noted that the comparison between the flow model and the experiments is yet only qualitative. The following conclusions are drawn:

- The measurements with the line injection permeability measuring device at the NLR on biaxial, triaxial and quadriaxial fabrics, show an anomalous permeability for 45° orientation (K^{45}). The permeability is significantly higher compared to the permeabilities in machine direction K^0 and cross direction K^{90}. The deviations are the largest for the biaxial fabric and the smallest for the quadriaxial fabric. The origin is unknown.

- The repeatability of the measurements is fairly good for all three test rigs. The variation in the permeability is relatively low. The ratio between the maximum and the minimum measured permeability was found to equal roughly 1.2–1.8

for the majority of the measurements. This is well within the limits resulting from the network permeability predictions (max. 2.5).

– The method to analyse the images from the flow front and subsequently calculate the permeability is found to perform well. The position of the flow front can be determined accurately and at a large number of points in time. The accuracy of the permeability calculated from the acquired data is improved. Moreover, the method is less time consuming than a manual analysis of the flow front.

- The saturated permeability is consistently higher than the unsaturated permeability, according to the results of the measurements at the NLR and the UT. However, the differences are not significant for the NLR results, due to the amount of variation on the measured values, whereas the difference is significant for the UT results. The ratio between the unsaturated and saturated permeability is not constant. There is no relation found between both.

– The permeability of fabric B3, measured with the UT test rig is roughly five times as high as the permeabilities measured with the test rig of the NLR for the same type of fabric and a comparable fibre content. The difference could not be explained.

– A good correspondence was found between the permeabilities of the triaxial NCF measured with the set–up of the NLR and with that of the KU Leuven. The permeability in the first principal direction is relatively low for the KU Leuven measurement compared to the NLR measurement (maximal factor 3 difference), but the differences between the second principal directions are not significant. However, the high value of the permeability for the 45° orientation (K^{45}), as measured by the NLR, could not be reproduced by the measurements at the KU Leuven. Consequently, the results are considered to be erroneous.

– The results of the measurements on the single layer biaxial NCFs in undeformed and sheared configuration correspond with the results presented in the literature. The initial increase and subsequent decrease of the first principal permeability for an increasing shear angle is explained by three simultaneously occurring phenomena:

  1. the alignment of the fibres in the flow direction (increase);
  2. an increase of the fibre content due to the shearing (decrease);
  3. the size of the SYDs, which decrease up to a shear angle of roughly 30° after which they remain constant (vanishing decrease).

  The last phenomenon follows from the geometrical model presented here and was not recognised by others.

– The anisotropy of the fabrics is found to deviate from the theoretically estimated values (based on the theory of superposition of ply permeabilities). The results of the NLR are close to the theoretical value on the average, but exhibit a large amount of scatter. The anisotropy of the triaxial material is slightly

underestimated. The results obtained at the KU Leuven indicate a higher degree of anisotropy than the theory predicts, for both undeformed and sheared fabrics. The deviations from the theory are explained by:

1. Initial misalignments that can be up to 7–8°;
2. Neglect of the transverse permeability of a ply;
3. Flow enhancement in the machine direction by the stitch threads;

– The large amount of scatter in the anisotropy of the permeability measured at the NLR is a result of the low correlation between the three individual measurements that are required to construct the complete permeability tensor in the case of a line injection measurement. This is a serious shortcoming of the line injection strategy.

– The high degree of anisotropy predicted by the model is not confirmed by the experiments. A more appropriate description of the permeability in the edge sections of the SYDs will improve the prediction of the model. It was not possible to quantify the anisotropy based on the available experimental data.

– The measured reorientation of the principal directions during shear could not be related to the theory found in the literature, nor be explained by the effect of the stitches.

– The permeability test rig developed at the UT proved to enable a relatively large number of measurements per unit of time. The reproducibility of the results is fairly good.

– The mass of the resin container was measured during the measurements with the rig of the KU Leuven and that of the UT. Comparison between the data revealed that the larger load cell used at the KU Leuven, suffered more from noise than the smaller one used at the UT. Consequently, the measured decrease of mass could not be related to progression of the flow front for the KU Leuven measurements, whereas it could for the measurements at the UT, although only in the saturated part of the measurement. The initial part of the curves of the UT measurements is strongly distorted due to vibrations in the first part of the experiment.

Chapter 5

Conclusions & Recommendations

The relation between the internal structure of a textile reinforcement and its permeability was investigated in this research project. A methodology was described to implement the variability, observed in the internal structure, in the prediction of the permeability of undeformed and sheared textile reinforcements. The methodology applies for the class of Non–Crimp Fabrics (NCF). Three main topics were presented:

1. A description of the internal geometry, including the variation and the effect of shear deformation;
2. A flow model based on the geometrical model;
3. A qualitative comparison between experimental permeability data, measured at three different institutes, and the results of the flow model.

The internal geometry of a Non–Crimp Fabric was analysed. It was found that the distortions, induced by the stitch threads piercing through the fabric, form meso–level gaps. The dimensions of these Stitch Yarn induced fibre Distortions (SYD) were found to vary. This variation was analysed in detail for unsheared and sheared fabrics. Consequently, the geometrical model can be linked to a fabric deformation model.
It was assumed that the permeability of the fabric is dominated by the flow behaviour in the SYDs, since the dimensions of the SYD are an order of magnitude larger than the free space between the filaments inside a fibre bundle.
A network of channels was defined, based on the dimensions of the SYDs and the stitch characteristics of the material. The variation on the dimensions of the SYDs was applied to the network, rather than to a single unit cell. This network, representing a biaxial $\pm 45^{o}$ fabric was analysed in detail. The conclusions that can be drawn are that:

1. The variations in the internal structure of a Non–Crimp Fabric have a significant effect on the macroscopic permeability of the fabric.

2. It is not sufficient to average over a sufficiently large number of single unit cells, such as a single SYD. A coupled network is required to obtain an accurate prediction of the permeability and its variation.

3. The spatial distribution of the dimensions of the SYDs in the network has a significant effect on the normalised permeability.

The permeabilities in the two principal directions were analysed for a network in which the variation on the SYD dimensions is randomly distributed over the network. The measured SYD dimensions were used as an input. The permeabilities were compared to the principal permeabilities of the idealised situation without a variation on the SYD dimensions. It was found that the averaged permeability does not only depend on the averaged SYD dimensions, but also on the variance of the set of widths. The permeability in the machine direction was found to be $\approx 85\%$ of the permeability in the idealised network. A single unit cell cannot capture this effect.
The difference is less in the second principal direction, since the permeability of the network with a variation in widths remains nearly equal to the permeability of a network without any variation on the averaged SYD dimensions.
Variations in the order of 5–10% were found for the randomly distributed SYD dimensions. These variations are reflected in a significant variation in the macroscopic permeability. Both variations are similar in magnitude.
Various spatial distributions of the SYD widths over the network were analysed. It was shown that a lower and upper bound can be derived. It appears that the amount of ordering in the spatial distribution determines how closely the lower and upper bounds are approximated. The difference between the lower and upper bounds is a factor of 2.5 for the SYD dimensions and variations that were used here.

The network model shows that the variations in the permeability up to a factor of 2.5 can be predicted for a biaxial NCF, depending on the spatial distribution of the SYD dimensions over the network. Hence, a significant amount of the measured differences in the permeability values can be explained from the variation in and distribution of the SYD dimensions.
However, the amount of variation on the experimentally determined permeability is not completely explained by the network model, as was shown by the measurements on different Non–Crimp Fabrics at different institutes. The main conclusion that can be drawn from the experimental data is that the line injection strategy can lead to erroneous results if the permeability is measured in a direction that does not correspond to the main direction. An unknown amount of transverse flow will result if the pressure gradient is not in one of the principal directions.

A number of suggestion arose from the above conclusions and the more detailed conclusions presented at the end of each chapter. The recommendations for further research are:

– Optimise the analysis of the dimensions of the SYDs. The main issue is automation of the analysis procedure which is currently done by hand. Various

technologies are available to be used, for example digital image analysis or textile porosity measurements.

- Establish a correlation between the length and the width of the SYD, as well as a correlation between the dimensions of neighbouring SYDs. This will improve the prediction of the channel permeabilities and it will provide information on the spatial distribution of the SYDs and consequently enhance the prediction of the permeability. In line with this, a parameter that indicates the level of order in the distribution is suggested to facilitate the link between the spatial distribution and the network permeability.
- Enhance the predictions of the anisotropy, by a better approximation of the flow resistance in the fabric around the edge sections. This implies the incorporation of the impregnation behaviour of the fibre bundles. The anisotropy of the currently implemented model is too high compared to data provided by the experiments.
- Develop the model such that a quantitative comparison with experimental data and other numerical codes can be made. The focus was on the qualitative side of the model, but the step to a qualitative model is required to use the model in a practical design or develop environment.
- Implement the stitch thread in the model. The permeability prediction is enhanced if the possibility to vary the stitch pattern is included.
- Develop a methodology to implement the interaction between different layers. This thesis has provided a number of suggestions to this end. This allows the analysis of multi layer effects. It is likely that the flow behaviour differs for multiple layer networks compared to a single layer network.
- Extend the model to a three dimensional model. The implementation of a model for the stitch thread as well as the interaction between different layers, allows the analysis of flow in the out–of–plane direction of the fabric. This is seen as an important extension of the model, since knowledge on the transverse permeability becomes more important due to the application of Resin Transfer Moulding processes for large, relatively thick composite components. Moreover, the textile reinforcement is often impregnated in transverse direction if vacuum driven processes, such as Resin Infusion under Flexible Tooling, are applied.
- The work on a permeability measuring device developed at the University should continue with improvements on the sensor system. The flow front sensor system appears to work reasonably, but the signal is weak and often shortcut by the carbon fibres. Improvements to increase the reliability of the sensor is strongly recommended. Furthermore, the test rig is a promising measuring device, since it is largely automated and allows relatively short cycle times of the measurements. Consequently, it is possible to perform a relatively large amount of measurements, which contributes to a better understanding of the variations in the measured permeabilities from an experimental point of view.

– Participation in a benchmark project is considered to be of utmost relevance. The industry, but also the research area, will benefit from a standardised measuring method, providing reliable data for production process simulation as well as model verification.

Bibliography

[1] H.G.S.J. Thuis. Falcom wp2 task plan. Technical Report FALCOM G4RD-CT-00694 - WP2, NLR, 2002.

[2] H.G.S.J. Thuis, J.F.M. Wiggenraad, and H.P.J. de Vries. Composite landing gear components made with RTM. In *Proceedings of the AHS International 60th Annual Forum and Technical Display*, 2004.

[3] H.G.S.J. Thuis. Samenwerkingsproject "RTM" - NLR - universiteit twente. Technical Report SC-2000-036, NLR, 2001.

[4] S. Lomov, A. Durie, I. Verpoest, R. Akkerman, and R. Loendersloot. Experimental and theoretical study of the permeability of (un)sheared, multilayer carbon fibre non-crimp fabrics. June 2002.

[5] R.S. Parnas. *Liquid Composite Molding*. Hanser, 2000.

[6] R. Akkerman. *Productietechniek, hoe maakt u het?* Universiteit Twente, 2004. oratie.

[7] K. Potter. *An Introduction to Composite Products*. Chapman & Hall, 1st edition, 1997.

[8] S.K. Mazumbar. *Composites Manufacturing - Materials, Product and Process Engineering*. CRC press, 1st edition, 2002.

[9] R.H.W. ten Thije, R. Loendersloot, and R. Akkerman. Material characterization for finite element simulation of draping with non-crimp fabrics. In *Proceedings of ESAFORM, Salerno, Italy*, pages 859–862, 2003.

[10] S.V. Lomov, M. Barburski, Tz. Stoilova, I. Verpoest, R. Akkerman, R. Loendersloot, and R.H.W. ten Thije. Carbon composites based on multiaxial multiply stitched preforms. part III: Biaxial tension, picture frame and compression tests of the preforms. *Composites Part A*, 36:1188–1206, 2005.

[11] A. Voskamp. Over–braided preforms for structural components. In *Proceedings of the International Symposium on Composite Manufacturing*, 2002. [CD–edition].

[12] J.F.A. Kessels and R. Akkerman. Prediction of the yarn trajectories on complex braided preforms. *Composites Part A*, 33(8):1073–1081, 2002.

[13] M. Bannister. Challenges for composite into the next millenium – a reinforcement perspective. *Composites Part A*, 32:901–910, 2001.

[14] C.D. Rudd, M.R. Turner, A.C. Long, and V. Middleton. Tow placement studies for liquid composite moulding. *Composites Part A*, 30:1105–1121, 1999.

[15] H. Darcy. *Les fontaines publiques de la Ville de Dyon*. Dalmont, Paris, 1856.

[16] S.G. Advani, M. v. Bruschke, and R.S. Parnas. *Flow and Rheology in Polymer Composites Manufacturing*, volume 10 of *Composite Materials Series*. Elsevier Science B.V., 1994. Chapter 12.

[17] J.G. Williams, C.E.M. Morris, and B.C. Ennis. Liquid flow through aligned fiber beds. *Polymer Engineering and Science*, 14(6):413–419, 1974.

[18] B.R. Gebart. Permeability of uni–directional reinforcements for RTM. *Journal of Composite Materials*, 26(8):1100–1133, 1992.

[19] R.C. Lam and J.L. Kardos. The permeability and compressibility of aligned and cross-plied carbon fibre beds during processing of composites. In *Proceedings of Annual Technical Conference – ANTEC*, pages 1408–1412, 1989.

[20] G.L. Batch, Y.-T Chen, and C.W. Macosko. Capillary impregnation of aligned fibrous beds: Experiments and model. *Journal of Reinforced Plastics and Composites*, 15:1027–1051, 1996.

[21] J.D. Muzzy, Y. Zhang, and J. Bradly. Flow of thermoplastics through fibre assemblies. In *Proceedings of FPCM-5, Plymouth*, pages 71–78, 1999.

[22] T.G. Gutowski, Z. Cai, S. Bauer, D. Boucher, J. Kingery, and S. Wineman. Consolidation experiments for laminate composites. *Journal of Composite Materials*, 21:650–669, 1987.

[23] P. Ferland, D. Guittard, and F. Trochu. Concurrent methods for permeability measurements in resin transfer molding. *Polymer Composites*, 17(1):149–158, 1996.

[24] E.B. Belov, S.V. Lomov, I. Verpoest, T. Peeters, D. Roose, R.S. Parnas, K. Hoes, and H. Sol. Modelling of permeability ot textile reinformcements: Lattice Boltzmann method. *Composites Science and Technology*, 64:1069–1080, 2004.

[25] K. Hoes, D. Dinescu, H. Sol, M. Vanheule, R.S. Parnas, Y. Luo, and I. Verpoest. New set-up for measurement of permeability properties of fibrous reinforcements for RTM. *Composites Part A*, 33:959–969, 2002.

[26] K. Hoes, D. Dinescu, M. Vanheule, H. Sol, R.S. Parnas, E. Belov, and S. Lomov. Statistical distribution of permeability values of different porous materials. In *Proceedings of ECCM-10, Brugge*, 2002. [CD-edition].

[27] K. Hoes. *Development of a New Sensor-based Set-up for Experimental Permeability Identification of Fibrous Media*. PhD thesis, Vrije Universiteit Brussel, 2003.

[28] K. Hoes, D. Dinescu, H. Sol, R.S. Parnas, and S. V. Lomov. Study of nesting induced scatter of permeability values in layered reinforcement fabrics. *Composites Part A*, 35:1407–1418, 2004.

[29] T.S. Lundström, R. Stenberg, R. Bergström, H. Partanen, and P.A. Birkeland. In-plane permeability measurements: Stability, repeatability and reproducibility. *Proceedings of ICCM-12*, 1998.

[30] T.S. Lundström, B.R Gebart, and E. Sandlund. In-plane permeability measurements on fiber reinforcements by the multi cavity parallel flow technique. *Polymer Composites*, 20(1):146–154, 1999.

[31] A. Endruweit, A.C. Long, F. Robitaille, and C.D. Rudd. Influence of stochastic fibre angle variations on the permeability of bi–directional textile fabrics. *Composites Part A*, 37:122–132, 2006.

[32] H.G.S.J. Thuis. Measurement of permeability for different non-crimped fabrics. Technical Report FALCOM G4RD-CT-00694 - WP2.1.2, NLR, 2002.

[33] T.S. Lundström, V. Frishfelds, and A. Jakovics. A statistical approach to permeability of clustered fibre reinforcements. *Journal of Composite Materials*, 38(13):1137–1149, 2004.

[34] S.V. Lomov, G. Huysmans, Y. Luo, R.S. Parnas, A. Prodromou, I. Verpoest, and F.R Phelan. Textile composites: Modelling strategies. *Composites Part A*, 32:1379–1394, 2001.

[35] S.V. Lomov, G. Huysmans, and I. Verpoest. Hierarchy of textile structures and arxhitectures of fabric geometry models. *Textile Research Journal*, 71(6):534–543, 2001.

[36] S.V. Lomov, T. Truong Chi, I. Verpoest, T. Peeters, D. Roose, P. Boisse, and A. Gasser. Mathematical modelling of internal geometry and deformability of woven preforms. *International Journal of Forming Processes*, 6:413–442, 2003.

[37] I. Verpoest and S.V. Lomov. Virtual textile composites software WiseTex: Integration with micro-mechanical, permeability and structural analysis. *Composites Science and Technology*, 65:2563–2574, 2005.

[38] A.C. Long, F. Robitaille, C.D. Rudd, and I.A. Jones. Modelling strategies for textile composites. In *Proceedings of ICCM-14 Conference, San Diego, USA*, 2004. [CD-Edition].

[39] F. Robitaille, A. Long, M. Sherburn, C.C. Wong, and C. Rudd. Predictive modelling of processing and performance properties of textile composite unit cells: Current status and perspectives. In *Proceedings of ECCM-11 Conference, Rhodos, Greece*, pages –, 2004. [CD-Edition].

[40] J.-F. Delerue, S.V. Lomov, R.S. Parnas, I. Verpoest, and M. Wevers. Pore network modelling of permeability for textile reinforcements. *Polymer Composites*, 24(3):344–357, 2003.

[41] F. Robitaille, C.C. Wong, A.C. Long, and C.D. Rudd. Systematic predictive permeability modelling using commercial CFD and dedicated calculation method. In *Proceedings of ICCM-14 Conference, San Diego, USA*, pages –, 2004. [CD-Edition].

[42] C.C. Wong, F. Robitaille, A.C. Long, and C.D. Rudd. Prediction of the effects of fiber architecture on permeability using the stream–surface method. In *Proceedings of FPCM-7, Newark Delaware*, pages 393–398, 2004.

[43] www.tecabs.org. Website tecabs project. viewed January 2006.

[44] A.C. Long, C.D. Rudd, M. Blagdon, and P. Smith. Characterizing the processing and performance of aligned reinforcements during preform manufacture. *Composites, Part A*, 27:247–253, 1996.

[45] A.C. Long, C.D. Rudd, M. Blagdon, K.N. Kendall, and M.Y Demeri. Simulation and measurement of reinforcement deformation during preform manufacture. *Polymer & Polymer Composites*, 4(5):335–341, 1996.

[46] A.C. Long, B.J. Souter, and F. Robitaille. Mechanical modeling of in-plane shear and draping for woven and non-crimp reinforcements. *Journal of Thermoplastic Composite Materials*, 14:316–326, 2001.

[47] P. Šimáček and S.G. Advani. Permeability model for a woven fabric. *Polymer Composites*, 17(6):887–899, 1996.

[48] F.R. Phelan jr and G. Wise. Analysis of transverse flow in aligned fibrous porous media. *Composites Part A*, 27(1):25–34, 1996.

[49] C. Binétruy and J. Pabiot. Effects of fabric architectural heterogenities on effective and saturated permeabilities in RTM. *Proceedings of ICCM-12*, 1998.

[50] C. Binétruy, B. Hilaire, and J. Pabiot. The interactions between flows occuring inside and outside fabric tows during RTM. *Composites Science and Technology*, 57:587–596, 1997.

[51] E.A.D. Lamers. *Shape Distortins in Fabric Reinforced Composite Products due to Processing Induced Fibre Reorientation*. PhD thesis, University of Twente, April 2004.

[52] M.L. Diallo, R. Gauvin, and F. Trochu. Key factors affecting the permeability measurements in continuous fiber reinforcements. *Proceedings of ICCM-11*, 1997.

[53] S.V. Lomov, I. Verpoest, T. Peeters, D. Roose, and M. Zako. Nesting in textile laminates: Geometrical modelling of the laminate. *Composites Science and Technology*, 63(7):993–1007, 2003.

[54] T.S. Lundström and B.R. Gebart. Effect of perturbation of fibre architecture on permeability inside fibre tows. *Journal of Composite Materials*, 29(4):424–443, 1995.

[55] R. Loendersloot and R. Akkerman. A least square approximation of annular flow. In *Proceedings of FPCM-6, Auckland*, pages 53–62, 2002.

[56] U. Huber and M. Maier. Flow behaviour in saturated and unsaturated uni–directional fibre beds - a flow model. In *Proceedings of FPCM-6, Auckland*, pages 85–95, 2002.

[57] G. Bechtold and L. Ye. Influence of fibre distribution on the transverse flow permeability in fibre bundles. *Composite Science and Technology*, 63:2069–2079, 2003.

[58] F.D. Dungan, M.T. Senoguz, A.M. Sastry, and D.A. Faillaci. On the use of Darcy permeability in sheared fabrics. *Journal of Reinforced Plastics and Composites*, 18(5):472–484, 1999.

[59] R.S. Parnas and A.J. Salem. A comparison of the uni–directional and radial in-plane flow of fluids through woven composite reinforcements. *Polymer Composites*, 14(5):383–394, 1993.

[60] S.V. Lomov, E.B. Belov, T. Bischoff, S.B. Ghosh, T. Truong Chi, and I. Verpoest. Carbon composites based on multiaxial multiply stitched preforms. part I: Geometry of the preform. *Composites Part A*, 33:1171–1183, 2002.

[61] S.V. Lomov, I. Verpoest, M. Barburski, and J. Laperre. Carbon composites based on multiaxial multiply stitched preforms. part II: KES-F characterisation of the deformability of the preforms at low loads. *Composites Part A*, 34:359–370, 2003.

[62] T. Truong Chi, M. Vettori, S.V. Lomov, and I. Verpoest. Carbon composites based on multiaxial multiply stitched preforms. part IV: - Mechanical properties of composites and damage observation. *Composites Part A*, 36(9):1207–1221, 2005.

[63] R. Loendersloot, S.V. Lomov, R. Akkerman, and I. Verpoest. Carbon composite based on multiaxial multiply stitched preforms. part V: Geometry of sheared biaxial fabrics. *Composites Part A*, 37:103–113, 2006.

[64] F. Edgren and L.E. Asp. Approximate analytical constitutive model for non-crimp fabric composites. *Composites Part A*, 36(2):173–181, 2005.

[65] CEN TC 249. Reinforcement – specifications for multiaxial multi-ply fabrics. pren 13473-1, CEN, 2000-07.

[66] J. Wenström. Report on ncf processing behaviour and quality with standard carbon yarns. Technical Report FALCOM G4RD-CT-00694 - WP2.1-1, Devold AMT, 2003.

[67] F. Robitaille, B.R. Clayton, A.C. Lond, B.J. Souter, and C.D. Rudd. Geometric modelling of industrial preforms: Warp-knitted textiles. *Proceedings of the Institute for Mechanical Engineering Part L*, 214:71–90, 2000.

[68] F. Robitaille, A.C. Long, and C.D. Rudd. Geometric modelling of textiles for prediction of composite processing and performance characteristics. *Plastics, Rubber and Composites*, 31(2):66–75, 2002.

[69] T. Truong Chi, M. Vettori, S.V. Lomov, and I. Verpoest. Multi-axial multiply carbon fabric reinforced epoxy composites: Mechanical properties and investigation of initial damage. In *Proceedings of ICCM-14*, 2003. [CD-edition].

[70] T. Truong Chi. *The Mechanical Performance and Damage of Multiaxial Multi-Ply Carbon Fabric Reinforced Composites*. PhD thesis, Katholieke Universiteit Leuven, November 2005.

[71] J. Wiggers, A.C. Long, P.Harrison, and C.D. Rudd. The effects of stitch architecture on the shear compliance of non-crimp fabrics. In *Proceedings of sixth ESAFORM Conference on Material Forming*, pages 851–854, 2003.

[72] A.P. Mouritz, K.H. Leong, and I. Herszberg. A review of the effect of stitching on the in-plane mechanical properties of fibre-reinforced polymer composites. *Composites Part A*, 28(12):979–991, 1997.

[73] C. Weimer and P. Mitschang. Aspects of the stitch formation process on the quality of sewn multi-textile-preforms. *Composites Part A*, 32(10):1477–1484, 2001.

[74] F. Edgren and L.E. Asp. Approximate analytical constitutive model for non-crimp fabric composites. Technical Report SICOMP 01-075, SiComp, 2003.

[75] P. Fernberg, I. Öhgren, A. Holmberg, and S. Lundström. Description of local processing models. Technical Report FALCOM G4RD-CT-00694 - WP4.3-1, SiComp, 2003.

[76] C. Lekakou, S. Edwards, G. Bell, and S.C. Amico. Computer modeling for the prediction of the in-plane permeability of non-crimp stitch bonded fabrics. *Composites Part A*, pages in–print, available online May 2005.

[77] M. Schneider, K. Edelmann, and U. Tiltmann. Quality analysis of reinforcement structures for composites by digital image processing. In *Proceedings of SAMPE Europe, Paris*, volume 25, pages 267–272, 2004.

[78] T.S. Lundström. The permeability of non-crimp stitched fabrics. *Composites, Part A: Applied Science and Manufacturing*, 31:1345–1353, 2000.

[79] M. Nordlund and T.S. Lundström. The effect of geometrical features of non-crimp fabrics on the permeability. In *Proceedings of ECCM-11 Conference, Rhodos, Greece*, 2004. [CD-Edition].

[80] M. Nordlund, T.S. Lundström, V. Frishfelds, and A. Jakovics. Permeability network model for non-crimp fabrics. *Composites Part A*, pages in–print, Available online April 2005.

[81] S. Darpier, A. Pagot, A. Vautrin, and P. Henrat. Influence of the stitching density in the transverse permeability of non-crimped new concept (nc2) multiaxial reinforcements: Measurements and predictions. *Composites Science and Technology*, 62:1979–1991, 2002.

[82] M. Nordlund, T.S. Lundström, V. Frishfelds, and A. Jakovics. Permeability network of non-crimp fabrics. In *Proceedings of FPCM-7 Conference, Newark Delaware*, pages 373–377, 2004.

[83] R. Loendersloot, R.H.W. ten Thije, S.V. Lomov, R. Akkerman, and I. Verpoest. Geometry, compressibility and porosity of sheared non-crimp fabrics. In *Proceedings of SiComp Conference, Piteå*, 2003. CD-edition.

[84] C. Lekakou, S. Edwards, G. Bell, and S.C. Amico. Computer modeling for the prediction of the in-plane permeability of non-crimp stitch bonded fabrics. In *Proceedings of FPCM-7, Newark Delaware*, pages 361–365, 2004.

[85] R. Loendersloot, S.V. Lomov, R. Akkerman, and I. Verpoest. Architecture and permeability of sheared carbon fibre non-crimp fabrics. In *Proceedings of SAMPE Europe, Paris*, pages 141–148, 2003.

[86] R. Loendersloot, R.H.W. ten Thije, R. Akkerman, and S.V. Lomov. Permeability prediction of non-crimp fabrics based on a geometric model. In *Proceedings of ECCM-11 Conference, Rhodos, Greece*, 2004. [CD-Edition].

[87] R. Akkerman, R.H.W. ten Thije, and R. Loendersloot. Appendix II - permeability, drapeability and compressibility - three interrelated properties. Technical Report FALCOM G4RD-CT-00694 - WP4.3-1 - App II, University Twente, 2003.

[88] G.A. Korn and T.M. Korn. *Mathematical Handbook for Scientists and Engineers*. McGraw-Hill, 2 edition, 19..

[89] R.J. Larsen and M.L. Marx. *Statistics*. Prentice-Hall, Inc, 1990.

[90] C.M. Jarque and A.K. Bera. Efficient test for normality, homoscedasticity and serial independence of regression residuals. *Economics Letters*, 6:255–259, 1980.

[91] C.M. Jarque and A.K. Bera. A test for normality of observations and regression residuals. *International Statistical Review*, 55:163–172, 1987.

[92] G.G. Judge, R. C. Hill, W. E. Griffiths, H. Lutkepohl, and T.-C. Lee. *Introduction to the Theory and Practice of Econometrics*. Wiley, New York, 2nd edition, 1988.

[93] M. Budhu. *Soil Mechanics and Foundations*. John Wiley & sons INC, 2000.

[94] S. Kawabata. *The standardisation and Analysis of Hand Evaluation*. Osaka, 1975.

[95] N.G. Ly and E.F. Denby. A CSIRO inter-laboratory trial of the KES-F for measuring fabric properties. *Journal of the Textile Institute*, 79(2):198–206, 1988.

[96] A. Shojaei and S.R. Ghaffarian. Modelling and simulation approaches in the resin transfer molding process: A review. *Polymer Composites*, 24(4):525–544, 2003.

[97] J.E. Drummond. Laminar viscous flow through regular arrays of paralelle solid cylinders. *International Journal of Multiphase Flow*, 10(5):515–540, 1984.

[98] J.B. Keller. Viscous flow through a grating or lattice of cylinders. *Journal of Fluid Mechanics*, 18(1):94–96, 1964.

[99] A.S. Sangani and A. Acrivos. Slow flow past periodic arrays of cylinders with application to heat transfer. *Journal of Multiphase Flow*, 8(3):193–206, 1982.

[100] A.S. Sangani and C. Yao. Transport processes in random arrays of cylinders. ii. viscous flow. *Physics of Fluids*, 31(9):2435–2444, 1988.

[101] M.V. Bruschke and S.G. Advani. Flow of generalized newtonian fluids across a periodic array of cylinders. *Journal of Rheology*, 3(37):479–498, 1993.

[102] T.A.K. Sadiq, S.G. Advani, and R.S. Parnas. Experimental investigation of transvers flow through aligned cylinders. *International Journal of Multphase Flow*, 21(5):755–774, 1995.

[103] H.C. Brinkman. A calculation of the viscous force exerted by a flowing fluid on a dense swarm of particles. *Applied Scientific Research A*, 1:27–34, 1947.

[104] H.C. Brinkman. On the permeability of media consisting of closely packed porous particles. *Applied Scientific Research A*, 1:81–86, 1947.

[105] E.B. Belov, S.V. Lomov, I. Verpoest, T. Peters, D. Roose, K. Hoes, H. Sol, and R.S. Parnas. Modelling of permeability of textile reinforcements: Lattice Boltzmann method. In *Proceedings of ECCM-10, Brugge*, 2002. [CD-edition].

[106] K.M. Pillai. Governing equations for unsaturated flow through woven fiber mats. part 1. isothermal flows. *Composites Part A*, 33:1007–1019, 2002.

[107] K.M. Pillai and S.G. Advani. Numerical simulation of unsaturated flow in woven fibre preforms during the resin transfer molding process. *Polymer Composites*, 19(1):71–80, 1998.

[108] J. Slade, K.M. Pillai, and S.G. Advani. Investigation of unsaturated flow in woven braided and stitched fiber mats during mold-filling in resin transfer molding. *Polymer Composites*, 22(4):491–505, 2001.

[109] J. Happel and H. Brenner. *Low Reynolds Number Hydrodynamics*. Martinus Nijhoff, first (paperback) edition, 1983.

[110] F.M. White. *Fluid Mechanics*. Mechanical Engineering Series. McGraw-Hill International Editions, fourth edition, 1999.

[111] G.K. Batchelor. *An Introduction to Fluid Dynamics*. Cambridge University Press, 1 edition, 1967.

[112] G.A. Evans, J.M. Blackledge, and P.D. Yardly. *Analytical Methods for Partial Differential Equations*. Springer, 2000.

[113] W. Ruijter. A numerical approach to the permeability of non-crimp fabrics. Master's thesis, University of Twente, 2004.

[114] F. Desplentere, S.V. Lomov, and I. Verpoest. Mold filling simulations for RTM: Influence of the scatter of preform permeability. In *Proceedings of FPCM-7, Newark Delaware*, pages 405–410, 2004.

[115] R.M.E.J. Spiering and H.J. Grootenboer. Eindige elementen-methode in de werktuigbouwkunde. Technical report, Universiteit Twente, Faculteit der Werktuigbouwkunde, 1993.

[116] M.J. Fagan. *Finite Element Analysis – Theory and Practice*. Addison Wesley Longman Limited, 2 edition, 1996.

[117] G.H. Golub and C.F. van Loan. *Matrix Computations*. The John Hopkins University Press, Baltimore London, third edition, 1996.

[118] R. Loendersloot and R. Akkerman. Comparison of permeability experiments and explanations of experimental scatter based on geometric models. Technical Report FALCOM G4RD-CT-00694 - WP5.3.0.1, UT, 2005.

[119] T.S. Lundström, R. Stenberg, R. Bergström, H. Partanen, and P.A. Birkeland. In-plane permeability measurement: a nordic round-robin study. *Composites Part A*, 31(1):29–43, 2000.

[120] Y. Luo, I. Verpoest, K. Hoes, M. Vanheule, H. Sol, and A. Cardon. Permeability measurement of textile reinforcements with several test fluids. *Composites Part A*, 32(10):1479–1504, 2001.

[121] J. Summerscales. The effect of permeant on the measured permeability of a reinforcement. In *Proceedings of FPCM-7, Newark Delaware*, pages 471–476, 2004.

[122] Y. Luo. *Resin Transfer Moulding of Knitted Fabric Reinforced Composites*. PhD thesis, KU Leuven, May 2001.

[123] Q. Liu and R.S. Parnas. New set–up for permeability measurement. In *Proceedings of FPCM-7, Newark Delaware*, pages 451–457, 2004.

[124] H.C. Stadtfeld, F. Weyrauch, and P. Mitschang. Standardizeable permeability work cell for fibrous reinforcements. In *Proceedings of FPCM-7 Conference, Newark Delaware*, pages 459–463, 2004.

[125] T. Luthy and P. Ermanni. Linear direct current (ldc) resistance and ultrasonic measurements for on-line lcm-process monitoring. *Centre of Structure Technologies, Swiss Federal Institute of Technology Zurich*, 2001.

[126] D.R. Nielsen and R. Pitchumani. Closed-loop flow control in resin transfer molding using real-time numerical process simulation. *Composites Science and Technology*, 62(2):283–298, 2002.

[127] C. Williams, J. Summerscales, and S. Grove. Resin infusion under flexible tooling (RIFT): a review. *Composites Part A*, 27:517–524, 1996.

[128] J. Park and M.K. Kang. A numerical simulation of the resin flim infusion process. *Composite Structures*, 60:431–437, 2003.

[129] A. Mammami and B.R. Gebart. Analyis of the vacuum infusion molding process. *Polymer Composites*, 21(1):28–40, 2000.

[130] V. Antonucci, M. Durante, M. Giordano, L. Nicolais, and C. Vitiello. Numerical simulation and experimental characterization of RIFT process. In *Proceeding of the 14th International Conference on Composite Materials*, 2004. [CD-edition].

[131] M.K. Kang, W.I. Lee, and H.T. Han. Analysis of vacuum bag resin transfer molding process. *Composites Part A*, 32:1553–1560, 2001.

[132] J.F.A. Kessels, A.S. Jonker, and R. Akkerman. Fully 2.5d flow modeling of resin infusion under flexible tooling using unstructured meshes and wet and dry compaction properties. *Composites Part A*, submitted, 2006.

[133] S.H. Ahn, W.I. Lee, and G.S. Springer. Measurements of the three-dimensional permeability of fiber preforms using embedded fiber optic sensors. *Journal of Composite Materials*, 29(6):714–733, 1995.

[134] P.B. Nedanov, S.G. Advani, S.W. Walsh, and W.O. Ballata. Determination of the permeability tensor of fibrous reinforcements for vartm. *Advances in Aerospace Materials and Structures*, 58:79–88, 1999.

[135] S.M. Walsh. In-situ sensor method and device. *United States Patent*, (5,210,499), May 1993.

[136] S.M. Walsh and R.V. Mohan. Sensor-based control of flow fronts in vacuum-assisted RTM. *Plastics Engineering*, 55(10):29–32, 1999.

[137] A. Saouab, J. Bréard, P. Lory, B. Gardarein, and G. Bouquet. Injection simulations of thick composite parts manufactored by the RTM process. *Composites Science and Technology*, 61:445–451, 2001.

[138] R. Loendersloot. Design of a permeability measuring tool. Technical Report DE-2300-02/UT - CTW.02/TMK.5406, University of Twente, June 2002.

[139] R. Loendersloot. Design of a through thickness permeability instrument. Technical Report DE-2300-03/UT, University of Twente, June 2005.

[140] M.M.J. Tibben. 1-D Permeabiliteitsmeting. Master's thesis, Saxion Hogeschool Enschede, July 2003. UT-NLR-WP2000-2.

[141] J. Elmarasy. Kz-Permeabiliteitsmeting. Master's thesis, Saxion Hogeschool Enschede, June 2004. UT-NLR-WP2000-06.

[142] S. Amico and C. Lekakou. An experimental study of the permeability and capillary pressure in resin-transfer moulding. *Composites Science and Technology*, 61:1945–1959, 2001.

[143] S. Bickerton, E.M. Sozer, P. Šimácek, and S.G. Advani. Fabric structure and mold curvature effects on preform permeability and mold filling in the RTM process. part I. experiments. *Composites Part A*, 31:423–438, 2000.

[144] S. Bickerton, S.G. Advani, R.V. Mohan, and D.R. Shires. Experimental analysis and numerical modeling of flow channel effects in resin transfer molding. *Polymer Composites*, 21(1):134–153, 2000.

[145] M.L. Diallo, R. Gauvin, and F. Trochu. Experimental analysis and simulation of flow through multi-layer fiber reinforcements in liquid composite molding. *Polymer Composites*, 19(3):246–256, 1998.

[146] A. Endruweit and P. Ermanni. The in-plane permeability of sheared textiles. experimental observations and a predictive conversion model. *Composites Part A*, 35:439–451, 2004.

[147] R. Gauvin, F. Trochu, Y. Lemenn, and L. Diallo. Permeability measurement and flow simulation through fiber reinforcement. *Polymer Composites*, 17(1):34–42, 1996.

[148] B.R. Gebart and P. Lidström. Measurement of in-plane permeability of anisotropic fiber reinforcements. *Polymer Composites*, 17(1):43–51, 1996.

[149] A. Hammami, F. Trochu, R. Gauvin, and S. Wirth. Directional permeability measurement of deformed reinforcement. *Journal of Reinforced Plastics and Composites*, 15:552–562, 1996.

[150] K.K. Han, C.W. Lee, and B.P. Rice. Measurements of the permeability of fiber preforms and applications. *Composites Science and Technology*, 60:2435–2441, 2000.

[151] C.L. Lai and W.B. Young. Model resin permeation of fiber reinforcements after shear deformation. *Polymer Composites*, 18(5):642–648, 1997.

[152] C. Lekakou, M.A.K. Johari, D. Norman, and M.G. Bader. Measurement techniques and effects on in-plane permeability of woven cloth in resin transfer moulding. *Composites Part A*, 27:401–408, 1996.

[153] T.S. Lundström, S. Toll, and J.M. Håkanson. Measurement of the permeability tensor of compressed fibre beds. *Transport in Porous Media*, 47:363–380, 2002.

[154] R.S. Parnas, J.G. Howard, T.L. Luce, and S.G. Advani. Permeability characterization. part 1: A proposed standard reference fabric. *Polymer Composites*, 16(6):429–445, 1995.

[155] R.S. Parnas, K.M. Flynn, and M.E. Dal-Favero. A permeability database for composite manufacturing. *Polymer Composites*, 18(5):623–633, 1997.

[156] S.P. Haanappel and I.G.H.M. van der Sligte. Ontwerp en implementatie van een RTM proefopstelling en microscopy beeldverwerking. Master's thesis, Christelijke Hogeschool Windesheim, May 2004. AP:W.03.3.03/UT-NLR-WP2000-05.

[157] S.P. Timoshenko and J.N. Goodier. *Theory of Elasticity*. McGraw-Hill, third edition 1987 edition, 1934 (McGraw-Hill 1987).

[158] K.L. Adams and L. Rebenfeld. In-plane flow of fluids in fabrics: Structure/flow characterization. *Textile Research Institute*, 57:647–654, 1987.

[159] K.L. Adams, W.B. Russel, and L. Rebenfeld. Radial penetration of a viscous liquid into a planar anisotropic porous medium. *International Journal of Multiphase Flow*, 14(2):203–215, 1988.

[160] J.R. Weitzenböck, R.A. Shenoi, and P.A. Wilson. Radial flow permeability measurement. part A: Theory. *Composites Part A*, 30:781–796, 1999.

[161] J.R. Weitzenböck, R.A. Shenoi, and P.A. Wilson. Radial flow permeability measurement. part B: Application. *Composites Part A*, 30:797–813, 1999.

[162] F. Robitaille, A.C. Lond, and C.D. Rudd. Permeability prediction for industrial preforms. *Plastics, Rubber and Composites*, 31(6):238–248, 2002.

[163] P. Smith, C.D. Rudd, and A.C. Long. The effect of shear deformation on the processing and mechanical properties of aligned reinforcements. *Composites Science and Technology*, 57:327–344, 1997.

[164] S. Lawford. Finite-sample quantiles of the Jarque–Bera test. Working paper, Department of Economics and Finance, Brunel University, 2004.

[165] MathWorks Inc. *Matlab 7.0 R14*. MathWorks Inc, 2003.

[166] DIN 51 562. Messung der kinematischen Viskosiät mit dem Ubbelohde-Viskosimeter. Technical report, Deutsche Normen, 1967.

[167] ANSI. Glass capillary kinematic viscometers - specifications and operating instructions, 1994. ISO 3105.

Appendix A

Measured SYD Dimensions

The measured data of the widths b and lengths l of the SYDs and their respective dimensionless representations κ and λ of the fabrics B1, B2 and B3 are collected in this appendix. The averaged values and scatter of relaxed and sheared configurations is presented in table A.1 to table A.4. The histogram data of widths and lengths of the three fabrics are tabulated in table A.5 to table A.7. The histograms themselves are presented in section A.3.

A.1 Averaged Values and Scatter

Table A.1: *Averaged values for the width b including the scatter s for various shear angles. A lognormal distribution of the data is assumed.*

		B1			B2			B3		
	γ [°]	$\bar{b}$ [mm]	s^- 10^{-2}[mm]	s^+	$\bar{b}$ [mm]	s^- 10^{-2}[mm]	s^+	$\bar{b}$ [mm]	s^- 10^{-2}[mm]	s^+
top	0	0.28	1.15	1.20	0.16	1.04	1.12	0.28	1.96	2.11
	15	–	–	–	–	–	–	0.20	1.38	1.49
	30	0.18	1.18	1.28	0.17	1.06	1.13	0.12	1.04	1.15
	45	0.21	1.53	1.66	0.18	1.08	1.16	0.12	0.86	0.93
	60	–	–	–	–	–	–	0.12	0.79	0.85
bottom	0	0.43	1.72	1.79	0.38	1.17	1.21	0.27	1.41	1.48
	15	–	–	–	–	–	–	0.19	1.11	1.18
	30	0.34	1.79	1.89	0.33	1.51	1.59	0.16	1.06	1.14
	45	0.33	1.50	1.57	0.33	2.45	2.66	0.17	0.95	1.01
	60	–	–	–	–	–	–	0.15	1.17	1.28

Table A.2: *Averaged values for the length l including the scatter s for various shear angles. A lognormal distribution of the data is assumed.*

		B1			B2			B3		
	γ [°]	$\bar{l}$ [mm]	s^- [mm]	s^+	$\bar{l}$ [mm]	s^- [mm]	s^+	$\bar{l}$ [mm]	s^- [mm]	s^+
top	0	5.05	–	–	4.09	0.19	0.20	7.44	0.33	0.35
	15	–	–	–	–	–	–	6.99	0.33	0.35
	30	5.07	0.27	0.29	4.75	0.20	0.21	5.88	0.39	0.42
	45	4.18	0.33	0.36	4.66	0.21	0.23	6.22	0.47	0.52
	60	–	–	–	–	–	–	6.67	0.54	0.59
bottom	0	7.15	–	–	3.54	0.15	0.16	7.86	0.28	0.30
	15	–	–	–	–	–	–	5.55	0.27	0.28
	30	4.60	0.21	0.22	5.40	0.27	0.29	5.63	0.26	0.27
	45	4.58	0.24	0.26	4.97	0.31	0.33	6.09	0.44	0.48
	60	–	–	–	–	–	–	6.49	0.37	0.40

Table A.3: *Averaged values for the dimensionless width κ including the scatter s for various shear angles. A lognormal distribution of the data is assumed.*

		B1			B2			B3		
	γ [°]	$\bar{\kappa}$ [-]	s^- [-]	s^+ [-]	$\bar{\kappa}$ [-]	s^- [-]	s^+ [-]	$\bar{\kappa}$ [-]	s^- [-]	s^+ [-]
top	0	3.14	0.13	0.14	1.81	0.12	0.13	3.93	0.27	0.30
	15	–	–	–	–	–	–	2.75	0.19	0.21
	30	2.02	0.13	0.14	1.96	0.12	0.13	1.72	0.15	0.16
	45	2.40	0.17	0.19	2.02	0.12	0.13	1.75	0.12	0.13
	60	–	–	–	–	–	–	1.64	0.11	0.12
bottom	0	4.94	0.20	0.20	4.35	0.13	0.14	3.83	0.20	0.21
	15	–	–	–	–	–	–	2.70	0.16	0.17
	30	3.83	0.20	0.22	3.80	0.17	0.18	2.20	0.15	0.16
	45	3.72	0.17	0.18	3.78	0.28	0.30	2.33	0.13	0.14
	60	–	–	–	–	–	–	2.15	0.16	0.18

Table A.4: *Averaged values for the dimensionless length λ including the scatter s for various shear angles. A lognormal distribution of the data is assumed.*

		B1			B2			B3		
	γ [°]	$\bar{\lambda}$ [-]	s^- [-]	s^+ [-]	$\bar{\lambda}$ [-]	s^- [-]	s^+ [-]	$\bar{\lambda}$ [-]	s^- [-]	s^+ [-]
top	0	1.99	–	–	0.81	0.04	0.04	2.37	0.11	0.11
	15	–	–	–	–	–	–	2.23	0.11	0.11
	30	2.00	0.11	0.11	0.94	0.04	0.04	1.87	0.12	0.13
	45	1.65	0.13	0.14	0.93	0.04	0.04	1.98	0.15	0.16
	60	–	–	–	–	–	–	2.12	0.17	0.19
bottom	0	2.82	–	–	1.34	0.06	0.06	2.50	0.09	0.09
	15	–	–	–	–	–	–	1.77	0.08	0.09
	30	1.82	0.08	0.09	2.05	0.10	0.11	1.79	0.08	0.09
	45	1.81	0.10	0.10	1.88	0.12	0.13	1.94	0.14	0.15
	60	–	–	–	–	–	–	2.07	0.12	0.13

A.2 Histogram Data

Table A.5: *Histogram frequency data of fabric B1 for various shear angles (counts per column, total count is 100), for a normal and logarithmic distribution of the dimensions.*

		width b						length l					
		top			bottom			top			bottom		
	γ [°]	0	30	45	0	30	45	0	30	45	0	30	45
linear		15	4	9	4	4	3	–	9	14	–	7	4
		27	20	21	3	15	4	–	23	27	–	32	22
		0	27	25	17	24	5	–	20	24	–	43	33
		27	15	20	13	28	15	–	15	9	–	10	22
		7	16	11	17	15	12	–	17	10	–	3	9
		13	9	4	24	9	15	–	6	1	–	2	5
		7	5	5	1	2	17	–	2	6	–	1	2
		2	1	3	13	1	14	–	2	4	–	0	2
		0	2	1	5	0	11	–	3	2	–	1	0
		2	1	1	3	2	4	–	3	3	–	1	1
logarithmic		5	1	1	1	2	1	–	6	2	–	3	1
		10	2	4	3	2	2	–	5	5	–	3	3
		27	10	5	3	4	3	–	14	18	–	16	7
		0	11	16	4	18	4	–	19	11	–	35	24
		27	19	16	26	19	14	–	15	23	–	26	22
		7	22	23	17	26	11	–	20	12	–	9	21
		5	17	19	24	16	14	–	9	12	–	3	13
		15	9	6	1	8	22	–	4	4	–	3	5
		2	6	8	13	3	18	–	3	7	–	0	3
		2	3	2	8	2	11	–	5	6	–	2	1

Table A.6: *Histogram frequency data of fabric B2 for various shear angles (counts per column, total count is 100), for a normal and logarithmic distribution of the dimensions.*

		width b						length l					
		top			bottom			top			bottom		
	γ [°]	0	30	45	0	30	45	0	30	45	0	30	45
linear		3	7	5	2	1	6	6	4	5	2	6	12
		19	23	15	2	3	7	6	6	12	9	38	26
		26	29	20	3	11	3	22	16	19	28	33	26
		22	22	18	27	9	21	30	33	26	25	11	15
		12	8	13	9	20	15	20	12	18	21	1	8
		10	7	11	7	17	12	8	13	7	5	5	4
		6	3	6	30	14	12	3	7	9	5	2	3
		0	0	7	9	12	10	3	3	1	1	2	2
		1	0	3	6	8	8	0	2	1	3	1	2
		1	1	2	5	5	6	2	4	2	1	1	2
logarithmic		1	2	3	1	1	1	3	2	3	1	4	6
		2	3	2	1	0	3	3	4	4	1	3	6
		0	8	7	2	2	3	1	3	7	8	23	13
		5	17	22	17	8	6	16	11	15	17	29	15
		29	23	6	13	6	3	20	25	18	24	23	28
		18	23	21	9	14	17	31	22	23	24	6	11
		24	13	19	7	23	18	12	15	12	14	4	11
		13	8	5	30	21	19	9	9	13	4	4	1
		6	2	12	15	15	15	3	4	2	5	3	5
		2	1	3	5	10	15	2	5	3	2	1	4

Table A.7: *Histogram frequency data of fabric B3 for various shear angles (counts per column, total count is 100), for a normal and logarithmic distribution of the dimensions.*

		width b										length l									
		top					bottom					top					bottom				
	γ [°]	0	15	30	45	60	0	15	30	45	60	0	15	30	45	60	0	15	30	45	60
linear		5	12	12	9	10	4	3	16	3	7	3	19	8	11	6	3	9	3	9	6
		9	8	38	26	37	5	6	18	6	24	6	16	25	19	17	7	9	4	35	19
		20	9	19	26	30	4	21	37	34	16	15	25	27	30	26	11	24	19	29	18
		20	11	14	19	11	11	13	23	36	25	13	14	23	16	19	13	15	28	12	19
		17	20	7	7	5	25	30	4	3	11	18	10	11	7	14	21	15	17	7	16
		16	15	5	5	3	23	11	0	8	9	16	6	2	8	6	18	11	18	2	15
		3	17	1	3	3	12	9	0	4	4	11	6	1	2	6	12	7	7	2	6
		6	2	3	3	0	7	3	1	3	1	6	2	0	4	4	12	7	1	2	0
		1	5	0	1	0	4	0	0	1	1	9	0	1	1	0	2	0	2	0	0
		3	1	1	1	1	5	4	1	2	2	3	2	2	2	2	1	3	1	2	1
logarithmic		1	6	2	2	3	2	1	2	1	3	2	9	3	2	1	2	4	3	2	3
		1	6	4	7	2	2	2	0	2	0	2	12	1	4	1	1	8	0	4	3
		7	4	6	10	17	3	2	14	6	4	3	14	7	7	3	7	5	3	7	12
		5	8	20	16	25	2	8	1	1	13	14	18	12	11	8	10	20	4	18	12
		1	7	23	21	19	8	17	27	33	22	12	16	25	19	16	11	12	19	29	18
		21	10	14	15	19	15	12	38	35	17	15	13	26	27	22	22	14	32	20	16
		20	23	17	16	7	24	31	13	4	19	19	6	17	11	21	19	15	19	9	16
		21	22	6	6	4	23	20	3	9	14	16	8	5	10	14	17	12	15	5	17
		9	9	4	5	3	15	3	0	6	5	11	2	1	6	11	10	7	3	4	2
		4	5	4	2	1	6	4	2	3	3	6	2	3	3	3	1	3	2	2	1

A.3 Histograms

The histograms of the measured data for all three fabrics and all applied shear angles are collected in this section. The raw data on the lengths of the SYDs of fabric B2 in relaxed configuration was not available. The dotted and solid lines are the normal and lognormal distribution functions based on the averaged value and estimated standard deviation of the measured data.

A.3.1 Fabric B1

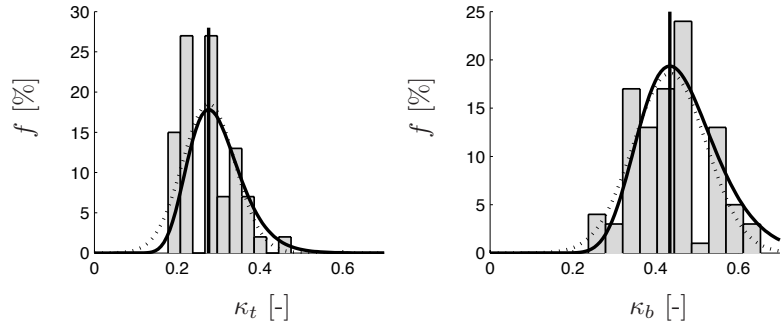

(a) *top face* (b) *bottom face*

Figure A.1: *Histograms of the dimensionless width κ for fabric B1 in relaxed configuration.*

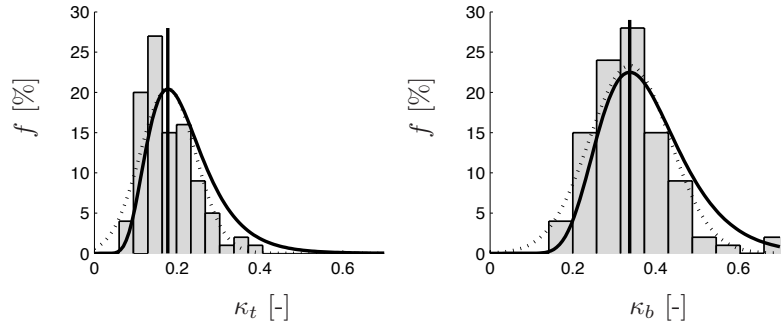

(a) *top face* (b) *bottom face*

Figure A.2: *Histograms of the dimensionless width κ for fabric B1 in 30° sheared configuration.*

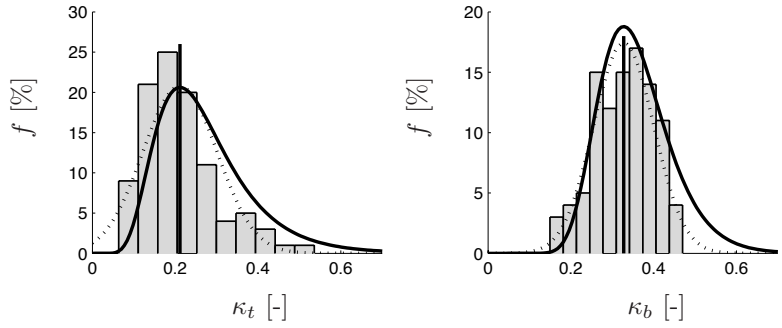

(a) *top face* (b) *bottom face*

Figure A.3: *Histograms of the dimensionless width κ for fabric B1 in 45° sheared configuration.*

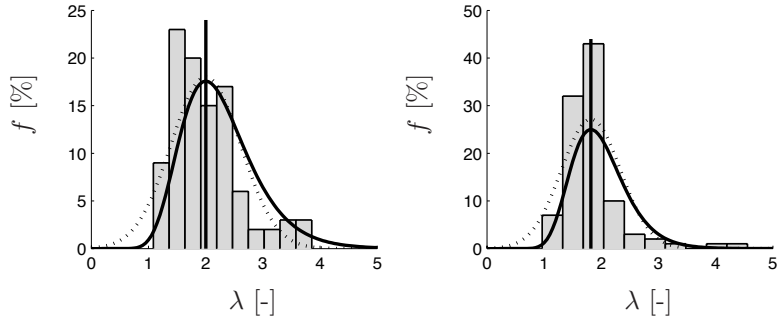

(a) *top face* (b) *bottom face*

Figure A.4: *Histograms of the dimensionless length λ for fabric B1 in 30° sheared configuration.*

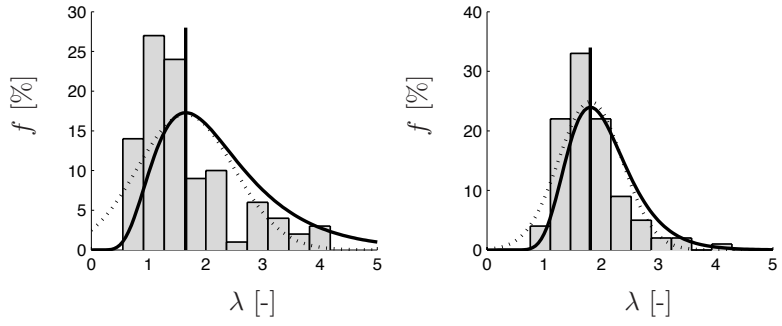

(a) *top face* (b) *bottom face*

Figure A.5: *Histograms of the dimensionless length λ for fabric B1 in 45° sheared 3 configuration.*

A.3.2 Fabric B2

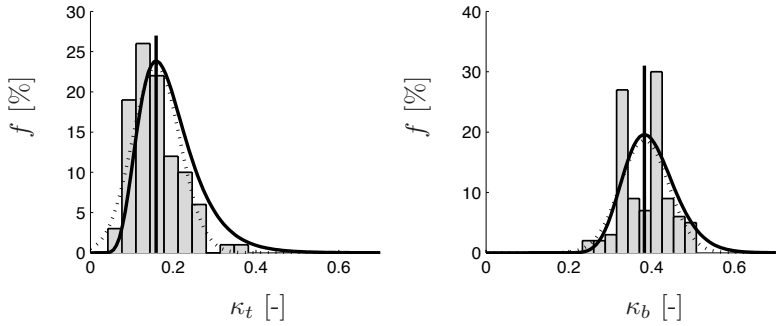

(a) *top face* (b) *bottom face*

Figure A.6: *Histograms of the dimensionless width κ for fabric B2 in relaxed configuration.*

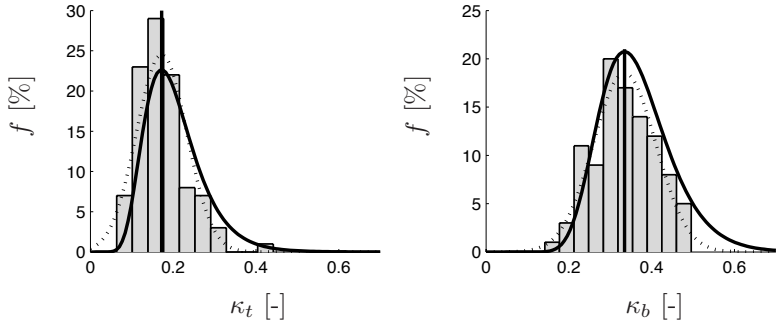

(a) *top face* (b) *bottom face*

Figure A.7: *Histograms of the dimensionless width κ for fabric B2 for γ=30°.*

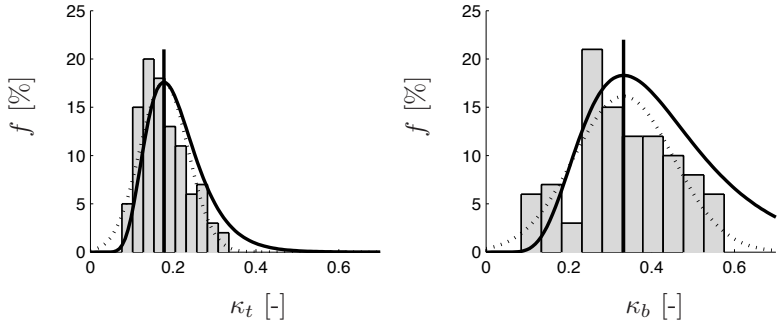

(a) *top face* (b) *bottom face*

Figure A.8: *Histograms of the dimensionless width κ for fabric B2 for γ=45°.*

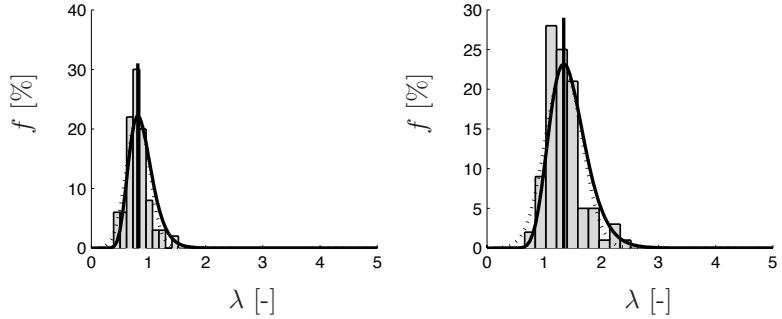

(a) *top face* (b) *bottom face*

Figure A.9: *Histograms of the dimensionless length λ for fabric B2 in relaxed configuration.*

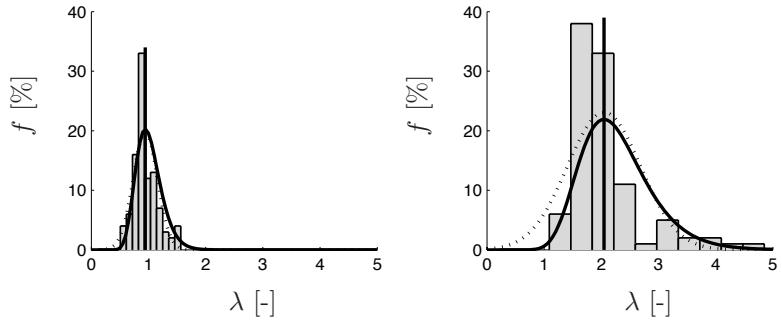

(a) *top face* (b) *bottom face*

Figure A.10: *Histograms of the dimensionless length λ for fabric B2 for γ=30°.*

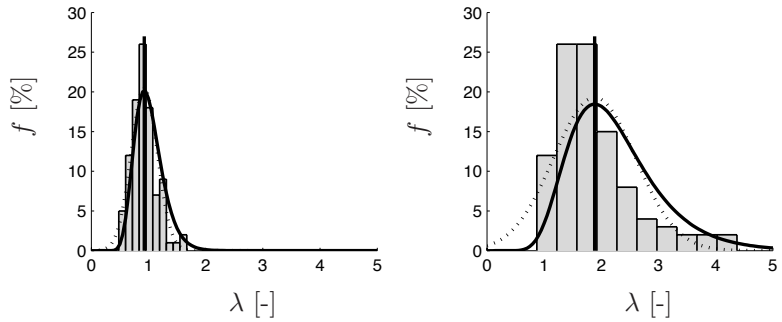

(a) *top face* (b) *bottom face*

Figure A.11: *Histograms of the dimensionless length λ for fabric B2 for γ=45°.*

A.3.3 Fabric B3

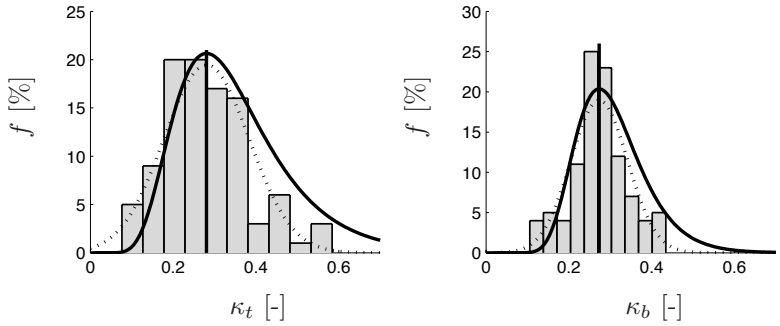

(a) *top face* (b) *bottom face*

Figure A.12: *Histograms of the dimensionless width κ for fabric B3 in relaxed configuration.*

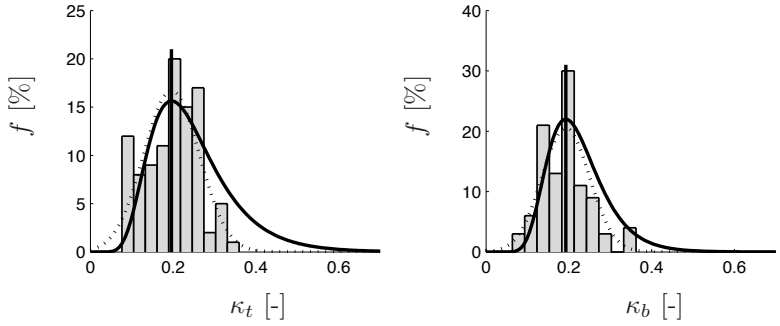

(a) *top face* (b) *bottom face*

Figure A.13: *Histograms of the dimensionless width κ for fabric B3 for γ=15°.*

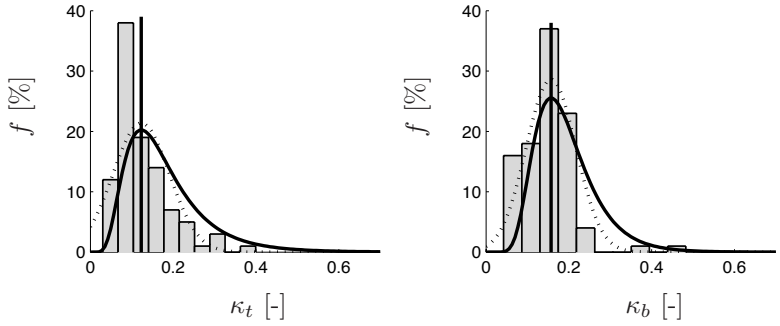

(a) *top face* (b) *bottom face*

Figure A.14: *Histograms of the dimensionless width κ for fabric B3 for γ=30°.*

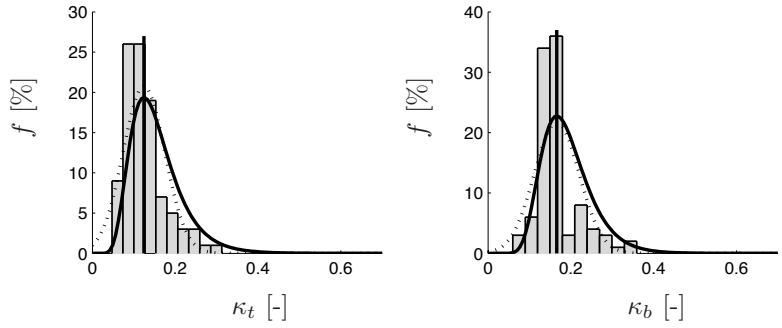

(a) *top face* (b) *bottom face*

Figure A.15: *Histograms of the dimensionless width κ for fabric B3 for γ=45°.*

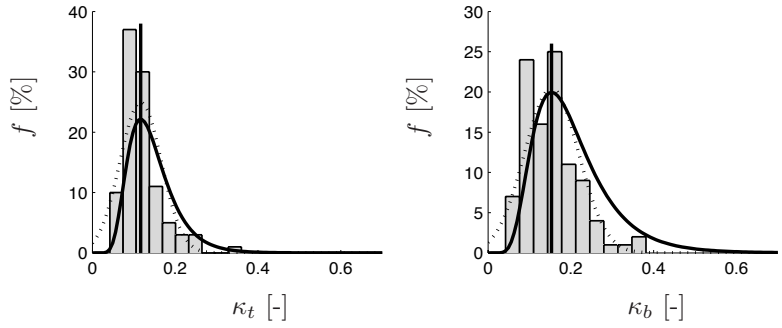

(a) *top face* (b) *bottom face*

Figure A.16: *Histograms of the dimensionless width κ for fabric B3 for γ=60°.*

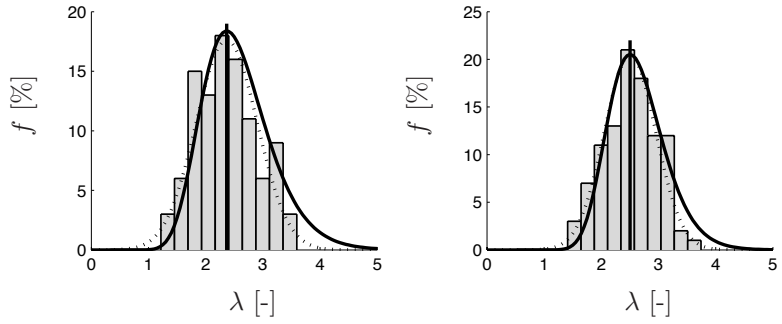

(a) *top face* (b) *bottom face*

Figure A.17: *Histograms of the dimensionless length λ for fabric B3 in relaxed configuration.*

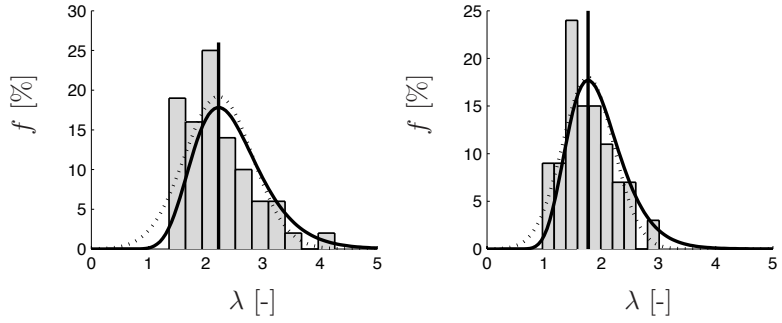

(a) *top face* (b) *bottom face*

Figure A.18: *Histograms of the dimensionless length λ for fabric B3 for γ=15°.*

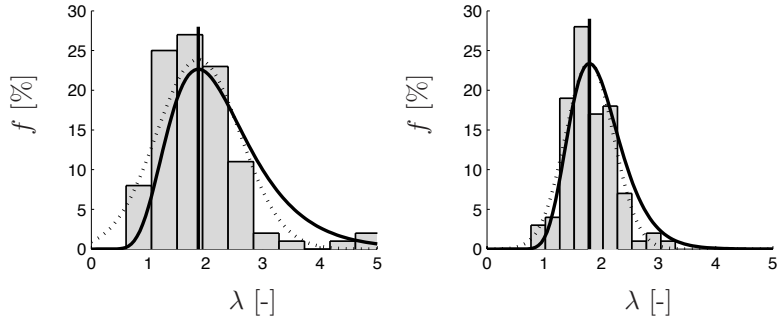

(a) *top face* (b) *bottom face*

Figure A.19: *Histograms of the dimensionless length λ for fabric B3 for γ=30°.*

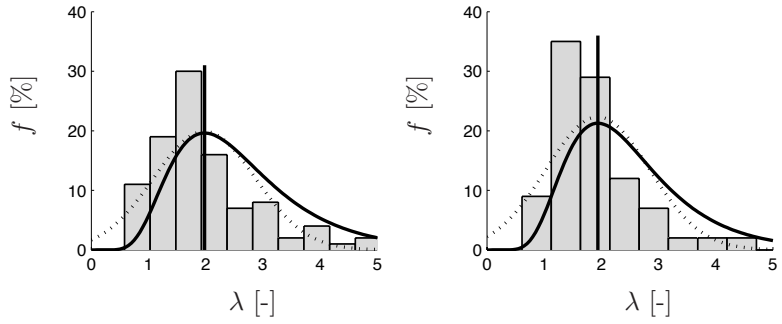

(a) *top face* (b) *bottom face*

Figure A.20: *Histograms of the dimensionless length λ for fabric B3 for γ=45°.*

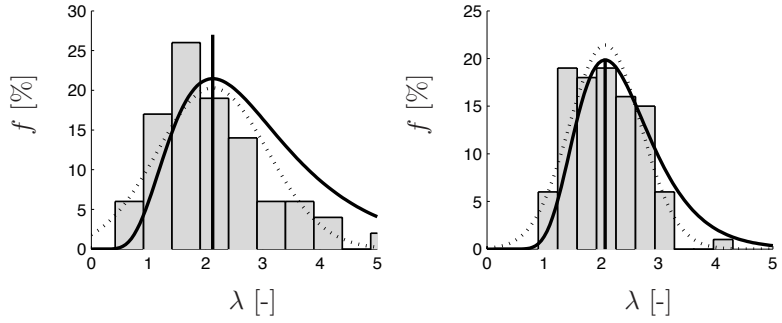

(a) *top face* (b) *bottom face*

Figure A.21: *Histograms of the dimensionless length λ for fabric B3 for γ=60°.*

Appendix B

Statistics of the Experimental Data

A large amount of experimental data is collected for the dimensions of the Stitch Yarn induced fibre Distortions (SYD). A decent statistical treatment of the data is prerequisite, especially since the aim of the research is to analyse the effect of the variations in the internal geometry (on micro–level) on the (macro–scale) permeability. This appendix deals with the statistical methods that were employed to analyse the data.

B.1 Terminology & Functions

Statistics – it may be too sharp to state that most engineers have limited knowledge on statistics, but it is certainly useful to introduce a number of terms and functions that are considered to be relevant here. Given a set X of experimental data x, with:

$$X = \{x_1, x_2, \ldots, x_i, \ldots, x_n\}. \tag{B.1}$$

It is then possible to calculate a mean μ and a standard deviation σ. The mean μ is the expected value of the measured quantity and is also referred to as $E(X)$. The standard deviation is based on an assumed distribution of the measured data X. In most cases, or maybe it is better to say *naturally* in the literal sense of the word, a normal distribution is found: the tendency of data, depending on a large number of parameters, to be normally distributed is proven in the central limit theorem [89]. Normal distributions are also referred to as Gaussian distributions. The normal distribution is a continuous probability function $f(x)$, stating that the probability P that a value x of the set (or measurement of the same quantity) lies between a and b, equals:

$$P(a \leq x \leq b) = \int_a^b f(x)\mathrm{d}x. \tag{B.2}$$

The probability function of a normal distribution with mean μ and standard deviation σ is defined as:

$$f(x) = \frac{1}{\sigma\sqrt{2}} \cdot \mathrm{e}^{-\frac{1}{2}\left(\frac{x-\mu}{\sigma}\right)^2}. \tag{B.3}$$

The solution of the integral in (B.2) for a normal distribution is:

$$P(a \leq x \leq b) = \frac{1}{2}\left(\mathrm{erf}\left(\frac{\mu-a}{\sigma\sqrt{2}}\right) - \mathrm{erf}\left(\frac{\mu-b}{\sigma\sqrt{2}}\right)\right), \tag{B.4}$$

with erf () the error function defined as:

$$\mathrm{erf}\,(x) = \frac{2}{\sqrt{\pi}} \int_0^x \mathrm{e}^{-t^2}\mathrm{d}t. \tag{B.5}$$

A frequently observed variation of the normal distribution is the lognormal distribution. The natural logarithm of the data is taken after which the mean $\mu_{\ln}$ and standard deviation $\sigma_{\ln}$ are determined.

Generally, the standard deviation σ can only be estimated. The most common and most accurate estimator s of σ, for a set of n elements is:

$$s = \sqrt{\frac{1}{n-1}\sum_{i=1}^{n}(x_i - \mu)^2}. \tag{B.6}$$

The term in the square root is known as the variance. It is also the second central moment of the data. The k^{th} central moment of a data set is defined as:

$$m_k = \frac{1}{n-1}\sum_{i=1}^{n}(x_i - \mu)^k. \tag{B.7}$$

Note that the first central moment equals zero by definition. The third and fourth central moments are used to determine the skewness and kurtosis of a set of data, which are both briefly discussed in section B.5. The skewness and kurtosis are important parameters in the goodness–of–fit tests for example utilised to verify the assumption of normality of a set of data. Prior to that, some details on the behaviour of data sets are discussed.

B.2 Significant and Confidence Intervals

It is certainly worth noting that statistics only formulate statements in a probabilistic way. It may very well be that the measured quantities do not exhibit the properties assumed in the statement. This is explicitly pointed out by the confidence intervals. A certain assumption, for example, holds in – typically – 95% percent of the cases.

Solving (B.2) for the boundaries a and b, which are symmetrically positioned around the averaged value μ, such that $P(a \leq x \leq b)$ equals 0.95 yields the 95% confidence interval for the averaged value of the data. Or: the averaged value will be in this range in 95% of the measurements. It can be found that the 95% confidence interval for the averaged value equals for a normal distribution:

$$\mu_{95\%} \in \left(\bar{x} - \frac{1.96\sigma}{\sqrt{N}}, \bar{x} + \frac{1.96\sigma}{\sqrt{n}} \right), \tag{B.8}$$

with $\bar{x}$ the arithmetical averaged value of the measured data, n the sample size and σ the standard deviation, which may be the estimated standard deviation s. Tabulated values of the cumulative area under the probability function $f(x)$ are used to find the value 1.96 [89].
Inversely, it is found that:

$$\mu_{68\%} \in \left(\bar{x} - \frac{\sigma}{\sqrt{N}}, \bar{x} + \frac{\sigma}{\sqrt{n}} \right), \tag{B.9}$$

Given a data set of measured values, such as the dimensions of the SYDs for various shear angles, it can be stated that the difference between the averaged values of the different sets is referred to as significant if the averaged values are separated at least $4/\sqrt{n}$ or $2/\sqrt{n}$ times the standard deviation for a 95% or 68% confidence interval respectively. Once again it is pointed out that the large amount of presented experimental results does not justify firm statements on a presumed behaviour of the measured quantity. Formulations like “a significant difference” or “an obvious drop of...” are easily used, but terms like “suggested behaviour” are far more appropriate.

B.3 Histograms

The distribution of the data set x is graphically shown by a histogram. It shows the frequency of the occurrence that a certain element of the set x lies in a predefined subrange of the entire domain of values of x. A convenient way to compare the histogram data with the normal distribution based on the mean and standard deviation estimated from the set of data is to plot the distribution function on top of the histogram. It may even be useful to plot different distribution functions on top of a single histogram, as was the case in the section 2.3. An example of a histogram including two distribution functions is presented in figure B.1.
A scaling is required to plot the distribution function and histogram correctly with respect to each other. The fraction of the data in the central column of the histogram can be determined, assuming that the data set exhibits a perfectly normal distribution, by solving (B.4) for $a = \mu - w_c/2$ and $b = \mu + w_c/2$, with w_c the width of a single column:

$$P\left(\mu - \frac{w_c}{2} \leq x \leq \mu + \frac{w_c}{2}\right) = \frac{1}{2}\left(\text{erf}\left(\frac{w_c}{2\sigma\sqrt{2}}\right) - \text{erf}\left(\frac{-wc}{2\sigma\sqrt{2}}\right)\right). \tag{B.10}$$

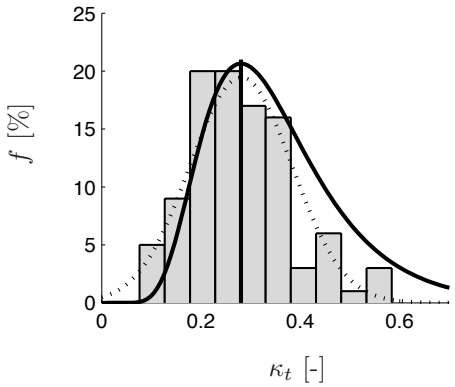

Figure B.1: *Histogram of the dimensionless width κ of the top face for fabric B3. The dotted and solid lines are the normal and lognormal distribution functions based on the averaged value and estimated standard deviation of the measured data.*

This value is used to scale the normal distribution function (note: the exponent in (B.3) equals 1 for $x = \mu$). The distribution function for a normal distribution of the data, that is plot in the histograms presented in the thesis is:

$$f(x) = P\left(\mu - \frac{w_c}{2} \leq x \leq \mu + \frac{w_c}{2}\right) \cdot \mathrm{e}^{-\frac{1}{2}\left(\frac{x-\mu}{\sigma}\right)^2} \cdot 100\%. \tag{B.11}$$

The function $f(x)$ in the case of lognormal distribution of the data is derived analogously.

B.4 Statistical Test

A statistical test is a test whether a statistical value or statement is presumably correct (note that absolute correctness is never achieved). A null hypothesis is formulated, for example, stating that the standard deviation of a certain set is significantly larger than that of a second set, or that the data set exhibits a certain distribution. The hypothesis is transformed to a single value, the statistical value F_s, e.g. the estimated standard deviation or the deviation from the presumed distribution. This value is then compared to the critical value, which depends on the test and on the level of significance. The null hypothesis cannot be rejected if the conditions are met, otherwise, the hypothesis must be rejected.
The normality of a distributions of the dimensions of the SYD is tested. Two null hypotheses are formulated:

1. H_0: the data is distributed according to a normal distribution;
2. H_0: the data is distributed according to a lognormal distribution;

The applied statistic test is the Jarque–Bera normality test [90–92]. This is a commonly applied test for normality and is available in MATLAB©. The test value is computed by [164]:

$$F_s = \frac{n}{6}\left(\frac{m_3^2}{m_2^3} + \frac{1}{4}\left(\frac{m_4}{m_2^2} - 3\right)^2\right), \tag{B.12}$$

with m_k the k^{th} central moment of the data, see equation (B.7). The critical value of the test F_c is usually the statistic value of a $\chi^2_{1-\alpha,k}$ distribution with two degrees of freedom (k). The level of significance α is typically 0.05. $\chi^2_{1-\alpha,k}$ is tabulated in many

Table B.1: *Normality of the distributions of the dimensionless width and length of the fabrics B1, B2 and B3 according to the Jarque–Bera goodness–of–fit test (critical value: $F_c = 5.991$).*

			κ				λ			
			linear		logarithmic		linear		logarithmic	
		γ	H_0	F_s	H_0	F_s	H_0	F_s	H_0	F_s
B1	top	0	–	–	–	–	–	–	–	–
		30	1	18.17	0	0.20	1	25.03	0	1.96
		45	1	29.53	0	0.01	1	27.82	0	3.63
	bottom	0	–	–	–	–	–	–	–	–
		30	1	41.11	0	3.85	1	463.68	1	43.45
		45	0	2.58	1	9.06	1	81.92	0	3.04
B2	top	0	1	21.63	0	3.23	1	29.90	0	4.10
		30	1	59.94	0	0.13	1	12.65	0	0.81
		45	0	5.24	0	1.32	1	9.54	0	0.02
	bottom	0	0	2.07	0	3.50	1	36.05	0	3.38
		30	0	1.33	0	5.57	1	136.70	1	21.65
		45	0	2.72	1	10.71	1	56.01	0	2.56
B3	top	0	1	6.56	0	4.12	0	1.82	0	2.39
		15	0	2.01	1	9.98	1	19.07	0	3.01
		30	1	70.71	0	0.57	1	133.95	0	2.90
		45	1	31.18	0	0.48	1	26.78	0	0.06
		60	1	151.01	0	2.69	1	15.74	0	2.49
	bottom	0	0	0.10	1	17.84	0	0.41	0	4.24
		15	1	6.51	1	6.60	0	4.68	0	1.76
		30	1	370.35	1	18.64	1	9.78	1	13.24
		45	1	42.77	0	2.21	1	113.01	0	2.33
		60	1	18.84	0	1.37	0	3.37	0	2.45

statistics books (for example [89]). F_c is 4.605, 5.991, 7.378 and 9.210 for $\alpha = 0.10$, $\alpha = 0.05$, $\alpha = 0.025$ and $\alpha = 0.01$ respectively.
The results of both tests are presented in table B.1. The left part of the table presents

the results of the two tests on the dimensionless width κ, the second those on the dimensionless width λ. A value of 1 for H_0 implies rejection of the hypothesis, a value of 0 implies the hypothesis cannot be rejected.

B.5 Skewness and Kurtosis

The skewness ψ_s and kurtosis ψ_k of a distribution are two commonly used characteristics to test whether a distribution deviates from a normal distribution. The skewness measures the asymmetry of a distribution, that is the amount of data to the left or the right of the mean. A negative skewness implies that the data is more spread out to the left of the mean, a positive skewness corresponds to more spread to the right. The skewness ψ_s of a distribution is calculated by:

$$\psi_s = \frac{E(x-\mu)^3}{\sigma^3} = \frac{\sum_{i=1}^{n}(x_i-\mu)^3}{(n-1)\sigma^3} = \frac{\frac{1}{n-1}\sum_{i=1}^{n}(x_i-\mu)^3}{\left(\sqrt{\frac{1}{n-1}\sum_{i=1}^{n}(x_i-\mu)^2}\right)^3}. \tag{B.13}$$

The kurtosis is a measure for the amount and magnitude of the values below or above the normal distribution. A normal distribution has a kurtosis of 3. A kurtosis less than 3 indicates a less outlier prone distribution, a value above three a more outlier prone distribution [165]. The kurtosis ψ_k is defined as:

$$\psi_k = \frac{E(x-\mu)^4}{\sigma^4} = \frac{\sum_{i=1}^{n}(x_i-\mu)^4}{(n-1)\sigma^4} = \frac{(n-1)\sum_{i=1}^{n}(x_i-\mu)^4}{\left(\sum_{i=1}^{n}(x_i-\mu)^2\right)^2}. \tag{B.14}$$

The skewness and kurtosis are determined for all data sets, see table B.2. Both a normal and lognormal distribution is assumed. A smaller skewness is observed for the majority of the analysed data sets assuming a lognormal distribution (6 exceptions on κ, 3 on λ). In nearly all cases, the kurtosis is closer to 3 under the assumption of a lognormal distribution (only 3 exceptions on κ, from which one out of the set of exceptions of the skewness, and 3 on λ).

Table B.2: *Skewness and kurtosis the distributions of the dimensionless width κ and dimensionless length λ of the fabrics B1, B2 and B3 for various shear angles.*

			κ				λ			
			linear		logarithmic		linear		logarithmic	
		γ	ψ_s	ψ_k	ψ_s	ψ_k	ψ_s	ψ_k	ψ_s	ψ_k
B1	top	0	0.92	3.36	0.42	2.77	–	–	–	–
		30	0.95	4.00	-0.06	2.87	1.11	4.20	0.33	2.87
		45	1.17	4.41	-0.01	3.11	1.25	3.84	0.38	2.50
	bottom	0	0.31	2.72	-0.24	2.98	–	–	–	–
		30	1.06	5.45	-0.17	3.98	2.48	12.60	0.82	5.91
		45	-0.22	2.39	-0.75	3.19	1.46	6.51	0.31	3.67
B2	top	0	0.94	4.40	-0.29	3.75	0.95	5.02	-0.12	4.04
		30	1.26	5.99	0.03	3.23	0.78	3.91	0.00	3.51
		45	0.55	2.80	-0.18	2.62	0.71	3.65	-0.02	3.00
	bottom	0	-0.10	2.37	-0.45	2.83	1.16	4.95	0.30	3.75
		30	0.04	2.49	-0.57	3.36	1.94	7.42	0.95	4.39
		45	0.10	2.26	-0.80	3.37	1.46	5.37	0.39	3.26
B3	top	0	0.61	3.42	-0.49	3.28	0.17	2.48	-0.37	2.82
		15	-0.07	2.37	-0.77	2.75	0.99	3.94	0.38	2.63
		30	1.57	5.83	0.18	2.99	1.67	7.78	-0.04	3.91
		45	1.17	4.56	0.12	2.81	1.14	4.24	-0.03	2.95
		60	1.81	8.01	0.37	3.41	0.92	3.80	-0.37	3.30
	bottom	0	0.06	3.17	-0.88	4.23	-0.02	2.74	-0.51	3.11
		15	0.54	3.72	-0.53	3.77	0.52	2.81	-0.01	2.40
		30	1.97	11.83	-0.49	4.98	0.52	4.23	-0.56	4.49
		45	1.26	5.12	0.09	3.78	1.78	6.99	0.27	3.59
		60	0.93	4.15	-0.29	3.04	0.45	3.18	-0.25	2.47

Appendix C

Duct Flows

The channels in the network model presented in section 3.2 are assumed to have a constant circular shaped cross–section. The pressure gradient is constant in channels with a constant radius (for the stationary, incompressible flow that is assumed here). Hence, linear elements can be applied in the finite element discretisation. The radii of the channels are based on the dimensions of the SYD. A derivation of the equivalent radii is presented here.

The flow in the channel is one–dimensional. The solution of the axial fluid velocity u is found by solving the impulse equation on an infinitesimally small part of the flow domain, as depicted in figure C.1. The equations are derived in the cylindrical coordinates (x, r, θ) rather than in the cartesian coordinates (x, y, z).

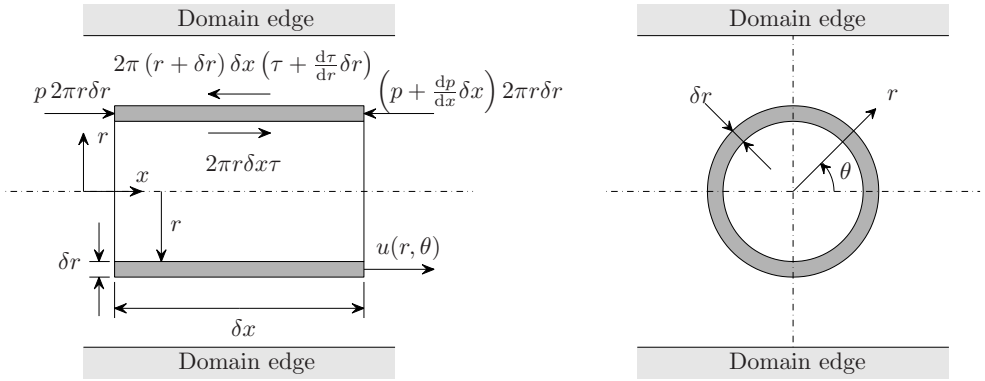

Figure C.1: *The impulse acting on an infinitesimally small part of the flow domain. p: pressure; τ: shear stress; (x, r, θ): cylindrical coordinates; δ: infinitesimally small part.*

The total impulse on the infinitesimal small part is given by:

$$\begin{aligned} p\,\pi r\delta r - \left(p + \frac{\mathrm{d}p}{\mathrm{d}x}\delta x\right) 2\pi r\delta r + 2\pi r\delta x\tau - 2\pi\left(r+\delta r\right)\delta x\left(\tau + \frac{\mathrm{d}\tau}{\mathrm{d}r}\delta r\right) = \\ -2\pi\delta x\delta r\, r\frac{\mathrm{d}p}{\mathrm{d}x}r - 2\pi\delta x\delta r\, r\frac{\mathrm{d}\tau}{\mathrm{d}r} - 2\pi\delta x\delta r\tau - 2\pi\delta x\delta r\frac{\mathrm{d}\tau}{\mathrm{d}r}\delta r = \\ -2\pi\delta x\delta r\left(r\frac{\mathrm{d}p}{\mathrm{d}x} + \frac{\mathrm{d}(\tau r)}{\mathrm{d}r}\right) = 0. \end{aligned} \tag{C.1}$$

The higher order term (last term on the second line of (C.1)) is neglected to obtain the final result. The constitutive equation:

$$\underline{\boldsymbol{\sigma}}_d = 2\mu\underline{\boldsymbol{D}}, \tag{C.2}$$

and the definition of the deviatoric rate of deformation $\underline{\boldsymbol{D}}$:

$$\underline{\boldsymbol{D}} = \frac{1}{2}\left(\boldsymbol{u}\,\boldsymbol{\nabla} + \boldsymbol{\nabla}\boldsymbol{u}\right), \tag{C.3}$$

are substituted in the part between brackets of the last equation of (C.1), resulting in:

$$\tau = -\mu\frac{\mathrm{d}u(x,r,\theta)}{\mathrm{d}r}. \tag{C.4}$$

$$r\frac{\mathrm{d}p}{\mathrm{d}x} - \mu\frac{\mathrm{d}}{\mathrm{d}r}\left(r\frac{\mathrm{d}u(x,r,\theta)}{\mathrm{d}r}\right) = 0. \tag{C.5}$$

The velocity profile $u(x,r,\theta)$ is solved by a double integration over r, leading to the general solution, formulated as:

$$u(x,r,\theta) = \frac{1}{4\mu}\frac{\mathrm{d}p}{\mathrm{d}x}r^2 + \psi, \tag{C.6}$$

$$\nabla^2\psi = 0, \tag{C.7}$$

with $u(x,r,\theta)$ the fluid velocity in axial direction, μ the viscosity and ψ an arbitrary function. The problem is now reduced to finding the function ψ, *id est* solving a homogeneous second order partial differential equation. The general solution for ψ is [112]:

$$\begin{aligned} \psi = a_0 + b_0\ln r + \\ \sum_{k=1}^{\infty}\left(a_k r^k\cos k\theta + b_k r^k\sin k\theta + c_k r^{-k}\cos k\theta + d_k r^{-k}\sin k\theta\right). \end{aligned} \tag{C.8}$$

The coefficients in this general function depend on the shape of the domain and the boundary conditions. Here, only the function representing the flow in a channel with a circular cross–section is relevant. This velocity profile is represented by:

$$u(x,r,\theta) = \frac{r^2 - r_{out}^2(x)}{4\mu}\frac{\mathrm{d}p}{\mathrm{d}x}, \tag{C.9}$$

with $r_{out}(x)$ the radius of the channel, that can vary along the axial coordinate x. The flow Φ through a channel is found by integrating the velocity profile over the cross–sectional area $\mathcal{A}$ of the channel:

$$\Phi = \int_{\mathcal{A}} u(x,r,\theta)\,\mathrm{d}\mathcal{A} = \int_{\theta=0}^{2\pi}\int_{r=0}^{r_{out}(x)} u(x,r,\theta) r \mathrm{d}r\mathrm{d}\theta. \tag{C.10}$$

Substitution of (C.9) in (C.10) leads to:

$$\Phi = \frac{\pi r_{out}^4(x)}{8\mu}\frac{\mathrm{d}p}{\mathrm{d}x}. \tag{C.11}$$

The flow in the channel is constant, since the fluid is incompressible. It is therefore possible to rewrite (C.11) and solve the resulting equation for the pressure:

$$\mathrm{d}p = -\frac{8\mu\Phi}{\pi} r^{-4}(x)\mathrm{d}x; \tag{C.12}$$

$$p(x) = -\frac{8\mu\Phi}{\pi}\int_{x=0}^{L} r^{-4}(x)\mathrm{d}x, \tag{C.13}$$

with L the length of the channel. The integral in (C.13) cannot be calculated analytically in all cases. However, an analytical solution is available provided the function $r_{out}(x)$ is either a polynomial or can be approximated by a polynomial (for example by means of a Taylor series approximation). Here, a linear function for the radius is employed, based on the wedged shape of the SYDs. The resulting channel is depicted in figure C.2.

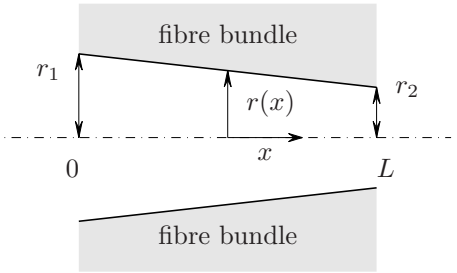

Figure C.2: *A linearly varying channel radius is used to describe the shape of the SYD in the plane of the fabric.*

The function describing the linearly varying channel radius, with radii r_1 at $x = 0$ and r_2 at $x = L$ is given as:

$$r(x) = \frac{r_2 - r_1}{L}x + r_1, \tag{C.14}$$

This equation is substituted in the integral in (C.13), which is subsequently solve. The solution of the pressure $p(x)$ reads:

$$p(x) = -\frac{8\mu\Phi L}{3\pi\left(\frac{r_2 - r_1}{L}x + r_1\right)^3 (r_2 - r_1)}; \tag{C.15}$$

The pressure drop over the channel equals:

$$\Delta P = p(x)\big|_{x=L} - p(x)\big|_{x=0} = -\frac{8\mu\Phi L}{3\pi r_2^3 (r_2 - r_1)} + \frac{8\mu\Phi L}{3\pi r_1^3 (r_2 - r_1)}. \tag{C.16}$$

Rearranging the variables in (C.16) results in an expression for the flow Φ, that is compared to (C.11), with the outer radius r_{out} replaced by the equivalent radius r_E:

$$\Phi = \frac{3\pi r_1^3 r_2^3}{8\mu (r_2^2 + r_1 r_2 + r_1^2)} \frac{\Delta P}{L} = \frac{\pi r_E^4}{8\mu} \frac{\Delta p}{L} \tag{C.17}$$

Note that the pressure gradient is expressed as the pressure drop Δp divided by the channel length L. The radius of a channel, that has an equal resistance compared to a channel with a linearly varying channel radius, is found to be:

$$r_E = \left(\frac{3 r_1^3 r_2^3}{r_1^2 + r_1 r_2 + r_2^2}\right)^{\frac{1}{4}}. \tag{C.18}$$

Note that $r(x)$ defined in (C.14) is replaced by the hydraulic radius for a channel with a non–circular cross–section. The hydraulic radius is:

$$r_h(x) = \frac{2\mathcal{A}(x)}{\mathcal{P}(x)} = \frac{\pi r(x)^2}{\pi r} = \frac{b(x)h(x)}{(b(x) + h(x))}, \tag{C.19}$$

with $b(x)$ and $h(x)$ the width and height, defined as functions of the axial coordinate. The relation between the equivalent radius r_E of the channel and the permeability of the channel K is found by comparing (C.17) (or (C.11)) with Darcy's law:

$$\Phi = \frac{\pi r_E^4}{8\mu} \frac{\mathrm{d}p}{\mathrm{d}x} = \frac{K}{\mu} \frac{\mathrm{d}p}{\mathrm{d}x} \Rightarrow K = \frac{\pi r_E^4}{8}. \tag{C.20}$$

This equation is used to determine the individual channel permeabilities in the network formulation, with r_E as defined in (C.18), derived using the hydraulic radius (C.19) to determine the radii r_1 and r_2. The height is assumed constant, $h(x) = h$, and the width linearly variable along the axial coordinate, analogously to (C.14).

Appendix D

Finite Element Discretisation

A finite element discretisation [115, 116] was implemented to solve the permeability of the network, as was explained in chapter 3. Some additional comments on the finite element formulation are collected in this appendix.
The system of nodes and element representing the flow domain is depicted in figure D.1. The figure shows a set of six repetitive blocks, indicated by the dashed lines. The dimensions of a repetitive block are $A \times B$, *id est* for the studied fabrics roughly 5×2mm.
The linear element interpolation function $\boldsymbol{N}(x)$ that is used, reads:

$$\boldsymbol{N}(x) = \{1 - x, x\}^T, \tag{D.1}$$

with x the normalised coordinate between two adjacent nodes. The method of Galerkin [115, 116] was used, combined with Darcy's law as the constitutive equation. The resulting system of equations is:

$$\int \frac{\partial \boldsymbol{N}}{\partial x} \frac{K}{\mu} \cdot \frac{\partial p}{\partial x} \, \mathrm{d}x = \int \frac{\partial \boldsymbol{N}}{\partial x} \frac{K}{\mu L} \frac{\partial \boldsymbol{N}}{\partial x} \mathrm{d}x \cdot \boldsymbol{p} = \boldsymbol{M} \cdot \boldsymbol{p} = \boldsymbol{\varphi}, \tag{D.2}$$

with $\boldsymbol{p}$ the vector containing the nodal pressures, $\boldsymbol{\varphi}$ the vector containing the nodal fluxes and $\boldsymbol{M}$ the system matrix.
The finite element discretisation is implemented in MATLAB©. A direct solving routine is employed, combined with a Jacobi–preconditioner [117] to control the condition of the system matrix $\boldsymbol{M}$.
The matrix $\boldsymbol{M}$ is constructed by superposition of the sub matrices:

$$\boldsymbol{M} = \sum_{e=1}^{N_E} \boldsymbol{M}_{sub}^{(e)}; \tag{D.3}$$

$$\boldsymbol{M}_{sub}^{(e)} = \boldsymbol{P}^{(e)} \cdot \frac{\partial \boldsymbol{N}^{(e)}}{\partial x} \frac{K^{(e)}}{\mu L^{(e)}} \left(\frac{\partial \boldsymbol{N}^{(e)}}{\partial x} \right)^T \cdot \left(\boldsymbol{P}^{(e)} \right)^T, \tag{D.4}$$

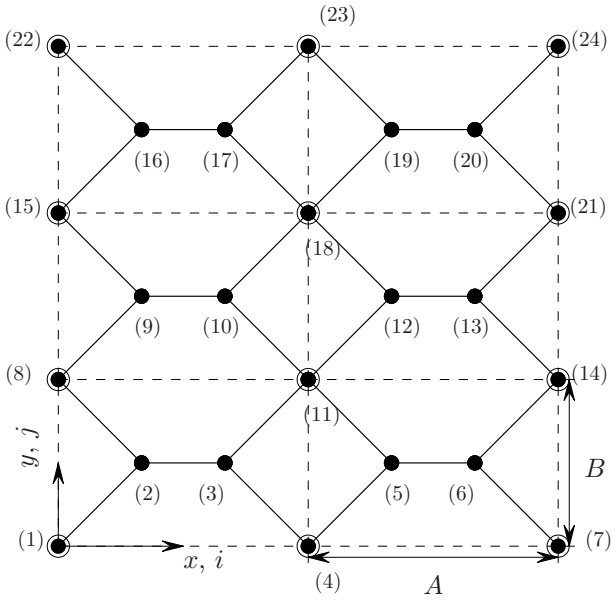

Figure D.1: *Elements (lines) and nodes (dots with corresponding numbers) representing the network of flow channels. The dashed lines indicate the repetitive blocks of the system. The encircled nodes correspond to the centres of the SYDs.*

with $P^{(e)}$ a $N_{DOF} \times 2$ matrix with:

$$\begin{aligned} P^{(e)}(i,1) &= 1 \quad i = \text{first node of element } e; \\ P^{(e)}(j,2) &= 1 \quad j = \text{second node of element } e; \\ P^{(e)}(k,1) = P^{(e)}(k,2) &= 0 \quad k \neq i \wedge k \neq j. \end{aligned} \tag{D.5}$$

The matrix $\boldsymbol{M}$ is a band matrix. This allows efficient storage of the matrix, which is essential if the number of degrees of freedom becomes large. The total number of nodes and degrees of freedom (DOF) N_{tot} equals:

$$N_{tot} = (3N_1 + 1) \times N_2 + N_1 + 1, \tag{D.6}$$

for a system consisting of $N_1 \times N_2$ repetitive blocks.
The condition of the matrix affects the accuracy of the results. The condition of the matrix depends partly on the variation of the absolute values in the matrix. A large ratio between the largest number and the smallest number results in a large condition number (read: a poor condition).
Applying the boundary conditions results in unit values on the diagonal of the matrix[1]. The condition of the matrix is consequently rather poor. Therefore the matrix is

[1]The channel permeability values are of the order of 10^{-12} m^4, see section 3.1.2.

scaled prior to applying the boundary conditions. A Jacobi preconditioning of the matrix scales the elements in the matrix such that the values on the diagonal equal 1. Applying the Jacobi preconditioning [117] results in the following steps:

1. Given $\boldsymbol{M} \cdot \boldsymbol{p} = \boldsymbol{\varphi}$, calculate $\boldsymbol{D} = \mathrm{diag}\,(\boldsymbol{M})$;
2. Scale the element matrix: $\widehat{\boldsymbol{M}} = \sqrt{\boldsymbol{D}^{-1}} \cdot \boldsymbol{M} \cdot \sqrt{\boldsymbol{D}^{-1}}$;
3. Scale the right hand side vector: $\widehat{\boldsymbol{\varphi}} = \sqrt{\boldsymbol{D}^{-1}} \cdot \boldsymbol{\varphi}$;
4. Solve $\widehat{\boldsymbol{p}}$ from $\widehat{\boldsymbol{M}} \cdot \widehat{\boldsymbol{p}} = \widehat{\boldsymbol{\varphi}}$;
5. Scale the solution to obtain the solution of the original system: $\boldsymbol{p} = \sqrt{\boldsymbol{D}^{-1}} \cdot \widehat{\boldsymbol{p}}$.

The condition of the matrix significantly improves if the scaling is applied. However, the condition number is still relatively high for larger matrices. In practice, this implies that the size of the network that can be analysed is limited by the condition number of the system matrix $\boldsymbol{M}$. The accuracy ε of the solution is related to the order of the condition number ζ and the order of the convergence tolerance e according to:

$$\mathcal{O}(\varepsilon) = \mathcal{O}(e) + \mathcal{O}(\zeta) \tag{D.7}$$

The convergence tolerance of direct solvers is the machine precision, which is 10^{-16}. An accuracy of 10^{-10} results for a condition number of $\mathcal{O}(10^5)$.
The condition number ζ of the element matrix $\boldsymbol{M}$ is plotted in figure D.2. The condition number increases rapidly with increasing number of degrees of freedom. However, systems up to $4{\cdot}10^4$ degrees of freedom can be solved with sufficient accuracy (extrapolated condition number $\approx 4 \cdot 10^9$, the dashed line in figure D.2 represents the extrapolation).

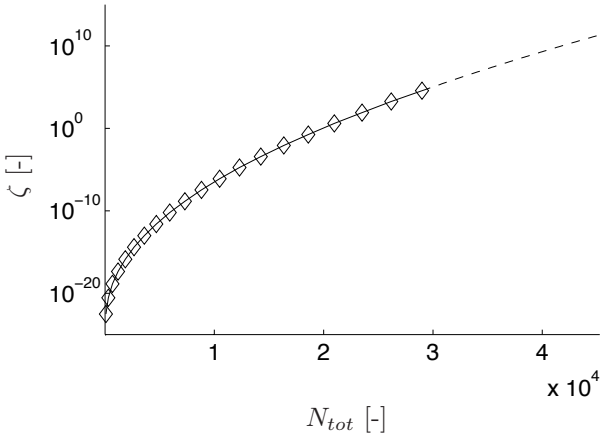

Figure D.2: *The averaged condition number ($n_{sets} = 5$, $n_{permu} = 5$) of the element matrix versus the number of degrees of freedom. The network size varies from 1 to 20 times the base configuration. The dotted line is an extrapolation.*

Appendix E

Pressure Field During Impregnation

The pressure field inside the mould is derived in this appendix. The resulting force that is exerted on the mould, results in a deflection of the mould. The deflection of the mould is undesirable, since it is generally not measured during the measurement. Moreover, the permeability strongly depends on the fibre content. Hence, unexpected results may be observed if the mould deflection is not controlled.
A field in which mould deflection is as inevitable as wanted, is the field of Resin Infusion under Flexible Tooling. The varying cavity height needs to be accounted for explicitly, as for example explained by Kessels [132].
The pressure field is derived by substitution of Darcy's law in the continuity equation, leading to a differential equation which is solved for the pressure p. Darcy's law reads:

$$\Phi = \frac{\underline{\underline{\boldsymbol{K}}}}{\mu} \cdot \boldsymbol{\nabla} p, \tag{E.1}$$

with Φ the volumetric flow, $\underline{\underline{\boldsymbol{K}}}$ the permeability tensor, μ the dynamic viscosity of the fluid and $\boldsymbol{\nabla} p$ the pressure gradient. Hence, it hence follows that:

$$\nabla \cdot \boldsymbol{u} = \nabla \cdot \left(\frac{\underline{\underline{\boldsymbol{K}}}}{\mu} \boldsymbol{\nabla} p \right) = 0 \rightarrow \nabla^2 p = 0. \tag{E.2}$$

Note that a scaling of the axis is required in case of an anisotropy material. The boundary conditions to solve the differential equation read:

$$\begin{aligned} p\big|_{x=x_0} &= P_{inj}; \\ p\big|_{x=x_f} &= 0, \end{aligned} \tag{E.3}$$

where the subscript 0 refers to the start position and the subscript f to the location of the flow front. The pressures are relative to the ambient pressure. The pressure

field in case of a line injection is derived as:

$$\frac{\partial^2 p}{\partial x^2} = 0; \tag{E.4}$$

$$p(x) = \frac{x_f - x}{x_f - x_0} P_{inj}, \tag{E.5}$$

with x the flow direction of the fluid. The pressure field in case of a radial injection is found applying polar coordinates, rewriting (E.4) to:

$$\frac{1}{r}\frac{\partial}{\partial r}\left(r\frac{\partial p}{\partial r}\right) = 0; \tag{E.6}$$

$$p(r) = \frac{\ln r_f - \ln r}{\ln r_f - \ln r_0} P_{inj} = \frac{\ln \frac{r}{r_f}}{\ln \frac{r_0}{r_f}} P_{inj}. \tag{E.7}$$

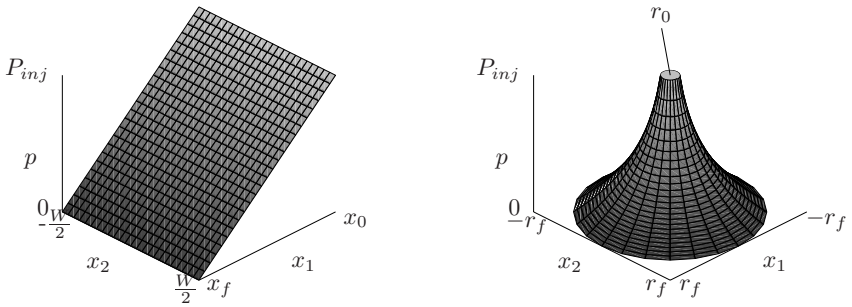

(a) *Line injection.* (b) *Radial injection.*

Figure E.1: *Pressure fields for linear and radial injection. W is the width of the mould, x_0 is the location of the injection line, r_0 is the radius of the injection point, x_f and r_f are the linear and radial distances to the flow front.*

The pressure fields for a line injection and a radial injection are depicted in figure E.1. The pressure gradients in the mould for linear and radial injection are given by:

$$\frac{\partial p}{\partial x} = -\frac{1}{x_f - x_0} P_{inj}; \tag{E.8}$$

$$\frac{\partial p}{\partial r} = -\frac{1}{r \ln \frac{r_0}{r_f}} P_{inj}, \tag{E.9}$$

respectively. The pressure gradient is constant for linear injection, whereas it is proportional to the inverse of the radius for a radial injection. This leads to large differences in the fluid flow and a less stable flow (irregular shape of the flow front, constantly changing its irregularity as the flow front advances). Consequently, the reproducibility of the radial injection technique is more prone to inaccuracies in the preform than the linear injection technique. Small deviations near the centrally located injection point can cause relatively large deviations in the flow front at larger distances from the injection point.

Appendix F

Permeability 1D Flow

The permeability tensor is derived based on three individual measurements in case of a one–dimensional permeability experiment. The mathematics required to determine the principal permeabilities based on the three measured permeability values is presented here.
The three individual measurements are performed with different orientations of the fabric with respect to the coordinate system of the mould. The fabric orientation is the angle of the machine direction of the fabric with respect to the flow direction in the mould.
Let $\boldsymbol{x}^G$ be the coordinate system of the mould and $\boldsymbol{x}^P$ the principal coordinate system, as depicted in figure F.1. The yet unknown angle θ is the angle between both

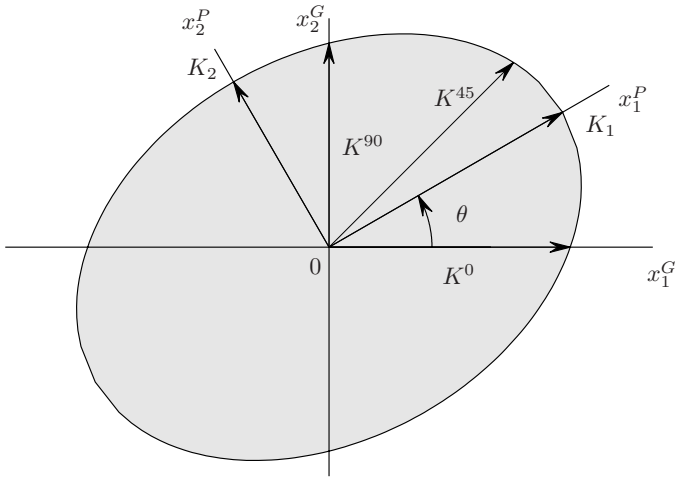

Figure F.1: *The principal permeabilities K_1 and K_2 are calculated based on the three measured permeabilities K^0, K^{45} and K^{90}. The angle θ is the angle between the principal directions $\boldsymbol{x}^P$ and the global coordinate system $\boldsymbol{x}^G$.*

coordinate systems. Any set of three mutually different fabric orientations could be used, but in practice the orientations 0^o, 45^o and 90^o are used. Hence, the measured values K^0, K^{45} and K^{90} are obtained from the measurements.
The three measured permeabilities K^0, K^{45} and K^{90} define an ellipse, which major and minor axis correspond to the principal directions x_1^P and x_2^P respectively. This ellipse can be described in coordinates of the global coordinate system ($\boldsymbol{x}^G$) and in the coordinates of the principal coordinate system ($\boldsymbol{x}^P$). Moreover, the principal directions can be expressed in terms of the global directions. This is sufficient to solve the principal permeabilities in terms of the three measured permeabilites.
The function describing an arbitrarily oriented ellipse reads:

$$a_1 \left(x_1^G\right)^2 + a_2 x_1^G x_2^G + a_3 \left(x_2^G\right)^2 = 1, \tag{F.1}$$

with a_i constants. (Note that the origin of the ellipse corresponds to the origin of the global coordinate system). The function describing the same ellipse in principal coordinates reads:

$$\left(\frac{x_1^P}{K_1}\right)^2 + \left(\frac{x_2^P}{K_2}\right)^2 = 1. \tag{F.2}$$

The relation between the two coordinate systems is given by:

$$\boldsymbol{x}^P = \boldsymbol{R} \cdot \boldsymbol{x}^G, \tag{F.3}$$

with $\boldsymbol{R}$ the rotation matrix:

$$\boldsymbol{R} = \begin{bmatrix} \cos\theta & \sin\theta \\ -\sin\theta & \cos\theta \end{bmatrix}. \tag{F.4}$$

The measurements provide three points, in global coordinates, on the ellipse:

$$\begin{aligned} \boldsymbol{x}_{(1)}^G &= \left\{K^0, 0\right\}; \\ \boldsymbol{x}_{(2)}^G &= \left\{\tfrac{1}{\sqrt{2}}K^{45}, \tfrac{1}{\sqrt{2}}K^{45}\right\}; \\ \boldsymbol{x}_{(3)}^G &= \left\{0, K^{90}\right\}. \end{aligned} \tag{F.5}$$

The coefficients a_i are determined with the coordinates defined in (F.5):

$$\begin{aligned} a_1 \left(K^0\right)^2 + a_2 K^0 \cdot 0 + a_3 0^2 = 1 \Rightarrow a_1 &= \frac{1}{\left(K^0\right)^2}; \\ a_1 \left(\frac{K^{45}}{\sqrt{2}}\right)^2 + a_2 \left(\frac{K^{45}}{\sqrt{2}}\right)^2 + a_3 \left(\frac{K^{45}}{\sqrt{2}}\right)^2 = 1 \Rightarrow a_2 &= \frac{2}{\left(K^{45}\right)^2} - \frac{1}{\left(K^0\right)^2} - \frac{1}{\left(K^{90}\right)^2}; \\ a_1 0^2 + a_2 \cdot 0 \cdot K^{90} + a_3 \left(K^{90}\right)^2 = 1 \Rightarrow a_3 &= \frac{1}{\left(K^{90}\right)^2}. \end{aligned} \tag{F.6}$$

The coefficients a_i can also be expressed in terms of the principal permeabilities. The principal coordinates in (F.2) are expressed in the global coordinates:

$$\left(\frac{x_1^G\cos\theta + x_2^G\sin\theta}{K_1}\right)^2 + \left(\frac{x_2^G\cos\theta - x_1^G\sin\theta}{K_2}\right)^2 = 1, \tag{F.7}$$

and after the terms in the equation are rearranged:

$$\left(\left(\frac{\cos\theta}{K_1}\right)^2 + \left(\frac{\sin\theta}{K_2}\right)^2\right)x_1^G + \left(\frac{1}{K_1^2} - \frac{1}{K_2^2}\right)2\sin\theta\cos\theta\, x_1^G x_2^G + \left(\left(\frac{\sin\theta}{K_1}\right)^2 + \left(\frac{\cos\theta}{K_2}\right)^2\right)x_2^G = 1, \tag{F.8}$$

from which the solution of a_i follows as:

$$\begin{aligned} a_1 &= \left(\frac{\cos\theta}{K_1}\right)^2 + \left(\frac{\sin\theta}{K_2}\right)^2; \\ a_2 &= \left(\frac{1}{K_1^2} - \frac{1}{K_2^2}\right)2\sin\theta\cos\theta; \\ a_3 &= \left(\frac{\sin\theta}{K_1}\right)^2 + \left(\frac{\cos\theta}{K_2}\right)^2. \end{aligned} \tag{F.9}$$

Subtracting a_2 from a_1, using both (F.6) and (F.9), leads to the equality:

$$\left(\cos^2\theta - \sin^2\theta\right)\left(\frac{1}{K_1^2} - \frac{1}{K_2^2}\right) = \frac{1}{\left(K^0\right)^2} - \frac{1}{\left(K^{90}\right)^2}. \tag{F.10}$$

Substitution of (F.10) in the solution for the coefficient a_2 in (F.9) and comparing it to the solution of (F.6) gives:

$$\begin{aligned} &\frac{\sin 2\theta}{\cos 2\theta}\left(\frac{1}{\left(K^0\right)^2} - \frac{1}{\left(K^{90}\right)^2}\right) = \frac{2}{\left(K^{45}\right)^2} - \frac{1}{\left(K^0\right)^2} - \frac{1}{\left(K^{90}\right)^2} \Rightarrow \\ &\tan 2\theta = \left(\frac{2}{\left(K^{45}\right)^2} - \frac{1}{\left(K^0\right)^2} - \frac{1}{\left(K^{90}\right)^2}\right)\left(\frac{\left(K^0\right)^2\left(K^{90}\right)^2}{\left(K^{90}\right)^2 - \left(K^0\right)^2}\right). \end{aligned} \tag{F.11}$$

Similarly, the summation of the coefficients a_1 and a_2, using both (F.6) and (F.9), results in:

$$\frac{1}{K_1^2} + \frac{1}{K_2^2} = \frac{1}{\left(K^0\right)^2} + \frac{1}{\left(K^{90}\right)^2}. \tag{F.12}$$

This can be used to express K_2 in terms of K_1, K^0 and K^{90}, which is then substituted in solution of a_1:

$$\frac{\cos^2\theta}{K_1^2} + \left(\frac{1}{\left(K^0\right)^2} + \frac{1}{\left(K^0\right)^2} - \frac{1}{K_1^2}\right)\sin^2\theta = \frac{1}{\left(K^0\right)^2}. \tag{F.13}$$

The expression for K_1 is obtained after some rearrangements:

$$K_1 = \sqrt{\frac{\left(K^0\right)^2 \left(K^{90}\right)^2 \cos 2\theta}{\left(K^{90}\right)^2 \cos^2\theta - \left(K^0\right)^2 \sin^2\theta}}. \tag{F.14}$$

The solution for K_2 is found similarly, by expressing K_1 in terms of K_2, K^0 and K^{90}.

The three equations to determine the orientation of the principal directions and the principal permeabilities, based on the three measured permeabilities K^0, K^{45} and K^{90}, are:

$$\theta = \frac{1}{2}\arctan\left(\frac{2\left(K^0\right)^2\left(K^{90}\right)^2 - \left(K^{45}\right)^2\left(K^{90}\right)^2 - \left(K^0\right)^2\left(K^{45}\right)^2}{\left(K^{45}\right)^2\left(\left(K^{90}\right)^2 - \left(K^0\right)^2\right)}\right); \tag{F.15}$$

$$K_1 = \sqrt{\frac{\left(K^0\right)^2 \left(K^{90}\right)^2 \cos 2\theta}{\left(K^{90}\right)^2 \cos^2\theta - \left(K^0\right)^2 \sin^2\theta}}; \tag{F.16}$$

$$K_2 = \sqrt{\frac{\left(K^0\right)^2 \left(K^{90}\right)^2 \cos 2\theta}{\left(K^0\right)^2 \cos^2\theta - \left(K^{90}\right)^2 \sin^2\theta}}. \tag{F.17}$$

The anisotropy α reads:

$$\alpha = \frac{K_2}{K_1} = \sqrt{\frac{\left(K^{90}\right)^2 \cos^2\theta - \left(K^0\right)^2 \sin^2\theta}{\left(K^0\right)^2 \cos^2\theta - \left(K^{90}\right)^2 \sin^2\theta}}. \tag{F.18}$$

Note that K^{45} can be written in terms of K^0 and K^{90}, if the orientation of the principal directions correspond to the global directions, *id est* $\theta = 0$. The coefficient a_2 in (F.6) equals zero in that case, from which directly follows:

$$\frac{2}{\left(K^{45}\right)^2} - \frac{1}{\left(K^0\right)^2} - \frac{1}{\left(K^{90}\right)^2} = 0 \rightarrow K^{45} = \frac{\sqrt{2}K^0K^{90}}{\sqrt{\left(K^0\right)^2 + \left(K^{90}\right)^2}}. \tag{F.19}$$

Let $K^0 = K_1$ and $K^{90} = K_2$, which follows from $\theta = 0$. The expression (F.19) can then be rewritten to:

$$K^{45} = \frac{\alpha\sqrt{2}}{\sqrt{1+\alpha^2}}K^0. \tag{F.20}$$

with the anisotropy α defined as:

$$\alpha = \frac{K_2}{K_1}. \tag{F.21}$$

The permeability K^{45} equals K^0 if α equals 1, which is expected for isotropic material. Similarly, it shows that a high value of K^{45} (read: higher than K^0 or K^{90}) can only be found if the principal directions are rotated with respect to the directions of K^0 or K^{90}, since the fraction in (F.20) cannot exceed a value of one. The rotation approaches 45° if K^{45} is large compared to K^0 and K^{90}.

Appendix G

Permeability 2D Flow

The applied method to calculate the permeability from a two–dimensional flow is based on the assumption that the shape of the flow front is elliptical. The position of the flow front is analysed at a number of points in time and elliptical coordinates are employed to determine the permeability. The theory can be found in [122, 158–161]. An elliptical flow front is depicted in figure G.1. It shows all the relevant parameters:

- The global coordinate system $\boldsymbol{x}^G$, generally aligned with the rig, but strictly taken arbitrarily defined;
- The principal coordinate system $\boldsymbol{x}^P$ of the ellipse, also referred to as the local coordinate system;
- The major and minor radii $\boldsymbol{r}$ of the ellipse;
- The angle θ between the two coordinate systems;
- The translation $\boldsymbol{x}^0$ between the two coordinate systems;
- The radius r_0 of the inlet;
- The position of the flow front $\boldsymbol{x}_f$.

The procedure to derive the principal permeabilities and their orientation from the flow front, acquired at a series of (equidistant) moments in time t_i, involves the steps:

1. Determine the major and minor radii $\boldsymbol{r}$ and the orientation θ of the flow front ellipses at the different moments in time.
2. Apply elliptical coordinates and express Darcy's law and the major and minor radii in these coordinates.
3. Fit an anisotropy that applies best for all acquired flow front ellipses.
4. Calculate the major permeabilities K_1 and K_2 from the fitted anisotropy.

The different items of the procedure are discussed separately.

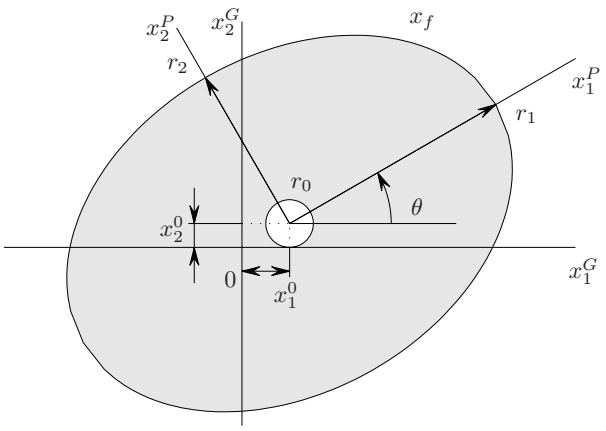

Figure G.1: *Elliptical flow front, with major and minor radii* (r_1, r_2) *in an arbitrarily defined global coordinate system* (x_1^G, x_2^G)*. The principal directions of the ellipse correspond to the local coordinate system* (x_1^P, x_2^P)*, rotated over an angle* θ *with respect to the global coordinate system and translated over* (x_1^0, x_2^0)*.* r_0 *is the radius of in the injection point and* $\boldsymbol{x}_f$ *is the position of the flow front.*

Least Squares Fit of an Ellipse The ellipse is fitted through the flow front position points employing a least squares algorithm for multiple variables. The procedure is explained in detail in [122].
The general description of an ellipse oriented in an arbitrary direction and with an arbitrary offset $\boldsymbol{x}^0$ (see figure G.1) is:

$$a_1\chi_1^2 + a_2\chi_1\chi_2 + a_3\chi_2^2 + a_4\chi_1 + a_5\chi_2 = 1, \tag{G.1}$$

with:

$$\boldsymbol{\chi} = \boldsymbol{x}^G - \boldsymbol{x}^0. \tag{G.2}$$

In other words the ellipse is described by a second order polynomial $\boldsymbol{\wp}_2(\boldsymbol{\chi})$ with coefficients $\boldsymbol{a}$, which allows us to write this formula in a somewhat more compacted form:

$$\boldsymbol{\wp}_2(\boldsymbol{\chi}) \cdot \boldsymbol{a} = 1. \tag{G.3}$$

Note that $\boldsymbol{\wp}_2$ is defined as a vector. Its length corresponds to the number of basic polynomial functions and thus to the number of coefficients $\boldsymbol{a}$.
A best fit is obtained if the sum of the squared deviations in all measured positions with respect to the ellipse is minimal:

$$\min f(\boldsymbol{a}) = \min\left(\sum_{i=1}^{n} \left(\boldsymbol{\wp}_2(\boldsymbol{\chi}_i) - 1\right)^2\right). \tag{G.4}$$

The minimum of $f(\boldsymbol{a})$ is found by evaluation of the partial derivatives:

$$\frac{\partial f}{\partial \boldsymbol{a}} = \boldsymbol{0}. \tag{G.5}$$

Solving the resulting system of linear equations yields the coefficients $\boldsymbol{a}$.
Alternatively the ellipse can be expressed in the principal directions $\boldsymbol{x}^P$ as:

$$\left(\frac{x_1^P}{r_1}\right)^2 + \left(\frac{x_2^P}{r_2}\right)^2 = 1, \tag{G.6}$$

with r_1 and r_2 the major and minor radii of the ellipse (as indicated in figure G.1). This relation is equal to (G.1), since both describe the same ellipse, but in a different coordinate system. The principal coordinates $\boldsymbol{x}^P$ can be expressed in the arbitrary coordinates $\boldsymbol{x}^G$ according to:

$$\boldsymbol{x}^P = \boldsymbol{R} \cdot \boldsymbol{\chi} = \boldsymbol{R} \cdot \left(\boldsymbol{x}^G - \boldsymbol{x}^0\right), \tag{G.7}$$

with $\boldsymbol{x}^0$ a linear translation and $\boldsymbol{R}$ the rotation matrix.

$$\boldsymbol{R} = \begin{bmatrix} \cos\theta & \sin\theta \\ -\sin\theta & \cos\theta \end{bmatrix}. \tag{G.8}$$

Substituting this relation into (G.1) yields – after some rearrangements – the solution[1] for the ellipse radii $\boldsymbol{r}$, the angle θ between the arbitrary and principal direction and the linear translation $\boldsymbol{x}^0$:

$$\boldsymbol{r} = \left\{ \begin{array}{c} \sqrt{\dfrac{1 - \wp_2(\boldsymbol{x}_0) \cdot \boldsymbol{a}}{a_1 \cos^2\theta + \frac{a_2}{2}\sin 2\theta + a_3 \sin^2\theta}} \\ \sqrt{\dfrac{1 - \wp_2(\boldsymbol{x}_0) \cdot \boldsymbol{a}}{a_1 \sin^2\theta - \frac{a_2}{2}\sin 2\theta + a_3 \cos^2\theta}} \end{array} \right\}; \tag{G.9}$$

$$\theta = \frac{1}{2}\arctan\left(\frac{a_2}{a_1 - a_3}\right); \tag{G.10}$$

and

$$\begin{bmatrix} 2a_1\cos\theta + a_2\sin\theta & 2a_3\sin\theta + a_2\cos\theta \\ -2a_1\sin\theta + a_2\cos\theta & -a_2\sin\theta + 2a_3\cos\theta \end{bmatrix} \cdot \boldsymbol{x}^0 = -\boldsymbol{R}^T \cdot \left\{ \begin{array}{c} a_4 \\ a_5 \end{array} \right\}. \tag{G.11}$$

As discussed above, the orientation and consequently principal directions of the ellipses approximating the flow front position, are calculated from the experimental data. As a result, the calculated orientation of the ellipses can show changes during the progress of the experiment, as can the translation (or: the location of the centre). Theoretically, the orientation of the ellipse is undefined for unsheared orthogonal material (*id est* $K_1 = K_2$, a circular flow front) and the centre coincides exactly with the centre of the inlet. In practice the flow front is never a perfect circle and the least square approximation finds an ellipse with a certain orientation and a certain translation of the centre. It is suggested to fix the orientation and centre of the ellipse

[1] Compare the results obtained in appendix F, which is essentially the same, except for the linear translation $\boldsymbol{x}^0$

prior to fitting the measured data points and compare these results with the 'free' fit. A large deviation either suggest a poor fit, or local variations in the permeability.
A similar procedure can be followed for sheared fabrics: the orientation of the ellipse corresponds to the bisectrix of the smallest angle between the two fibre directions for balanced fabric, according to Lai and Young [151].
The second order polynomial (G.1) (or (G.3)) reduces to:

$$a_1 \left(x_1^G\right)^2 + a_2 x_1^G x_2^G + a_3 \left(x_2^G\right)^2 = 1. \tag{G.12}$$

Flow Front in Elliptical Coordinates A transformation to elliptical coordinates is applied. The mathematics behind coordinate transformation can – amongst others – be found in Happel [109].
The continuity equation, combined with Darcy's law in principal coordinates for an anisotropic material is represented by:

$$\boldsymbol{K} \cdot \frac{\partial^2 P'}{\partial \left(\boldsymbol{x}^P\right)^2} = 0, \tag{G.13}$$

with P' the dimensionless pressure, defined as:

$$P' = \frac{P - P_f}{\Delta P}. \tag{G.14}$$

The partial differential equation is reduced to a Laplace equation by applying the scaling:

$$\boldsymbol{x}' = \left\{ \begin{array}{c} \alpha^{\frac{1}{4}} \\ \alpha^{-\frac{1}{4}} \end{array} \right\} \cdot \boldsymbol{x}. \tag{G.15}$$

The anisotropy of the permeability is α: the ratio between the second and the first principal permeabilities, or the ratio between the squared minor and major axes of the ellipse:

$$\alpha = \frac{K_2}{K_1} = \left(\frac{r_2}{r_1}\right)^2. \tag{G.16}$$

Thus, (G.13) reduces to:

$$\nabla^2 P' = 0, \tag{G.17}$$

with the boundary conditions:

$$\begin{aligned} &P = P_0 \quad \text{at} \quad \left\{ \begin{array}{c} \alpha^{-\frac{1}{2}} \\ \alpha^{\frac{1}{2}} \end{array} \right\} \cdot \left(\frac{\boldsymbol{x}}{r_0}\right)^2 = 1; \\ &P = P_f \quad \text{at} \quad \Omega'_f(\boldsymbol{x}, t). \end{aligned} \tag{G.18}$$

The coordinate transformation to elliptical coordinates $\boldsymbol{\xi}$ is:

$$\begin{aligned} x'_1 &= L_f \cosh\xi \cos\eta; \\ x'_2 &= L_f \sinh\xi \sin\eta, \end{aligned} \tag{G.19}$$

with L_f half of the focal length of the inlet ellipse:

$$L_f = r_0 \left(\alpha^{-\frac{1}{2}} - \alpha^{\frac{1}{2}} \right)^{\frac{1}{2}}. \tag{G.20}$$

with r_0 the radius of the inlet and α the anisotropy of the principal permeabilities K_1 and K_2, as defined in (G.16).
A plot of the elliptical coordinates in a cartesian coordinate system is presented in figure G.2. The ellipses correspond to constant ξ and the lines to constant η. The two foci of the ellipse ($\xi \to 0$, $\eta = 0 \wedge \eta = \pi$) are indicated by a dot.

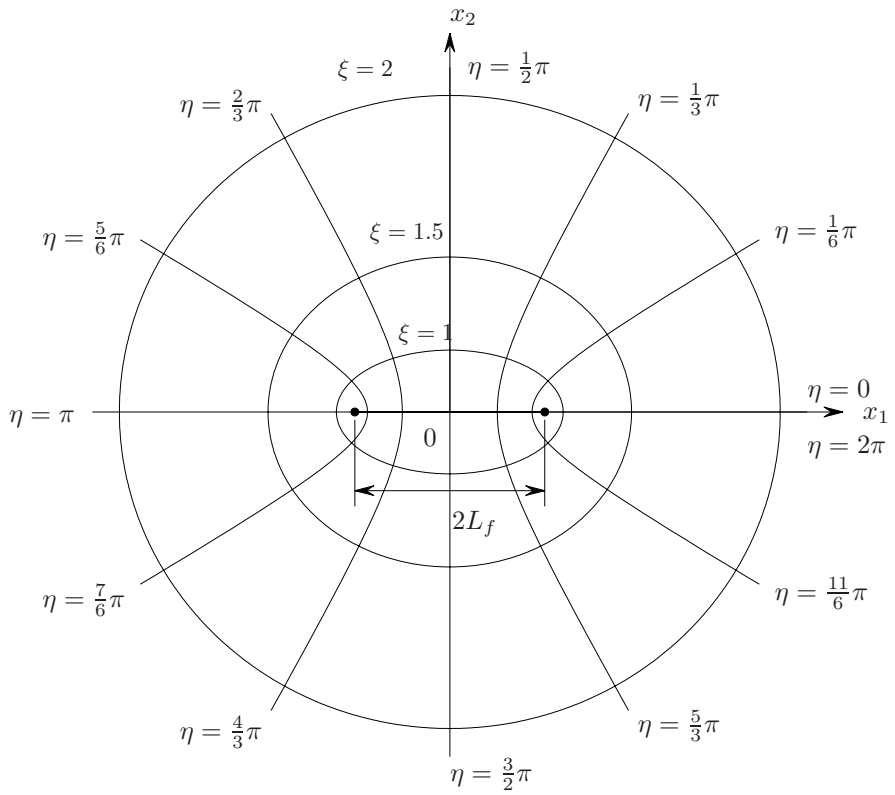

Figure G.2: *The two–dimensional elliptical coordinates (ξ, η) in a (x_1, x_2) cartesian coordinate system. The foci $\boldsymbol{x} = (\pm L_f, 0)$ are indicated by a dot. The ellipses correspond to a constant value of ξ and $\eta \in [0, 2\pi]$, the outwardly directed lines to a constant value of η and $\xi \in [0, \pm\infty]$.*

The coordinate transformation also affects the nabla (∇) and laplace (∇^2) differential operators:

$$\nabla = \boldsymbol{h}^J \cdot \left(\frac{\partial}{\partial \boldsymbol{\xi}} \right); \tag{G.21}$$

$$\nabla^2 = \boldsymbol{h}^{J^2} \cdot \left(\frac{\partial^2}{\partial \boldsymbol{\xi}^2} \right), \tag{G.22}$$

with h^J the metrical coefficient, that can be derive from:

$$\frac{1}{h^{J^2}_i} = \sum_{j=1}^{3} \left(\frac{\partial x_j}{\partial \xi_i} \right)^2, \quad (i = 1, 2, 3) \tag{G.23}$$

$\boldsymbol{h}^J$ is equal for both direction ξ and η (and unity for x_3) and written as single value rather than a vector:

$$h^J = \frac{1}{L_f \left(\sinh^2 \xi + \sin^2 \eta \right)^{\frac{1}{2}}} = \frac{1}{L_f \left(\cosh^2 \xi - \cos^2 \eta \right)^{\frac{1}{2}}}. \tag{G.24}$$

The Laplace equation (G.17) still holds, but now with respect to the elliptical coordinates $\boldsymbol{\xi}$ and with the boundary conditions:

$$\begin{aligned} &P = 1 \quad \text{at} \quad \xi = \xi_0 = \ln \left(\frac{1 + \alpha^{\frac{1}{2}}}{(1 - \alpha)^{\frac{1}{2}}} \right); \\ &P = 0 \quad \text{at} \quad \Omega'_f(\boldsymbol{\xi}, t), \end{aligned} \tag{G.25}$$

with $\Omega'_f(\boldsymbol{\xi}, t)$ the flow front boundary.
Darcy's law, relating the superficial velocity $\boldsymbol{u}$ to the pressure gradient ∇P is written as:

$$\boldsymbol{u} = -\frac{K_{eff}}{\mu} \nabla P, \tag{G.26}$$

with K_{eff} the effective permeability, defined as $K_{eff} = \sqrt{K_1 K_2}$ and μ is the fluid viscosity. Substitution of the transformed nabla operator yields an expression of the superficial flow $\boldsymbol{u}$ as a function of the pressure gradient in ξ and η direction:

$$\boldsymbol{u} = -\frac{K_{eff} \Delta P}{\mu} h^J \nabla P'. \tag{G.27}$$

The pressure gradient is now considered to be a function of ξ only[2]. This means that the flow front is assumed to be perfectly elliptical. The pressure and pressure gradient

[2]This approximation is allowed according to Adams *et al.* [159], who compared the approximated analytical solution with a numerical solution in which the pressure gradient in η–direction was not neglected

are assumed to reduce to:

$$P'(\xi) = \frac{\xi_f - \xi}{\xi_f - \xi_0}; \tag{G.28}$$

$$\frac{\mathrm{d}P'}{\mathrm{d}\xi} = \frac{-1}{\xi_f - \xi_0}. \tag{G.29}$$

Substitution of (G.28) in (G.27), yields an expression for the superficial velocity $\boldsymbol{u}$:

$$\boldsymbol{u} = \frac{K_{eff}\Delta P}{\mu}\frac{h^J}{\xi_f - \xi_0}; \tag{G.30}$$

Secondly, the flow front velocity can be expressed as the time derivative of the coordinates:

$$\boldsymbol{v} = \left.\frac{\mathrm{d}\boldsymbol{x}}{\mathrm{d}t}\right|_{\xi=\xi_f} = \left(h^J\right)^{-1}\left.\frac{\mathrm{d}\boldsymbol{\xi}}{\mathrm{d}t}\right|_{\xi=\xi_f}. \tag{G.31}$$

Again, the η dependence is neglected. Combining (G.30) and (G.31) results in a first order differential equation of the flow front coordinate ξ_f. Note that the superficial velocity has to be divided by the porosity ϕ.

$$\boldsymbol{v} = \frac{\boldsymbol{u}}{\phi}. \tag{G.32}$$

$$\frac{\mathrm{d}\xi_f}{\mathrm{d}t} = \frac{K_{eff}\Delta P}{\mu\phi}\frac{\left(h^J\right)^2}{\xi_f - \xi_0}. \tag{G.33}$$

with

$$\xi_f = \xi_0 \quad \text{at} \quad t = 0. \tag{G.34}$$

A solution of this differential equation is:

$$F(\xi_f,\eta) = (\xi_f - \xi_0)\left(\frac{\sin 2\xi_f}{4} + \frac{\xi_f}{2}\right) - \frac{\cos^2\eta\,(\xi_f - \xi_0)^2}{2} + \frac{\cosh 2\xi_0 - \cosh 2\xi_f}{8} + \frac{\xi_0^2 - \xi_f^2}{4} = \frac{\alpha}{1-\alpha}\,\frac{K_1\Delta P}{\phi\mu r_0^2}\,t. \tag{G.35}$$

Note that the function value of $F(\xi_f,\eta)$ is not constant on the perimeter of the flow front ellipse.

Fit of the Anisotropy The flow front ellipses, obtained from the images of the digital video, allow the evaluation of $F(\xi_f,\eta)$ in different points. The function $F(\xi_f,\eta)$ can be evaluated in a number of specific points, namely at the locations $\boldsymbol{x}^P = \{r_1, 0\}$ and $\boldsymbol{x}^P = \{0, r_2\}$. The elliptical extents $\boldsymbol{\xi}$ can be derived explicitly for these coordinates:

$$\begin{aligned} \boldsymbol{x}^P = \{r_1, 0\} &\rightarrow \boldsymbol{\xi} = \left\{\operatorname{arccosh}\frac{\alpha^{\frac{1}{4}} r_1}{L_f}, 0\right\} \\ \boldsymbol{x}^P = \{0, r_2\} &\rightarrow \boldsymbol{\xi} = \left\{\operatorname{arcsinh}\frac{\alpha^{-\frac{1}{4}} r_2}{L_f}, \frac{\pi}{2}\right\}, \end{aligned} \tag{G.36}$$

The elliptical extents of the flow front ellipses at all available points in time are evaluated employing (G.36). The function values of $F(\xi_f, \eta)$ are proportional to the time according to (G.35). The function values of $F(\xi_f, \eta)$ based on the experimental data do not necessarily lie on a straight line, as is shown in figure G.3. The deviation arises from the varying anisotropy and orientation of the ellipses, which were mentioned earlier. Moreover, the flow is unstable in the beginning of the measurement, resulting in a non–linear behaviour of $F(\xi_f, \eta)$ during the first seconds of the measurement. Generally, a stable situation is obtained after 5–10 seconds.

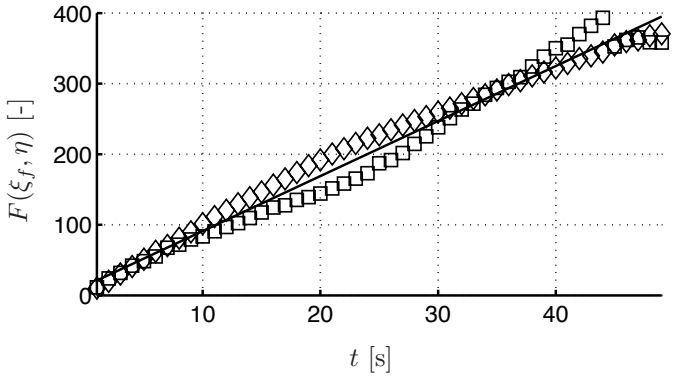

Figure G.3: *The function values $F(\xi_f, \eta)$ versus the time (□: $F(\xi_f, \eta)$ for $\boldsymbol{x}^P = \{r_1, 0\}$, ◇: $F(\xi_f, \eta)$ for $\boldsymbol{x}^P = \{0, r_2\}$). The solid line indicates the fitted, straight line, that follows from the theory. (Data from fabric B1 –* Saertex *$\pm 45^o$)*

The anisotropy α in the last function of (G.35) applies to all flow front ellipses, which not necessarily corresponds to the value of the anisotropy calculated by the fitting procedure. An optimisation procedure is employed to find an overall anisotropy that fits best with the ellipse anisotropies. The anisotropy as defined in (G.16) is therefore relaxed: α in (G.20) is substituted by an iterated anisotropy $\tilde{\alpha}$ for all ellipses. The aim of the optimisation procedure is to find an anisotropy $\tilde{\alpha}$ for which the deviation between the function values of $F(\xi_f, \eta)$ and the straight line $F_{theo}(t) = a_1 \cdot t + a_2$ (the straight line in figure 4.2) is minimal, with a_1 the slope of the line and a_2 a constant. A least square approximation is employed for this purpose.

Major and Minor Permeability The function $F(\xi_f, \eta)$ is then plotted as a function of the time. The anisotropy has to be solved iteratively. The optimal anisotropy minimises the deviation with the slope of the least square fitted line. The slope a_1 of the line is proportional to the permeability in the first principal direction:

$$a_1 = \frac{K_1 \Delta P}{\phi \mu r_0^2} \frac{\alpha}{1-\alpha} \rightarrow K_1 = \frac{a_1 \phi \mu r_0^2}{\Delta P} \frac{1-\alpha}{\alpha}. \tag{G.37}$$

The minor permeability K_2 is found by multiplying the major permeability with the anisotropy, according to (G.16).

Appendix H

Datasheets

H.1 Polyol

APPLICATIONS

- *Negatives, moulds, masters and mock-ups using the unfilled product or filled with RZ 30150 mineral filler in order to limit exotherm and to get easy machining.*
- *Thermoforming masters using the product filled with RZ 209/6 aluminium powder in order to increase thermal conductivity.*

PROPERTIES

- *Good impact resistance*
- *Fast demoulding*
- *Low shrinkage*
- *Low viscosity*
- *Easy–to–use mix ratio (1:1 by weight)*
- *High filler content possible while retaining a low viscosity*

Physical Properties

Composition		Part A Polyol	Part B Isocyanate	Unfilled mixing	Mixing filled with RZ 30150
Mixing ratio by weight		100	100	–	360
Aspect		liquid	liquid	liquid	liquid
Colour		off–white	light amber	beige	beige
Brookfield LVT viscosity at 25°C (mPa·s)		55	45	50	2700
Density of parts before mixing	ISO 1675–85	0.91–0.97	1.07–1.13	–	–
Density of cured mixing	ISO 2781–88	–	–	1.05–1.11	1.64–1.70
Pot life at 25°C on 200g (min)				3'20–3'40	

Mechanical Properties at 23°C (1)

			Unfilled mixing	Mixing filled with 360 phr RZ 30150
Hardness	ISO 868–85	Shore D1	70	82
Flexural modulus of elasticity	ISO 178–93	MPa	1100	3900
Flexural strength	ISO 178–93	MPa	42	46
Compressive strength	ISO 604–93	MPa	38	54
Charpy impact resistance	ISO 1791/D	kJ/m^2	25	–

(1): Average values obtained on standardised specimens/Hardening 14 hours at 60°C.

Thermal and Specific Properties at 23°C (1)				
			Unfilled mixing	Mixing filled with 360 phr RZ 30150
Glass Transition Temperature	T.M.A.–Mettler	°C		80
Linear shrinkage (thickness 50mm)		%	–	0.23
Coefficient of thermal expansion [+20,+70]°C	T.M.A.–Mettler	10^{-6} K^{-1}	–	76
Demolding time at 25°C				
– thickness:10mm		min.	45	
– thickness:40mm		min.		30

PROCESSING CONDITIONS

Before use part A (polyol) must be mixed until both colour and aspect become homogeneous. Both parts (polyol and isocyanate) must be mixed at a temperature above 18°C according to the mix ratio indicated on this technical data sheet. For casting thicknesses above 5mm it is recommended to add a filler as follows:

- *up to 360 phr of RZ 30150 filler (mineral filler)*
- *up to 400 phr of RZ 209/6 filler (aluminium powder)*

for thicknesses no more than 40 mm.

STORAGE CONDITIONS

Shelf life of both components is 12 months in a dry place and in their original unopened containers at a temperature between 15 to 25°C. Isocyanate is UV sensitive. It must be kept in its original container protected from the light. Any open can must be tightly closed under dry inert gas (dry air, nitrogen, etc.).

HANDLING PRECAUTIONS

Normal health and safety precautions should be observed when handling these products:

- *ensure good ventilation*
- *wear gloves and safety glasses*

For further information, please consult the product safety data sheet.

PACKAGING

Part A	*Part B*
1×4.5kg	*1×4.5kg*
6×0.9kg	*6×0.9kg*
1×18.0kg	*1×18.0kg*
1×50.0kg	*1×50.0kg*

GUARANTEE

Information of our technical data sheet is based on our present knowledge and the result of tests conducted under precise conditions. It is the responsibility of the user to determine the suitability of AXSON products for his application under his own conditions. AXSON refuses any guarantee about the compatibility of a product with any particular application. AXSON disclaims all responsibility for damage from any incident which results from the use of these products. The guarantee conditions are regulated by our general sale conditions.

H.2 Ardrox BioPen p6f5

Please read the technical information and safety data sheets before use.

CONTENTS

- R36/38. Irritating for the eyes and the skin.
- S24/25. Avoid contact with the eyes and the skin.
- S26. Flush extensively with water and apply for expert medical advice in case of contact with the eyes.
- S37/39 Wear appropriate gloves and a protection for the eyes and face.

COMPANY INFORMATION

Company	: Chemetall
Country	: Netherlands
Streetaddress	: IJsselstraat 41
Postal Code	: NL-5347 KG
City	: Oss
Phone	: +31 412 681 888
Fax	: +31 412 631 675
Web	: http://www.chemetall.be
Direct Contact	: info.benelux@chemetall.com

Appendix I

Viscosity Measurements

I.1 Viscosity & Temperature Dependence

The viscosity of Polyol was measured as a function of the temperature. A plate–plate viscosity measurement in oscillating mode was used. The parameters for the measurement are presented in table I.1.

Table I.1: *Measuring conditions and settings for the plate-plate viscosity measurement performed by the NLR.*

Diameter plates	[mm]	40
Gap	[μm]	200
Mode		oscillating
Frequency	[Hz]	1.59
Target strain	[-]	0.375
Temperature range	[^{o}C]	20–40

The temperature is varied between 20^{o}C and 40^{o}C, with steps of 5^{o}C. The temperature was kept constant for a period of 10–15 minutes, during which the actual measurement is performed. A temperature rate of 1^{o}C/minute was applied to increase the temperature to the next level. The temperature profile during the measurement is depicted in figure I.1. The time spans over which the viscosity is determined for each temperature level, is indicated by Δt_i.
The viscosity is averaged over the time span in which the temperature is kept at a constant level. The sample rate of is approximately 1/15Hz, resulting in 20 to 40 data points over which the viscosity is averaged. The mean value of the viscosity for each temperature is depicted in figure I.2. The variability is indicated by the error bars. The variation s is defined as:

$$s = \frac{t_{0.95}(N-1)\sigma}{\sqrt{N}}, \tag{I.1}$$

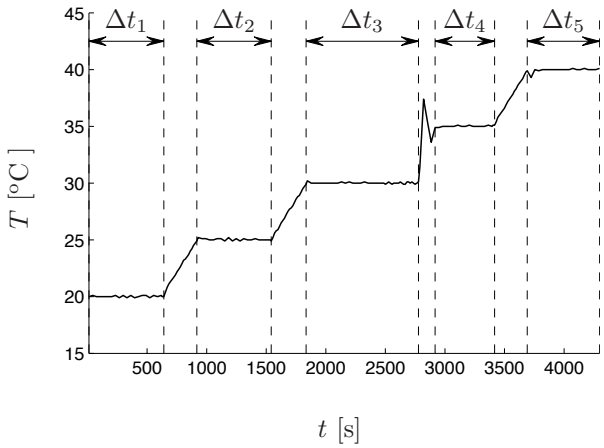

Figure I.1: *The temperature profile during the measurement. Δt_i refers to the time span over which the viscosity is determined for the i^{th} temperature level.*

with $t_{0.95}$ the student–t distribution with $N-1$ degrees of freedom and a 95% confidence interval, σ the estimated standard deviation and N the number of elements in the set. The values of the means and variations are collected in table I.2.

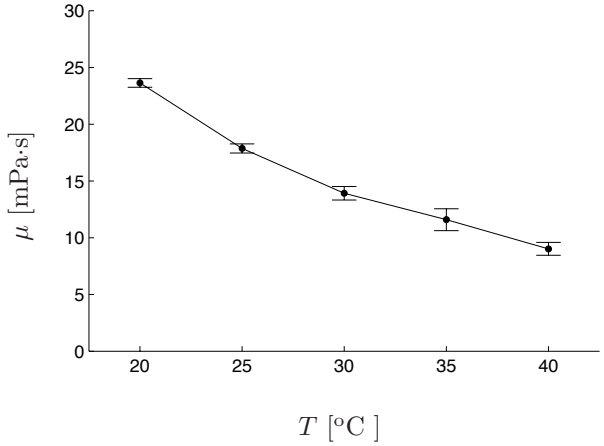

Figure I.2: *The viscosity of Polyol as a function of the temperature. The error bars indicate the variation on the measured mean for each temperature level.*

Table I.2: *The viscosity for different temperatures. The mean value $\bar{\mu}$, variation s and number of data points N at each temperature level T.*

T [°C]	$\bar{\mu}$ [mPa·s]	s [mPa·s]	N [-]
20	23.64	0.38	22
25	17.87	0.40	22
30	13.91	0.59	45
35	11.59	0.96	19
40	9.02	0.59	20

I.2 Capillary Viscometer Measurements

The viscosity of the Polyol–BioPen mixture was measured using a capillary viscometer (Schott Geräte, ref. no. 053 92). A schematic drawing of a capillary viscometer is presented in figure I.3. A complete description of the measurement can be found in [166, 167].
The time that the fluid level needs to drop from the upper timing mark (m_1) to the lower timing mark (m_2) is a measure for the viscosity of the fluid. The entire device is submerged in a water reservoir which temperature is controlled (≈20°C for these measurements). A capillary with a diameter of 1.03mm was used (capillary 'II' [166, 167]), which is suitable for viscosities between 10 and 100mPa·s.
The relation between the time span t and the viscosity for the given capillary is [166, 167]:

$$\mu = 0.1003 \cdot 10^{-6} \rho t, \tag{I.2}$$

with ρ the density of Polyol which is $0.94 \times 10^3 \mathrm{kg \cdot m^{-3}}$. The density of the mixture is unknown and is hard to determine, since the mixing ratio was only measured roughly. The density of pure Polyol was used.
Three fresh samples were prepared (6:1, 12:1 and 28:1 volume ratio) and one sample of used Polyol–BioPen mixture is measured (mixing ratio 25:1 by volume). Three measurements were performed for each sample. The temperature of the water was measured prior to each measurement. The results are presented in table I.3.

Table I.3: *Measured viscosities of all samples (μ in mPa·s and T in °C).*

	6:1		12:1		28:1		25:1	
	μ	T	μ	T	μ	T	μ	T
1	29.48	19.1	28.78	20.2	28.61	20.1	34.51	20.6
2	29.50	20.6	28.93	19.2	28.55	19.8	34.52	20.4
3	29.57	20.3	28.79	20.2	28.52	20.4	34.48	20.2
$\bar{\mu}$	29.52		28.83		28.56		34.50	

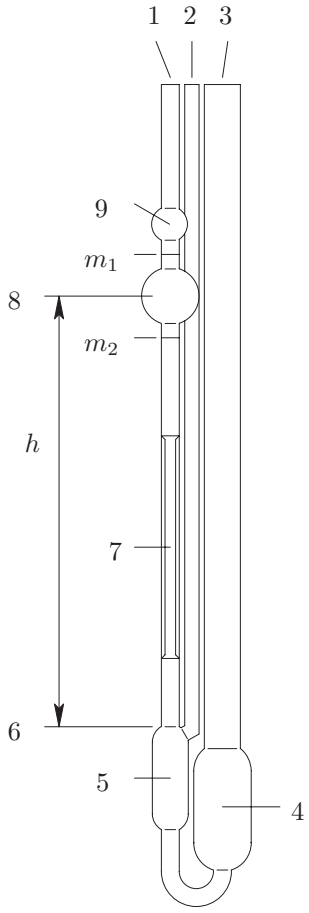

1: Capillary tube
2: Venting tube
3: Filling tube
4: Reservoir
5: Reference level vessel
6: Dome–shaped top part
7: Capillary
8: Measuring sphere
9: Pre–run sphere
m_1: Upper timing mark
m_2: Lower timing mark
h: Mean hydrostatic head

Figure I.3: *Schematic drawing of a capillary viscometer.*

The mixing ratio hardly influences the viscosity. The time of usage of the mixture has a stronger effect, which may either be caused by water absorption of the Polyol, or by small particles in the mixture from the experiments (the sample was not filtered after each time it was used). The mixture used in the experiments was: 1148.9 grams Polyol and 51.8 grams Ardrox BioPen, which is roughly 25:1 by volume.

Appendix J

Data In–Plane Measurements

This appendix contains the experimental data of the experiments that were described in chapter 4. The abbreviations for the fabrics refer to the following fabrics (as in the main text):

B1	Biaxial	±45°	tricot warp knitted fabric	(Saertex)
B2	Biaxial	0°/90°	tricot/chian warp knitted fabric	(Saertex)
B3	Biaxial	±45°	chain warp knitted fabric	(Devold)
T	Triaxial	+45°/90°/-45°	chain warp knitted fabric	(Devold)
Q	Quadriaxial	+45°/0°/-45°/90°	chain warp knitted fabric	(Devold)

J.1 NLR

Table J.1: *The orientation θ of the machine direction of the fabric with respect to the tooling, the measured pressure differences ΔP_{unsat} and ΔP_{sat} for the unsaturated and saturated flow, the point in time t_{unsat} at which the unsaturated permeability (activation of second pressure transducer) is determined and the start of the saturated flow t_{sat} and the flow rate Φ, the (un)saturated permeabilities (K_{unsat} and K_{sat}) and the anisotropy α, including its upper and lower limit.*

	θ [°]	ΔP_{unsat} [bar]	ΔP_{sat} [bar]	t_{unsat} [s]	t_{sat} [s]	Φ [$m^3 \cdot s^{-1}$]$\times 10^{-6}$	K_{unsat} [m^2]$\times 10^{-11}$	K_{sat} [m^2]$\times 10^{-11}$	α [-]	α [-]
B3	0	1.49	1.45	630	795	0.27	9.63	11.9		
		0.81	0.71	540	795	0.27	6.35	7.07		
		0.77	0.70	555	780	0.28	6.24	7.05		
	45	0.01	0.01	–	–	0.33	489.0	594.1		
		0.02	0.02	–	–	0.44	511.3	356.8	$0.97^{+0.40}_{-0.32}$	$1.02^{+0.41}_{-0.33}$
		0.02	0.02	–	–	0.36	1173	321.9		
	90	0.70	0.66	–	–	0.28	6.25	8.19		
		0.61	0.65	–	–	0.25	6.80	8.27		
		0.49	0.44	–	–	0.25	8.54	10.08		
T	0	0.65	0.44	465	690	0.27	5.49	9.27		
		0.76	0.58	525	705	0.27	5.22	7.12		
		0.43	0.41	105	165	0.28	7.79	7.05		
	45	0.21	0.17	–	–	0.27	19.70	27.70		
		0.17	0.13	–	–	0.27	25.03	32.03	$0.40^{+0.15}_{-0.12}$	$0.31^{+0.17}_{-0.08}$
		0.12	0.12	–	–	0.26	31.40	38.65		
	90	1.82	1.72	330	525	0.27	2.18	2.43		
		1.74	1.56	390	540	0.27	2.42	2.59		
		1.39	1.17	360	555	0.27	2.89	3.44		
Q	0	0.53	0.34	375	555	0.27	8.45	13.97		
		0.72	0.52	330	480	0.27	7.79	10.03		
		0.21	0.18	315	495	0.29	17.09	28.37		
	45	0.15	0.12	–	–	0.26	31.38	40.66		
		0.14	0.14	–	–	0.26	31.27	36.09	$1.29^{+0.71}_{-0.62}$	$0.88^{+0.78}_{-0.38}$
		0.14	0.14	–	-	0.27	33.36	37.22		
	90	0.41	0.37	525	750	0.28	14.24	14.97		
		0.42	0.37	525	714	0.28	13.18	14.12		
		0.35	0.31	555	705	0.28	15.56	16.62		

J.2 KU Leuven

Table J.2: *Settings and measured injection pressure of the various measurements on the fabrics B1, B2 and T using the KU Leuven test–rig (shear angle γ; cavity height h_c; fibre content V_f; injection pressure P_{inj}, with averaged $\bar{P}$, variation σ) and the parameters (M_0, M_{max}, t^*, a) of the power–law fit for the mass flow rate, including the relative error ε of the fit.*

				P_{inj} [bar]		Mass flow parameters				
	γ[°]	h_c [mm]	V_f [%]	$\bar{P}$	σ	M_0 [kg]	M_{max} [kg]	t^* [s]	a [-]	ε [-]
B1	0	0.5	36.18	1.10	0.011	0	0.030	5.63	0.82	0.0062
	0	0.5	36.18	1.10	0.017	0	0.057	3.89	0.64	0.0268
	0	0.5	36.18	1.09	0.010	0	0.037	22.97	0.74	0.0187
	0	0.5	36.18	0.61	0.011	0	0.056	4.37	1.51	0.0029
	30	0.5	41.78	0.61	0.014	0	0.058	4.26	1.95	0.0034
	30	0.5	41.78	0.61	0.011	0	0.055	3.72	1.30	0.0027
	30	0.5	41.78	0.61	0.011	0	0.061	4.50	1.30	0.0040
	45	0.5	52.17	0.62	0.012	0	0.071	10.83	1.09	0.0112
	45	0.5	52.17	0.61	0.013	0	0.086	6.64	1.04	0.0093
	45	0.5	52.17	0.62	0.011	0	0.070	12.51	0.99	0.1015
B2	0	0.5	36.97	1.10	0.011	0	0.038	3.23	0.72	0.0049
	0	0.5	36.97	1.11	0.031	0	0.040	0.85	0.75	0.0037
	0	0.5	36.97	1.10	0.031	0	0.027	5.64	0.77	0.0061
	0	0.5	36.97	0.61	0.012	0	0.064	2.59	1.30	0.0047
	30	0.5	42.68	1.09	0.016	0	0.078	2.93	1.91	0.0021
	30	0.5	42.68	0.61	0.011	0	0.062	4.80	1.70	0.0035
	30	0.5	42.68	0.61	0.014	0	0.064	5.61	1.47	0.0043
	45	0.5	52.28	0.61	0.024	0	0.062	10.91	1.03	0.0287
	45	0.5	52.28	0.61	0.012	0	0.063	10.21	1.07	0.0272
	45	0.5	52.28	0.61	0.012	0	0.052	5.75	1.16	0.0102
T	0	4.0	56.25	2.03	–	–	–	–	–	–
	0	4.0	56.25	1.52	–	–	–	–	–	–
	0	4.0	56.25	1.52	–	–	–	–	–	–

J.3 UT

Table J.3: *Settings and results of the measurements on the fabric B3 performed with the test–rig of the UT (fibre content V_f; cavity height h_c; pressure drop ΔP; permeability in machine direction K^0; volumetric flow Φ). The permeabilities between brackets are the equivalent values for a fibre content of 56.69%. The superscript 1 refers to the permeability based on a fit through all 6 data points, whereas the superscript 2 refers to the permeability based on a fit through the last 4 data points only.*

layers	V_f	h_c	ΔP [bar]		K^0 [m^2]$\times 10^{-9}$			Φ
[–]	[%]	[mm]	unsat	sat	unsat^1	unsat^2	sat	[m^3·s^{-1}]
1	50.28	0.6	0.56	0.50	0.75 (0.39)	0.92 (0.48)	2.56 (1.34)	1.56
1	50.28	0.6	0.57	0.51	0.76 (0.39)	0.90 (0.47)	2.88 (1.54)	1.75
1	50.28	0.6	0.65	0.57	0.65 (0.34)	0.85 (0.44)	1.53 (0.79)	1.04
1	50.28	0.6	0.67	0.56	0.76 (0.39)	0.88 (0.46)	2.64 (1.37)	1.76
1	50.28	0.6	0.72	0.62	0.86 (0.45)	0.96 (0.50)	5.17 (2.69)	3.82
2	54.85	1.1	0.85	0.69	0.44 (0.36)	0.54 (0.45)	0.64 (0.53)	0.97
2	54.85	1.1	0.61	0.54	0.41 (0.34)	0.53 (0.44)	0.49 (0.40)	0.59
2	54.85	1.1	1.04	0.83	0.38 (0.31)	0.53 (0.43)	0.90 (0.75)	1.65
4	57.45	2.1	1.62	1.10	0.29 (0.32)	0.45 (0.49)	0.91 (0.99)	4.22
4	57.45	2.1	1.51	1.12	0.44 (0.45)	0.53 (0.58)	0.86 (0.93)	4.03
4	57.45	2.1	1.46	1.04	0.45 (0.49)	0.57 (0.62)	0.78 (0.85)	3.41
4	57.45	2.1	1.49	1.02	0.46 (0.50)	0.55 (0.60)	1.03 (1.11)	4.39
4	57.45	2.1	1.48	1.10	0.40 (0.44)	0.50 (0.54)	1.07 (1.16)	4.96

Nawoord

Uiteraard begrijp ik dat dit een van de weinige delen in het proefschrift is, dat door velen niet alleen gelezen, maar zelfs *grondig* gelezen zal worden. Niet zo vreemd natuurlijk, want dit is hét hoofdstuk waar misschien ook u/jij genoemd zal worden. Daarnaast is het ook eindelijk eens een stukje luchtige tekst na al die taaie kost.

Dat stelt mij echter onmiddellijk voor twee problemen. Ten eerste het schrijven van een vlot leesbaar stukje tekst, met liefst hier en daar een snufje humor, dat óók nog eens niet te lang is. Of dat uiteindelijk gelukt zal zijn, is niet aan mij om te oordelen, laat staan er op vooruit te lopen. Het is echter ook niet het belangrijkste dat ik hiermee beoog te bereiken. Het tweede probleem is van belangwekkender aard: het behelst de onmogelijke taak om een volledige lijst van personen te produceren, die al dan niet bewust bijgedragen hebben aan de succesvolle afronding van de afgelopen vier en een half jaar.

Het complementeren van de lijst mag dan misschien een heikele zaak zijn, het begin is het absoluut niet. Niet omdat het traditie en gebruik is om je promotor als eerste te noemen, maar omdat je, eenmaal op dit punt aanbeland, weet dat hij zo'n cruciale rol gespeeld heeft, dat je er simpelweg niet om heen kan hem als eerste te noemen. Remko, bedankt voor de bron van motivatie die je geweest bent voor mij in de afgelopen jaren, de mogelijkheden die je me geboden hebt, en de – in geval van aanwezigheid – altijd openstaande deur. Ook 'buiten werktijd'.

Meteen daarop volgend: Stepan Lomov. Tijdens mijn verblijf in Leuven werkte ik onder zijn motiverende leiding, resulterend in een duidelijk herkenbare invloed in de inhoud van dit proefschrift: De tijd in Leuven heeft me een goede schop in de eindrichting gegeven. Daarnaast heb ik Stepan Lomov ook mogen leren kennen als een vriendelijk en gastvrij man, onder andere tijdens de keren dat ik bij hem (en zijn vrouw Almira) thuis hartelijk ontvangen werd met heerlijk eten, lekkere wijn en goede gesprekken. Stepan: Хотя вы всегда просили меня писать по–голландски, в этот раз я напишу по–русски – огромное спасибо за плодотворное сотрудинчество, которое, я надеюсь, мы продолжим и в будущем.*

Vanuit het NLR was Marcelo 'o Brasileiro' Müller betrokken bij het project. Het enthousiasme waarmee hij telkens naar Enschede afreisde of ons op het NLR ontving, mag dan misschien voornamelijk door de herinnering aan het IAF gevoed zijn geweest, zijn inzet voor het project is daardoor eerder meer dan minder gewaardeerd door mij. Daarnaast heeft het NLR altijd garant gestaan voor – vanzelfsprekende – hulp in

praktische zin: het leveren van grondstoffen voor experimenten, het verrichten van metingen, het geven van advies. Het enthousiasme waarmee dat gedaan werd is echter níet zonder meer vanzelfsprekend: heren bedankt!
Voor de leden van de 'gebruikers commissie' van het UT–NLR project geldt hetzelfde: hun bijdrage bleef niet beperkt tot tweemaal per jaar op komen draven. Telkens ervoer ik een betrokken en kritische houding ten opzichte van het project en mijn werk.
En dan – ook heel klassiek – zijn nu mijn (oud–)collega's aan de beurt. "Jongens, bedankt!" Nee, zó makkelijk komen jullie er niet vanaf. Allereerst: zonder de praktische inzichten en de hulp van Laurent zou het experimentele werk dat ik verricht heb van hetzelfde niveau zijn als mijn mountainbike niveau. Dan: de opbouwende kritieken van Ton zijn mij bijzonder waardevol gebleken tijdens het schrijven. En verder hebben Edwin, Sebastiaan, René, Blasimir, Robert, Roy, Erik, Durk, Salma en Ashok en alle (oud–)collega's van de vakgroep Technische Mechanica, garant gestaan voor een bijzonder prettige werk(–leef)omgeving, waarin discussies over modellen, discretisaties, partiële differentiaties en andere voor velen minder enerverende onderwerpen, moeiteloos afgewisseld werden met fietsen, mountainbiken, bier, film, politiek en alle andere zaken waar je het zoal op een vrijdag over hebt.
Daarbij aansluitend wil ik ook de studenten noemen die hun HBO of UT eindopdracht binnen mijn onderzoeksveld hebben gedaan. Zonder hen was het experimentele werk beperkt gebleven en was de opzet van het netwerk model zeker stroever gelopen. Rien, Marc, Nanne, Gerrit–Jan, Sebastiaan, Ivho, Johannes, Ivo en Wout: bedankt voor jullie bijdrage en de leuke samenwerking!
Hoe voorspelbaar – en evenzo, hoe noodzakelijk, want: hoe volstrekt hulpeloos ben je zonder zo nu en dan binnen te kunnen lopen voor wat snoep, een nutteloos babbeltje en al die onnoembare, maar wél relevante dingen die Debbie, Belinda en Tanja voor mij geregeld hebben in de afgelopen jaren.
I had more collegues than just those in Enschede. Well, in fact they are not just collegues, but more than that: they are friends. The "Marie Curie" group, formed in Leuven. All of you had a large impact on me as a person. We worked very hard in Leuven, but there was always time for a 'beer seminar' – and I hope we will find opportunities for more beer seminars in the future. Marcin and Ania's wedding was the first outside Leuven; where and why will we meet in the future? To all of you*:
Ericka: La question essentielle n'est pas tant celle de la langue, Malgache, Français, Anglais, ou Suédois, mais plutôt celle de la façon dont je pourrais te remercier pour ton amitié depuis notre rencontre à Leuven.
Marcin: Rzadko można spotkać kogoś tak otwartego, szczerego i życzliwego jak Ty. Zawsze będę Wam wdzięczny za niespotykanie ciepłe przyjęcie przez Ciebie, Anie i Wasze rodziny podczas Waszego wesela.
Sergey: Получая от тебя самые лучшие виски, водку и текилу, ты и Света также принесли мне хорошую дружбу и верных друзей.
Dmitry: Определенно, что в будущем, кроме машиностроения ты найдешь себя и в философии, и в поэзии, и в литературе. Вот почему с тобой всергда чертовски приятно выпить пива (Hoegaarden).
David: Si te acuerdas? "De Wiering" – donde todos los Españoles se reunion? Bueno, una cerveza más y nos vamos a casa!

Matteo: Parmigiano e pere – Chi pensava potessero essere una buona combinazione? Chi pensava che un Italiano e un Olandese potessero instaurare un così bel rapporto?
En dan de anderen in Leuven: Isabel, Hilde, Thanh, Bart (Vangrimde), Frederik én – zeer belangrijk – de technici Jo, Kris, Manuël, Bart: zonder jullie was het experimentele werk dat ik in Leuven heb gedaan *zeker en vast* nooit gelukt!
En dan natuurlijk niet te vergeten: Stella Artois, Hoegaarden, Leffe, Florival, Grimbergen, Corsendonk, Morte Subite, Orval, Westmalle, Duvel, Maredsous, Karmeliet, Ramée, Tongerlo, Grolsch – jullie inspiratie is onmisbaar geweest!
Nog even terug naar Enschede: de Bata hardloop ploeg: Marieke, Genie, Ekke, Jaap, Clemens, Marco. Een aantal is afgevallen (misschien ook in kilo's...?), door vertrek uit Enschede of blessures. Desalwelteplus: het hardlopen is dankzij jullie altijd een uitermate ontspannende bezigheid geweest!
Hèhè – dat waren geloof ik de collega's. Er waren – gelukkig – nog meer mensen. Toen ik uit Leuven terug kwam, dreigde ik een klein beetje in een gat te vallen. Dat dat niet gebeurde is te danken aan een bijzondere groep vrienden: Betine, Peter en Mariska, broer Michael en Gerja, zusje Mariëlle en Johan. Jullie vriendschap is een enorme steun voor mij geweest in de laatste jaren van mijn promotie.
Ik ben blij dat het me gelukt is om tot aan het einde te blijven volleyballen. Sport doe je voor je eigen ontspanning, maar als je team en de vereniging niet zo leuk zijn als De Kater is, dan haak je toch af. Volleyballers en volleybalsters: bedankt!
Ik heb het niet vol kunnen houden om elke woensdag naar Westerhaar te rijden; De drumband – ik kon jullie gewoon even niet meer bijbenen. Mijn afwezigheid in de laatste periode van mijn promotie is echter zeker geen reflectie van de hoeveelheid plezier en ontspanning die ik door de jaren heen bij SDG genoten heb. De beste omschrijving hiervan is zonder meer: 'Winterswijk, de Boemel'.
Wim, Tineke, Marleen en Mathijs – jullie zijn een soort tweede familie voor mij. Al die geweldige vakanties, ver weg van alle stress en druk die er in de laatste tijd op mij lag, zijn voor mij onmisbaar (geweest)!
Als laatste: een onvoorwaardelijke bron van steun, waarvan ik me misschien niet altijd zo bewust ben geweest, maar gelukkig zeker in de laatste periode wel. Pap, Mam, bedankt voor jullie steun en het vertrouwen dat jullie altijd in me gehad hebben.

Enschede, April 2006

* The help of Igor Burchitz, Laurent Warnet, Paweł Owczarek, Blasimir Villa Rodriguez and Marco Razzetto with the translations is gratefully acknowledged.